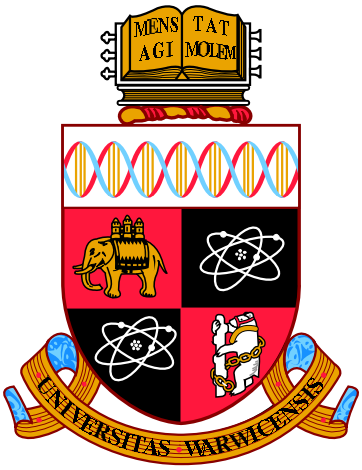

Multi-modal MHD Oscillations in the Solar Corona, and their use in Coronal Seismology

by

Timothy Duckenfield

Thesis

Submitted to the University of Warwick

for admission to the degree of

Doctor of Philosophy

Department of Physics

August 2020

THE UNIVERSITY OF WARWICK

Contents

List of Figures

List of Tables

Acknowledgments

It is a pleasure to thank many people for their help in the course of writing this thesis. I would especially like to thank Valery Nakariakov for his help and direction throughout my PhD. This included fruitful discussions, answering my myriad questions, and opportunities to attend workshops and conferences in far flung places. I am grateful for the stellar support and understanding imparted from my colleagues; Anne-Marie Broomhall, David Pascoe, Dmitrii Kolotkov and Sergey Anfinogentov. Their help with outreach, an appreciation of Markov chain Monte Carlo methods for inferring Bayesian statistics, the wonders of non-linearity and the baffling language of computers respectively. I also thank Alex Seaton, Chloe Pugh, Christopher Goddard, Tishtrya Mehta and Katie Kosak for illuminating discussion. I would like to thank Laura Fryer for her dedication to velocity picking. Finally I would like to thank my better half Jennifer Bendelow whose saintly patience, sage advice and sheer intelligence were always inspirational.

Declarations

This thesis is submitted to the University of Warwick in support of my application for the degree of Doctor of Philosophy. It has been composed by myself and has not been submitted in any previous application for any degree or other university. I declare that this thesis is my own work except where indicated.

The work presented in this thesis is based on the following peer-reviewed journal articles previously published by the author:

- *T. J. Duckenfield, C. R. Goddard, D. J. Pascoe, and V. M. Nakariakov. Observational signatures of the third harmonic in a decaying kink oscillation of a coronal loop.* Astron. Astrophys.*, 632:A64, dec 2019. ISSN 14320746. doi: 10.1051/0004-6361/201936822. URL https://ui.adsabs.harvard.edu/abs/2019A{&}A...632A..64D*. This forms the basis of Chapter 2.

- *T. J. Duckenfield, S. A. Anfinogentov, D. J. Pascoe, and V. M. Nakariakov. Detection of the Second Harmonic of Decay-less Kink Oscillations in the Solar Corona.* Astrophys. J.*, 854(1):L5, feb 2018. ISSN 2041-8213. doi: 10.3847/2041-8213/aaaaeb*. This forms the basis of Chapter 3.

The author acknowledges the contribution of Laura Fryer to the work conducted in Chapter. 4.

Some the results (indicated) have been partly reported at the following scientific conferences and workshops:

- UKMHD 2018, 26$^{\text{th}}$ - 28$^{\text{th}}$ March 2018, St Andrews, UK
  Part of the 60$^{\text{th}}$ British Applied Mathematics colloquium.
  Contributed talk: *Detection of the second harmonic of decay-less kink oscillations.* Pertains to: Chapter 3.

- BUKS 2018, 3rd - 7th September 2018, Tenerife, Spain

  Workshop "Waves and instabilities in the Solar Atmosphere" held in La Laguna, organised by the Instituto de Astrofisica de Canarias (IAC).

  Contributed talk: *First detection of the second harmonic of decay-less kink oscillations in a solar coronal loop.* Pertains to: Chapter 3.

- ISW 2018, 10rd - 7th September 2018, Irkutsk, Russia

  International Workshop "Eruptive energy release processes on the Sun and stars: origins and effect" held in the Institute of Solar-Terrestrial Physics SB RAS.

  Contributed talk: *Higher harmonics in decay-less kink oscillations: detection and implications.* Pertains to: Chapter 3.

- 9th Coronal Loops Workshop, 11th - 14th June 2019, St Andrews, UK

  Workshop held by the Solar & Magnetospheric Theory Group, University of St Andrews.

  Poster presentation: *Using spatio-temporal analysis of transverse loop oscillations.* Pertains to: Chapter 2.

- Invited seminar, 20th September 2019, IKI – Space Research Institute of Russian Academy of Sciences, St Petersburg, Russia

  Seminar: *Using slow modes from sunspots to probe the thermal structuring of coronal loops.* Pertains to: Chapter 4.

Abstract

The solar atmosphere is a dynamic, inhomogeneous environment which acts as a natural plasma laboratory for a keen community of observers and researchers at the forefront of modern physics. Colossal plasma non-uniformities on the Sun are seen to host a wide variety of magnetoacoustic oscillatory motions, which may be used as probes into the local plasma conditions using the theory of long wavelength, large scale magnetohydrodynamics (MHD): this process is known as coronal seismology. The focus of this thesis is to contribute to the detailed observation of these waves and their use in coronal seismology, particularly the usefulness of observing multiple harmonics and understanding of dispersion.

Fast kink-mode oscillations of coronal loops, observed as rapidly decaying transverse displacements, are a well-understood wave mode used for seismology. The simultaneous detection of multiple harmonics can provide more information, allowing one to match the observed dispersion with that predicted by theory. Extreme ultraviolet observations of a coronal loop hosting a standing kink oscillation are analysed using image processing and time series techniques. The presence of two simultaneous harmonics is revealed, a fundamental mode at a period of ~ 8 minutes and its third harmonic at ~ 2.6 minutes. The ratio of periods $P_1/3P_3$ was found to be ~ 0.87, whose departure from unity indicates a non-uniform distribution of kink speed through the loop. For all locations, the ratio of damping time to period for the two harmonics were found to agree within error, validating the widely assumed 1d resonant absorption theory used to explain a kink oscillation's rapid damping. This is the first time a measurement of the signal quality for a higher harmonic of a kink oscillation has been reported with spatially resolved data.

One exciting development in coronal seismology is the recent detection of decay-less oscillations, which are a different regime of fast-kink oscillations omnipresent in coronal loops. The first detection of a coronal loop exhibiting multi-modal decay-less oscillations is presented, in which both the loop's fundamental mode ($P_1 = 10.3^{+1.5}_{-1.7}$ minutes) and its second harmonic ($P_2 = 7.4^{+1.1}_{-1.3}$ minutes) are detected. To make this detection possible, the observational data was passed through a novel motion magnification algorithm to accentuate transverse oscillations. An illustration of seismology using the ratio $P_1/2P_2 \sim 0.7$ to estimate the density scale height is presented. The existence of multiple harmonics has implications for understanding the driving and damping mechanisms for decay-less oscillations, and adds credence to their interpretation as standing kink mode oscillations.

There is a myriad of MHD oscillation modes, and whilst fast-kink modes are observed as transverse displacements of the plasma non-uniformity, slow modes may be observed as intensity enhancements. Analysis of such propagating slow modes observed in a fan of coronal loops above a sunspot is performed. The instantaneous velocities and periods of these intensity enhancements are measured and compared in different temperature passbands and azimuthal angles. The waves seen in the 171Å channel (~ 0.6 MK) appeared slower than when observed co-spatially in the 193Å (~ 1.58 MK). This contradicts the expectation that the phase speed is approximately the local sound speed, which varies as the square root of the temperature. This discrepancy is resolved by attributing the difference in apparent velocity to different inclination angles, which are estimated to be $9^\circ \pm 3^\circ$ from the vertical for the waves seen in 193 Å, and $19^\circ \pm 4^\circ$ when seen in 171 Å. This provides some evidence supporting the theory that coronal loops are formed of several distinct, unresolved strands of different temperature.

From the theoretical point of view, the dispersion relation governing slow MHD modes in the presence of a wave-induced misbalance between the plasma heating and cooling mechanisms is developed. The thin flux tube approximation is used to account for finite-β effects, and thermal conduction is also included. The dispersion relation in the limits of weak non-adiabaticity and strong non-adiabaticity with finite-β is identified. It is found that the characteristic timescales of this

imbalance (e.g. damping time) may be expressed in terms of the partial derivatives of the combined heating/cooling function with respect to constant gas pressure and constant magnetic pressure. Moreover, these characteristic timescales for the thermal misbalance coincide with typical MHD wave periods for a large range of densities and temperatures typical of the corona. Thus in the general case the dispersion on slow waves by the wave-induced thermal misbalance should not be neglected, and its inclusion may resolve some contradictions that have arisen when attributing the rapid damping of slow modes to thermal conduction or compressive viscosity alone.

Instability criteria for the slow mode and entropy (thermal) mode are expressed in terms of a parameterisation of the unknown coronal heating function, under this thin flux tube approximation. Finally, noting that observations of slow modes in the corona do not show over-stability, and that the thermal mode does not appear to be unstable in general (with the exception of coronal rain), a new way of constraining the coronal heating function is presented.

Chapter 1

Introduction

In order to gain information about the Sun's behaviour and state through the study of magnetoacoustic waves in its atmosphere, appreciation for the Sun's composition, and the transfer of energy – from liberation in the core through to the observation of sunlight – is necessary. Such phenomenological understanding must be married with a mathematical model of the waves themselves. When these are unified to provide a context, the scrutinising of waves becomes a powerful tool with which the Sun may be probed.

1.1 The Sun

It is no exaggeration to say that the Sun has been central to humanity for our entire existence. All life on Earth owes its existence to the Sun's energy, and countless cultures have worshipped and deified Earth's host star. Philosophers such as Socrates have even equated the Sun with the "idea of goodness" itself, proposing that what sunlight is to making the unknown visible, so goodness is to being, or put another way sight without light is like a mind without goodness – it is only through illumination by the Sun that we can see the world around us (as written by Plato, book 6 Republic). This sentiment remains as true nowadays as ever, and as our knowledge of the universe expands our need for understanding plasma physics becomes increasingly important in order to address challenges such as harnessing nuclear fusion or protecting the satellites that form the backbone of modern infrastructure. The Sun acts as a 24 hour natural plasma laboratory, representing a dizzyingly wide array of different spatial scales, plasma densities and temperatures, and hosting the largest waves ever resolved in both space and time. Although in galactic terms the Sun is rather middling – middle aged at 4.5 billion years old, middle sized at radius $R_\odot \approx 6.96 \times 10^8$ m, middle weight class at a mere $M_\odot \approx 1.99 \times 10^{30}$ kg, middle rotation rate at about 27 days, and even sitting in

the middle of the famous Hertzsprung-Russell diagram – the Sun expresses complex behaviour that challenges researchers on even the most fundamental points.

The solar magnetic field is the main culprit in this complexity, and though it does have a dipolar component the magnetic field in general is very inhomogeneous. The magnetic field and the plasma are conjoined such that as one moves, the other is dragged with it. Consequently the existence of flows and plasma inhomogeneities necessarily imply some non-uniform magnetic field. Importantly for Earth's space weather, this solar magnetic field explosively releases colossal amounts of energy through non-ideal processes such as *magnetic reconnection*. Observations of increasing resolution and sensitivity from the last few centuries show that these processes lead to a dynamic atmosphere rich with transient phenomena. These include short-lived hot jets called *spicules*, impulsive explosions such as *flares* and *coronal mass ejections* – with released energy that can go beyond the equivalent of 20 million nuclear bombs – also cold regions of intense magnetic field called *sunspots*, mountains of plasma as heavy as 100 billion kilograms levitating above the surface called *prominences*, the constant shedding of material into the *solar wind* with fluctuating speed and intensity, the list goes on. Thus the Sun's reputation in astronomy as an average, simple, slowly evolving ball of plasma does a disservice to its many veiled mysteries. One way to unveil these mysteries is *coronal seismology*, which this thesis is about: the detection and analysis of waves and oscillations observed in the corona, combined with analytic theory or numerical modelling of the wave modes, allowing the local plasma parameters to be determined.

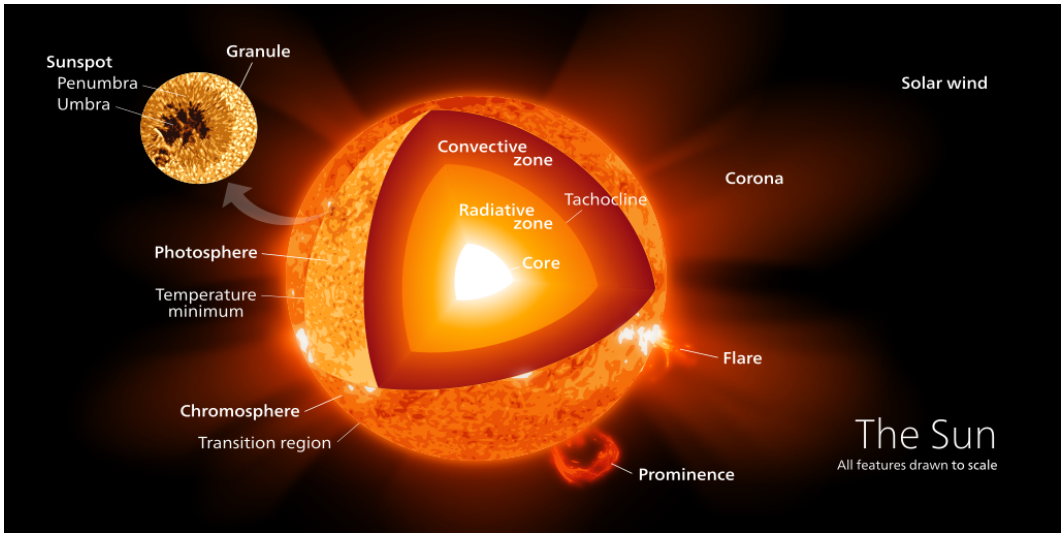

Figure 1.1: Structure of the Sun. – *Attribution: Kelvinsong (License: CC BY-SA 3.0)*

1.1.1 The solar interior

The Sun is modelled as a perfect sphere of radius $R_\odot$, made of plasma comprised predominantly of hydrogen and to a lesser extent helium (Payne 1925). Inside is a core extending out to $\sim 0.25 R_\odot$ in which nuclear fusion takes place (e.g. Severino 2017). This process is called *solar nucleosynthesis*, which predominantly converts hydrogen into helium plus a photon and a neutrino through the so-called proton–proton chain. The temperature of the core is roughly 15 MK, and is incredibly dense at $150\,000\,\mathrm{kg\,m^{-3}}$ from the pressure of the entire weight of the Sun, balanced by the fusion energy pushing outwards. The plasma is gravitationally stratified in the radial direction, thus the plasma conditions are insufficient to sustain any fusion outside the core. Above the core lies the *radiative zone*, starting at $20\,000\,\mathrm{kg\,m^{-3}}$ and about half the core temperature, extending out to about $0.7 R_\odot$ and in which the dominant energy transport mechanism is thermal radiation. At its outer boundary the temperature has dropped to 1.5 MK and the plasma density to $200\,\mathrm{kg\,m^{-3}}$, meaning that heavier ions such as carbon, oxygen and iron can hold on to some electrons and impede radiation. As a consequence the plasma starts to convect, carrying heat rapidly up convection cells whilst cooling and expanding, and so the region that lies above the radiative zone is called the *convection zone*. This continues up to the surface of the Sun known as the *limb*, which marks the beginning of the solar atmosphere.

At any one time there are thousands of resonant acoustic modes ringing inside the Sun, the frequencies and amplitudes of which are observed at the Sun's surface through variations of brightness or surface displacement. By inverting all these waves (also called p-modes) through a model one can infer the interior structure – this is *helioseismology* (Broomhall et al. 2014), our main source of information about the solar interior. The typical period of these trapped acoustic modes as seen on the photosphere is 5 minutes, and are of a very different nature to the waves observed in the corona. Helioseismic waves have pressure gradient as their main restoring force, they are trapped in a resonant cavity because of refraction, they are stochastically excited and they are damped by turbulent convection. Although there are some similarities with their counterparts in the corona, helioseismic waves require a different treatment and are not discussed further.

At the interface between the convection and radiation zones lies a crucial region known as the *tachocline*. The plasma below the tachocline rotates as a solid body, whilst above the Sun undergoes differential rotation (rotation rate varies with latitude). This means the tachocline is home to large shear flows and is believed to be critical to the generation of the solar magnetic field through a process known as the solar dynamo. There is consensus that the inductive action of fluid motions inside

the Sun regenerates the magnetic field in a cycle, the various effects of which are collectively called the *solar cycle*. There is much debate on the precise details, such as the necessity of the different flows such as meridional circulation (for example see the discussion within Dikpati and Gilman 2007). Nonetheless it is established that there is strong periodicity of approximately 22 years, such that every 11 years the (surface) solar magnetic dipole reverses its orientation. This is accompanied with the domination of a certain magnetic polarity (on average) in one of the hemispheres of the Sun, visible in the many transient small-scale magnetic structures which appear.

1.1.2 The lower atmosphere of the Sun: photosphere, chromosphere and transition region

This solar surface corresponds to a relatively thin region of the solar atmosphere called the *photosphere*, which at only 500 km thick is less than one thousandth of the solar radius (from centre to limb) and thus looks sharp from 1 AU away. The photosphere is roughly 6500 K at its base, 4900 K at its top, and is fairly well approximated as a thermal radiator. The photosphere is tenuous compared to Earth at approximately 10^{-6} kg m^{-3} – 100,000 times less dense than the air at sea level – however the photosphere is highly stratified with a pressure scale height of the order of less than 100 km. The photosphere is the top of the convective zone, and energy is transported both by convection and liberated through radiation.

The name 'photosphere' means sphere of light, which is apt because the photosphere is the region where the plasma becomes optically thin to visible light and hence photons can escape unimpeded to reach the observer's eyes. These photons from the Sun were originally created in the core as part of nucleosynthesis, but due to constant Thomson scattering as they pass through the Sun these photons take $\sim 1.7 \times 10^5$ years to emerge from the photosphere (Mitalas and Sills 1992).

The light from the photosphere is observed to have a continuous spectrum with an absorption spectrum removed from it. The continuous spectrum is generated by the peculiar negative hydrogen ion H^- (Wildt 1939), a proton holding on to two electrons. The second electron is very unstable and easy to knock out, so instead of having a distinct orbital to quantum jump to (absorbing/releasing a photon with a predetermined wavelength), H^- can absorb/emit a large range of photon wavelengths in the ultraviolet, visible and infrared range. The negative hydrogen ion only forms in the intermediary region of the photosphere since the base contains many hydrogen ions (lone protons) and orphaned electrons, whereas the top is cool enough for neutral hydrogen atoms to form. This absorption spectrum arises because ions in the atmosphere above the photosphere (such as helium and iron) absorb their spectral lines before the light reaches Earth.

Observing the incredibly bright light from the photosphere e.g. Figure 1.2, the "boiling" convective motions of the plasma are clearly seen as *granulation* and *supergranulation* cells (regions of horizontal flows). The upper photosphere is dominated by large velocities from convective overshoot. Granules have a horizontal spatial size of ∼1 Mm, last between 1–20 minutes, are present over the entire surface of the Sun and are separated by sprawling, thin, dark inter granular lanes of some hundreds of kilometres width. In these regions are strong downflows and bundles of magnetic field are concentrated, which may lead to phenomena such as shocks (when the flow is super-sonic) and the *chromospheric network* of magnetic field above. Supergranules are more long-lived and larger, with typical scales of 10–20 Mm and lasting days. In theory the photosphere is in constant turbulent motion, although the precise nature of the turbulence is still being investigated – it is quite different to "textbook" incompressible, isotropic, hydrodynamic turbulence.

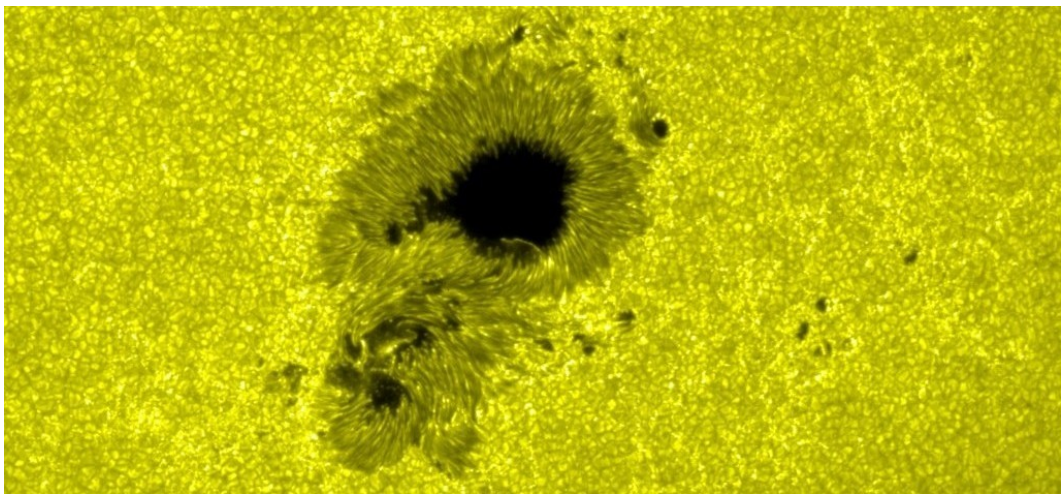

Figure 1.2: Image of a sunspot and the surrounding photosphere from Hinode SOT G-band filter on December 13, 2006. The internal structure (umbra and penumbra) are clearly visible, as is granulation on the solar surface.

Being the first directly observable portion of the Sun most of our knowledge of the solar magnetic field comes from observations of the photosphere, from instruments such as the Michelson-Doppler Imager (MDI) on board the Solar and Heliospheric Observatory (SOHO) spacecraft, and its successor the Helioseismic and Magnetic Imager (HMI) on the Solar Dynamics Observatory (SDO) satellite (Lemen et al. 2012). Using the Zeeman effect and the light polarisation one can estimate the line of sight (LoS) magnetic field strength, and when mapping this spatially across the solar disk one forms a *magnetogram* such as the top panel of Figure 1.3. Magnetograms are limited by LoS effects, and so for example the polar regions likely have much stronger magnetic polarities than shown, and only reflect the magnetic field at

the photosphere, which may be very different to its counterpart in the corona. Nonetheless due to their trustworthiness, magnetograms are universally used to understand the solar magnetic field, particularly as the input for coronal magnetic field extrapolations (e.g. Bellot Rubio and Orozco Suárez 2019).

A prominent feature of magnetograms are *sunspots*. Sunspots are discussed in detail in Subsection 1.1.6, but put briefly they are roughly circular regions of plasma with a typical diameter between 5 Mm and 60 Mm, which are cooler and depressed compared to the plasma around it due to a strong kilogauss magnetic field (some 1000 times stronger than around it). This magnetic field inhibits convection and cools the plasma, making the spots appear dark. Sunspots live between hours and weeks, with bigger spots living longer – usually surviving one or more Carrington rotations. Sunspots often appear in groups, and the atmospheres above sunspots tend to have more magnetic filamentation and activity. The atmosphere above a sunspot is usually perturbed enough from the quiet Sun that it forms an *active region*, where high energy phenomena such as flares are more prevalent because of the additional source of energy provided by the magnetic field. The number of sunspots and active regions act as a proxy for solar activity, such that through the 11 year cycle the number of spots is fewer at solar minima, rises to solar maxima, and falls back to solar minima again.

In order to understand the solar atmosphere, it is necessary to appreciate its temperature profile, denoted in Figure 1.4. From the centre of the Sun through to the photosphere the temperature decreases radially. Counter-intuitively, at the outer boundary of the photosphere the temperature reaches a local minimum ($\sim 4500\,\mathrm{K}$) beyond which it increases again. A steady increase to 10 000 K over some 1500 km is accompanied with decreasing density, until at approximately 2000 km above the solar limb, the temperature rockets up to over a million Kelvin. This jump occurs in only 100 km in what is known as the *transition region*, whilst the region between it and the photosphere is known as the *chromosphere*. The hot, tenuous atmosphere above the transition region is known as the *corona*, named for its crown-like structure seen during eclipses. Bluntly, solar physicists still do not fully understand why the corona is hot. This is known as the *coronal heating problem*. Thermal conduction (discussed in Sec. 4.1.2) presumably acts against the large temperature gradient between the corona and the chromosphere, and energy is constantly being radiated away through radiative losses, although the exact rates are difficult to calculate due to radiative transfer and the wide variation of temperature and density. Therefore some non-thermal heating mechanism(s) must balance these losses, and there is consensus that the energy must originate from the solar magnetic field, yet the precise mechanisms remain a mystery (for a recent review see De Moortel and Browning

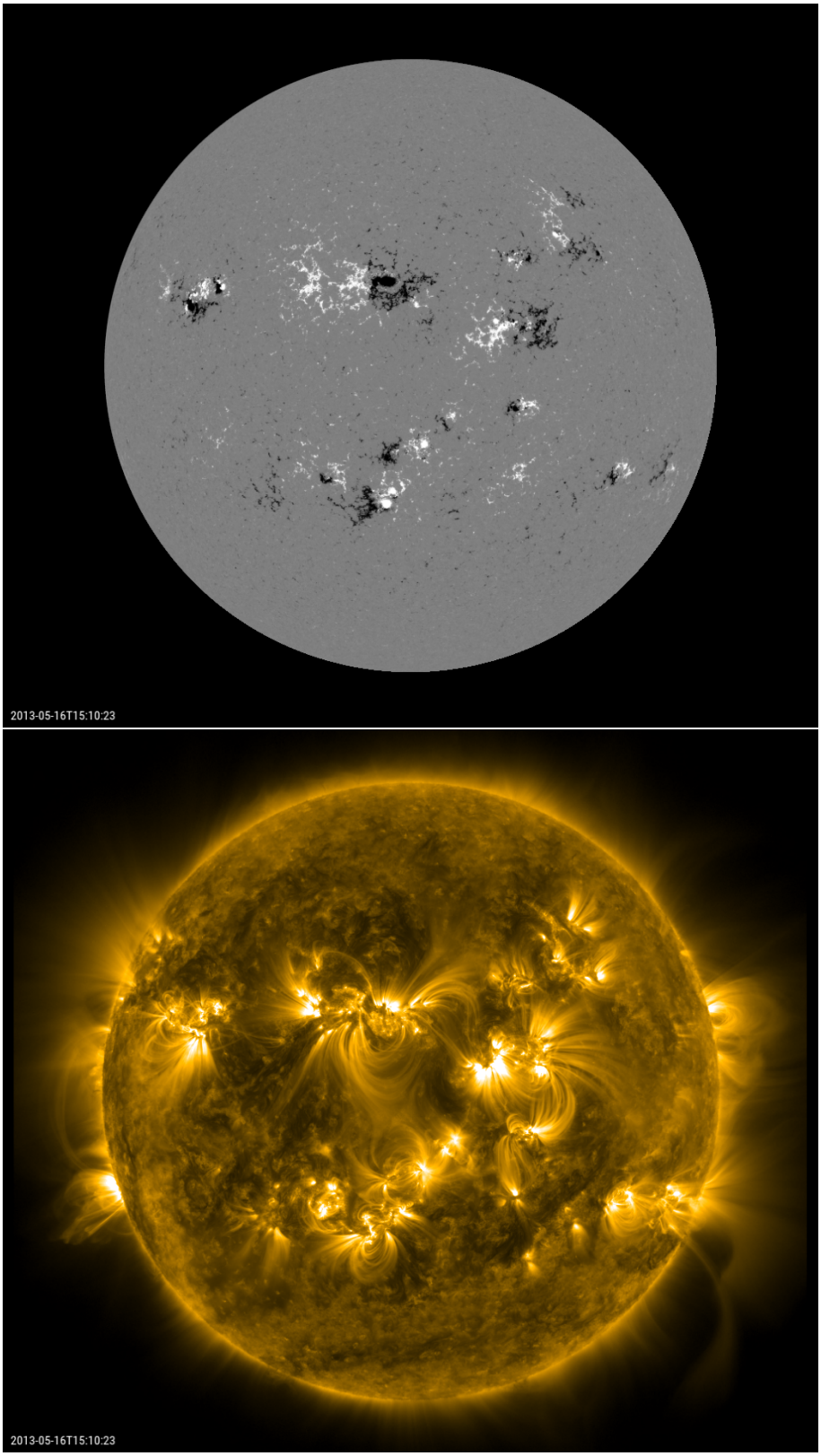

Figure 1.3: Magnetogram taken by SDO/HMI [*top*] and image of the corona taken by SDO/AIA at 171 Å [*bottom*] taken simultaneously on the 16$^{\text{th}}$ May 2013.

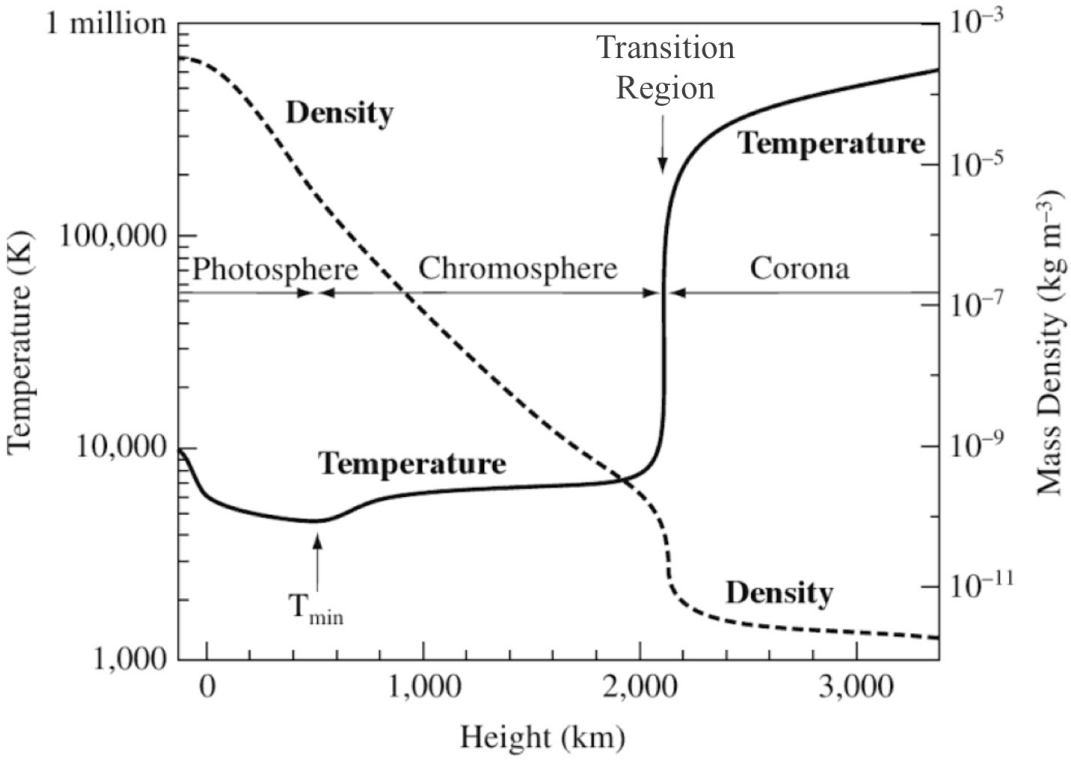

Figure 1.4: The variation of mean temperature (solid line) and density (dashed line) upon height in the quiet solar atmosphere, starting from the base of the photosphere [adapted from Priest (2014)].

2015).

The chromosphere comprises of partially ionised plasma observed in the optical, ultraviolet and X-ray spectral bands. The name meaning "sphere of colour" comes about from its distinctive red colour seen during a total eclipse, where the otherwise overwhelming (white) light from the photosphere is blocked. The reddish hue originates from the hydrogen Balmer series, and one of the most popular filters used to observe the chromosphere is the Hα spectral line ($n : 3 \rightarrow 2$) at 656.28 nm due to the presence of abundant ionised hydrogen: a beautiful example is Figure 1.5. Unlike the photosphere, the chromosphere (and corona) have emission spectra with only a discrete number of spectral lines, corresponding to the transition energies of ions in the host plasma which scatter the broad spectrum from the photosphere into very narrow and unique wavelengths. The absorption lines seen in the photospheric light are the same lines as the direct emission spectra from the higher atmosphere, because they correspond to the same transitions of the same atoms/ions only in reverse. For example, carbon can be thrice ionised (C IV) at a temperature of ~ 6000 K, so looking only at the wavelength that corresponds to the

photons of 1600 Å emitted in this process, the photosphere may be observed whilst not seeing the plasma above it. This may be used to observe different layers of the Sun simultaneously with different wavelengths, since the different ionisations will correspond to different temperatures and hence heights.

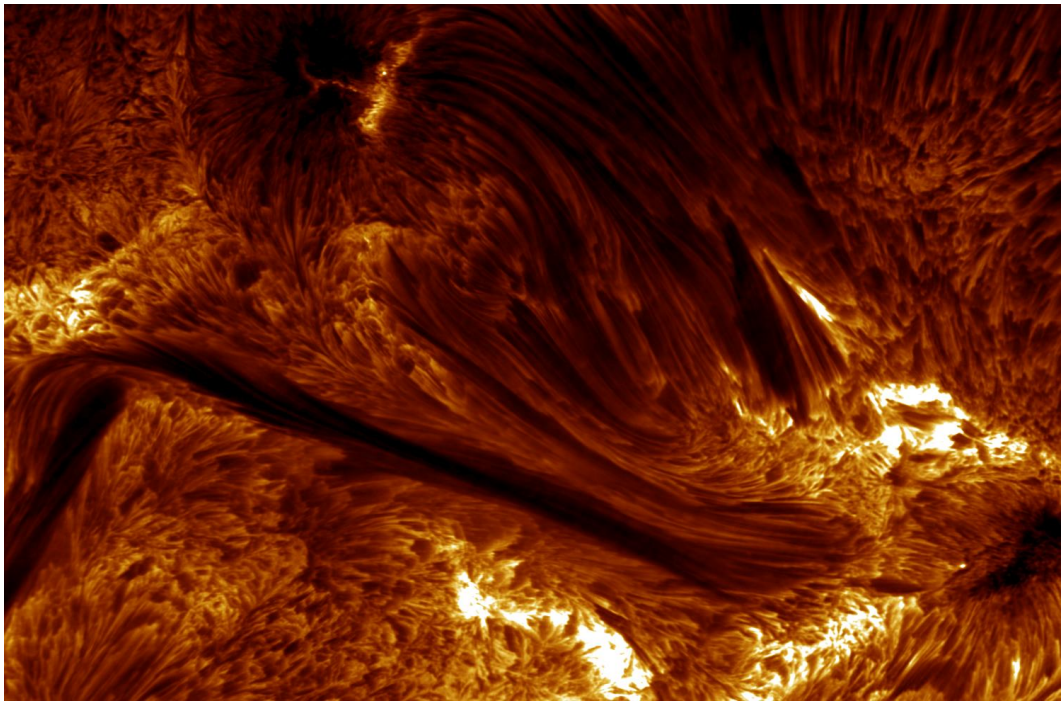

Figure 1.5: High resolution image of the lower chromosphere, in the Hα wavelength on August 22$^{\text{nd}}$ 2003, taken Swedish 1-m Solar Telescope (SST) operated by the Royal Swedish Academy of Sciences.

The chromosphere is inhomogeneous, both spatially with hot and cold plasmas coexisting next to each other, and temporally with the presence of many jets and waves. One well known chromospheric phenomenon is that of *spicules*, which are transient, upward directed plasma jets ∼500 km wide that appear off-limb like hair similar to the structures seen in Figure 1.5. Their origin is debated, though it is generally agreed that they form in regions of strong magnetic field (Zaqarashvili et al. 2007). In general the chromospheric magnetic field expands with height (decrease in density) to form wineglass-shaped funnels, which guide multitudes of waves generated in the photosphere upward through the atmosphere, adjusting their properties along the way (Brady and Arber 2016). These funnels are not static, showing swirls sometimes charmingly called "solar tornados" which are difficult to interpret, as the swirls are actually less than half of a full revolution (Shetye et al. 2019) – they could be chromospheric counterparts to vortex motions in the photosphere, or an Alfvén

wave (see Subsec. 1.2.2).

When considering the chromosphere, neither imaging nor spectral observations are easy to interpret (Subsec. 1.1.4). The magnetic field becomes increasingly important in the chromosphere, such that the effects of thermal gas pressure and magnetic pressure are of the same order which imbues complexity (see Subsec. 1.2.1). Whilst one may reasonably assume Local Thermodynamic Equilibrium (LTE) for the photosphere, this is not appropriate for the chromosphere (nLTE). This is to say that in the former, gas collisions are sufficient to maintain the gas and emitted photons in a thermodynamic equilibrium so all properties of the plasma may be determined by a single local temperature. For the chromosphere, there are insufficient gas collisions (also known as *kinetic effects*) meaning each atom/ion and its energy level populations are specified separately – the gas may still be in some statistical equilibrium, but it is not determined by a single temperature. Further, the chromosphere is subject to many complicated physical processes, our understanding of which is known to be incomplete. Fractional ionisation (which may itself be out of equilibrium) introduces large uncertainty on anything involved with chemistry, such as radiative transfer, adding further complexity. The chromosphere is thus very difficult to model numerically.

The upshot of all these factors is that models of the solar atmosphere are limited (often in low dimensions) to considering only one aspect of the entire inter-dependent system – after all the chromosphere strongly interacts with photospheric motions through gas motions and interacts with coronal plasma thermally and its magnetic structure. This is a serious hindrance to solar physics because the chromosphere holds a large fraction of the solar atmosphere's energy budget. Radiative losses are the most significant source of energy loss in the chromosphere, being greater than that for the corona due to the higher densities. Progress of solar physics will be severely limited until the chromosphere and its effects are fully represented.

Much research is dedicated to probing the way energy is transported upwards (other than radiation, much of which escapes) through the chromosphere into the corona for it to be dissipated, for example looking for oscillations in spicules and direct observations of upward propagating magnetic waves. A key aspect of this energy transport must be the sustained sharp temperature gradient of the transition region, which jumps some 80,000 K in only a few thousand kilometres. This height change is so small compared to the gravitational scale height that the pressure remains fairly constant, so the density must drop an order of magnitude in the same region. The transition region exists on a permanent basis and is not smoothed out, although it has a very dynamic nature. The transition region is very difficult to resolve with current instruments, not least because hydrogen is fully ionised by

these temperatures and so only heavier ions such as Carbon (C IV), Oxygen (O IV), Sulphur (S VI) and Silicon (Si IV) emit in transition region plasma. These emit photons only in the ultraviolet range and hence only space borne instruments are suitable. Current instruments can only resolve plasma waves on the order of minutes and, at best, seconds and so may be missing some important contributions from high frequency oscillations.

1.1.3 The upper atmosphere of the Sun: corona

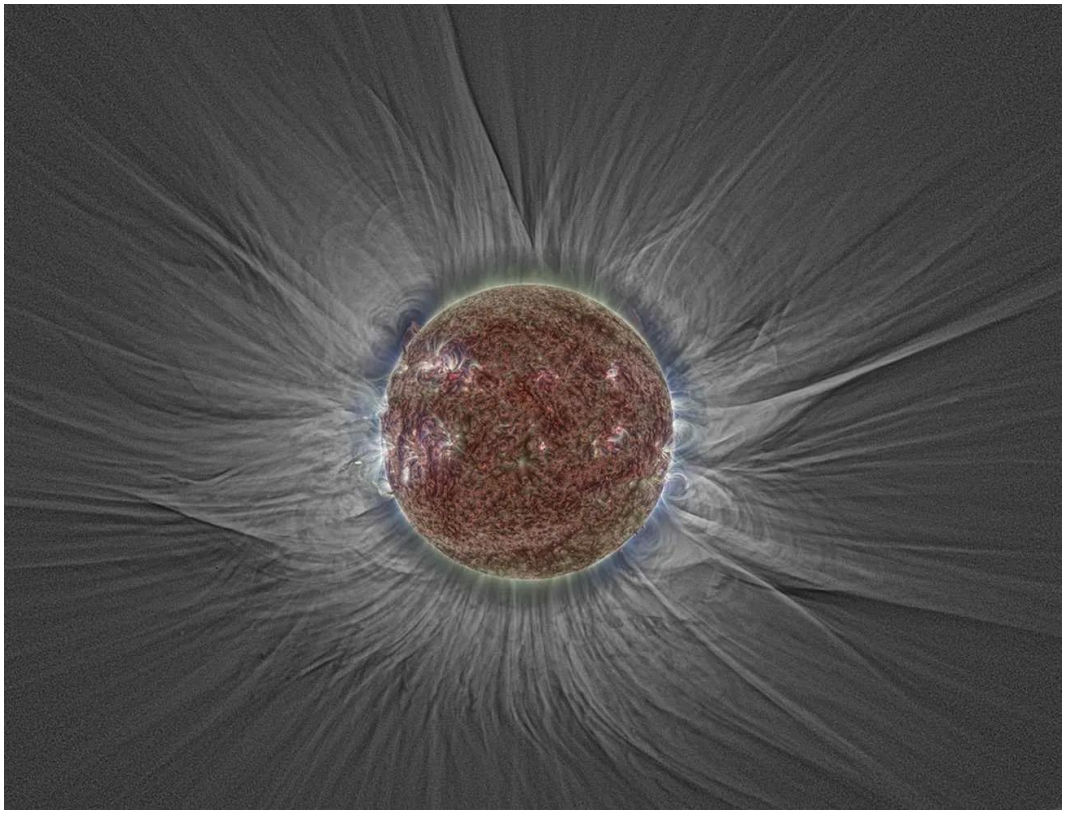

Figure 1.6: A white light and extreme ultraviolet composite of the corona, made of observations on 20$^{\text{th}}$ March 2015 – a total solar eclipse for Earth. The white light image is a combination of 29 exposures made from Longyearbyen, Svalbard, and aligned using the Phase Correlation technique (Druckmuller 2009). This is overlaid with a combination of 304 Å (red), 171 Å (green), 211 Å (blue) EUV channels from SDO/AIA. Each of the channels were processed using Multiscale Gaussian Normalisation (MGN) prior to combination, which makes the images less diffuse and brings out sharper detail (Morgan and Druckmüller 2014). This figure was taken from Yeates et al. (2018).

Above the transition region at ~ 2000 km above the visible surface begins the hot (> 1 MK) and tenuous corona. When viewed through a channel such as 171 Å

(corresponding to iron eight times ionised Fe IX, temperature $\sim 600\,000\,\mathrm{K}$), such as the bottom panel in Figure 1.3 or Figure 1.6, it is clear that the corona can be partitioned into active regions, coronal holes and the quiet Sun. Coronal holes are darker areas of the corona with lower density and temperature, and the visible plasma structures have a unipolar "open field topology", meaning they are rooted on the solar surface and extend radially outwards. There is a known link between coronal holes and the solar wind – for a review on coronal holes, please refer to Cranmer (2009). The quiet sun has little magnetic structure and few explosive events occur, such as soft x-ray jets. The term quiet sun is often synonymous with non-active sun, its structure thought to be dominated by the supergranulation convective pattern on the surface which leads to somewhat weak, spatially small, transient magnetic field concentrations in the atmosphere. However it contains important physics that still needs to be understood, since a significant fraction of the photospheric magnetic flux resides within the quiet Sun, and the coronal heating mechanism(s) must occur in all regions of the corona (Bellot Rubio and Orozco Suárez 2019); it may be the case that multiple heating mechanisms act with varying effectiveness in the different solar regions.

By contrast to the other regions, active regions are areas of intense dynamic activity where the topology is most complex, and contain one or more sunspots. Since active regions are more dynamic they are important for space weather, and they are labelled with a number (e.g. AR 12899) and tracked – the most widely used labelling is done by the National Oceanic and Atmospheric Administration in the United States (NOAA). The corona is magnetically (as opposed to gas pressure) dominated, and it may be reasonably assumed that plasma structures in the corona align with the magnetic field to a great extent. Thus the complex structures in active regions are caused by exceptionally inhomogeneous magnetic fields, which were generated in the convective zone and rose through the photosphere and chromosphere from magnetic buoyancy. The magnetic structures observed in the corona are clearly correlated with the magnetic polarities observed on the photosphere, however because the chromosphere lies between it may be misleading to assume a one-to-one correspondence. In the corona, structures are made visible because coronal plasma is optically thin to the majority of observed emissions, so the intensity of its radiation is proportional to the square of the density (integrated along the LoS), making plasma non-uniformities brighter than the surrounding plasma. This implies that active regions are denser than the quiet Sun. One important and omnipresent structure is the *coronal loop*, often referred to as the "building block" of the corona and are described in Subsection 1.1.5. There are also low-lying loops in the chromosphere and transition region, but these are less easy to observe. Since the condition of the

magnetic field being "frozen in" to the plasma is relaxed further down the atmosphere compared to the corona due to partial ionisation, theorists have aimed foremost to understand the rich physics of coronal loops, before extending downwards.

This magnetic complexity in active regions often leads to instabilities, which can lead to explosive releases of energy in the form of *flares* or eruptions. These are thought to happen as a result of the restructuring of the magnetic field in a nonlinear process called *magnetic reconnection*, discussed further in Subsection 1.2.4. Flares release large amounts of energy rapidly, in the form of X-rays (through bremsstrahlung), gamma rays, energetic (non-thermal) protons and electrons, optical and UV radiation, and subsequent effects may lead to distinctive *radio bursts*. On the Sun, in 100 to 1000 seconds flares release energy that can temporarily raise the temperature of planet-sized regions of plasma up to 20 million K and accelerate particles to near the speed of light. Flares follow a power law spectrum of magnitudes, so the occurrence rate changes with energy like $dN/dE \propto E^{-1.8}$, while the exact power law is debated (particularly at low energies). During solar maximum there can be dozens of smaller flares a day, whilst the largest flares releasing some 10^{32} erg occur maybe a few times per a solar cycle. There are also supposed *nanoflares* that lie beyond the current sensitivity of instruments to detect (sometimes invoked to provide coronal heating), which would occur very frequently if the power law holds. On the Sun, flares can outshine the quiet Sun at X-ray and radio wavelengths. Flares in the visible sunlight are far rarer, particularly in unresolved (Sun-as-a-star) observations and are called white-light flares (for more information, see the references within Duckenfield and Broomhall 2019). Even when one is detected, the enhancement of white light in a solar flare is typically much less than 10%. The number of flares is intrinsically linked to the number of active regions which is modulated by the solar cycle, and so the flare occurrence rate is also modulated by solar cycle. Flares, and their associated eruptions and magnetic field reconfigurations, are well known sources of magnetoacoustic waves in the corona.

A familiar phenomenon seen in the corona are *prominences*, condensations of chromospheric plasma that levitate in the far hotter corona, suspended against gravity by the magnetic field. When on-disk they are often referred to as filaments, since they tend to be long and thin and rarely straight. Appearing over timescales of just under a day, quiescent prominences can exist for many hours or days before fading or erupting, and even when appearing steady prominences are not static but have been shown to be constantly flowing. Prominences are subject to various oscillatory motions, which may be used to perform seismology – however the complications regarding chromospheric plasma, such as partial ionisation and unknown heating function, remain a limitation. For a review of prominences and seismology thereof,

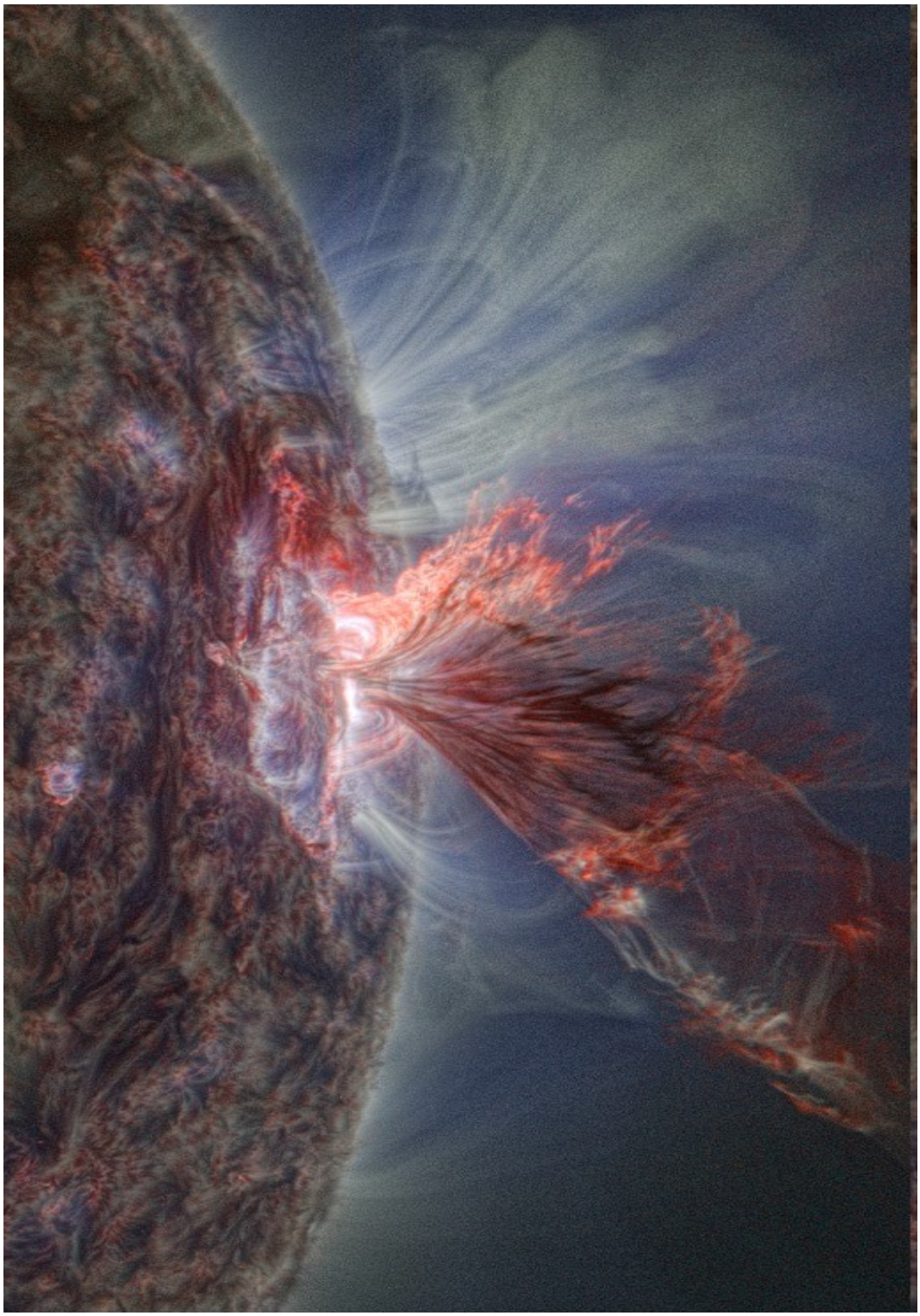

Figure 1.7: Processed image of the corona after two large (M7.6 and M5.5) flares, observed using three ultraviolet wavelengths simultaneously in different colours, clearly showing an erupting filament. This observation is from July 23$^{\text{rd}}$ 2016, taken by SDO/AIA channels 304 Å (red), 171 Å (green), 211 Å (blue) and was subsequently processed with the PM-NAFE algorithm described in Druckmüller (2013). This figure was adapted from one made by Miloslav Druckmüller.

please refer to Arregui et al. (2018). Prominences and their supporting magnetic field may also be subject to instability and erupt, which can lead to expulsion of the prominence in a *coronal mass ejection* (CME) or a failed eruption, in which the complicated overarching magnetic field (or another reason) prevents the material of some two orders of magnitude denser than the coronal plasma around it from escaping (Török and Kliem 2005). One dramatic example of an erupting prominence is shown in Figure 1.7, which shows the plasma filament is cooler and denser than the coronal plasma around it. If the plasma does escape in a CME, a lot of material and bundled magnetic field can stream outwards through the solar system reaching the orbit of Earth in 2–4 days, accompanied by radio bursts and particles accelerated to near-relativistic speeds called solar energetic particles (SEPs). There is a great deal still to learn about CME forecasting, transit times, magnetic field orientation, association with flares (e.g. Byrne et al. 2013). For example current best estimates of CME arrival times still have approximately 10-hour mean absolute errors. Considering the terrible impact CMEs could wreak on Earth's infrastructure, particularly for satellite, aviation and power grids, any additional pre-warning for eruptive events in the corona would be very important – this is one of the aims of coronal seismology. When a CME is ejected toward (or directly away from) Earth it is known as a *Halo CME* due to the apparent large angular extent, and may be seen with a coronagraph such as SOHO/LASCO. An example non-halo coronal mass ejection is shown in Figure 1.8.

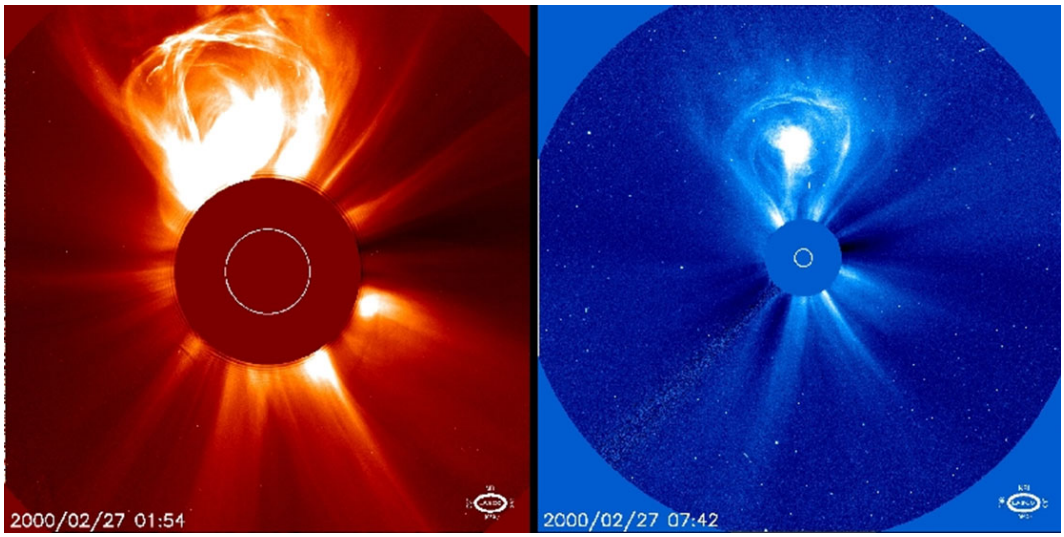

Figure 1.8: White light images of a coronal mass ejection taken by the satellite instrument SOHO/LASCO. The left hand image was taken with the C2 coronagraph and the right hand image taken with the C3 coronagraph at a slightly later time.

Often when referencing the corona, researchers are specifically alluding to its lower portion which extends from the solar limb out to several solar radii, since this may be observed from Earth and its satellites. This is the case for this thesis. Beyond this point the atmosphere of the Sun is generally referred to as the solar wind, and in-situ measurements are more often used than imaging measurements, however there is no well-defined boundary. It is known that beyond a few $R_\odot$ the solar wind becomes supersonic (though this varies with latitude), however due to the non-uniformity of the corona and solar wind this boundary is patchy, jumbled and ever changing. This non-uniformity, and lack of a boundary, is clear in Figures. 1.8 and 1.6; the large and (radially) extended structures visible that look like candle flames are known as *helmet streamers*. This shape is indicative of closed magnetic field lines, which are drawn up to a point by the (accelerating) solar wind. The acceleration of the solar wind to supersonic speeds was a seminal result deducted by Eugene Parker in 1957, who showed that although the corona feels the solar gravity, it conducts heat so well that beyond a certain point the flow outwards becomes supersonic (Parker 1965). Parker also famously pointed out that the rotation of the Sun would leave an imprint on the magnetic field being transported by the solar wind, leading to the *Parker spiral*, in which the solar wind in the plane of the solar system viewed from above would appear like a spiral, likened to a ballerina's skirt. The solar wind is subject to many interesting phenomena such as self interactions ("co-rotating interaction regions"), the formation of a "heliospheric current sheet", interactions with planetary magnetic fields, oscillations and more.

It is known that there are two distinct states of solar wind, dubbed *fast* and *slow*, though the exact solar wind speeds are constantly fluctuating. The fast solar wind is known to originate in coronal holes and the polar regions, both of which have an open magnetic field structure. However the mechanism behind the acceleration of the fast solar wind is still an open question. The slow solar wind originates from a belt around the equator known as the *streamer belt*, although the mechanisms behind its generation are strongly debated. The typical speed of the fast solar wind is about 750 ± 250 km s^{-1}, whilst the typical slow speed may be less than half of that at 300–550 km s^{-1}. Plasma composition from the fast solar wind matches that from the photosphere, whereas plasma from the slow solar wind are similar to the closed field corona, at least in terms of average elemental abundances (Kepko et al. 2016). Well beyond the orbit of Neptune (at 75–90 Au), the solar wind slows down to subsonic speeds again in the *termination shock*, then passes through a turbulent region known as the *heliosheath* before finally stopping at the *heliopause*. These are caused by the ram pressure of the solar wind decreasing to match opposing pressure of the interstellar medium.

1.1.4 Observing the solar atmosphere

Instruments used to observe the solar atmosphere fall into two broad categories: imaging and spectroscopic. Imaged observations allow wave propagation and spatial coherence to be seen. Complementarily, spectrographs have the advantage that many spectral lines formed at different layers can be observed simultaneously, thus seeing how wave parameters change with height.

Spectral techniques study in detail the profile(s) of a specific spectral line(s), using measurements of the line shift (e.g. from average Doppler velocity), width (e.g. from thermal Doppler broadening), any asymmetry etc to deduce properties of the gas such as temperature and density. Line of sight velocities measured in coronal lines are especially useful for studying waves, which induce Doppler shifts. For instance, line of sight velocities were used to differentiate the signatures of persistent upflows from persistent oscillations, both seen in the corona in Tian et al. (2012). Some example spectra are shown in Figure 1.9, which show significant enhancement and broadening with respect to the average profile – indicating a sudden heating event has occurred which led to the penumbral bright dot.

One outstanding issue in solar physics are observations of persistent Doppler redshifts of up to $15\,\mathrm{km\,s^{-1}}$ in spectral lines formed in the temperature range 0.1–0.25 MK, roughly the lower transition region and upper chromosphere (Peter and Judge 1999). Spectral lines above these temperatures in the upper transition region show average blueshifts (Ugarte-Urra and Warren 2011), implying an average flow upwards which is understandable considering the outgoing *solar wind*. Yet redshifts imply an average flow (or wave motions) downward from the transition region into the chromosphere. This is puzzling because such mass flow threatens the existence of the upper atmosphere of the Sun. Complex 3D simulations of the solar atmosphere have been run in recent years addressing this issue, such as the Bifrost radiative MHD code (Carlsson et al. 2016; Zacharias et al. 2018).

Ratios between pairs of spectral lines can be used to estimate other parameters, a notable example being the density of emitting plasma. Comparing the line intensity between Fe XII 195.12 Å and Fe XII 196.64 Å allows an estimate of the plasma density to be made (some examples being performed in Nishizuka and Hara 2011; Van Doorsselaere et al. 2008). This is of paramount importance for coronal seismology because the uncertainty on the plasma density contributes a huge proportion of the uncertainty to the final seismological result – put another way, coronal seismology and estimates of the plasma density are extremely complementary. Analysis of line profiles is not done in this thesis, although the importance of combining spectral and imaging data can not be overstated.

The corona is visible in white light, originally from the photosphere and

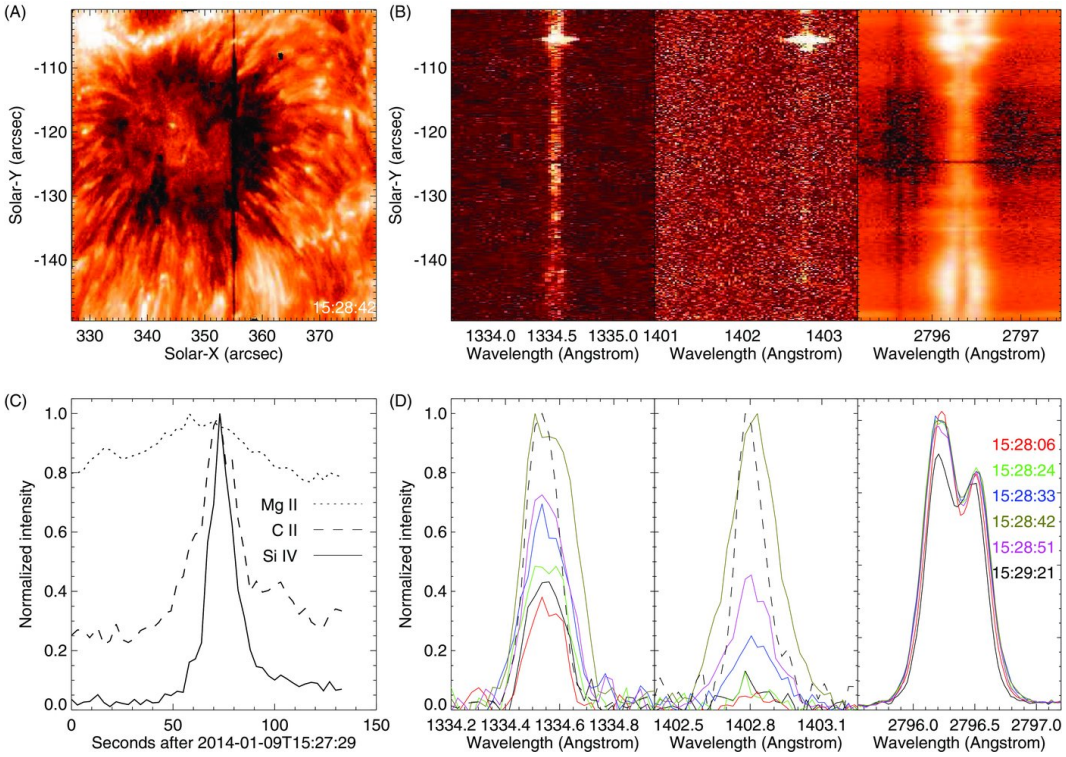

Figure 1.9: Observation of a penumbral bright dot, showing an EUV image from SDO/AIA and three spectral line profiles observed by IRIS, taken from Tian et al. (2014b). A) EUV image (1400 Å) with the slit location used by IRIS overlaid. B) Spectra of C II (1334.53 Å), Si IV (1402.77 Å), and Mg II K (2796.35 Å) along the slit. C) Evolution of line intensities, normalised to unity. D) Line profiles normalised to unity, with different times superimposed. The average penumbral line profile for C II and Si IV are shown as dashed lines.

scattered on free electrons. However the corona is only visible in this way when occulting the photosphere, as happens naturally during an eclipse – such as the white light images in Figure 1.6 – or with a *coronograph* such as the Large Angle and Spectrometric Coronagraph (SOHO/LASCO) on board the Solar & Heliospheric Observatory (SOHO) mission. Coronal plasma may be seen in X-ray and harder emission, but tends to be either far hotter at 15–30 MK, or of a non-thermal nature (that is, out of thermodynamic equilibrium, when the electron temperature is much higher than the ion temperature). Thus X-ray emission is mainly used to study flaring activity. The Sun is also very active in radio and microwave, although images in these wavelengths are far more diffuse due to insufficiently large antenna (in terms of the wavelength).

The strongest emission from the solar corona which is suitable for continuous *imaging* observation is at extreme ultraviolet (EUV) wavelengths in the range 10 nm

to 100 nm, dominated by individual emission lines formed across a wide range of temperatures. There are many wavelengths of interest; the absence of gas collisions allows so-called "forbidden transitions" to also be observed. Imaging telescopes utilise filters which preferentially allow the transmission of a narrow range of frequencies (or *passband*). A typical passband is sensitive to a spectral range about 5 Å to 10 Å wide, which is integrated across wavelength to give a single intensity value per pixel (Raftery et al. 2013). Within this range, one or a couple of spectral lines are prominent (usually), although their relative contribution to the spectrum can change dramatically with temperature and/or density. In this way we image different heights in the solar atmosphere. The most notable instruments for the corona using EUV channels are the (now defunct) Transition Region And Coronal Explorer (TRACE) satellite (Handy et al. 1999), and its successor the Atmospheric Imaging Array (AIA) onboard the Solar Dynamics Observatory (SDO), which was launched atop an Atlas V rocket on February 11, 2010 as part of NASA's in 2010 as part of NASA's Living with a Star program (Lemen et al. 2012). The satellite carried two other instruments

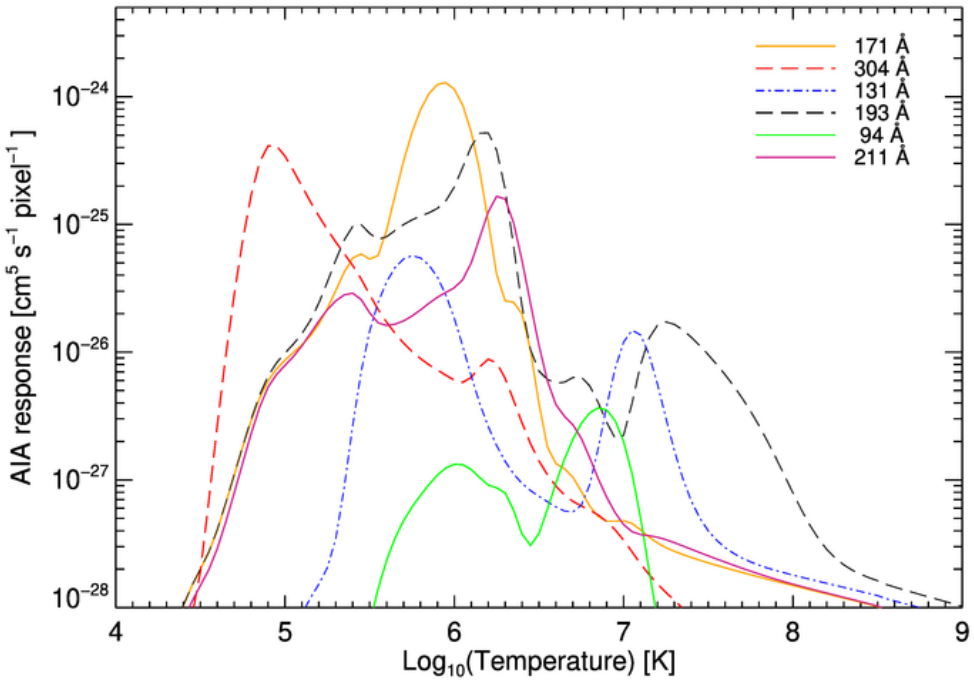

Figure 1.10: Temperature response functions for six EUV channels of SDO/AIA used in this thesis (Lemen et al. 2012). Calculated using version 9.0.1 of the CHIANTI atomic physics package (Dere et al. 1997, 2019).

in addition to AIA: the Helioseismic and Magnetic Imager (HMI) and the Extreme Ultraviolet Variability Experiment (EVE). EVE measures the EUV irradiance from the Sun in multiple channels, including one that overlaps GOES (in soft X-ray) and can be useful in detection of flares in the same way. HMI provides line-of-sight magnetogram data which have a cadence of 45 s and a precision of 10 G.

The AIA instrument takes full disc images of the solar corona in ten different channels (listed in order of descending temperature), seven of which are in EUV: Fe VIII, XX and XXIII (131 Å), Fe XVIII (94 Å), Fe XVI (335 Å), Fe XIV (211 Å), Fe XII and XXIV (193 Å), Fe IX (171 Å), and He II (304 Å). There are also two UV channels: the C IV line (1600 Å) and the continuum emission (1700 Å), which correspond to the transition region/upper photosphere, and temperature minimum respectively. Finally there is also a white light channel (4500 Å) imaging the photosphere. The data from SDO/AIA has a (usual) cadence of 12 seconds and plate scale of 0.6 arcseconds per pixel, of which there are 4096×4096 continuously monitoring the Sun out to a distance 1.28 $R_\odot$ in the East-West and North-South direction. The EUV imaging data from SDO/AIA and other sources may be freely retrieved in the Flexible Image Transport System (FITS) format from the Joint Science Operations Centre (JSOC). For preliminary browsing of the abundant solar data prior to downloading the FITS files, the excellent visualisation tool JHelioviewer was used (Müller et al. 2017). The data in this thesis is manipulated and analysed in the programming language IDL (Interactive Data Language), with some functions used from the solar software library (SSW) (Freeland and Handy 1998).

The temperature response functions for the AIA channels used in this work may be seen in Figure 1.10. There is overlap in many of the channels, and not all channels have a single peak: comparison of intensity values for the same pixel at different wavelengths may help differentiate which peak is contributing most to the emission. Note that if the equilibrium temperature of the plasma is on the hotter wing of the contribution function, an increase of temperature counter intuitively leads to a decrease in brightness. Several advantages of the 171 Å channel for observing the warm corona are clear, being single peaked and with a large response around 1 MK. The 171 Å passband response function is also highly consistent between many instruments (Raftery et al. 2013), making this channel one of the most widely used for seismology. Other EUV instruments include the PROBA-2 spacecraft (LYRA and SWAP) (often used for studying flare data, see Dominique et al. 2018), and the Solar Terrestrial Relations Observatory (STEREO) mission which aimed to give stereoscopic images of the Sun by having one satellite ahead and one behind Earth in orbit, however the latter has since stopped working. Extremely high resolution EUV imaging data of the corona at 0.3–0.4 arcseconds, 5 second cadence has been

obtained for a short duration using a sounding rocket, Hi-C (e.g. see Williams et al. 2020).

The intensity of the plasma emission for the optically thin corona depends on temperature and density, and is integrated along the Line Of Sight (LoS). The effect of temperature may be accounted for by using the *differential emission measure* (DEM) function $DEM(T)/dT \propto n_e^2 \cdot (dh/dT)$ to reconstruct the amount of emitting plasma in a column dh at different temperatures (and therefore in the solar atmosphere, heights). The electron density n_e is the measurable quantity that is used to find the plasma density, but ions may also radiate and thus contribute to the DEM – so it is usual to assume a ratio between electron density and ion (elemental hydrogen) density. An important point to note is that the emission measure $\int (DEM/dT)dT$ of optically thin plasma is proportional to the density *squared*. A given instrument has an instrumental response function $R(T, \lambda, n_e, A)$ of which the filter response function is a major part, and where A is an abundance factor which incorporates the parameters related to the atomic physics of the plasma. The total EUV intensity at a wavelength λ $[I_\lambda]$ is thus

$$I_\lambda = \int R(T, \lambda, n_e, A) \frac{DEM(T, dh)}{dT} dT. \tag{1.1}$$

The simultaneous observation of the intensity in many wavelengths of the corona allow inversions to estimate the plasma DEM. From the obtained DEMs, temperatures and densities may be estimated. For example measurements of a narrow DEM have previously been used to infer the isothermality of coronal loops (Aschwanden and Nightingale 2005). A detailed example of a DEM implementation and subsequent analysis may be found in Aschwanden et al. (2013). However this is an ill-posed inversion, subject to unknown systematic errors and so different implementations of calculating the DEM may arrive at different results (see for example the discussion in Reale 2014). Nor is the interpretation of a DEM profile straight-forward, it not being clear how to differentiate the influence of unresolved substructure such as multiple strands or KHi vortices (Van Doorsselaere et al. 2018). Nonetheless DEMs form an important tool in the study of coronal emission, and must be appreciated in order to maximise the contribution of coronal seismology; DEM analysis is not performed in this thesis.

Restricting attention to the information embedded within a single bandpass, waves in the solar corona are frequently studied using *time-distance maps*, two-dimensional subsets of the data with one axis being time and the other a one-dimensional distance coordinate along a selected *slit* in the images. These slits do not necessarily have to be straight (but usually are picked to be so), and are often

averaged over several pixels in the spatial direction perpendicular to the slit in order to increase signal to noise. The slope on a time-distance map corresponds to an apparent velocity (some discussion may be found in Yuan and Nakariakov 2012). In order to reduce blurriness, time-distance maps may be convolved with a filter aimed at sharpening the edges in one or both directions. For example, adding the original time-distance map (dimensions (t, x)) with an offline version (as in, a version of the data processed parallel and distinct to the "main" data flow) which has been convolved with the kernel

$$\text{(Sharpening filter)} \quad \begin{bmatrix} 0 & -1/2 & 0 \\ 0 & 1 & 0 \\ 0 & -1/2 & 0 \end{bmatrix} \tag{1.2}$$

results in sharper edges in the spatial direction only, which may be useful for delineating different structures or checking a tracking routine (for instance in Nisticò et al. 2014). This filter was used in this thesis for choosing events and verifying other processes but only offline, not on the data from which oscillation profiles were fitted. Time-distance maps formed from the *running difference* or *base difference* images, in which each frame of the data has the previous or base frame subtracted from it, are also commonly used to see the data only where there is movement or a change in intensity from e.g. waves (an example is found in Aschwanden and Schrijver 2011).

There are also processing techniques aimed solely at improving the EUV image for display purposes, such as compressing the dynamic range of intensity values to improve contrast, and the widely used Multi-Gaussian Normalisation (MGN) which adjusts different spatial scales to bring out fine detail (e.g. Fig. 1.6), using a vector of different sized Gaussian filters (Morgan and Druckmüller 2014).

Waves may be resolved through changes in intensity which lead to bright structures on the time-distance map, or through transverse displacements of the structure itself. Tracking the displacement of the inhomogeneity through some fitting routine yields a time series of the oscillation profile, which may be used for seismology (see App. C for information on how this tracking is done for the data in this thesis). Another way of analysing the EUV imaging data is by extracting the intensity of an individual pixel or collection of pixels as a function of time.

1.1.5 Coronal loops

When looking at coronal plasma near the surface, the prevalence of distinct loops is remarkable. Coronal loops are thought to be regions of confined coronal plasma bounded by a *flux tube*, an isosurface of constant magnetic flux such that all points

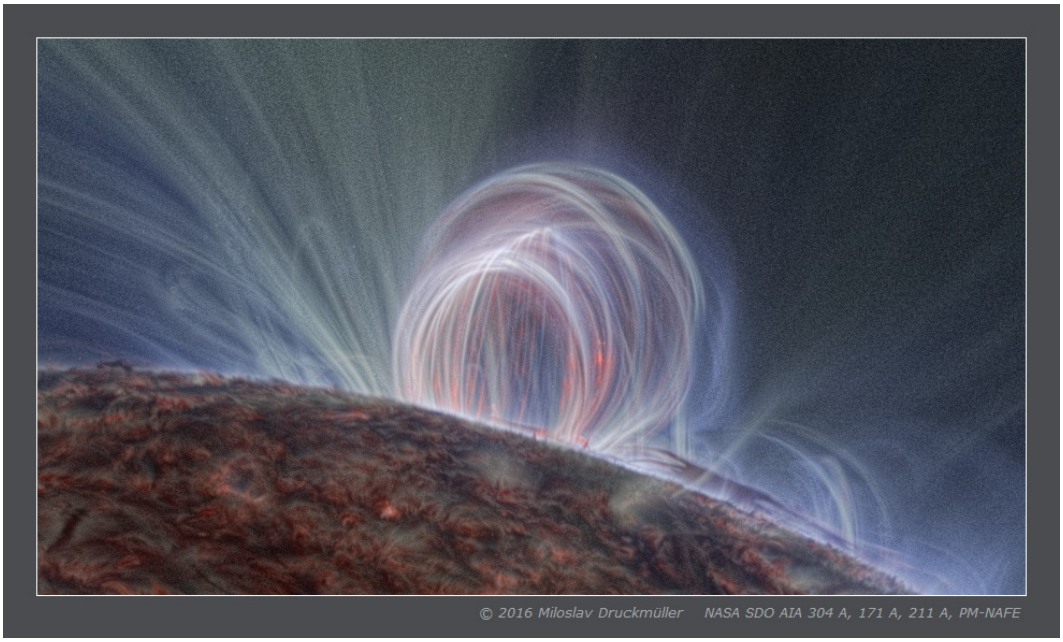

Figure 1.11: Coronal loops, observed using three ultraviolet wavelengths simultaneously in different colours and with additional processing. This active region observation is from July 19$^{\text{th}}$ 2012, taken by SDO/AIA channels 304 Å, 171 Å, 211 Å and was subsequently processed with the PM-NAFE algorithm by Miloslav Druckmüller, described in Druckmüller (2013).

are tangential to the magnetic field, with a magnetic field line as its axis. The magnetic flux through a cross section taken at any point along the axis of a flux tube is equal – consequently the tube is wider if the magnetic field strength drops, and vice versa. Coronal loops are approximately semicircular arcs with lengths of roughly 100 Mm, although deviations from semi-circularity are common and there is a wide range of lengths spanning two orders of magnitude. In general the agreement between the observed topology of active region loops and coronal magnetic field extrapolations is good, meaning coronal loops seem indeed to follow magnetic field lines and are often used to visually appraise an extrapolation (e.g. Kang et al. 2019b); although why loops form about some field lines and not others is an open question. The magnetic field strength within a coronal loop is not well known. Extrapolations of the magnetic field from the photosphere are widely used, however, penetrating through the chromosphere and transition region leads to uncertainty from unknown currents and non–force-free conditions. The fact that coronal loops exhibit generally much less expansion with height than potential field models also underscores the inadequacy of potential field extrapolations. Some measurements of magnetic field strength have been made, through nonlinear force-free models and vector magnetograms (e.g.

Anfinogentov et al. 2019), or through seismology: for example Wang et al. (2007, 34 ± 14 G) and Nakariakov and Verwichte (2005, especially section 3.3). However the routine, accurate and precise measurement of a coronal loop's magnetic field strength is not yet common – this is a key aim of coronal seismology.

Coronal loops do not necessarily contain flows, however pressure differentials at the loop footpoints may lead to siphon flows. Doppler measurements (spectrographs) have also implied persistent upflows at some loops' footpoints providing plasma to populate the loop (Tian et al. 2012), whilst other measurements have also implied persistent downflows. It is difficult to diagnose the presence of specific flows for certain, because of the difficulties in interpreting redshifts and blueshifts along the line of sight. Nonetheless both ubiquitous sub-Alfvénic flows (of the order $100\,\mathrm{km\,s^{-1}}$) and, in the case of flares and other explosive events, super-Alfvénic flows have been reported (Keiling et al. 2016).

Coronal loops are generally vertical from the solar surface reaching heights of some 50 Mm, though many have some inclination away from the normal and a few can be extremely inclined, particularly when looking at many loops rooted at the same sunspot. Thus coronal loops experience gravitational stratification. However in the corona, loops are generally considered to be thermally isolated from each other because thermal conduction across the field is suppressed. It is therefore expected each loop experiences a different density scale height, since this is dependant on temperature. It is common to classify coronal loops as *cool* (< 1 MK), *warm* (~ 1.5 MK) and *hot* (> 2 MK), and each EUV passband is more suited to studying one category more than the others. For example, hot loops were first studied with SOHO/SUMER in the Fe XIX and Fe XXI lines (formation temperature greater than 6 MK), and also seen in soft X-ray such as by Yokhoh/SXT. Cool and warm loops are mostly studied in EUV passbands, and the most common observations used nowadays for well-defined coronal loops are seen in the SDO/AIA 171 Å channel (some 600,000 K), but generally loops can be seen simultaneously in several passbands. There are observations showing that a loop is nearly isothermal along its length, very probably because of the strong thermal conductivity in the corona (e.g. Aschwanden and Nightingale 2005). There may be an observational bias at play, in only selecting loops that have an appreciable density at the apex – however the prevalence of such loops (and the rarity of loops which are only partially filled in a passband) justifies the need to understand such phenomena. Yet even a standard, quiescent loop from a simple active region may turn out to be complicated under detailed analysis. For example, Gupta et al. (2015) used spectroscopic observations from Hinode/EIS to conclude that the loop studied was indeed nearly isothermal, but also had non-uniform cross section and a non-symmetric density profile along the loop

such that it was overdense in one leg, and underdense in the other. One of the main conclusions of the study of active region loops observed by TRACE was that static loop models were poor at representing many AR loops (Winebarger et al. 2003).

It is often posited that a coronal loop is made of many parallel, individual strands (flux tubes) which are integrated over the line of sight, being too small to be resolved by SDO/AIA at some 10–100 km width. This complexity smeared over the LoS and instrumental resolution may explain why some observations are contradictory to each other and models (Mulu-Moore et al. 2011; Reid et al. 2020). On the other hand, nonlinear effects such as development of the Kelvin-Helmholtz instability in the transverse direction also explain some of the observations (Van Doorsselaere et al. 2018). Of course the development of instabilities could themselves lead to the loop forming multiple filaments as well (Antolin et al. 2014). An important parameter of coronal loops is the *filling factor*, which gives a measure of the ratio of effective emitting volume to total volume, i.e. how much of the plasma along the line of sight is in fact radiating in EUV and soft X-ray. This provides information on whether the observed structures are resolved or unresolved with the given instrument. Since reported filling factors have tended to be low (generally under 0.5) for the majority of instruments, this appears to support the idea of thin strands. The multi-thermal multi-stranded model of coronal loops also appears to be supported by recent observations taken at higher resolution taken by a rocket carrying the High-Resolution Coronal Imager (Hi-C 2.1) on its third launch, with cadence ∼4 s and a plate scale of 0.129 arcsec/pixel (Williams et al. 2020). Results discussed further in Section 4.2 using waves further hint also at a non-monolithic structure. However more evidence is required, and spatial structure is not in itself an explanation of the thermal structuring – for example it is unclear if coronal loops are heated at the footpoints, uniformly or in one spatial location that move around. The heating mechanism has a significant impact on the hydrostatic equilibrium and has receieved a lot of attention from the community – for a review about coronal loops see Reale (2014) and references therein.

The traditional understanding of a coronal loop is a flux tube filled with plasma denser than the surrounding plasma, with a density contrast of ∼3 between the external and internal plasma. This assumption has been tested recently through both seismology and careful analysis of the observed intensity emission (e.g. in Arregui et al. 2015; Goddard et al. 2017). This is described further in Chapter 2. It is worth noting that underdense loops could also appear brighter in a particular passband compared to the surrounding plasma in some cases. Nonetheless models and simulations of coronal loops usually consist of an overdense loop with a monolithic core of uniform density, surrounded by an inhomogeneous layer where the density

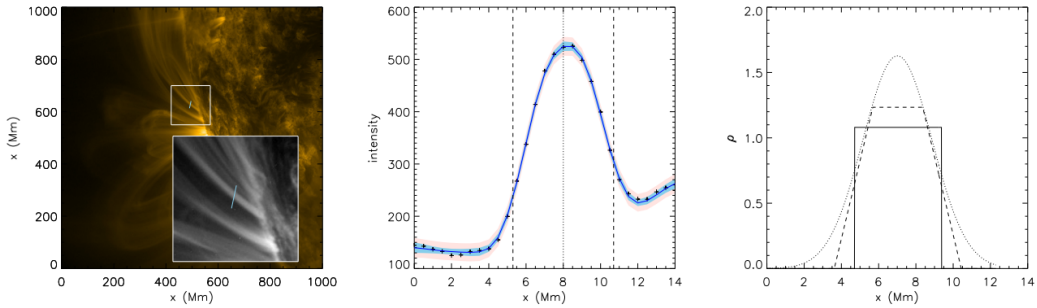

Figure 1.12: An example of a coronal loop's density profile being estimated from its emission. [*Left*] An image of the coronal loop being analysed, from SDO/AIA 171 Å data. The transverse cut being analysed is indicated in the magnified cutout. [*Middle*] The EUV intensity profile of the loop along the indicated slit, overlaid with the model (blue) and a 99% confidence interval (red). [*Right*] Three density profile models best fitted to the intensity profile. For this loop, the "step function" model was found to be preferred. This figure was adapted from Goddard et al. (2017).

drops off to form a transverse density profile (for example an Epstein profile). An example investigation of a loop's density structure is shown in Figure 1.12, for which it was found that a constant density profile was preferred but the Gaussian profile and constant profile with an inhomogeneous skirt could also generate the observed emission.

Models of coronal loops with an inhomogeneous layer are partly motivated by the elegant explanation for the observed rapid damping of transverse oscillations of the loop called *resonant absorption*, described in Subsection 2.1.1. Also there are many easy-to-use and generally applicable scaling laws relying on a monolithic loop, such as those given in Rosner et al. (1978), and so improvements need to be made and supported by further observations before the community abandons them for a multi-stranded model. Coronal loops are treated as distinct flux tubes in this thesis unless specified otherwise.

Coronal loops are dynamic and the chosen heating mechanism strongly affects the (apparent) equilibrium state. Loops can remain visible in a particular EUV channel for hours, days or weeks. Particularly hot loops (such as those seen in soft X-ray) tend to only last a few hours, and are often associated with flaring regions; loops can rapidly appear or disappear, especially if a flare occurs. The magnetic field also evolves: making loops contract, expand, shift position, get populated and evacuated and repopulated with different temperature plasma, and so on. The detection of long period (2–16 hour) pulsations in the EUV emission by coronal loops has been credited as the manifestation of so-called *thermal non-equilibrium* (TNE) cycles (first discussed in a solar context in Kuin and Martens 1982). The

coronal loop plasma undergoes condensation and evaporation cyclically, and can be total or partial. It is posited that these cycles are produced by highly-stratified and quasi-steady, long duration heating competing with radiative cooling – the cycle properties reflecting the specific spatiotemporal characteristics of the heating mechanism (Froment et al. 2018). If the coronal heating is sufficiently localised near the chromospheric footpoints of a coronal loop then plasma at the loop midpoint cannot achieve a thermal equilibrium, even for steady heating, forcing the loop into a limit cycle. During the cooling phases, condensations of colder plasma form that fall down in drops which are affected – but not necessarily aligned with – the magnetic field direction, and fall slower than free-fall. Such a droplet is known as *coronal rain*, and the plasma properties can be several orders of magnitude cooler and denser than the coronal plasma around its inception. A recent review of coronal rain and its link to TNE may be found in Antolin (2020). There is a distinction between TNE cycles and thermal instability – the former is a limit cycle, and implies no equilibrium state for the coronal loop exists, whilst the latter is a perturbation about an equilibrium. One may consider a system which evolves sufficiently slowly as an equilibrium, but the growth of perturbation must be quicker than the time evolution of the system. This could be the case for coronal loops – catastrophic cooling seems to happen much faster than the characteristic timescale of the TNE cycle.

A similar statement could be made for the characteristic periods of magnetoacoustic waves, which are observed to be of the order of seconds to tens of minutes and hence shorter than the lifetime of a loop in most cases. Waves have been shown to be ubiquitous in coronal loops, originally inferred by the time series of radio and X-ray flux and now are routinely observed in imaged and spectroscopic data. These observations of waves may contribute to our understanding of coronal loops, since they act as natural waveguides, are easily observed and the theory regarding magnetohydrodynamic (MHD) oscillations is well developed, and to which this thesis hopes to contribute.

1.1.6 Structure of sunspots and the atmosphere above them

Sunspots share a similar structure, though it should be remembered that they are often part of a sunspot group (active region) and evolve over time, with instances of sunspots colliding and merging, or breaking apart into smaller spots – an isolated, circular spot is relatively rare. Sunspots are formed of central *umbra*, with a typical magnetic field strength of 2–4 kG and a surface brightness of 20% that of the surrounding photosphere, emitting with a blackbody temperature of ∼3700 K (compared to rest of the photosphere at ∼5800 K). The plasma opacity in a sunspot is lowered through the effects of the H- ion in the cooler temperature and

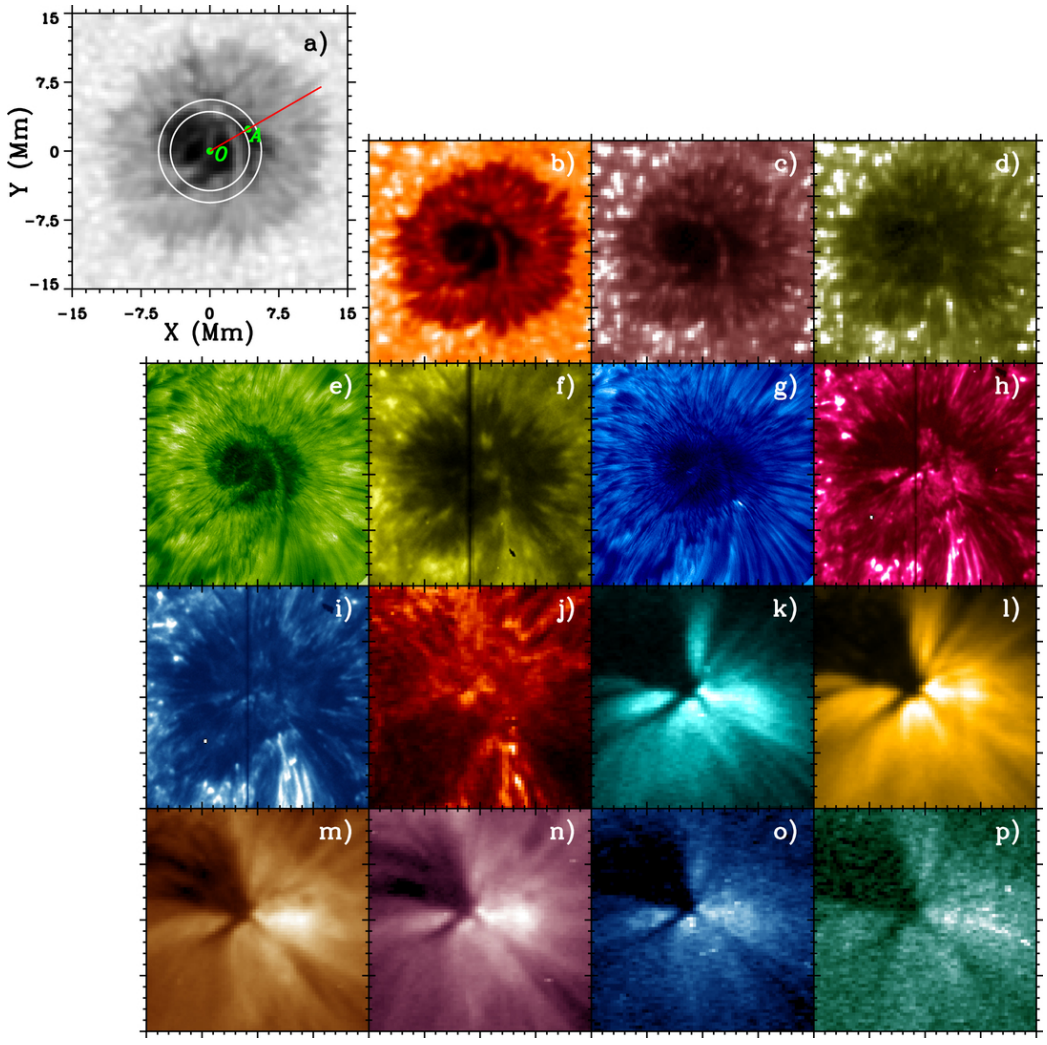

Figure 1.13: Example imaging data of a sunspot from 16 different channels, in ascending order of line-formation height or temperature. (a) HMI Fe I 6193 Å (continuum intensity), (b) HMI line-core intensity, (c) AIA 1700 Å, (d) AIA C IV 1600 Å, (e) NST H-α – 0.4 Å, (f) IRIS Mg II k 2796 Å, (g) NST H-α line center, (h) IRIS Si IV 1400 Å, (i) IRIS C II 1335 Å, (j) AIA He II 304 Å, (k) AIA Fe VIII/XXI 31 Å, (l) AIA Fe IX 171 Å, (m) AIA Fe XII/XXIV 193 Å, (n) AIA Fe XIV 211 Å, (o) AIA Fe XVI 335 Å, and (p) AIA Fe XVIII 94 Å. Zhao et al. (Taken from Figure 1 2016).

reduced density, meaning one sees further down in sunspots than the rest of the photosphere. This so-called *Wilson depression* means sunspots are sunken down by some ∼400-800 km, though this quantity is difficult to measure and varies between spots.

Surrounding the umbra is an annular *penumbra*, with ∼75% the surface brightness and ∼5400 K, and a characteristic radially decreasing magnetic field with edge values typically ∼1 kG. The standard picture of the magnetic field emanating from a sunspot is that it is very strong and mainly vertical in the umbra, and becomes inclined as one moves out to the penumbra, even highly so. Yet this can be difficult to verify, as spectropolarimetry is limited by uncertainty from Wilson depression and because non-LTE conditions limit the applicability of inversions. Observations of (photospheric) spectral lines show that the part of the penumbra closest to the limb have an average Doppler red shift, whilst the opposite (on disk) side has an average blue shift. Looking in detail the penumbra contains many dark filaments containing a plasma outflow from inner to outer penumbra at up to about 6 km/s, though precise values depend on resolution. This flow is fastest in the centre of the penumbra, ends at the outer boundary, and is called the *Evershed flow*.

Sunspots are well known sources of oscillations which travel up through the atmosphere. Many types of waves are abundant in sunspots and the atmosphere above them, often referred to as the sunspot's magnetosphere. Behaviour of these waves is different at the photosphere, chromosphere and in the corona, e.g. different periods, amplitudes. Waves in a sunspot's umbra are different to waves in its penumbra: probably due to different inclinations of magnetic field or the unknown nature of the umbra-penumbra boundary itself. Reviews of oscillations in and above sunspots may be found in Bogdan and Judge (2006), Khomenko and Collados (2015) and Sych (2016).

Of particular importance to this thesis, the most prominent oscillation period seen in the umbrae of sunspots lies at 5 minutes (3 mHz) in photospheric lines, changing to 3 minutes (5-6 mHz) in chromospheric lines. The 5 minute umbral oscillations are seen in the power spectra of the temporal variations of the velocity measured in photospheric spectral lines, often with a secondary peak at 3 minutes (Centeno et al. 2006). These 5 minute oscillations are not seen in intensity, probably due to the optically thick nature of the photospheric radiation, and are associated with photospheric acoustic oscillations. The 3 minute oscillations in the chromosphere are more pronounced, they are visible in both intensity and velocity power spectra, and appear as individual peaks in the latter rather than a continuation of the broad 5-minute peak. These 3 minute oscillations are usually taken to be upwardly propagating slow magneto-acoustic-gravity waves, travelling near the sound speed.

Theoretical modelling of 3 minute oscillations has been a challenge for several decades, and as yet there is no universal consensus that explains their origin or how the oscillation power and frequency in the three-minute band are distributed within the umbra of the sunspot at different altitudes. Part of the difficulty in understanding this region comes from the change in *plasma-β* (ratio of gas pressure to magnetic pressure), which is large in the photosphere and less than unity in the chromosphere and above, meaning the $\beta = 1$ boundary must lie somewhere within photosphere. Near this equipartition layer, the "pure" MHD modes detailed in Subsection 1.2.2 lose their meaning; waves will distribute their energy between the different branches of the dispersion relation through *mode conversion*, the coefficients of which depends strongly on the geometry, the inclination of the magnetic field, and wavenumber. One suggestion is that the 3 minute chromospheric oscillations might be resonant modes of sunspots, formed by a vertical cavity with reflective boundaries (albeit with different heights above the sunspot, as evidenced by Jess et al. 2012). Another suggestion is that the 3 minute periodicity derives from the interaction of upwardly propagating slow waves with the stratified plasma, which acts as a filter Zhugzhda and Dzhalilov (1982); Zhugzhda (1984). This is consistent with the vertical and horizontal structure of the oscillations observed, as well as their frequency content (Centeno et al. 2006; Marsh et al. 2008; Reznikova et al. 2012; Sych and Nakariakov 2014; Yuan et al. 2014). The 5 minute oscillations are simply the result of forcing from (ubiquitous) outside p-modes and weak convection, rather than eigenmodes of the umbra itself. Then the amplitude of wave modes with periodicities greater than 3 minutes (such as the 5 minute peak) become evanescent modes as they propagate up, whilst the 3-minute oscillations remain to dominate.

Looking in the upper chromosphere and into the transition region, a typical sawtooth pattern associated with amplitude steepening of upward propagating magnetoacoustic shocks has been made clear in many observations, such as in Tian et al. (2014a) and the spectropolarimetric observations in Centeno et al. (2006). These shocks lead to periodic three minute brightenings in the chromospheric umbrae called *umbral flashes*. Sometimes a distinction is made for "running penumbral waves" which appear as outwardly propagating oscillations in the core of the H-α line, found in the chromospheric penumbrae of sunspots, whose phase speeds decrease and periods increase with radius (Khomenko and Collados 2015). It is now agreed these are not distinct phenomena, but simply the chromospheric signature of the upwardly propagating magnetoacoustic waves generated in the photosphere along the inclined magnetic field, subject to line of sight effects (e.g. see Reznikova et al. 2012). Nonetheless, nonlinear waves are firmly detected at chromospheric and transition region heights.

It is well established that above the transition region, 3-minute oscillations are ubiquitous despite the considerable refraction and reflection presumably occurring at the transition region. These (slow) magnetoacoustic modes which propagate along coronal loop fans are seen in the form of the propagating intensity perturbations (see the review by De Moortel 2009). Many studies aim to link the photospheric p-modes with waves in the high chromosphere and above in the corona (Centeno et al. 2006; Jess et al. 2012; Marsh and Walsh 2006; Su et al. 2013; Zhao et al. 2016). This may be backed up by the observation that propagating intensity variations seen in loops connected to a sunspot tend to have periods clustered around 3 minutes, whilst loops not connected to a sunspot tend to have periods clustered around 5 minutes; this implies the underlying driver is photospheric buffeting of the loop footpoints, generating waves that can penetrate through the transition region (De Moortel et al. 2002a). Propagating modes in coronal loop fans above sunspots are the subject of Chapter 4.

Being themselves approximated as flux tubes, sunspots themselves also oscillate globally. Periodicities of hours have been detected in the microwave (gyroresonant) emission at 17 GHz with the Nobeyama RadioHeliograph (NoRH) (Chorley et al. 2010), which may be interpreted as radial global modes of sunspot oscillations. Oscillations of sunspots or entire active regions on the solar surface have been purported and modelled, relating to sunspot global eigenmodes (Dumbadze et al. 2017). Spiral wave patterns seen in the oscillations above sunspots have been attributed to the superposition of several (slow) modes of the sunspot itself, with different azimuthal wavenumbers m (Kang et al. 2019a; Sych and Nakariakov 2014). Through heavy Fourier filtering of the H-α line core, it has been shown that a chromospheric umbra is compatible with a transverse $m = 1$ magnetoacoustic (kink) mode (Jess et al. 2017) – although a low β plasma was assumed . The area and intensity of a sunspot umbra has been shown to oscillate in phase for at least one (preliminary) case, implying a direct detection of an umbral $m = 0$ (sausage) mode (Feng et al. 2020). See also the theory of magnetic pores developed in Moreels et al. (2015), which are similar to the umbrae of sunspots.

1.2 Magnetohydrodynamics

1.2.1 Approximating plasmas with magnetohydrodynamics

In any mathematical treatment of plasma physics one must use approximations to make any headway, since describing all the constituent particle locations and velocities is virtually impossible. In some situations it is appropriate to describe the particle velocity distribution function at each point in the plasma, which may be

different from the usual Maxwell-Boltzmann distribution, and evolve this distribution function with time (Boltzmann's equation). Such a treatment is called a *kinetic* theory, an important example being the use of the *Vlasov equations* to evolve this distribution. A kinetic description is often necessary for collisionless plasmas, such as the plasma in inertial confinement fusion, and cases where the particle distribution is highly non-thermal such as in flares. In other situations it is appropriate to average over the distribution function and describe the plasma in terms of velocity moments of the particle distribution function, such as density. Such fluid models lose physics such as wave-particle effects, but are appropriate if the plasma has enough collisions to keep the plasma velocity distribution sufficiently close to a Maxwell–Boltzmann distribution. Making further approximations one may treat the plasma as a single fluid, assuming the flow of ions and electrons are the same (as opposed to more complicated two-fluid models). One of the most powerful, and generally applicable theories explaining how plasmas and magnetic fields interact is that of *Magnetohydrodynamics*, abbreviated to 'MHD'. MHD is a fluid theory expressed in macroscopic parameters, appropriate for the large length and time scales this thesis is concerned with (coronal loops, sunspots, and other long wavelength plasma motions) since single particle effects and microscopic processes can be neglected. For the corona (magnetic field strength $B \approx 10\,\mathrm{G}$, electron density $n_e \approx 10^{14}\,\mathrm{m}^{-3}$) we consider situations where the following assumptions are satisfied:

1. Characteristic times $\gg$ timescales of typical collisional processes, e.g. electron plasma frequency $\approx 9 \times n_e \approx 2 \times 10^8\,\mathrm{Hz}$.

2. Characteristic scales $\gg$ length scales of typical collisional processes, e.g. Larmor radius $\approx 7 \times 10^{-2}\,\mathrm{m}$

3. Non relativistic plasma velocities.

The typical periods in observations of coronal oscillations used in coronal seismology are of the order of minutes and the length scales are of the order of hundreds of kilometres (for example the SDO/AIA cameras have ~ 0.6 arcsecond/pixel resolution $\approx 435\,\mathrm{km}$), so MHD may be applied. It should be clear that during explosive events such as flares, additional effects must be included either on top of the MHD framework, or replaced with a kinetic theory.

The self–consistent set of equations that govern magnetohydrodynamics are the result of combining Maxwell's equations governing electromagnetism and the Navier–Stokes equations controlling fluid mechanics, describing ρ the plasma mass density and p the kinetic pressure. The electric field does not appear directly and is expressed in terms of the magnetic field $\vec{B}(\boldsymbol{x}, t)$, because in electrically

conducting fluids (such as coronal plasma) any accumulation of charge is immediately redistributed through an electric current $\vec{J}$. The equations may be written as

$$\frac{\partial \rho}{\partial t} + \vec{\nabla} \cdot (\rho \vec{v}) = 0, \qquad \textbf{(Mass conservation)} \tag{1.3}$$

$$\rho \frac{D}{Dt}(\vec{v}) = -\vec{\nabla} p + \frac{1}{\mu}(\vec{\nabla} \times \vec{B}) \times \vec{B} + \mathcal{F}, \quad \textbf{(Momentum conservation)} \tag{1.4}$$

$$\frac{D}{Dt}\left(\frac{p}{\rho^{\gamma}}\right) = \mathcal{L}, \qquad \textbf{(Energy equation)} \tag{1.5}$$

$$\frac{\partial \vec{B}}{\partial t} = \vec{\nabla} \times \left(\vec{v} \times \vec{B}\right) + \eta \left(\vec{\nabla}^2 \vec{B}\right). \qquad \textbf{(Induction equation)} \tag{1.6}$$

This set of eight equations, together with the ever-present $\nabla \cdot \vec{B} = 0$, determine the eight variables $\vec{B}(\boldsymbol{x}, t)$, $\vec{v}(\boldsymbol{x}, t)$, $\rho(\boldsymbol{x}, t)$ & $p(\boldsymbol{x}, t)$. Parameter η [$\mathrm{m^2 s^{-1}}$] is known as the *magnetic diffusivity*, related to the electrical conductivity through $\eta = 1/\mu_0 \sigma_c$ and usually taken to be constant. Recall mass density $\rho = mn$ with m the average particle mass and n the average particle density. One may use $\vec{\nabla} \times \vec{B} = \mu \vec{J}$ to calculate current $\vec{J}$, with μ the magnetic permeability. An equation of state is included to relate a temperature T to pressure p and density ρ. A commonly used example is the ideal gas law,

$$p = \frac{k_B}{m} \rho T \approx 2 n_e k_B T_e \tag{1.7}$$

where k_B is the Boltzmann constant, m is the mean particle mass, n_e is the total electron density and T_e is the electron temperature (recall in a plasma different species may have different thermodynamic distributions). The latter equation uses the assumption that the numbers of protons and electrons is roughly equal $n_e \approx n_p$, and the mass contribution of the electrons is negligible (thus $\rho \approx m_p n_e$). The mean particle mass m can vary with temperature, partial ionisation etc. Generally for the solar corona, an assumption of $m \approx 0.6\ m_p$ is used to account for heavier ions, being slightly higher than $0.5\ m_p$ if the plasma were composed of just protons and electrons. For example the most significant contribution to molecular weight in the corona is probably from helium ^{4}He, and assuming the ratio of H:He = 10:1 one can estimate $m \approx (10 \times 1 + 1 \times 4)/11 \times 0.5 \times m_p = 0.635\ m_p$.

Looking again at the governing MHD equations, the energy equation (Eq. 1.5) reduces to the adiabatic equation for $\mathcal{L} = 0$, with γ then having its usual meaning of adiabatic index. The term $\mathcal{L}$ represents a general energy loss or gain function that can include energy transferred through ohmic dissipation (j^2/σ), thermal conduction, radiative cooling, and a heating/cooling term Q to account for coronal heating.

Similarly, additional external forces such as gravity may be added to the right hand side of the momentum conservation equation depending on the situation, for example $\mathcal{F} = -\rho\vec{g}$. Dissipative forces and energy loss terms are discussed more in Subsection 1.2.3. It is sometimes useful to consider the Lorentz force in more detail. As can be seen from the cross product, this force always acts perpendicular to $\vec{B}$ and consequently, any fluid parcel moving along the field only experiences hydrodynamical forces. One can decompose the Lorentz force in the following way:

$$\begin{aligned}\vec{F}_L = \vec{J} \times \vec{B} &= \frac{1}{\mu_0}\left(\vec{\nabla} \times \vec{B}\right) \times \vec{B} \\ &= \frac{1}{\mu_0} \underbrace{\left(\vec{B} \cdot \vec{\nabla}\right)\vec{B}}_{\text{“magnetic tension”}} - \underbrace{\vec{\nabla}\left(\frac{B^2}{2\mu_0}\right)}_{\text{“magnetic pressure”}} .\end{aligned}$$

This is somewhat misleading since there is in fact some 'mixing' in terms of directions; this decomposition still has a mixture of terms along $\vec{B}$, visible if one considers a Frenet coordinate system. Nonetheless it clear that the forces in MHD are anisotropic and depend strongly on the magnetic field configuration. If the Lorentz force is zero the field configuration is a so-called *force-free field*, where any currents remain strictly parallel to the field. Force-free fields are used extensively in modelling the coronal magnetic field as the magnetic pressure dominates the gas pressure, allowing the mathematics to be simplified (for example Anfinogentov et al. 2019; Kang et al. 2019b). If any currents are further neglected, the field is a *potential* field (for instance see Yeates et al. 2018).

The set of Equations 1.3–1.6 leads to a bewildering variety of rich behaviour, so further approximations have to be made. Consider the terms of the induction equation; the first term on the right hand side is an advection, and the second term a diffusion. To evaluate the relative importance of both, consider the terms' ratio in a plasma with typical length scale l_0, time scale t_0 in a magnetic field of strength B_0:

$$\left.\begin{aligned}|\eta\vec{\nabla}^2\vec{B}| &\sim \eta\frac{B_0}{l_0^2} \\ |\vec{\nabla} \times (\vec{v} \times \vec{B})| &\sim \frac{v_0 B_0}{l_0}\end{aligned}\right\} \quad \Rightarrow \quad \frac{|\text{diffusion}|}{|\text{advection}|} \sim \frac{\eta}{v_0 l_0} = \frac{1}{R_m} \tag{1.8}$$

where we have defined the **magnetic Reynolds number** $R_m = v_0 l_0/\eta$. This is analogous to the Reynolds number used in fluid mechanics to compare the relative importance of viscosity to fluid inertia, here R_m compares the transport effect to

that of "leaking".

$$R_m \gg 1 \quad \Rightarrow \quad \text{advection dominates}$$
$$R_m \ll 1 \quad \Rightarrow \quad \text{diffusion dominates, so field lines "slip" through the fluid.}$$

For the solar corona, typical length scales are large on the order of megametres, there is large conductivity because of the high temperatures, and hence low magnetic diffusivity such that the classical value for the corona is $R_m \sim 6.8 \times 10^{13} \gg 1$ so the magnetic diffusion may be neglected (Braginskii 1965). The assumption of $\eta = 0$ is known as *Ideal MHD*, where the fluid is perfectly electrically conducting $\sigma_c \to \infty \;\Rightarrow\; \eta = 0$. A consequence of the magnetic field not diffusing through the plasma, shown by the remaining form of the induction equation, is that both of $\vec{v}$ and $\vec{B}$ advect each other – this is the statement that the magnetic field lines are "frozen in" to the plasma. Hence the plasma can move freely along field lines, but to move perpendicularly the magnetic field lines must be dragged along (and vice versa). This creates a restoring force that can support new wave modes. This result is referred to as *Alfvén's theorem*, which is to say the magnetic flux through any open surface $S(t)$ defined by its boundary that is co-moving with the plasma is conserved (Alfvén 1942).

$$\int_{S(t)} \vec{B} \cdot d\mathbf{A} = \text{constant}. \tag{1.9}$$

One of the most instructive quantities in MHD is the *plasma beta*, defined as the ratio of gas pressure to magnetic pressure

$$\beta \;=\; \frac{p_{[\text{gas}]}}{p_{[\text{mag}]}} \;=\; \frac{nk_BT}{B^2/2\mu_0} \;=\; \frac{2}{\gamma}\frac{C_\text{S}^2}{C_\text{A}^2}. \tag{1.10}$$

The physics in high β environments (gas pressure dominates) is very different to that in low β environments (magnetic energy density dominates). The quiet photosphere has $\beta \gg 1$ (with the notable exception of sunspots) whereas the corona has $\beta \ll 1$, with values in active regions usually taken to be between 0.01 to 0.5 (for example a value of 0.1–0.3 was inferred in Nisticò et al. 2017) During flares and eruptive events the plasma beta can rise, and cooler plasmas such as prominences have higher beta than their surroundings. For example, through Doppler observations of standing oscillations in flaring loops and combining with MHD wave theory, the plasma-β in flaring loops has been estimated at 0.15–0.91 Wang et al. (2007). The chromosphere is approximately the region for which $\beta \approx 1$, demonstrating again why chromospheric physics is generally more difficult than coronal physics.

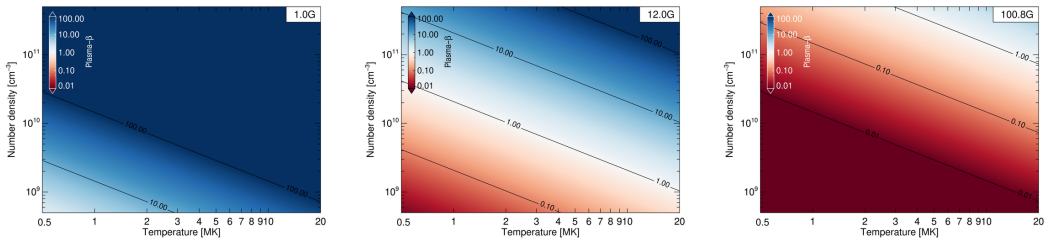

Figure 1.14: Plasma beta as a function of temperature and density for three representative magnetic field strengths: 1 G [left], 12 G [middle] and 100 G [right]. Red is $\beta < 1$, white is $\beta = 1$, red is $\beta > 1$,

1.2.2 MHD modes of plasma structures

In order to arrive at the equation(s) governing magnetohydrodynamic waves, we first linearise the system of MHD equations from Section 1.2 with respect to an equilibrium, in which we assume $\vec{v}_0 = \vec{0}$. Viscosity is neglected to simplify things, (it is possible to incorporate this later) and ignore gravity, to allow for homogeneity. Let the subscript 0 denote a constant equilibrium value around which we are perturbing. Perturbations will be denoted with a subscript 1, and considered to be small. So we write $\vec{B}(\boldsymbol{x},t) = \vec{B}_0 + \vec{B}_1(\boldsymbol{x},t)$, $\vec{v}(\boldsymbol{x},t) = \vec{v}_0 + \vec{v}_1(\boldsymbol{x},t)$ $\rho(\boldsymbol{x},t) = \rho_0 + \rho_1(\boldsymbol{x},t)$, $p(\boldsymbol{x},t) = p_0 + p_1(\boldsymbol{x},t)$. Recall the speed of sound is defined through

$$C_{\mathrm{S}}^2 = \gamma \frac{k_B}{m} T_0 = \gamma \frac{p_0}{\rho_0}, \tag{1.11}$$

assuming the ideal gas law holds, and γ is the ratio of specific heats $\gamma = C_{P[\mathrm{gas}]}/C_V$. We now insert these into the ideal MHD equations, but instead of Equation 1.5 we use an approximation of the evolution of p as

$$\frac{Dp}{Dt} + \gamma p \vec{\nabla} \cdot \vec{v} = 0, \tag{1.12}$$

since this makes the necessary substitutions later a little easier. Dropping all nonlinear terms like $\rho_0(\vec{v}_1 \cdot \vec{\nabla})\vec{v}_1$ (so especially $\frac{D}{Dt} \to \frac{\partial}{\partial t}$) yields;

$$\frac{\partial \rho_1}{\partial t} + \rho_0 \vec{\nabla} \cdot \vec{v}_1 = 0, \tag{1.13}$$

$$\rho_0 \frac{\partial}{\partial t}(\vec{v}_1) = -\vec{\nabla} p_1 + \frac{1}{\mu_0}\left[(\vec{\nabla} \times \vec{B}_1) \times \vec{B}_0 + (\vec{\nabla} \times \vec{B}_0) \times \vec{B}_1\right], \tag{1.14}$$

$$\frac{\partial p_1}{\partial t} + \gamma p_0 \vec{\nabla} \cdot \vec{v}_1 = 0, \tag{1.15}$$

$$\frac{\partial \vec{B}_1}{\partial t} = \vec{\nabla} \times (\vec{v}_1 \times \vec{B}_0), \qquad \vec{\nabla} \cdot \vec{B}_1 \;=\; 0. \tag{1.16}$$

Using some vector identities and the MHD equations, we take the time derivative of (1.14) and solve for $\vec{v}_1$ by substitute in equations (1.13), (1.15) and (1.16) to give

$$\rho_0 \frac{\partial^2}{\partial t^2}(\vec{v}_1) = -\vec{\nabla}\left[-\gamma p_0 \vec{\nabla}\cdot\vec{v}_1\right] + \frac{1}{\mu_0}\left[(\vec{\nabla}\times\vec{B}_1)\times\vec{B}_0 + (\vec{\nabla}\times\vec{B}_0)\times\vec{B}_1\right]. \quad (1.17)$$

Defining the vectorial *Alfvén speed* $\vec{C}_A := \vec{B}_0/\sqrt{\mu_0\rho_0}$, and manipulating we can rewrite this as

$$\frac{\partial^2}{\partial t^2}(\vec{v}_1) = \left[(\vec{C}_\mathrm{A}\cdot\vec{\nabla})^2\mathbf{I} - (C_\mathrm{A}^2 + C_\mathrm{S}^2)\vec{\nabla}\vec{\nabla} - \vec{C}_A\cdot\vec{\nabla}(\vec{\nabla}\vec{C}_A + \vec{C}_A\vec{\nabla})\right]\vec{v}_1, \quad (1.18)$$

This is the general wave equation for ideal MHD, in a uniform medium. Notice that setting $\vec{C}_\mathrm{A} = \vec{0}$ returns the wave equation for sound waves, as it should. To get a dispersion relation we make the ansatz of plane waves, that is a Fourier expansion $\vec{v}_1(\mathbf{x}, t) = \vec{v}_1 \exp[i(\vec{k}\cdot\mathbf{x} - \omega t)]$. Then we can substitute $\partial/\partial t \to \omega$, $\vec{\nabla} \to \vec{k}$ and find an eigenvalue equation which may be written as

$$\begin{pmatrix} -k_\perp^2(C_\mathrm{A}^2 + C_\mathrm{S}^2) - k_\parallel^2 v_A^2 & 0 & -k_\perp k_\parallel C_\mathrm{S}^2 \\ 0 & -k_\parallel^2 C_\mathrm{A}^2 & 0 \\ -k_\perp k_\parallel C_\mathrm{S}^2 & 0 & -k_\parallel^2 C_\mathrm{S}^2 \end{pmatrix} \begin{pmatrix} v_{1x} \\ v_{1y} \\ v_{1z} \end{pmatrix} = -\omega^2 \begin{pmatrix} v_{1x} \\ v_{1y} \\ v_{1z} \end{pmatrix}, \quad (1.19)$$

where $k_\perp$ is the component of the wave number $\vec{k}$ in the direction perpendicular to the magnetic field, whilst $k_\parallel$ is the component along the field. Then finally the dispersion relation is derived through setting the determinant of this matrix to zero, such that it has a solution

$$\omega^2(\omega^2 - k_\parallel^2 C_\mathrm{A}^2)\left[\omega^4 - k^2(C_\mathrm{A}^2 + C_\mathrm{S}^2)\omega^2 + k_\parallel^2 k^2 C_\mathrm{A}^2 C_\mathrm{S}^2\right] = 0. \quad (1.20)$$

The two roots of this equation $\omega^2 = 0$ are known as the *entropy* or *thermal* modes. The entropy mode always has zero real part to its frequency, which is to say it has no propagation so is frozen in to the plasma flow. In an ideal plasma the entropy mode is characterised by perturbations of the thermodynamic variables. In the presence of non-adiabatic effects, the entropy mode is endowed with a purely imaginary component (some authors call this case specifically the thermal mode), physically meaning a decay or growth of a thermodynamic perturbation. Being a non-propagating spike in temperature and/or density it is often neglected in favour of studying the other (propagating) modes.

The remaining roots of the dispersion relation can be split into two independent subsets. The first set of (round) brackets correspond to **Alfvén waves** $\omega = \pm\vec{k}\cdot\vec{C}_\mathrm{A} = \pm k_\parallel C_\mathrm{A}$. These are waves purely involving the magnetic field, caused

by the tension in the magnetic field lines that travel along the field at the Alfvén speed $C_{\rm A}$. These are incompressive and transverse, which is to say they do not perturb the plasma density and the plasma is displaced in a direction perpendicular to k. The other solutions can be found by solving the bi-quadratic inside square brackets. These solutions are known as **magnetoacoustic waves**, since they combine both the tension recoil of the magnetic field lines and the compression motion of a sound wave. Their dispersion relation may be written as

$$\begin{aligned} &\omega = \pm\omega_{\rm slow,fast}\ , \\ &\omega_{\rm slow,fast} = k\sqrt{\frac{1}{2}(C_{\rm A}^2 + C_{\rm S}^2) \pm \frac{1}{2}\sqrt{(C_{\rm A}^2 + C_{\rm S}^2)^2 - 4(k_\parallel^2/k^2)C_{\rm A}^2 C_{\rm S}^2}}. \end{aligned} \tag{1.21}$$

Magnetacoustic modes always perturb the density (are compressive), in general are not purely longitudinal nor transverse, and their properties strongly depend on plasma-β and their angle with the magnetic field. One way to visualise these modes is through polar plots of phase velocity amplitude as a function of the angle of propagation with respect to a local magnetic field vector as shown in Figure 1.15 (note that such plots will change with the value of β). The magnitude of the line taken from the origin to the particular modes's curve for a given angle α, gives the speed of the mode in that direction relative to the magnetic field. As Figure 1.15 shows, the slow mode propagates mainly along the magnetic field direction (horizontal), the magnitude of which is close to the sound speed $C_{\rm S}$. In low-β regime, $C_{\rm S}^2 < C_{\rm A}^2$ since $2/\gamma$ is near unity – usually. The fast mode in general travels obliquely, and faster than the sound or Alfvén speed – in a uniform plasma fast waves propagate across the field at the so-called *fast speed* $C_{\rm F} = \sqrt{C_{\rm S}^2 + C_{\rm A}^2}$. The Alfvén mode propagates purely along the magnetic field at the Alfvén speed, seen as a single point for the group speed, upstream and downstream, although the phase speed can appear slower.

The highly filamented nature of the corona affects the highly anisotropic MHD waves very strongly. To understand the effect of plasma structuring, consider waves in a plasma cylinder stretched along the magnetic field, diagrammatically shown in Figure 1.16. By convention, the direction of the z-axis coincides with the axis of the cylinder, which is to say the co-ordinate z follows the magnetic field. Any flows with a radial component are moving across the magnetic field and are not considered in the equilibrium. Another common formulation is the 2d *slab geometry*, which is applicable for some situations like prominences and current sheets, and additional surface modes exist which are not considered here. Nonetheless a cylindrical geometry is natural for studying coronal loops, filaments, jets and other field aligned axial structures.

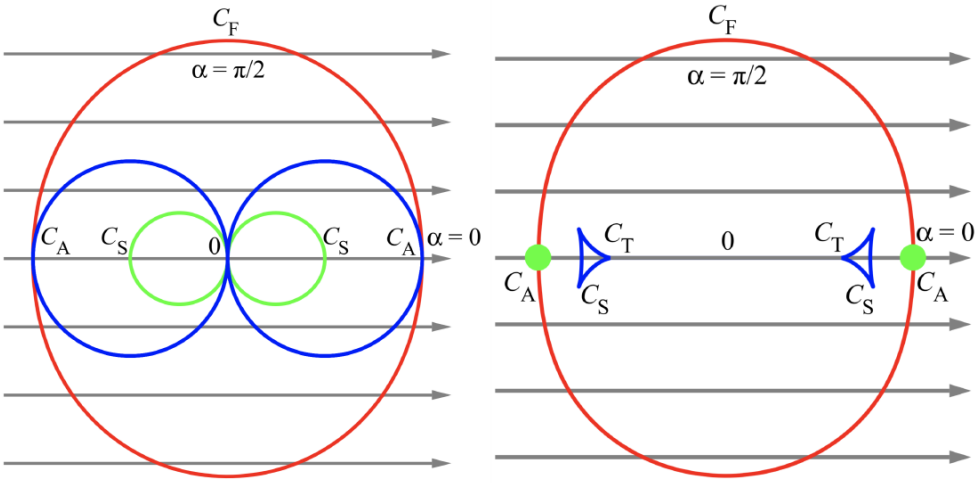

Figure 1.15: Polar plots for the phase speeds (ω/k) [left] and group speeds ($d\omega/dk$) [right] for the three MHD wave modes in a uniform plasma, under the assumption of low plasma-β. The speed for the Alfvén mode is plotted in green, the fast mode in red, the slow mode in blue. The angle α is with respect to the magnetic field, indicated by grey arrows.

As with all waves the presence of a characteristic length or time scale introduces wave dispersion. In this case the culprit is the radius a, with waves forced to propagate along the cylinder. Before, in the case of uniform medium (Eq. 1.20) all of the wave modes are dispersionless, which is to say that their phase velocities ω/k and group velocities $d\omega/dk$ are independent of frequency or wavelength. The distinction of Alfvén, magnetoacoustic and thermal modes is common to all MHD systems, since the magnetic field always provides a preferred direction. Further dispersion, from inhomogeneities for example, can modify these normal modes leading to the existence of surface and global modes, which may be unique to the spatial (or temporal) structure in which the wave is embedded. Therefore it is worth remembering that the statements made from this point forward about the different wave modes may not hold when considering situations in which a cylindrical geometry is inappropriate.

Assume the cylinder is in equilibrium, so the gas pressure p, density ρ and magnetic field experience a jump at the boundary $r = a$. The sound and Alfvén speeds are different inside and outside the tube. Balancing the total pressure (gas + magnetic) at the boundary, one can determine the density ratio of the cylinder through

$$\frac{\rho_e}{\rho_0} = \frac{2C_{S0}^2 + \gamma C_{A0}^2}{2C_{Se}^2 + \gamma C_{Ae}^2}. \tag{1.22}$$

This and other similar relations between the characteristic speeds will determine

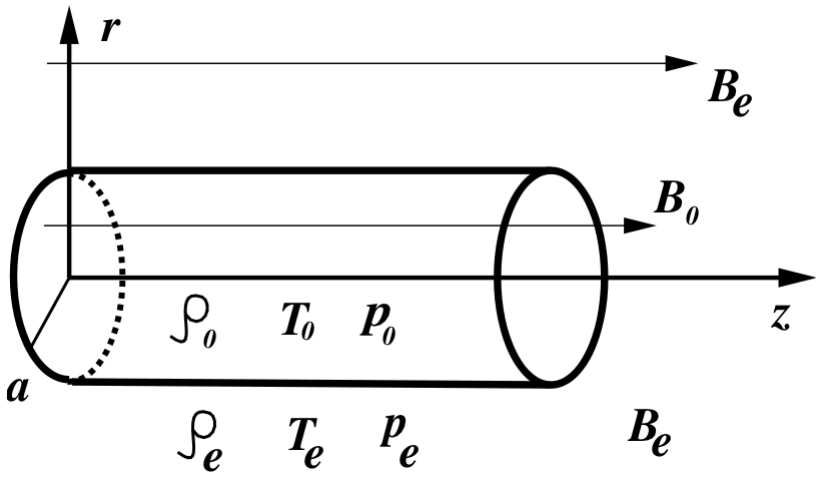

Figure 1.16: Diagram of a typical model for solar coronal plasma non-uniformities: a field–aligned plasma cylinder of radius a, filled in with a uniform plasma (parameters with subscript 0), and embedded in an external magnetised plasma (parameters with subscript e). This sketch was taken from Verwichte et al. (2005).

the properties of the MHD modes guided through the tube. The formal derivation for this cylinder's wave modes can be found in Edwin and Roberts (1983). Here we quote the key results; for the longitudinal wave number k_z directed along the cylinder axis, and azimuthal wave number m the dispersion relation is found to be

$$\rho_e(\omega^2 - k_z^2 C_{\rm Ae}^2)\kappa_0 \frac{I_m(\kappa_0 a)}{I'_m(\kappa_0 a)} + \rho_0(k_z^2 C_{\rm A0}^2 - \omega^2)\kappa_e \frac{K'_m(\kappa_e a)}{K_m(\kappa_e a)} = 0, \tag{1.23}$$

where $I_m(x)$ and $K_m(x)$ are the modified Bessel functions of order m, with the prime denoting a derivative with respect to its argument. This arises since the non-uniformity in the radial direction prevents us taking a Fourier transform in this direction, forcing us to match solutions at the boundary instead. Functions κ_0 and κ_e are the transverse (radial) wave numbers of the perturbations defined as

$$\kappa_i^2(\omega) = \frac{(k_z^2 C_{\rm Si}^2 - \omega^2)(k_z^2 C_{\rm Ai}^2 - \omega^2)}{(C_{\rm Si}^2 + C_{\rm Ai}^2)(k_z^2 C_{\rm Ti}^2 - \omega^2)}, \qquad i = 0, e. \tag{1.24}$$

These can be thought of as the refractive indices of the tube, and oscillatory modes that are confined to within the tube and evanescent outside must satisfy $\kappa_e^2 > 0$, referred to as *trapped modes*. Modes where $\kappa_e^2 < 0$ are known as *leaky modes* as they involve oscillations beyond $r = a$ and transfer energy out of the tube, understood mathematically as the angular frequency ω being complex and the mode's amplitude within the tube decreasing with time.

Considering only trapped modes (oscillatory within $r = a$, evanescent outside), there exist two bands of allowed phase speeds for the magnetoacoustic modes. Waves belonging to the first band, starting at C_{T0} up to C_{S0} (in the long wavelength limit), belong to the *slow magnetoacoustic* branch, which are at a maximum speed travelling along the magnetic field and go to zero as their wave vector becomes perpendicular to the field. For coronal loops these waves are highly oblique because their longitudinal wavelength is far greater than their transverse spatial scale, determined by a. Accounting for this obliqueness causes the wave speed to depend on the absolute value of the magnetic field, defined through the *tube speed*

$$C_{\mathrm{T}}^{-2} = C_{\mathrm{A}}^{-2} + C_{\mathrm{S}}^{-2} \qquad \Longrightarrow \qquad C_{\mathrm{T}} = \sqrt{\frac{C_{\mathrm{A}} C_{\mathrm{S}}}{C_{\mathrm{S}}^2 + C_{\mathrm{A}}^2}}. \tag{1.25}$$

Comparing the wavelength of the slow mode to the radius of the cylinder, short wavelength slow modes propagate at the sound speed C_{S} whilst in the long wavelength limit the slow mode propagates at the tube speed C_{T}. Clearly as the magnetic field strength grows infinitely strong ($\beta \to 0$) the tube speed degenerates to the sound speed. Thus in the low-β regime slow mode waves propagate near the sound speed, and can be thought of as modified slow magnetoacoustic waves that move mostly longitudinally (their induced longitudinal flows are faster than their radial flows). More information on these waves, also called longitudinal waves in the literature, may be found in De Moortel (2009).

The second band of phase speeds, from C_{A0} up to C_{Ae} comprises the *fast magnetoacoustic* waves, which propagate fastest perpendicular to the field and degenerate to Alfvén waves when travelling strictly parallel to the field. In a low-β plasma, the radial flows induced by the fast modes have much higher speeds than the longitudinal flows, making fast modes almost transverse.

Alfvén waves travel fastest when their wave vector points in the direction of the field (torsional waves at C_{A0}), slowing down in the oblique case, and reaching zero when perpendicular – they are incompressive so require the restoring force of the field. Since Alfvén modes are incompressive, their detection observationally is fraught with difficulty relying on Doppler-shift patterns, though observations have been reported (Kohutova et al. 2020).

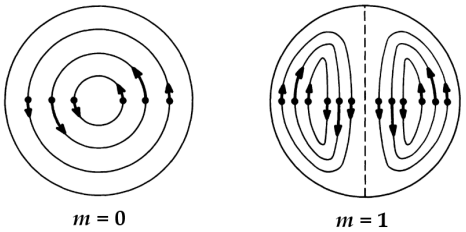

Figure 1.17: Cross-section of a flux tube showing the flow patterns associated with the two torsional Alfvén modes with the lowest transverse wavenumbers. Adapted from Spruit (1982).

Also, torsional Alfvén waves are not collective like the magnetoacoustic modes, in which the plasma moves as a whole. Instead torsional waves are fully determined by the exact magnetic surface on which they lie. This means if the Alfvén speed varies radially within a tube, that same tube can host many uncorrelated torsional modes at different propagation speeds, localised at different radii. This may be seen in the cross-sectional flow pattern of the Alfvén mode in Figure 1.17. In any realistic situation however, the pressure gradients from the induced shear flows, as well as small inhomogeneities in the plasma mean there is always some coupling between the different modes to some extent. Self-coupling may also occur due to nonlinear effects (that is, from a finite amplitude). One example of self-coupling which may be pertinent to the solar corona is that of Alfvén waves to their medium through the *ponderomotive force*, arising from the spatial derivative of the magnitude of the magnetic field. Since Alfvén waves deform the magnetic field, a ponderomotive force is created which in turn generates compressive waves in the same direction of propagation. These compressive waves travel alongside the Alfvén wave, but modify C_{A} leading to the self-coupling. These effects are potentially involved in the acceleration of the fast solar wind, and since this force accelerates ions but not neutrals, it has important consequences for the ionisation balance in the corona – termed the First Ionisation Potential (FIP) effect (Laming 2012). The coupling between different modes is also important for understanding the propagation of waves upwards from the photosphere to the corona, damping, and creating small scales that allow dissipation mechanisms to convert the wave energy into heat deposition (Brady and Arber 2016). However the precise mode coupling of upwardly propagating wave modes in such complicated geometries is not well understood, even for full 3D magnetohydrostatic numerical simulations such as explored in Riedl et al. (2019).

Typical speeds in solar corona regions range from a hundred to a few thousand $\mathrm{km\,s^{-1}}$. Figure 1.19 shows the dispersion diagram for the real phase speed solutions of trapped modes. From this it is clear that the band for slow mode oscillations is narrow, meaning that these waves are virtually dispersionless. By contrast the fast modes are extremely curved, meaning they are highly dispersive. The (torsional) Alfvén waves represented by the line $\omega/k_z = C_{\mathrm{A0}}$ are strictly dispersionless (torsional and oblique). Also shown is the variation of modes with m

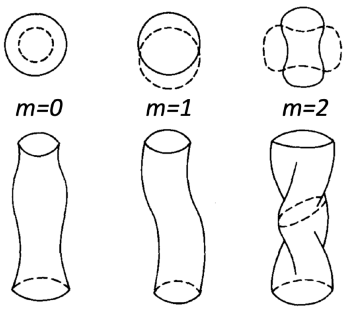

Figure 1.18: Spatial structure of the three lowest azimuthal modes of magnetacoustic oscillation of a plasma cylinder: sausage, kink and a fluting mode. Adapted from Spruit (1982).

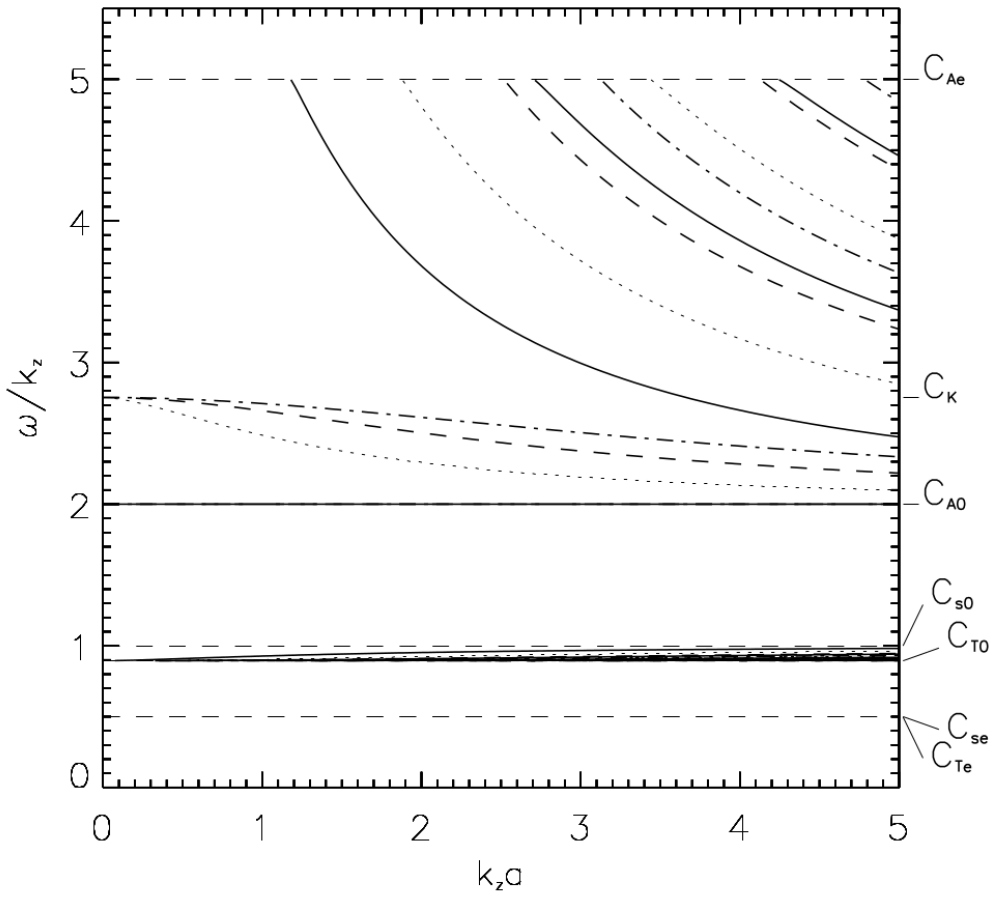

Figure 1.19: Dispersion diagram for the real phase speed solutions of Eq. 1.23, corresponding to trapped modes of MHD waves in a magnetic cylinder. Both axes are normalised, so the phase speeds ω/k_z are a function of longitudinal wave number k_z normalised to the radius a. The characteristic speeds are shown by horizontal (straight) lines, and are all normalised to the internal sound speed such that: $C_{\rm Se} = 1/2C_{\rm S0}$, $C_{\rm A0} = 2C_{\rm S0}$ and $C_{\rm Ae} = 5C_{\rm S0}$. The solid, dotted, dashed and dot-dash-dot curves correspond to solutions with azimuthal wave number $m = 0$, 1, 2 and 3 respectively. Looking in the band of fast mode solutions from $C_{\rm A0}$ upwards, the lowest curve of each style of line (m) represent the radial $\kappa = 0$ mode. Higher harmonics move up into the top right hand corner. This figure is adapted from Nakariakov and Verwichte (2005).

i.e. their azimuthal mode and hence azimuthal structure. A mode $m = 0$ is radially symmetric and known as a *sausage mode*, waves with $m = 1$ are *kink modes* and those with higher orders of m are known as *fluting modes*. The spatial structure of these modes is depicted in Figure 1.18. The fast-sausage modes are seen to have a cut-off at small wavenumbers, below which the waves are leaky not trapped – hence trapped sausage modes only exist under exceptional conditions such as flaring loops. Kink modes displace the axis of the cylinder and hence can be polarised either linearly, circularly or elliptically. In the long wavelength limit $k_z \to 0$, the phase (and group) speeds of all the fast modes except the first radial harmonic (l = 0) sausage-mode tend to the *kink speed* C_{K} where

$$C_{\mathrm{K}}^2 = \frac{B_0^2/\mu_0 + B_e^2/\mu_0}{\rho_0 + \rho_e} \tag{1.26}$$

$$\approx \frac{2}{1 + \rho_e/\rho_0} C_{\mathrm{A}0}^2 \quad \text{(in the low-}\beta\text{ limit)}. \tag{1.27}$$

Notice that this is close to the internal Alfvén speed.

For the purposes of coronal seismology, it is prudent to consider standing waves within the cylinder. This motivated by the coronal loop having a natural node at both ends, the wave being reflected by the dense photospheric/chromospheric material at/near the footpoints. This sets up boundary conditions in the z direction that quantise the wave number k_z, thus we introduce longitudinal wave number n that counts the number of maxima of the transverse displacements of the loop. If an observer is armed with n, m and κ the dispersion relation 1.23 can be used to find the frequency of the trapped magnetoacoustic mode. The dispersion becomes apparent in the dependence of each harmonic on frequency (determined by its wavelength via k), $k = k(\omega)$. Propagating modes can also develop if the wavelength λ of the wave is far smaller than the loop length, or if the wave is damped so quickly it does not have time to form a standing mode. In the propagating mode context, one may envision a localised excitation of one shape e.g. a Gaussian pulse, which subsequently propagates through the medium. The dispersion can then be thought of as different velocities (both direction and speed) for different frequency components. Thus over time, the initially localised wavepacket will have spread into a wave train. Either way, the existence of the modes is determined by the equilibrium properties of the plasma, hence coronal seismology.

In this report we are not concerned with higher orders of radial number κ, since this is related to the number of nulls in the Bessel functions i.e. the harmonics in the radial direction. Modes with $\kappa > 0$ are not detectable because current instruments

cannot resolve inside the cross-section of coronal loops. Generally speaking the fundamental mode $n = 1$ has the greatest amplitude due to frequency dependent damping mechanisms, and these are the ones most observed, although higher order harmonic kink modes ($m = 1$, $n = 2, 3 \ldots$, $\kappa = 0$) have been observed (Andries et al. 2009; Duckenfield et al. 2019; Pascoe et al. 2016a). The main MHD modes that are used for coronal seismology are thus the slow modes, the fast-sausage modes, the fast-kink modes and torsional Alfvén modes. It is important to remember that in the general case a perturbation of the plasma will lead to all three modes of oscillation being excited to various degrees, though clear observations of multiple modes simultaneously are rare (one exception being Nisticò et al. 2017). Nonetheless this thesis will focus on individual modes of oscillation; the use of fast-kink modes in coronal seismology is discussed further in Chapters 2 and 3, and the use of slow modes is expanded upon in Chapters 4 and 5.

1.2.3 Dissipation mechanisms

Ideal MHD is restrictive because it does not allow energy to be transferred between a wave and its medium. However dissipation mechanisms are important to understand, because of their role in wave damping and their possible contribution to the coronal heating problem. It is well known that in MHD, dissipative phenomena can be neglected at large scales, even if their repercussions may be felt on a large scale because their nonlinear effects may be non-local. The dissipation terms significant in MHD scales, such as viscous dissipation and thermal conduction, are proportional to the second derivative of the velocity field (laplacian ∇^2) meaning their effect scales with the square of the wavenumber k, and thus may be neglected for large scales. Looking at the induction equation 1.6, when the diffusion term is important it is clear that field variations on a length scale l_0 are destroyed over a diffusion time scale, $\tau_D = l_0^2/\eta$. So the smaller the length scale, the faster the magnetic field diffuses away. At length scales comparable to the gyroradii of ions in the plasma (Larmor radius), non-ideal effects come into play such as Hall currents (from separation of charges) which also dissipate energy.

Following (Kolmogorov) turbulence theory from hydrodynamics, it is common to separate spatial scales hierarchically into an "inertial range", large enough to neglect dissipation, and the "dissipative range" at smaller scales. Nonlinear effects (such as considering waves with finite amplitude) may lead to a *nonlinear cascade* of energy into higher wavenumbers, that is to say, energy is transferred from large scale motions into smaller spatial scales. This transfer to small spatial scales (larger wavenumbers) means dissipation is more effective. One of the manifestations of the nonlinear cascade is turbulence in the plasma, which may be observed as large

structures such as flows with large R_m forming smaller and smaller eddies until the dissipative range is reached (for example viscosity becomes important). There is a lot of effort within the community to understand the role of turbulence in MHD, for example it has been found that unidirectional Alfvén waves propagating through an inhomogeneity are sufficient for so-called "uniturbulence" to develop (Magyar et al. 2019). However the interaction between magnetic field and velocity field is complicated due to the anisotropy, plain hydrodynamical turbulence is poorly understood, and this thesis is concerned with linear MHD waves, so this subject is not discussed further.

The wave dissipation mechanisms most important under solar conditions are Ohmic dissipation, collisional friction dissipation (also known as ambipolar diffusion), viscous dissipation, and thermal conductivity (Khodachenko et al. 2006). Ohmic dissipation occurs wherever there is a current and electrical resistivity is finite, so for such dissipation to effectively heat the plasma, large currents over small spatial scales (R_m is small) are needed – meaning large magnetic field gradients. In the solar atmosphere *current sheets* (also known as tangential discontinuities) are common, where two regions of plasma with differently oriented magnetic fields are pressed together in a two dimensional sheet of small, finite width, leading to a large magnetic gradient and hence large electrical currents localised in the vicinity of the sheet. Over such short length scales diffusion effects (Ohmic dissipation) occur, annihilating some of the magnetic field and liberating the magnetic free energy into heat. Also magnetic reconnection occurs, more on this in Subsection 1.2.4. Based upon electron-ion collisions, most people use the approximation for electrical resistivity given by the so-called *Spitzer resistivity*, first formulated by Lyman Spitzer, which states that the electrical resistance decreases in proportion to the electron temperature as $T_e^{3/2}$ (Spitzer 1956; Spitzer and Seeger 1963).

The collisional friction forces appear due to the averaged relative motion of the plasma species, and thus may be neglected for the corona in which the plasma is fully ionised. The role of friction in partially ionised plasma – such as the chromosphere – is harder to ascertain, and demonstrates yet again how the chromosphere can be more complicated than the corona. The forces associated with the viscosity and thermal conductivity occur from collisions imparting momentum during the thermal motion of particles, and are important everywhere in the solar atmosphere. These dissipation mechanisms may be introduced to the system of MHD equations through the inclusion of a generalised Ohm's Law, $\vec{E} + \vec{v} \times \vec{B} = ...$ or (as is often the case) added as individual terms to the right hand side of the momentum and energy equations (for a compehensive example see section 4 in Khodachenko et al. 2006).

For example the viscosity may be estimated through the term

$$\mathcal{F}_{\text{vis}} = \rho\nu \left[\vec{\nabla}^2 \vec{v} + \frac{1}{3} \nabla \left(\nabla \cdot \vec{v} \right) \right], \tag{1.28}$$

where ν is the (assumed uniform) kinematic viscosity $[m^2 s^{-1}]$ of a viscous fluid as found in equation (7.5.2) of Aschwanden (2006). The anisotropy of the magnetic field makes this expression for the viscosity an oversimplification. In fact the term is better represented through a tensor, where the kinetic viscous coefficient(s) must depend on the magnitude and direction of the magnetic field. The anisotropic *transport coefficients* – quantities that categorise how energy is transported and, in particular, determining the effectiveness of dissipation – for a collision dominated plasma have been computed in the lengthy work by Braginskii (1965), considering both ion and electron species.

In the corona it is not usual to consider the effect of shear viscosity, because according to this tensor, the compressive viscosity (pertaining to flows strictly parallel to the magnetic field) is orders of magnitude larger than the shear viscosity. When the literature refers to "anomalously high viscosity", this is understood to mean the compressive viscosity is many orders higher than the value found in Braginskii (1965), and invoked to explain unusually high rates of dissipation. Anomolously high values of transport coefficients, compared to those computed in Braginskii (1965), have been recorded in magnetospheric and tokamak plasmas and are caused by effects from non-MHD scales (such as the electron scale). Some further discussion regarding compressive viscosity may be found in Chapter 4. Note that shocks are natural places for enhanced viscosity to occur because of the nonlinear cascade of energy to smaller scales (the compression of the plasma), so 'regular' dissipation becomes effective there. For more information about the potential role of shocks in heating the corona through viscosity see Reid et al. (2020) and references therein. It should be pointed out that numerical viscosity plays a vital role in the numerical stability of MHD simulations, as an example both a background viscosity and an effective 'shock viscosity' are used in the popular MHD simulation code *LARE3d* (Arber et al. 2001).

Thermal conductivity by electrons is hugely important in the solar corona. The high temperature of the solar corona compared to the cool chromosphere sets up a large thermal gradient, implying heat is conducted down through the transition region, where much energy is radiated away. Thermal conduction has traditionally been cited as the most important damping mechanism of slow magnetacoustic modes in hot loops, which is discussed in detail in Section 4.1. In strongly magnetised plasmas such as the corona, thermal conduction across the magnetic field is dramatically

depressed and is often neglected; in the corona the thermal conduction is usual taken to be proportional to the field-aligned temperature gradient. This results in a thermal conduction term that may be written (in a 1d sense with s the coordinate in the direction along the magnetic field) as

$$\mathcal{L} = \frac{\partial}{\partial s}\left(\kappa_{\parallel}\frac{\partial T}{\partial s}\right) \tag{1.29}$$

where $\kappa_{\parallel} = \kappa_0 T^{5/2}$ W m^{-1}K^{-1}, and $\kappa_0 = 7.8 \times 10^{-7} T^{5/2}$ ergs cm^{-1} s^{-1} K^{-1}, originating from a well-known Spitzer and Seeger (1963) result for thermal transport dominated by Coulomb collisions. This approximation is derived for fully ionised plasma, and valid for use in coronal loops when the electron mean free path is much less than the temperature scale height. Turbulent scattering () is thought to suppress the thermal conductive flux in some cases, while in other cases when the thermal conductive flux is no longer inhibited by scattering processes, it approaches an upper limit called the free-streaming case. In these cases the thermal conduction flux have a temperature dependence of $3/2$ and $-1/2$ respectively (Bradshaw et al. 2019).

Waves are also thought to lose energy through radiative cooling, in which the energy is not dissipated as heat but released as photons. The calculation of the radiative loss function is difficult and involved, due to the effects of recombination, non-equilibrium energy level populations, electron excitation rates and so on, all of which vary with temperature and ionisation. A major resource for the solar community concerning atomic data, including radiative loss as a function of temperature and density, is the freely available and regularly updated CHIANTI database (Dere et al. 1997, 2019). Radiative losses are strongly dependent on small changes in density and temperature, and are always present in the solar atmosphere. It is increasingly clear that the interplay between heating and cooling may have important dispersive effects on MHD waves, and radiative losses play an important part of this competition – this is discussed further in Chapter 5.

1.2.4 Plasma instabilities and nonlinear effects

Just as perturbations can lead to waves in the plasma, perturbations may also lead to instabilities. As a matter of nomenclature, this thesis will only refer to MHD "macro-instabilities" which cause major reconstructions of the plasma, leading to CMEs etc. This is in contrast to "micro-instabilities" which are abundant using in the kinetic regime, occurring in velocity space but restricted to microscopic scales (gyroradius etc). Mathematically one performs analysis of an instability using the dispersion relation for a perturbation; the sign of the imaginary part of ω determines stability, such that $Im(\omega) > 0$ means the configuration is unstable and

the perturbation grows, whilst $Im(\omega) < 0$ means the configuration is stable and the perturbation decreases. For example, consider a cylinder of plasma with an axial current, generating a purely toroidal field (called a plasma pinch) which is subjected to an axisymmetric perturbation of the equilibrium, compressed inwards say. In the equilibrium, the gas pressure force radially outwards is balanced by the Lorentz force directed inwards. At the 'neck' however, the cross section is reduced meaning the magnetic field strength there increases (radius of curvature decreases), strengthening the Lorentz force inwards and compressing the plasma. The gas pressure acts to evacuate the plasma in the neck, leaving nothing to counteract the radial inwards force – the neck implodes. Thus the equilibrium is unstable to the so-called *sausage instability*. Similarly, if the axis is perturbed, it transpires that this configuration is also unstable to the *kink instability*. Even in the presence of a stabilising axial magnetic field, certain wavenumbers are unstable to this instability. This may all be seen with the dispersion relation, and such instabilities have been invoked to explain the eruptions of flux ropes in the solar atmosphere such as in CMEs (Kang et al. 2019b; Török and Kliem 2005).

Another important example of instability is the *Kelvin–Helmholtz instability* (KHi) which appears in shear plasma flows. This is a well-understood hydrodynamical instability in which vortices across the interface are formed, and its threshold and growth rate between two magnetised plasma were derived analytically by Chandrasekhar (1961). There is interest in KHi due to its (and other associated shear instabilities') propensity to form small spatial scales and filamentous current sheets, and hence to drive dissipation of wave energy. The distinctive vortices associated with KHi have been observed before in CME eruptions, for example Foullon et al. (2011). However these vortices are triggered by massive plasma velocities parallel to the magnetic field, leaving open the question of KHi from the ubiquitous shear (azimuthal) flows in coronal plasma inhomogeneities such as loops. It is known that a flow-aligned magnetic field tends to stabilise sub-Alfvénic motions, and so may suppress the formation of KHi. For propagating Alfvén and kink waves, it is believed the phase behaviour of the azimuthal flow and magnetic field are such that they are stable to KHi. On the other hand, for standing modes this phase behaviour is different so the transverse flows in the oscillation antinodes are always unstable to KHi (Zaqarashvili et al. 2015), at least in the linear regime. In simulations of coronal loop oscillations, KHi is omnipresent and leads to a very mixed cross section, even for small amplitudes ($\leq 3\,\mathrm{km\,s^{-1}}$) (Antolin et al. 2014; Magyar and Van Doorsselaere 2016a). This can happen even when the loop motions do not set up a pattern of standing antinodes and nodes: for instance, a recent simulation by Pagano and De Moortel (2019) incorporating a realistic footpoint driver with "random buffeting"

driver whose power spectrum matches observations was found to be insufficient to even maintain the thermal structure of the loop without radiative losses, for realistic coronal densities and temperatures. Even in this case, KHi developed extremely quickly and made the loops unrecognisable in just over an hour.

Simulations imply this should be a universal property of all oscillating loops, which presents a mystery of why loops appear monolithic during and after kink oscillations. It is true that the line of sight integration, with emission line flux being proportional to density squared, would act to blur such mixed cross sections. Yet in simulations with coronal conditions KHi develops extremely rapidly, for example taking a characteristic oscillation period of a kink wave to be 300 seconds, then the time-scale for the instability is approximately 30 – 300 seconds (Hillier et al. 2019), depending on the amplitude, density gradient and density ratio. Further, the evolution of the tube seems to be dependant on the initial perturbation amplitude, suggesting the larger the amplitude the faster and more severe the deformations (demonstrated in the nonlinear numerical studies in Magyar and Van Doorsselaere 2016a; Terradas et al. 2008a). Yet this is not seen in decaying kink oscillations of loops greatly perturbed by a nearby eruption, such as that studied in Chapter 2 – in fact the loops appear to remain in one coherent structure without obvious filamentation and fragmentation. So the question remains: why is there so little observational evidence of KHi in coronal loops? One school of thought holds that KHi is indeed observed in coronal loops, but the spatial resolution is insufficient to resolve it. Instead, other signatures such as the arrows in Doppler time-distance diagrams, or evolving phase change between displacement and velocity should be searched for instead (Antolin et al. 2017), in a similar way perhaps to observations of prominences that match well to simulations of the KHi development and its interplay with resonant absorption (Okamoto et al. 2015).

Another school of thought is that a twisted magnetic field is thought to stabilise a tube to KHi, as was (only partially) demonstrated in Howson et al. (2017). However this twist can not be too great, else the loop is subject to the pinch instabilities (Terradas et al. 2008a). Moreover, twisted loops should have a sigmoid shape which is observed very rarely. Twisted flux tubes above a certain critical pitch can develop a helical kink instability, which may explain at least some of the eruptions in the solar atmosphere (Török and Kliem 2005). Perturbations to a flux tube with a twisted magnetic field necessarily leads to currents which subsequently form thin fragmented current sheets, and the magnetic field deviates from a potential magnetic field. It may also have an effect on the damping of MHD oscillations via resonant absorption (Subsec. 2.1.1), though this is weak (Howson et al. 2017). Twisting magnetic field can be a difficult effect to model correctly (e.g.

see Browning and Priest 1983), not least because the inclusion of twisted magnetic field permits the nonlinear generation of additional (azimuthal) harmonics. In some cases this lowers the threshold of instability required to trigger sudden avalanches of energy release (Reid et al. 2020). Magnetic twist is often neglected in theoretical models of MHD oscillations since it couples the different modes together, making concrete conclusions about one process very difficult. Nonetheless Barbulescu et al. (2019) have shown that, in the linear regime, magnetic shear can never prevent the onset of KHi at the loop boundary, and further, only for under certain conditions can the magnetic twist suppress the growth rate. Note that whilst KHi does not require nonlinearity in order to occur, once it occurs it can rapidly become nonlinear and so growth rates predicted from linear theory quickly become invalid.

When the amplitude of an MHD perturbation is no longer small compared to the equilibrium value, additional nonlinear effects come into play, providing alternative routes for the transfer of energy. Simulations of nonlinear effects of large-amplitude transverse oscillations of coronal loops were performed in (Magyar and Van Doorsselaere 2016a,b), in which it was found that KHi can affect the loop dynamics drastically, and that the multi-stranded model of coronal loops would be especially susceptible. Observational clues that nonlinear effects may be at work include a direct dependence of the oscillation period upon its amplitude, wave steepening from the excitation of higher harmonics (for example the oscillation evolving from a sinusoidal time profile into a triangular one), and non-stationarity (the oscillation parameters such as period are time dependent). Such nonlinear effects may be important in heating the plasma, for example the nonlinear cascade manifested as wave-steepening will make dissipation more effective in the vicinity of the steep wavefronts (which may shock). Often it is convenient to restrict attention to weakly nonlinear phenomena, which may be considered as corrections to the linear solutions.

A very commonly discussed nonlinear phenomenon in the solar atmosphere is magnetic reconnection. In the presence of a finite resistivity, magnetic field lines within some some small localised region can change their connectivity due to diffusive effects. Thus energy may be liberated from the magnetic field, which reaches a lower energy state (for example highly curved magnetic field lines reconnect into straight lines). This energy is mostly kinetic and may accelerate jets, and subsequent non-ideal processes convert this energy into heat, or excite waves and shocks. Magnetic reconnection is often used in solar physics as a "silver bullet", to explain some source or sink of energy, or invoked whenever regions of differently oriented magnetic field are pressed together in small spatial scales. The reality is that magnetic reconnection is not well understood, particularly its time-dependence and its effects in a three dimensional sense.

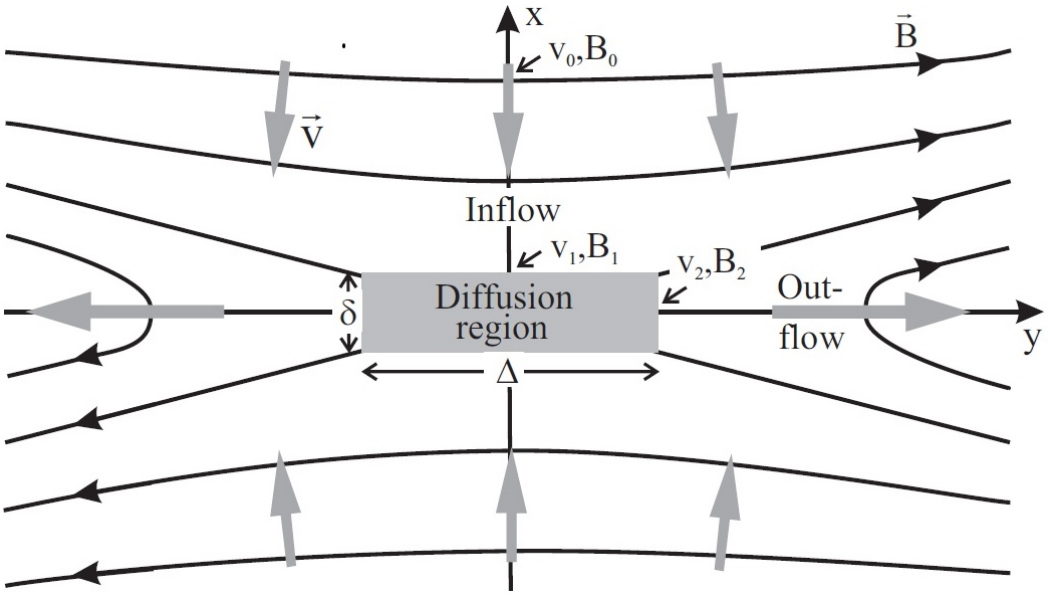

Figure 1.20: Classical depiction of two dimensional reconnection. The black curves represent magnetic field lines, the grey arrows velocity, and the rectangle a localised diffusion region in which reconnection occurs. This outlines the *Sweet-Parker* model, the first theoretical framework of magnetic reconnection in 1957.

Many cartoon drawings of curved field lines reconnecting into straight lines, with some indication of a flow, are used to explain a particular phenomenon. An infamous example of such a cartoon is shown in Figure 1.20. Yet such diagrams can be misleading, particularly under scientific scrutiny. Simulations abound and yet because of the change in connectivity, it is impossible to follow a single field line – such a discrete object no longer exists. Most theoretical models of magnetic reconnection are two dimensional, which can be fundamentally of a different character to the three dimensional case (though there are some situations in which a two dimensional model is appropriate, such as an elongated current sheet). The theoretical rates of reconnection are many orders of magnitude slower than the characteristic rising phase of a flare, for example, unless finely tuned additional effects are included. Another common misconception is that reconnection requires a magnetic null point – it does not, requiring only $\vec{E} \cdot \vec{B} \neq 0$ to have global implications – although magnetic nulls are regions where reconnection is likely to occur, especially in a "fan and spine" configuration (for example in Sun et al. 2013). Nor does reconnection necessarily lead to explosive energy releases – in three dimensions it is perfectly possible for magnetic field lines to diffuse into each other gradually, continuously breaking and reconnecting smoothly, so-called *magnetic slippage*.

This is not to say that explosive magnetic reconnection does not happen

– it certainly does occur, but current understanding of reconnection in such an inhomogeneous and dynamic environment as the Sun needs much more development before quantitative descriptions of its (small scale) effects can be believed.

1.2.5 The coronal heating problem

The standard view of coronal heating is that free magnetic energy is built up via the complexity of the magnetic field, driven at least partially due to shuffling of the magnetic field lines in the photosphere by convective motions. There is consensus that shocks originating from these acoustic modes produced below the photosphere may be significant for heating the lower chromosphere, however above the transition region the low-β plasma must be heated through other mechanisms. There is also consensus that although most of the energy injected by the photosphere is dissipated in the lower atmosphere, some penetrates upwards as non-potential magnetic field or motions such as waves. Then either through magnetic reconnection, or dissipation, or most likely both, this magnetic energy is dumped into the coronal plasma (De Moortel and Browning 2015). The spatial scales of this deposition must be less than all current observations' resolutions, likely to be between the order of centimetres (typical Larmor radius) and kilometres. Thus reconnection events must be smaller than traditional flares and are called *nanoflares*. Note that the term nanoflares has come to incorporate other small outbursts of energy, regardless of mechanism (for instance Taylor relaxation, or shocks). It is fairly easy to heat the corona because the plasma density is low and hence not much energy is required. The difficulty is keeping the corona hot. High thermal conductivity and a thermal gradient between the tenuous corona and the colder but far denser chromosphere drives a flux of energy downward. The coupling between the corona and chromosphere mean the latter must not be considered a passive layer between the photosphere and corona. All the while, plasma is radiating energy away and there is further mass and energy flowing away from the Sun in the ever-present solar wind. Thus the mechanism(s) for heating must operate predominantly on tenuous and magnetically-dominated plasma, be constant enough to maintain the long-lived corona, and be resilient to all manner of perturbations. There is growing evidence that coronal heating is non-steady, for example the fact that loops deviate far from hydrostatic solutions with constant heating, and the matching of bursty models with observed loop lifetimes (Schmelz and Winebarger 2015) while characteristic time scales of the heating are not understood.

The MHD Alfvén modes have often been studied in the context of coronal heating. Despite the well known reflection of Alfvén modes by the transition region, such modes are believed by some to carry sufficient energy flux upwards to heat the corona, while its observational evidence is absent (a review may be found in Arregui

2015). It should be kept in mind that the presence of waves does not necessarily imply heating, and the routes to dissipate energy are as important to understand as the waves themselves. Simulations suggest that Alfvén waves, excited by a photospheric driver, can couple to slow modes which subsequently shock and heat the chromosphere (Kudoh and Shibata 1999). However the speed of any turbulent energy cascade is unknown for full 3d models of the atmosphere, so it may be that other dissipation mechanisms become important. The role of turbulence (which may also be viewed as many incoherent Alfvén waves interacting) is also believed to be important (Van Ballegooijen et al. 2011). Also there can be several ways of coupling between different MHD modes. In a compressive medium, the ponderomotive force can convert between Alfvén and slow modes, mode coupling can occur at the $\beta = 1$ boundary, and flux tube expansion can also geometrically couple different modes. Thus how waves can carry energy from the photosphere, through the radically different chromosphere into the corona remains open. In addition, the energy flux in the waves themselves is still debated.

The exact properties of the heating mechanism are still unknown, to the extent that we do not know if heating depends on density ρ or magnetic field strength B or temperature T at all. The analysis of differential emission measure distributions provides some clues, for example in Schmelz and Winebarger (2015), but these are limited by the ambiguity of such measurements. Observations of coronal loops and the scaling law between magnetic field strength and loop length inferred from statistics has been suggested as a method for constraining coronal heating models, following from the seminal Rosner–Tucker–Vaiana models proposed in Rosner et al. (1978). A key paper in the development of this technique was Porter (1995), in which the scaling laws for a sample of 47 loops observed in soft X-ray (SXT aboard Yohkoh) were determined. Noting the observed lifetimes of coronal loops are much longer than their apparent cooling times, using quasi-static equilibrium theory it was concluded that volumetric scaling heating rate scales approximately with the inverse of loop length squared. The implications of this result on the various parameterisations $\mathcal{H}(B, \rho, L, V, R)$ predicted by different coronal heating models was then further explored in Mandrini et al. (2000). The authors concluded that so-called "stressing models" – in which energy is injected into the magnetic field by slow footpoint motions – were in much better agreement with observations than so-called "wave models", meaning energy is deposited by waves that are generated at the base of the corona. The variable of temperature is only implicitly included, and it is the parameters of the coronal loop such as length L (and R, which loosely is the loop major radius, modified by twist) that contain the information about temperature through their dependencies. More recently, a summary of past observational studies

using this approach has pointed out some of the potential shortcomings of using emission from individual coronal loops to provide constraints on the heating function (Fludra et al. 2017). Nonetheless a diagnostic is developed for the heating function for a subset of loops that are found close to static thermal equilibrium.

One limitation of this approach to constraining the heating function is that the precise structuring of coronal loops is still largely unknown, and without a detailed physical understanding of the loop's cross section, the averaging used to determine the exact parameterisation of the heating models may not be accurate (e.g. Vesecky et al. 1979). Another obvious limitation is that the proposed mechanisms are not likely to be mutually exclusive, and indeed some mechanisms may be important in locations in the parameter space where other mechanisms are not. In light of these shortcomings, a method using slow magnetoacoustic waves to probe the thermal equilibrium of the corona is discussed in Chapter 5.

1.3 Thesis outline

The research presented in this thesis concerns the application of coronal seismology, in particular the role of dispersion on such magnetoacoustic modes, and how this may affect observations. In this chapter an outline of the solar atmosphere and the theory of magnetohydrodynamical waves was laid out, both in order to give context to the observations and theory in the coming chapters.

In Chapter 2 the transverse *kink-mode* oscillation is the focus. The theory behind these ubiquitous oscillations is described, including the successes of the theory of resonant absorption as a damping mechanism. The advantages of using multi-modal observations to extract information about the plasma inhomogeneity (such as coronal loop) are explained. The first spatially resolved observation of a coronal loop oscillation comprising of the fundamental standing mode and its third harmonic is presented. A measurement of the signal quality for a higher harmonic is made and compared with the signal quality of the fundamental mode, the conclusion of which is validation of the 1d resonant absorption theory.

In Chapter 3 the focus is on a different regime of transverse oscillation, in which the amplitudes are much smaller and there can be little or no damping – hence these are named *decay-less* kink oscillations. Having only been recently detected, the history of observations and studies on decay-less oscillations is given. Many open questions about decay-less oscillations remain, such as their excitation mechanism and if they are subject to the same damping mechanisms that make large amplitude kink oscillations decay so rapidly. The first detection of a higher harmonic of a decay-less kink oscillations is presented. This was achieved using the novel processing

technique of motion magnification, and the potential for routine seismology using decay-less oscillations (which are extremely commonplace in the corona) is discussed.

Chapter 4 shifts from fast kink-mode oscillations to *slow mode* oscillations, which are commonplace in the lower corona. The theory behind slow mode oscillations is described, which are seen as disturbances of intensity. Observations of propagating intensity disturbances in a coronal fan are presented. Justification of their interpretation as slow-modes is given and the relationship between measured (instantaneous) velocity and period of the oscillations in multiple bandpass channels is discussed. The average apparent measured velocity ratio of 193 Å against 171 Å is found to contradict theoretical estimations of the velocity ratio. To resolve this result, the images in different bandpasses are interpreted to be observing waves in different strands along the line of sight, and so a conclusion regarding multi-thermal loops is made.

Chapter 5 describes the dispersion effects on slow magnetoacoustic waves by any (wave-induced) *misbalance between plasma heating and cooling processes*. This is important because the nature of the thermal equilibrium maintained between the coronal heating function and the energy losses of radiation and thermal conduction is poorly understood, but through these slow magnetoacoustic modes may be probed. The dispersion relation describing slow magnetoacoustic modes guided by a cylindrical magnetic flux tube, incorporating a wave-induced thermal misbalance term is derived, including finite-β effects. The limits of strong and weak non-adiabaticity are explored. This dispersion is shown to be relevant throughout the corona, which may resolve some issues surrounding understanding of slow mode damping. Finally the link between this theory and applying seismology to slow mode observations to constrain the unknown coronal heating function is discussed.

A summary of the results presented in this thesis, and a discussion of the myriad exciting potential avenues for future work, is given in Chapter 6.

This thesis includes several appendices, which do not present new results but provide additional detail on the processing techniques used in this thesis, since coronal seismology relies on extracting as much information as possible from observations of coronal oscillatory motions. Time series analysis, which was crucial for determining multiple periodicities within the data accurately, is detailed in Appendix A. In Appendix B the novel tool of motion magnification is explained, as is its application to coronal extreme ultra-violet image sequences taken of the corona. Appendix C explains the role of Bayesian statistics in seismology, providing a natural and principled framework within which we may quantitatively infer understanding of observations combined with model predictions and prior information, in a robust way that is easy to update.

Chapter 2

Kink oscillations and their use in coronal seismology

In this chapter, the fast-kink magnetoacoustic standing mode of coronal loops is discussed. A literature review of the myriad ways in which observations of these kink oscillations have been used in seismology, and more detail on the underlying theory of fast-kink modes, is given in Section 2.1. An observation of a coronal loop's standing kink mode is presented in Section 2.2. The simultaneous detection of the fundamental standing mode and its third (longitudinal) harmonic are verified, and analysed with the aim to reveal the relation between different harmonics' periods and quality factors. The loop's density profile and density contrast throughout the loop are probed, and the implications in using this observation to substantiate 1d resonant absorption theory are discussed in Section 2.3. This is the first time a measurement of the signal quality for a higher harmonic of a kink oscillation has been reported with spatially resolved data.

2.1 Introduction

Coronal seismology uses the modelling of magnetohydrodynamic (MHD) waves in plasma structures and the comparison with observations for the diagnostics of the plasma for the diagnostics of the coronal plasma (reviews may be found in Andries et al. 2009; De Moortel and Nakariakov 2012; Nakariakov et al. 2016b, and references therein). The interpretation of observations of transversely oscillating coronal loops as fast magnetoacoustic waves, of the $m = 1$ kink mode, is one of the most intensively performed examples of this. The existence of fast-kink modes in the solar corona was predicted in Roberts et al. (1984); Zajtsev and Stepanov (1975) in order to explain pulsations in radio and hard X-ray emission detected on Earth from the

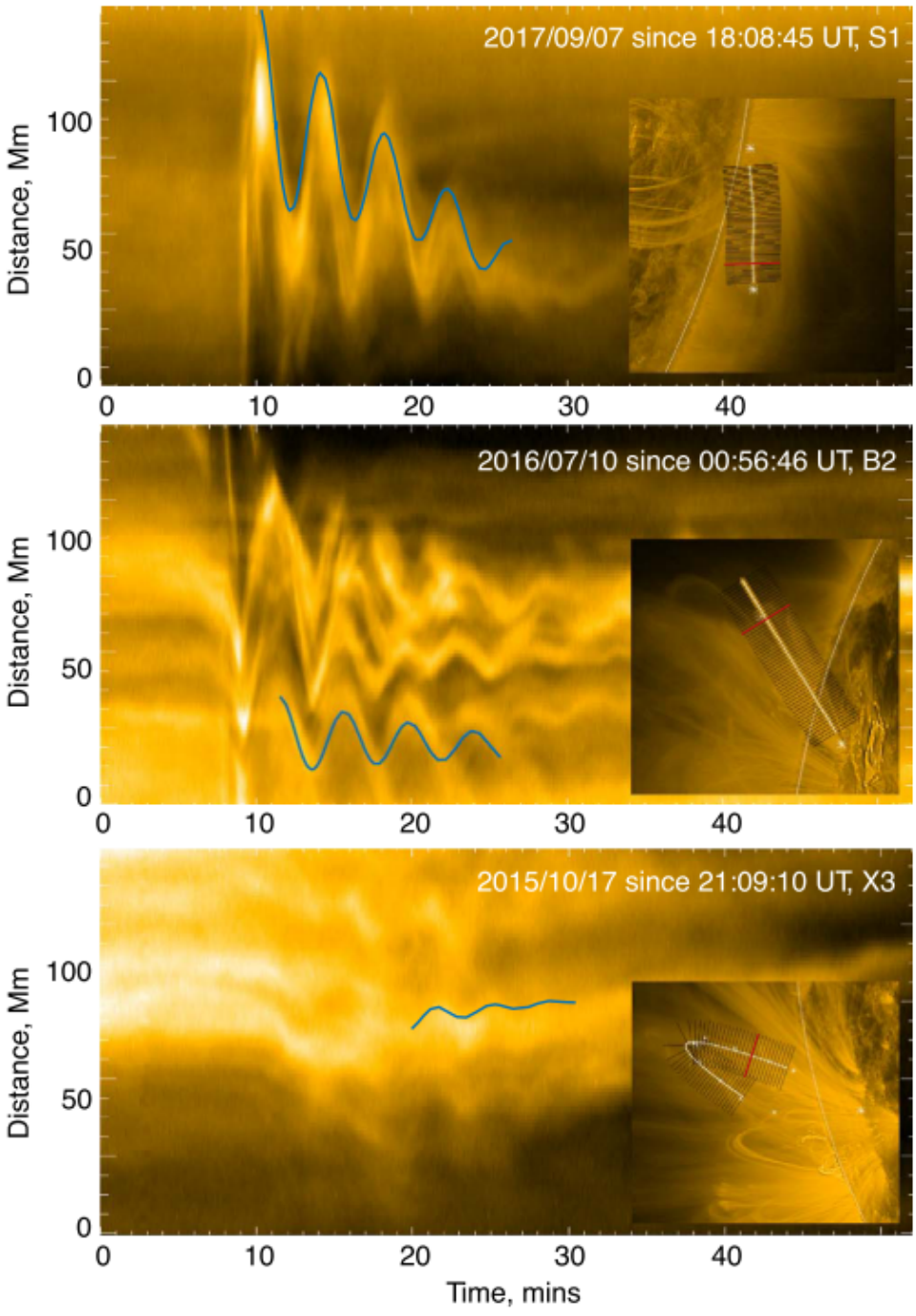

Figure 2.1: Three examples of kink oscillations, shown as time-distance maps and with insets showing the location off the solar disk. This figure was taken by Nechaeva et al. (2019).

Sun. These rely on the theory of the eigenmodes in a magnetic cylinder (Edwin and Roberts 1983; Zaitsev and Stepanov 1982). These well-used models for linear waves are described by dispersion relations obtained for uniform, equilibrium models of very thin, axisymmetric, long, and straight tubes. This theory has continued to be applied, both for numerical simulations and to observations since the first imaged detection of transverse loop oscillations, observed with TRACE (Aschwanden et al. 1999; Nakariakov et al. 1999). Often the approximations considered are good enough to extract useful information about the plasma via seismology, particularly when estimating the physical parameters averaged across the entire loop. This makes the study of kink oscillations particularly compelling because the structure of a coronal loop is poorly understood, both in terms of its thermal equilibrium, its density profile, and its stratification with height. The fact that loops are perturbed as an apparently uniform cylinder for at least several periods implies that the (standing) kink mode takes a spatial average over all these fiendishly interconnected variables, to arrive at the simple expression for the (loop averaged) kink speed

$$\langle C_{\rm K} \rangle = \frac{\lambda}{P_{\rm kink}}, \tag{2.1}$$

where $P_{\rm kink}$ is the measured period of the standing mode. For the fundamental standing mode in a coronal loop of length L, the wavelength $\lambda = 2L$. By relating the phase speed of an observed transverse oscillation to the kink speed (assuming a low-β plasma), one can rearrange for the magnetic field strength as

$$\left.\begin{aligned} C_{\rm K}^2 &\approx \frac{2}{1+\rho_e/\rho_0} C_{A0}^2 \\ C_{A0}^2 &= \frac{B_0^2}{\mu_0 \rho_0} \\ \frac{2L}{P_{\rm kink}} &\simeq \frac{\omega}{k} = C_{\rm K} \end{aligned}\right\} \quad \Longrightarrow \quad B_0 \approx \frac{L}{P_{\rm kink}} \sqrt{2\mu_0\rho_0 \left(1+\frac{\rho_e}{\rho_0}\right)}. \tag{2.2}$$

Thus by measuring the period of a standing transverse oscillation, the length of the host loop and making an estimate of the loop density and density contrast, the absolute magnetic field value may be obtained. This was first applied by Nakariakov and Ofman (2001), yielding a magnetic field strength of 13 ± 9 G, with much of the error originating from the uncertainty on the densities (and filling factor). Many subsequent examples of this seismology have also yielded values of magnetic field around 10 G and below. Some examples are the comprehensive seismological analysis of a flare-induced, vertically polarised (meaning the axis' direction of motion is radial to the Sun) kink mode yielding 4.0 ± 0.7 G in Aschwanden and Schrijver (2011),

analysis of the kink mode of a contracting loop to find 12.8 ± 2.0 G in Pascoe et al. (2017b), and the Doppler velocity observations of the kink mode of a trans-equatorial loop excited by a nearby CME finding a strength of 2.4 ± 0.6 G in Long et al. (2017b).

Detections of kink-mode oscillations in plasma inhomogeneities other than coronal loops have been reported and seismology applied. Examples include kink modes in polar plumes (Thurgood et al. 2014), in prominences (Arregui et al. 2018), in spicules (Verth et al. 2011), as propagating fast wave trains along open field lines (Goddard et al. 2016b), and within fibrils in the magnetic network in the chromosphere (Mooroogen et al. 2017). It has been claimed the corona is replete with the (upwardly) propagating form of the kink mode, using observations from large scale Doppler velocity data with the CoMP instrument (Morton et al. 2016; Tomczyk et al. 2007) and recently using an automated processing tool on imaging data (Weberg et al. 2020).

In observations of kink modes, clearly there are more variables than observables, so the seismological inversion is ill posed. There have been several ways to get around this fundamental problem: simultaneous spectroscopic observations to gain information about the density (Van Doorsselaere et al. 2008, who inferred $B_0 = 39 \pm 8$ G), or linking other observables with additional physics such as relating the damping rate to resonant absorption (below). In this chapter the use of multiple longitudinal harmonics is emphasised, but the reader should be aware that many other avenues of attack exist. In general the nature of having a few observables with reasonable constraints, well trusted formulae to relate the different variables, and additional sources of information which may be relevant, taken together make Bayesian inference a natural framework for this form of seismology (for a direct example see Arregui et al. 2019). The Bayesian framework is described in Appendix C. Combining other simplified models with the observations in this way, for example including gravitational density stratification, the forward modelled intensity profile or loop expansion, such seismological inversions may be used to estimate not only the Alfvén speed (Verwichte et al. 2013a), but also the coronal density scale height (Van Doorsselaere et al. 2007), the loop cross-section expansion (Verth et al. 2008), the transverse density profile (Goddard et al. 2017) or the longitudinal and cross-field magnetic field and density structuring (Verth et al. 2011).

Transverse oscillations of coronal loops are readily observed in EUV imagers, with sufficiently high spatial resolution and cadence. Examples of kink oscillations observed with SDO/AIA are shown in Figure 2.1. **The reason that the transverse motions of loops are chiefly attributed to the standing kink mode is the robust linear scaling of period of oscillation with loop length.** This

linear dependence follows directly from Equation 2.1. In statistical studies of kink oscillations, the measured oscillation periods range from just over a minute up to twenty minutes or so with a peak at 4–7 minutes, seen in loops with a roughly even distribution between 140 and 460 Mm, but from as short as 70 Mm and up to 600 Mm. The period is consistently found to be linearly dependent upon loop length, with a gradient of P [min] = 0.025 ± 0.001 L [Mm] for the 58 oscillations comprising Goddard et al. (2016a), and reaffirmed when an additional 48 events are included, in Nechaeva et al. (2019). There is a scatter in values due to different loops having different kink speeds (from density contrasts, magnetic field strengths), but doing a straight division one can estimate a typical kink speed of $C_{\rm K} \simeq 1330\,{\rm km\,s^{-1}}$. Taking the histogram of every event analysed individually, a modal kink speed of 900–1100 $\rm km\,s^{-1}$ and range of some 800–3300 $\rm km\,s^{-1}$ were found (see Fig. 2.2, duplicated from Goddard et al. 2016a). There may be observational biases at work: it is easier to find long loops and higher amplitude oscillations than short loops or small amplitude oscillations, and loops in active regions (which form the majority in these studies) tend to be denser than those in the quiet Sun.

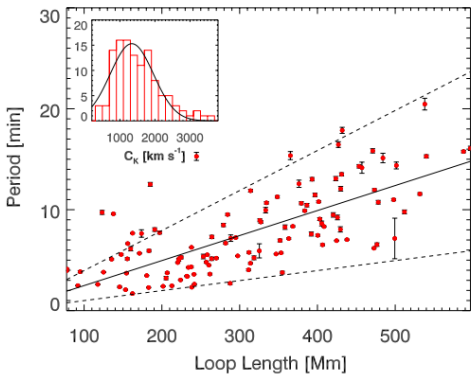

Figure 2.2: Scaling of period against loop length for 118 individual kink oscillations. [*Inset*] Histogram of kink speed values. The solid line of best fit gives C_K = 1330 km s^{-1}. Figure is taken from Goddard et al. (2016a).

It has emerged that there are two distinct regimes of kink oscillations; the first and most widely reported is large amplitude, rapidly decaying oscillations with displacements of the order of several loop minor radii and decay time of the order of several periods. These motions are the subject of this chapter. The second regime involves much lower amplitude oscillations that persist for far longer (over many periods) and in some cases grow over time – we call these *decay-less* kink oscillations, and are discussed further in Chapter 3. In either case, the fact that period (and as we shall see, the damping time) has been observed to scale linearly with the loop length L, implies that the transverse motions in both regimes are indeed standing kink modes.

The majority of (large amplitude, rapidly decaying) kink oscillations are excited by a mechanical displacement caused by a low coronal eruption, or at least the majority of those which are catalogued (Zimovets and Nakariakov 2015).

Because this mechanical impact is not necessarily co-planar to the loop, nor will the excitation necessarily affect the loop symmetrically (or perfectly anti-symmetrically), this mechanism is likely to excite multiple harmonics of the loop with varying efficiencies (for example consider the straight-forward driving of a thin flux tube with fixed ends in Ballai et al. 2008). In most cases only the fundamental standing mode of the loop is recorded, however due to rapid damping and the amplitude distributions of the even-numbered harmonics (node at apex) this is likely an observational bias rather than a quality of the excitation mechanism. Another way in which kink oscillations are excited is through the rapid change in magnetic topology, for example the contraction or expansion of a loop following the onset of a flare (Russell et al. 2015). This was observed in at least one case in Pascoe et al. (2017b), which confirmed that this excitation mechanism most efficiently excites the fundamental mode, and higher harmonics are not present. Another excitation mechanism is known to be the condensation of material (coronal rain), usually but not always at the loop apex, for example shown in the simulations of Kohutova and Verwichte (2017).

2.1.1 Damping through resonant absorption

One of the main features of these large amplitude kink oscillations is their rapid damping. Additional information for the determination of plasma parameters from seismology has been shown to reside in the oscillation's damping profile, for example being used to estimate the loop's density contrast in Aschwanden et al. (2003). The main mechanism by which trapped kink modes are thought to damp away is *resonant absorption* (Goossens et al. 2002; Hollweg and Yang 1988; Ruderman and Roberts 2002). The global kink mode is believed to couple to local azimuthal, incompressible Alfvén modes that reside in a resonant shell within the cylinder, transferring energy from the transverse motion of the cylinder into plasma motions within. These azimuthal (shear) motions can not be directly observed, although some (indirect) observational features of prominences have been shown to match simulations of these motions' interaction with KHi (Okamoto et al. 2015). The azimuthal motions are thought to occur in a narrow resonant region, which exists due to the wave guide having an inhomogeneous transverse structure which causes C_{A} to vary radially – only when the local Alfvén speed matches the phase speed of the collective motion (C_{K}) will these modes couple (Soler et al. 2013). Note that resonant absorption is a linear coupling, and a dissipation-less process. The azimuthal Alfvén modes themselves are believed to damp away through the process of *phase mixing*, in which neighbouring magnetic surfaces oscillate independently (recall the Alfvén mode is not collective) but in doing so become increasingly out of phase, inducing large velocity gradients (shears) which enhance local viscous dissipation, which may be thought of

as friction (Heyvaerts and Priest 1983; Ofman and Aschwanden 2002). However this has never been directly verified, and other dissipation mechanisms may occur such as KHi.

The ratio of the damping time $\tau_{\rm d}$ to the period was calculated for resonant absorption by Ruderman and Roberts (2002) for a thin-boundary layer and by Van Doorsselaere et al. (2004a) for thick boundaries, the latter finding that same dependence is a reasonable approximation though the damping rate is overestimated by up to 25%.

$$\frac{\tau_{\rm d}}{P_{\rm kink}} = \begin{cases} \dfrac{2}{\pi}\dfrac{1}{l_{\rm inhom}/a}\left(\dfrac{\rho_0+\rho_e}{\rho_0-\rho_e}\right) & \text{(thin boundary, } l_{\rm inhom}/a < 0.5\text{)} \\ \approx 0.75\dfrac{2}{\pi}\dfrac{1}{l_{\rm inhom}/a}\left(\dfrac{\rho_0+\rho_e}{\rho_0-\rho_e}\right) & \text{(thick boundary, } l_{\rm inhom}/a > 0.5\text{)} \end{cases} \tag{2.3}$$

for cylinder radius a, of which the fraction $l_{\rm inhom}/a$ is a non-uniform layer making an outside boundary, somewhat like a skirt. In the literature, the approximation $l \ll a$ is known as the *thin boundary* approximation, whilst the assumption $k_z \to 0$ is known as the *thin tube* approximation (for long-wavelength modes). Sharper density gradients in the loop allow resonant absorption to damp the kink mode more quickly; also sharper density gradients mean a greater continuous change in $C_{\rm A}$, and would increase the efficiency of any phase mixing.

Resonant absorption has been shown to work in some simulations with more complicated geometries, such as the multi-stranded loop (De Moortel and Pascoe 2012; Magyar and Van Doorsselaere 2016b; Terradas et al. 2008b) and also for propagating kink modes (Terradas et al. 2010). Simulations of loops undergoing resonant absorption have often relied on a transverse density profile which dissipation/heating cannot sustain, a clear weakness. However it is only a gradient in Alfvén frequency that is required, not necessarily a density gradient. Therefore a radial gradient in the magnetic strength may also lead to loops undergoing resonant absorption (for instance see Howson et al. 2019); it is good to stress that loops may not have a density enhancement (making them much harder to observe). Loops with a twisted magnetic field presumably have a similar radial magnetic field strength gradient, since the curvature force pointing inwards may balance the gradient force outward, and so could experience resonant absorption, but this has not yet been confirmed. It should be noted that previous studies of fast kink waves in flux tubes with a twisted magnetic field have found that the wave properties (except energy flux) are unaffected compared to the untwisted field case, at least in the linear regime (Lopin and Nagorny 2017).

An alternative presentation of resonant absorption is presented in Hindman

and Jain (2018); Thackray and Jain (2017), in which the dispersion relation for MHD modes is derived **not** for a single flux tube, but in a two-dimensional arcade. In this formalism the kink mode never exists separately but all modes are the fast coupled with the Alfvén mode, and have both an axial and radial wavenumber. The presence of an Alfvén singularity (physically, where the resonant layer resides) makes the mathematics difficult but essentially this formalism leads to the familiar resonant absorption damping the obliquely propagating waves, which are only visible for a single magnetic surface (the loop). Until this formalism is applied convincingly to observations of an entire coronal arcade, we do not consider this work further.

Other damping mechanisms to explain the rapid damping of kink oscillations have been proposed in the past. Enhanced dissipation and resistive damping were natural first choices, although the dissipation coefficients for the corona would need to be eight or nine orders of magnitude higher than the theoretically predicted values (or tiny Reynolds number) to match observations (Nakariakov et al. 1999). One of the effects of the curvature of coronal loops is the potential for the *wave tunnelling* of energy out into the surrounding plasma, made possible because of the varying Alfvén speed outside the loop required to maintain the equilibrium (in models and numerical simulations at least Van Doorsselaere et al. 2009). This lateral wave leakage would lead to damping for vertically polarised kink oscillations (the Alfvén speed likely varies more in the vertical direction), such as would be induced by a rapidly contracted/expanded loop. This mechanism has been investigated in a 2d slab geometry in Brady and Arber (2005), expanded upon to include a geometric correction for curved slabs in Brady et al. (2006), and applied to observations in Verwichte et al. (2006). However it was found in Terradas et al. (2006) that although both resonant absorption and wave leakage can occur in curved loops, the latter is typically weaker than the former, and the damping effect from wave leakage is probably overstated due to the (unrealistic) slab geometry used in models. Note that in general, loop curvature does not affect the efficiency of the resonant absorption mechanism significantly (Van Doorsselaere et al. 2009).

The triumph of resonant absorption as the leading explanation for damping of kink modes comes largely from the calculated decay rates and amplitude decay profiles matching observations pretty well, and the finding of a linear scaling of damping time with period as predicted by Equation 2.3. Such a scaling was found in Ofman and Aschwanden (2002) with TRACE data, confirmed by Verwichte et al. (2013b) with TRACE and CoMP data and (loosely) by Goddard et al. (2016a); Nechaeva et al. (2019) for SDO/AIA data. The last two of these statistical studies also found evidence of the nonlinear nature of the damping mechanism, which is stimulating research to the present day.

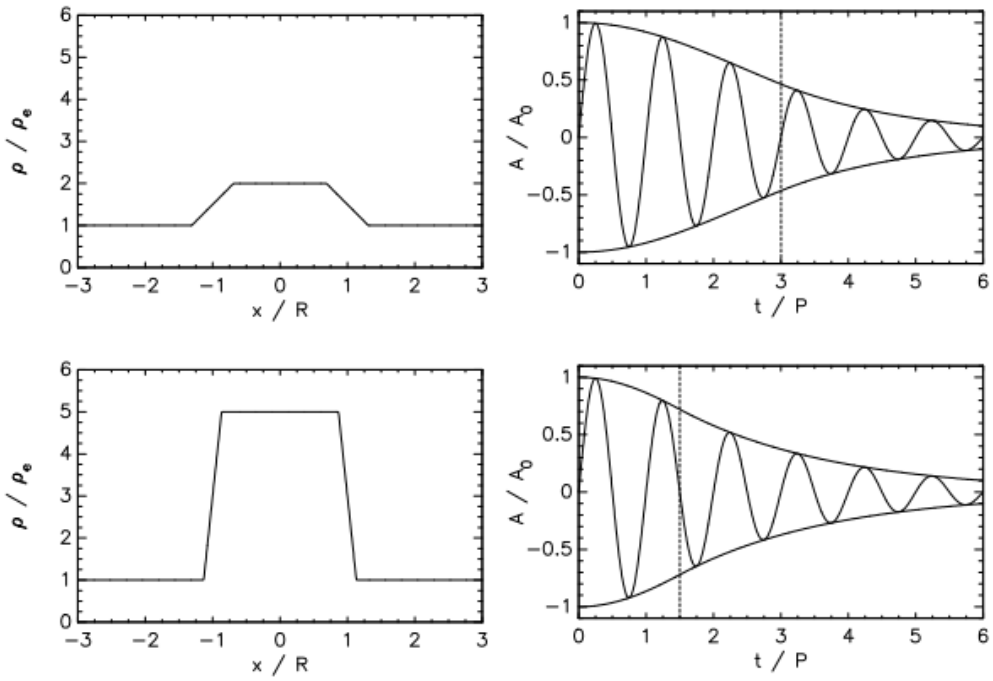

Figure 2.3: An illustration of using the kink oscillation's damping profile to infer the more likely transverse density profile. [*Left panels*] Two density profiles which produce the same resonant absorption damping rate, an example of the ill-posed nature of the seismological inversion. [*Right panels*] The damping envelopes corresponding to the density profile; note the difference in switch time (vertical dashed lines). Measuring the position of the switch time allows the density profiles to be distinguished. This figure was taken from Pascoe et al. (2017a).

The difficulty with resonant absorption is knowing the transverse density profile; the existence of an inhomogeneous layer between the (usually higher density) core and (lower density) background is a sufficient condition for resonant absorption to occur, and clearly from Equation 2.3 the ratio $l_{\rm inhom}/a$ has a large impact on the calculated rates (Soler et al. 2013, 2014). The work in Arregui et al. (2015) used Bayesian inference techniques to compare the seismological implications of three cross-field density profiles, finding that in most cases there is insufficient evidence to prefer one density model over another. An attempt to deconvolve the observed emission profiles of coronal loops and arrive at the density profile was made in Goddard et al. (2017), also utilising Bayesian inference - it was found that some evidence for thick inhomogeneous layers may be found. It is important to keep in mind at all times the theoretical shortcomings of such seismology, namely that there is no unique solution to the full seismological problem, as discussed in Arregui and

Goossens (2019).

Progress was made with the introduction to the community the idea of kink oscillations exhibiting two different damping profile regimes, with a switch time whose location depends only upon the density contrast ρ_0/ρ_e (and the driver profile) (Hood et al. 2013; Pascoe et al. 2013). It is proposed that the first stage of the oscillation is best described by a Gaussian spatial damping profile, and the second stage best described by an exponential spatial damping profile. The former is based on the approximation of a nonlinear, analytical damping rate for a loop with a thin inhomogeneous layer, which may be approximated as a Gaussian starting with zero gradient. For an analytical treatment, see Hood et al. (2013), and for the observational study see Pascoe et al. (2016b). The latter case of exponential damping arises from the fact that over time, the higher frequency components of the oscillation are damped quicker, leading to a exponential decay profile in the asymptotic state (for example see the analytical treatment in Terradas et al. 2010). By combining the damping profiles into a general profile with a switch time which may be determined, this extra observable has the potential to make the subsequent seismological inversion well posed. This was demonstrated in Pascoe et al. (2016c) and Pascoe et al. (2017a), in combination with forward modelling and again with Bayesian inference. Efforts to forward model kink oscillations to establish their veracity in terms of seismology have also been made in Chen and Peter (2015); Yuan and Doorsselaere (2016)

It was found in the simulations of Magyar and Van Doorsselaere (2016a,b) that high amplitude transverse oscillations are strongly subject to nonlinear effects, and in particular the nonlinear growth of Kelvin-Helmoltz instability. The interplay between resonant absorption and KHi was investigated in Antolin and Van Doorsselaere (2019), in which it was concluded that, in the presence of KHi, the width of the boundary layer would vary extremely over time. It may be argued then that 1D resonant absorption theory is overly simplistic, relying as it does on a single constant value for l_{inhom}/a. This thesis takes the view that the mismatch between the rapid, disruptive development of KHi seen in simulations versus observations of coronal loops, combined with our ignorance of what a coronal loop is, means that directly comparing the results of such simulations to the real corona should be done with caution. Instead of creating a simulation we choose to test the 1D resonant absorption theory with observations, through the theory's prediction of equal quality factor for different harmonics.

2.1.2 Multiple harmonics

In observations of oscillations in the solar corona, several cases of the detection of higher harmonics simultaneous with the fundamental mode have been reported.

[Please note that in this thesis, the term *harmonic* is preferentially used instead of overtone, where all standing modes have nodes at the loop footpoints, the fundamental standing mode of a coronal loop has wavelength $\lambda = 2L$, and the n^{th} harmonic has $\lambda = 2L/(n+1)$.] It is natural to expect the occurrence of higher parallel harmonics when a kink oscillation is impulsively excited, as is predominantly the case (Zimovets and Nakariakov 2015). A difficulty is that higher spatial harmonics damp faster according to resonant absorption theory, and since even the fundamental mode decays away within a few periods, the narrow timeframe to observe a higher harmonic makes their confident detection infrequent.

Early detections with TRACE data showed that multi-modal oscillations were not uncommon, but could suffer from large uncertainties, such as the first measurement of a double periodicity in Verwichte et al. (2004). Improved error analysis in Van Doorsselaere et al. (2007) allowed a slightly more confident re-analysis as well as a new detection. In De Moortel and Brady (2007) an oscillation was spatially resolved in TRACE data and anti-phase behaviour between the legs either side of the apex was observed, which is the expected behaviour for an even harmonic, standing mode – meaning this observation is likely of an unaccompanied second harmonic (a similar oscillation is seen in Long et al. 2017a). Kupriyanova et al. (2013) detected multiple periodicities in a flaring loop's microwave emission, concluding a multi-harmonic standing kink mode was probable. Similar conclusions were reached for a flaring loop seen in the hard X-ray and microwave wavelengths in Inglis and Nakariakov (2009), though subsequent investigations of the change in period ratio of sausage modes by flux tube expansion may also explain their results (Pascoe and Nakariakov 2016). More recently, Guo et al. (2015) analysed the simultaneous fundamental and second harmonic of a kink oscillation in an excited loop system seen with SDO/AIA. Also using AIA observations, Pascoe et al. (2016a) reported the spatial resolution of the fundamental and second harmonic, justifying their interpretation by invoking the ratio of oscillation periods, the spatial dependence of the amplitudes for each mode, and anti-phase oscillations of the loop legs for the second harmonic. Seismological studies by Pascoe et al. (2017a) and Pascoe et al. (2017b) found evidence of the simultaneous second and/or third harmonics when best-fitting the (anharmonic) oscillation profiles on time distance maps, in all cases of kink oscillations excited by external perturbations, consistent with the numerical simulations by Pascoe et al. (2009).

The observation of, and comparison between multiple harmonics (fundamental and its overtones) can provide more information for seismology, thus allowing one to match the observed dispersion with that predicted by theory. In principle, by observing multiple different harmonics the dispersion relation used for seismological

inversion can be verified. Conversely if the theoretical dispersion relation is assumed to be correct, one can attribute any observational departure from the theoretical dispersion relation to modifications, such as density stratification. In practice, this is often done through the comparison of the measured harmonic periods P_1/nP_n, that is, the ratio of the fundamental period P_1 to n times that of the n^{th} harmonic, P_n. For a dispersionless oscillation (that is to say when each harmonic has the same phase speed C_{K}), the ratio P_1/nP_n is unity for all n. Any departure from unity provides information about dispersion along the loop. This dispersion is assumed to be from the spatial variation of kink speed along the loop, which can be used to probe the plasma structure (Jain and Hindman 2012). In the low-β limit, the kink speed can vary as a function of z if either the density contrast changes, or the Alfvén speed changes, itself dependent upon the magnetic field strength and internal density (see Eq. 1.27).

The comparison of different wave modes to provide further seismological information was first demonstrated in Andries et al. (2005a) by using observations of a loop arcade hosting higher harmonics as reported in Verwichte et al. (2004). The detected departure from unity of $P_1/2P_2$ was attributed to the density stratification along the coronal loop and a value for the density scale height was determined. Any source of dispersion will impact the P_n/nP_n ratio for harmonic n, however the analytical studies in this area agree that longitudinal structuring along the loop has the greatest effect. As an example, long-wavelength kink modes of an unstratified magnetic cylinder are known to be weakly dispersive (see Fig. 1.19), yet upon investigation in McEwan et al. (section 2.1, 2006) this led to maximal shift in period ratio of only 4.75%. This is smaller than the observed departures, such as $P_1/P_2 = 1.81 \pm 0.25$ and 1.64 ± 0.23 reported in Verwichte et al. (2004), corresponding to departures from unity of $P_1/2P_2$ of between 10–20%.

Whilst early studies reported seismological inferences assuming the effect of density structuring – discussed in detail in Subsection 2.3.1 – there is a serious ambiguity between the effect of density structuring along the field, and magnetic field strength variation along the field (which is necessarily linked with flux tube expansion). Both effects will cause a change to the eigenfrequencies of the standing kink mode, reflected in the period ratios. Further, both density stratification and flux tube expansion are believed to be extremely common in coronal loops, such that both these effects will act upon the same standing kink mode. For the n^{th} harmonic, the effect of longitudinal structuring will depend on the spatial distribution of the harmonics' antinodes, since it is in these segments of the loop in which the kink speed is 'felt' more strongly and contribute more to the (weighted) average, $\langle C_{\text{K}} \rangle_n = 2L/(nP_n)$ (for example see Eq. 17 in Andries et al. 2009). Density

stratification in nearly all cases leads to a rarefied apex compared to the footpoints, so the kink speed is faster there and thus $P_1/nP_n < 1$. Flux tube expansion acts in the opposite way, since loops are thought to have lower magnetic field strengths at the apex leading to $P_n/2P_n > 1$ (e.g. Verth and Erdélyi 2008b). Therefore observations must provide further information to distinguish which mechanism is causing the dispersion. For a review on the use of multiple kink harmonics for seismology specifically, the reader is referred to Andries et al. (2009), also see the discussion in Subsection 2.3.1.

In some cases it may be possible to use the effect of dispersion on the *eigenfunctions* to better inform the seismology. However such effects are more subtle for observations to detect, for example a shift in the antinode positions of the first overtone towards the loop footpoint (e.g. see Fig. 4 in Verth and Erdélyi 2008b). Such changes are marginal for the fundamental mode, and the difficulties arising from determination of the polarisations and the 3 dimensional geometry of the loop has rendered this approach far less practical than measurement of the period ratio (Andries et al. 2009). Nonetheless attempts to locate the spatial locations of antinodes has been performed, for example in Guo et al. (2015). Similar considerations for sausage modes in curved expanding loops have showed that their shifted antinodes may confuse observations such as Inglis and Nakariakov (2009) between even- and odd- numbered modes. The methods of spatio-temporal observations outlined and applied in Section 2.2 may improve this outlook.

In the linear treatment of resonant absorption, since the damping time τ_n is proportional to the period P_n, the quality factor (signal quality) of the oscillation τ/P is the same for each harmonic n. The quality factor is determined by the physical properties of the loop, related to the loop's transverse density profile, specifically (in models) the density contrast ratio and the width of the inhomogeneous layer $l_{\rm inhom}$ (c.f. Eq. 1, Pascoe et al. 2016a). This should hold true regardless of dispersion modifying the period of the $n^{\rm th}$ harmonic from its expected value P_1/n, since the damping time should change accordingly. Before the results presented below, this fact had never been tested.

2.2 Observational signatures of the third harmonic in a decaying kink oscillation of a coronal loop

This section follows very closely my publication Duckenfield et al. (2019).

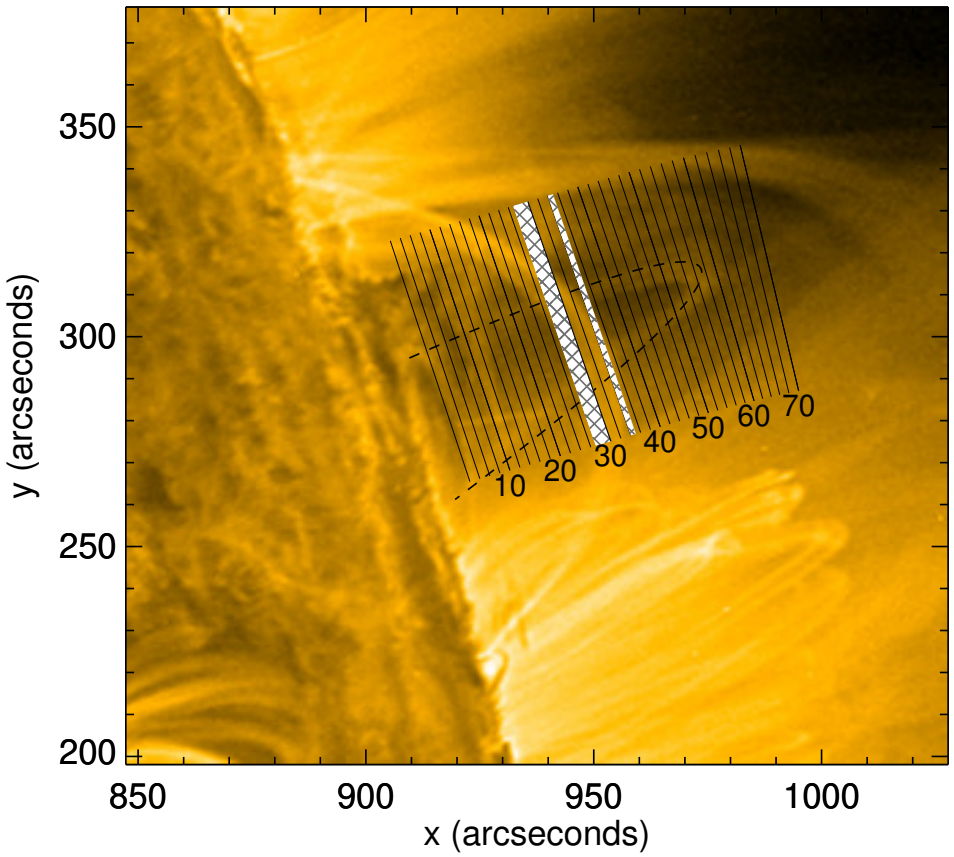

Figure 2.4: SDO/AIA 171 Å image of the loop, 2012 May 26 20:50 UT. Every other slit location used to extract time-distance data from is indicated. The slit nearest the limb is indexed 1, the slit nearest the apex is indexed 60, as indicated by the labelled slits with thicker lines. The white hashed areas denote noisy slits where data was not good enough to get reliable time series.

2.2.1 Observation

This analysis performed in this section is motivated by Pascoe et al. (2016c, 2017a) in which the event we now outline is referred to as Loop #2. The coronal loop of interest was observed on 26 May 2012 off the north easterly limb of the Sun in SDO/AIA EUV 171 Å, using data at its full cadence of 12 s and the usual AIA pixel size of 0.6 arcseconds. The loop is associated with NOAA active region 11484, which by this time has rotated out of view. The loop is observed from side-on, such that the plane of the loop is approximated to be perpendicular to the plane of sky. Another well-contrasted loop is seen perpendicular to the loop of interest, apparently crossing (in the field of view) about half-way up the loop of interest's leg, meaning

data from this region is unavailable. The loop of interest in Figure 2.4 has its axis approximately denoted by the dashed line. Its length is estimated as 162 ± 3 Mm, using the assumption of semi-circularity which appears reasonable. At approximately 20:38 UT the bundle of loops (of which this loop is part) is restructured. This appears to coincide with the emanation of a blast wave visible in 171 Å. As part of this restructuring, one footpoint of the loop of interest appears to 'jump' from approximately (890, 320) arcseconds to (900, 290) arcseconds, although the precise locations of the footpoint are subjective. Consequently the loop sways about its (new) equilibrium position with decaying amplitude for about one hour, after which the loop disappears out of the 171 Å passband. This event constitutes a standing kink oscillation, referenced in the kink oscillation catalogue compiled in Nechaeva et al. (2019) as Event 27 Loop 1.

For the loop of interest, data can only be obtained for one loop leg. Therefore 70 straight slits with a length of 100 pixels were created perpendicular to the loop plane – these are denoted by solid black lines in Figure 2.4. To reduce noise, each slit is averaged over a 5 pixel width perpendicular to the slit. Slits indexed 16 to 59 were of good enough quality to take into further analysis. For later plots, the slit index value is understood to be a spatial coordinate, ranging from just above the limb (on the loop leg near the footpoint) at slit 16, up to the loop apex which corresponds to slit 59. For each usable slit, time-distance maps were generated, some examples of which may be seen in Figure 2.5. The start and end times for these plots are 20:34 UT and 21:42 UT respectively. For each time-distance map, the loop axis was fitted at each instance of time to yield time series data following the procedure outlined in Pascoe et al. (2016c). Slits 27, 28, 29, and 34 were too noisy to take into further analysis, predominantly caused by signal from the edges of another loop overlapping the loop of interest.

2.2.2 Spectral analysis

To investigate the loop oscillation, we first examine the spectrum (wavelet transform) of each slits' time series. Figure 2.6 shows one such wavelet power spectrum for a slit part-way up the length of the loop. The wavelet plot clearly shows a strong spectral component between 7 and 8 minutes. Examining the time series further, a low amplitude departure from a harmonic signal is seen superimposed on the first few periods. This is realised in the wavelet plot as a feature at approximately a 3 minute period, lasting for the first 10 minutes or so and with a far lower spectral power than the component at 8 minutes. This is consistent with the features of a rapidly damped third harmonic, in line with the result reported in Pascoe et al. (2016c).

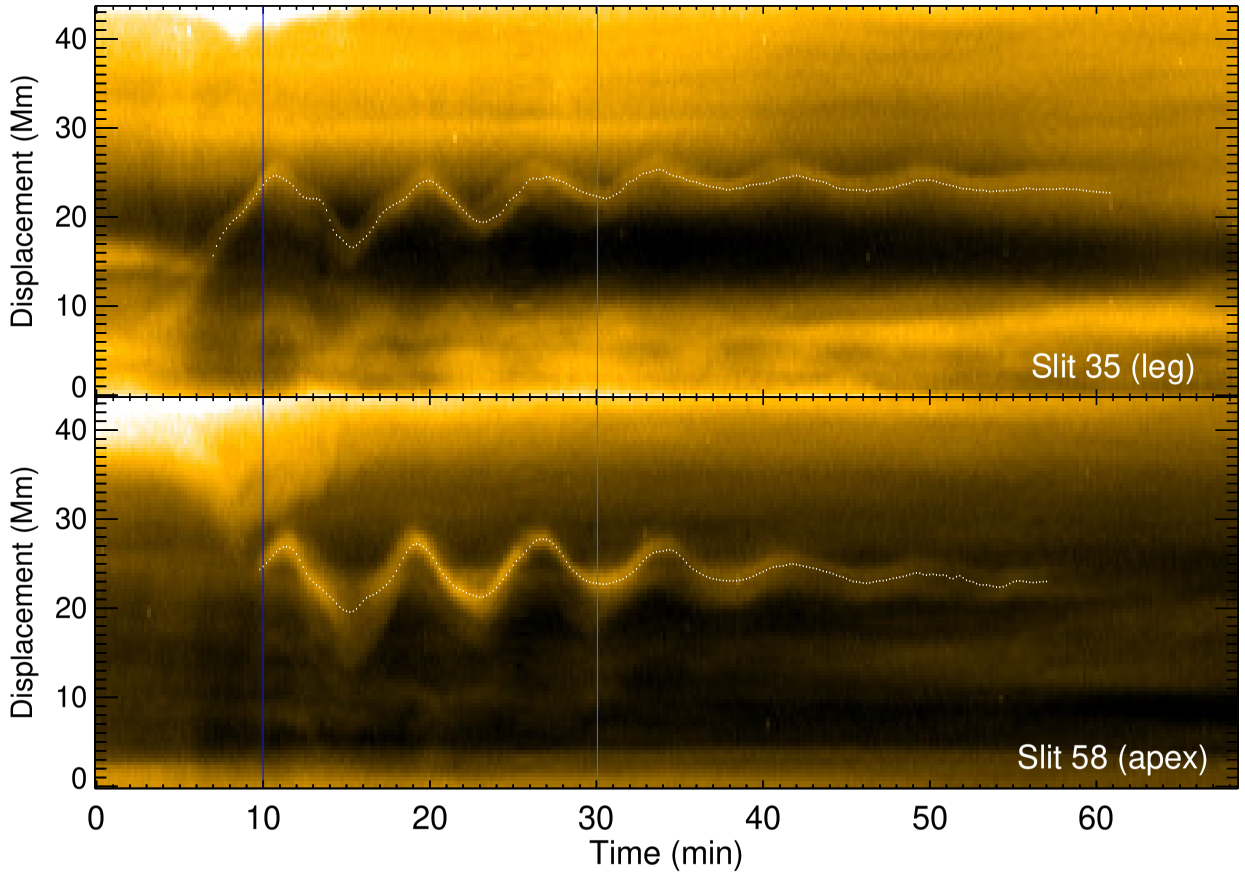

Figure 2.5: Time-distance maps from slit 35 [*top*] situated about half way up the loop leg, and slit 58 [*bottom*] near the loop apex. The overplotted white dotted line shows the fitted time series data. The blue vertical lines denote where data was cut before the spectral analysis and fitting. In real time these correspond to 20:44 UT and 21:04 UT.

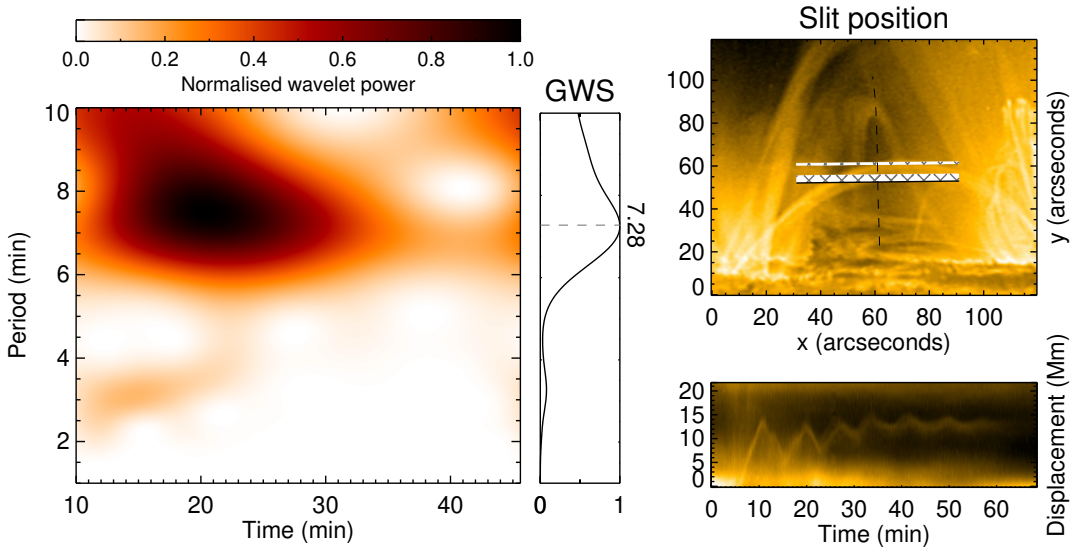

Figure 2.6: [*Left*] Morlet wavelet plot of the time series data corresponding to slit 26. [*Middle*] the global wavelet spectrum, normalised to its maximum value. The period of maximal global wavelet power for this slit's time series is found to be 7.28 minutes. [*Right top*] the SDO/AIA image, rotated for reader's convenience, on which the loop midplane (dashed line) and slit position (solid line) is overlaid. [*Right bottom*] Time-distance map for this slit (zoomed), from which the time series is extracted.

It can be seen in Figure 2.5 that the loop displacement at some spatial locations appears fairly harmonic, such as near the apex, while other locations show more anharmonic behaviour, especially in the first period of oscillation. Although we expect a higher harmonic to have more pronounced amplitude decay and so have its greatest influence at its inception, we must check if this spectral component truly is a third harmonic by investigating its spatial distribution along the loop. A third harmonic would be expected to have a node one third along the length of the loop, a point which should be visible from the AIA camera's perspective. To observe this node, the global wavelet spectrum (GWS) of each time series is calculated and plotted against height along loop (slit number) in Figure 2.7. Only data between 10 and 30 minutes (as indicated on Fig. 2.5) was used for this and subsequent analysis, motivated by the short duration of the spectral component at 3 minutes seen in Figure 2.6 and the expectation of rapid damping. The GWS is advantageous over a traditional Fourier decomposition due to the the presence of distinct spectral components lasting different lengths of time. The Fourier spectrum may not show significant spectral peaks where there are overtones, due to their

limited time duration compared to the Fourier basis vector (complex exponential). The alternative spectral decomposition of GWS can address this shortcoming since wavelet spectral analysis sacrifices the ability to distinguish two spectral peaks at very similar frequencies (which may be resolvable using Fourier decomposition) in order to gain information about when the spectral components are present. The dominant period in Figure 2.7 is 7.87 minutes, calculated as the peak of the sum of GWS amplitude over all slits. This periodicity exists over all slits considered but decreasing in amplitude towards the loop footpoint, that is to say having a single antinode at the apex. This matches expectations of the fundamental standing kink mode, and with this interpretation for a loop of this length (162 Mm), using the formula $C_{\mathrm{K}} \approx 2L/P_{\mathrm{kink}}$ yields a reasonable estimate of the averaged loop kink speed $C_{\mathrm{K}} \approx 0.69$ Mm s^{-1}.

Also visible in Figure 2.7 is a band of spectral amplitude for most slits at a period of approximately 3 minutes, lower amplitude than the dominant period and with an apparent dip at approximately slit 51. This matches expectations of a third harmonic, which is to say having a period of approximately $7.87/3 = 2.6$ minutes and a node existing one third of the way along the loop's axis. Due to the perspective seeing the loop side on, this node would appear at $r\sin(\pi/3)/r \approx 0.87$ of total loop height r, which matches the approximate position of slit $51/60 \approx 0.85$. The amplitude of the shorter period spectral component is an order of magnitude smaller than the fundamental, and is just discernible in the GWS. This is consistent with the excitation of kink modes by an external perturbation in simulations by Pascoe and De Moortel (2014, e.g. see Fig. 2).

2.2.3 Phase behaviour

To investigate the phase behaviour of the short period component, a bandpass filter is employed to separate this component from the dominant signal. The filter used was an ideal step function in Fourier space allowing periods between two and four minutes, setting all other frequencies to zero. Testing between filtering using the Fourier transform and filtering based on the wavelet transform showed no significant difference, so the more widely used Fourier filter was used. Filters of different shapes – ideal step function, Gaussian, Hanning, Hamming – and different bandwidths were also tested and none had any discernible advantage, and so the rectangular function was used to maximise spectral resolution. Zero padding the time series prior to the Fourier transform was used to minimise edge effects. As was the case for creating the GWS data, the time series used here were cut to the first 20 minutes. This was motivated by the short time duration of the spectral component seen in wavelet plots such as Figure 2.6.

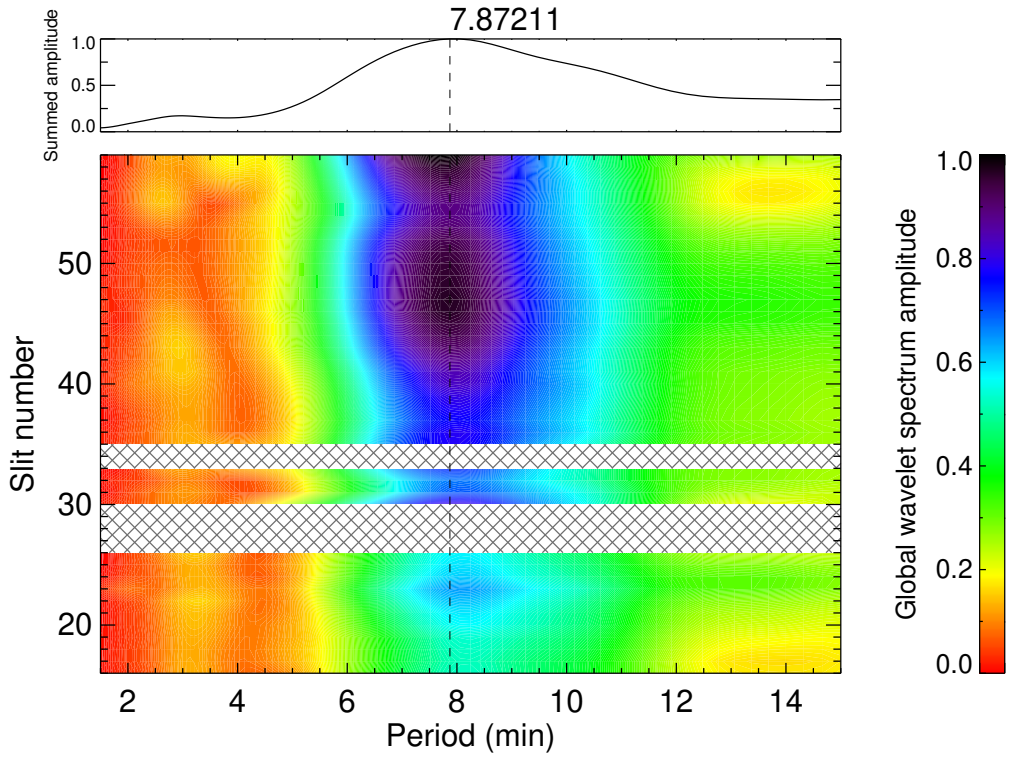

Figure 2.7: Two–dimensional distribution of spectral amplitude estimated from the Global Wavelet Spectrum per slit against period and slit number. [*Top*] amplitude summed across all slits shows a peak at $\sim$ 7.87 minutes. The hashed regions correspond to slits where the data was not good enough to get reliable time series, predominantly caused by an overlapping loop.

To examine the phase behaviour along the loop, reliance on fitting the data is not necessary. An alternative empirical method is to calculate the correlation between a chosen slit's time series and all others. A positive correlation close to +1 would indicate the oscillation is in phase at the spatial locations corresponding to the slit indices. If the correlation is 0 this would indicate either the oscillation is $\pi/2$ out of phase or there is no signal amplitude at one (or both) slits. A negative correlation close to -1 would imply the oscillation is in perfect anti-phase at the two spatial locations. Thus plotting this correlation against slit index gives a picture of how the oscillation phase varies across the loop, whilst the choice of reference slit location determines against which phase the others are measured. This method makes no assumption about the precise shape or period of the oscillatory components, making it more amenable to real data than fitting artificially exact sinusoids. In the ideal situation, comparison between loop legs may be performed, demonstrated in

Chapter 3, however useful information can be extracted even when considering only one loop leg.

For the fundamental mode of oscillation, the entire loop oscillates in phase and thus a plot of correlation value against slit number appears flat for all choices of reference slit. For the third harmonic one expects two nodes to occur along the loop, across which there should be a phase shift. For this observation's point of view, only one node would be visible. An illustrative example for the $n = 3$ case is given in the top panel of Figure 2.8. Data from the same side of the node are perfectly correlated with each other, switching to perfect anti-correlation when cross-correlated with data from the opposite side of the node. At the node of the third harmonic the correlations pass through zero (since there is no oscillatory signal in one time series). The correlations with respect to a point further down the loop leg, that is to say the opposite side of the node at slit 51, show the same behaviour but reflected. This pattern is seen when looking at cross correlations with respect to the leg (black), and also for cross correlations with respect to the apex (red) but reflected. The node position is also obvious as the point at which both the red and black curve intersect each other.

In the middle panel of Figure 2.8, the introduction of noise and bandpass filtering have had some effects. The cross correlations have deviated away from $+1$ and -1, the swap of the red and black curves happens over a larger number of slits, and the there is some asymmetry between them. All these features are also seen in the the real data in the bottom panel of Figure 2.8. There is more slit-to-slit variation than seen in the data, however this is probably because the real data were averaged over 5 pixels before forming time series. This averaging has a spatial scale of the same order as the distance between slits ($\sim$ 3 arcseconds), and so overlap between adjacent slits may act as a smoothing.

Referring to the bottom panel of Figure 2.8 we can see some of the expected phase behaviour of the filtered oscillation signal manifested in the cross-correlation data. There is a transition near slit 51, where the node of the third harmonic is expected, although this appears shifted. It is worth remembering the small-to-non-existent signal amplitude around this location, which means that the correlation is dominated by noise. This is compounded by the fact that there is uncertainty exactly where the node should be since we do not know exactly the loop length, height etc, so the 'true' node could lie anywhere nearby. The most negative correlation is -0.3. For real data, correlations very near -1 are unfeasible, and this oscillatory signal is on the edge of detectability, with low signal to noise and additional filtering required. Further, the side on perspective means that there are few slits available for analysis between the third harmonic node and the apex, all of which are potentially

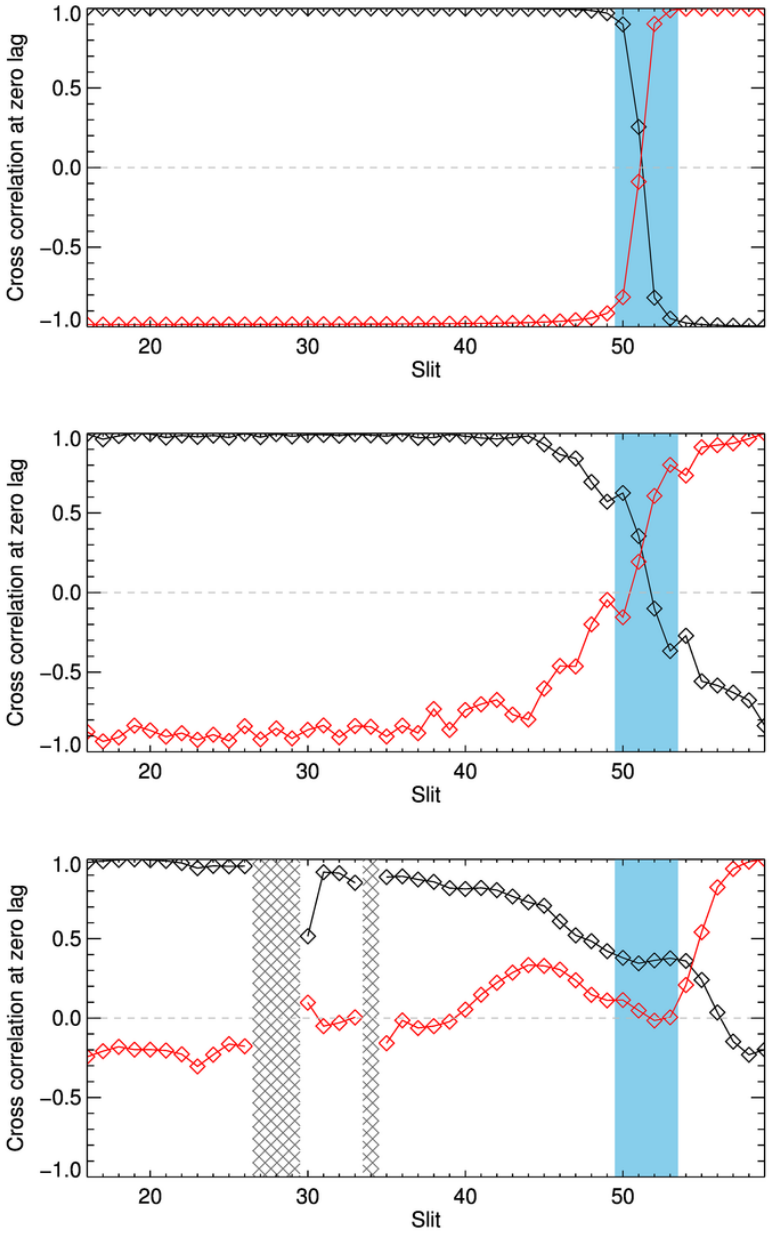

Figure 2.8: Plot showing correlation values calculated when a slit's time series is cross correlated with a reference slit. Cross correlation values with the reference slit near the apex (slit 59) are shown in red, and on the same plot, the cross correlation values with the reference slit near the leg (slit 19) are shown in black. The region marked by blue highlights where the amplitude of the third harmonic is low, and data is not trustworthy. [*Top*] The expected correlations, calculated using synthetically generated time series for a perfect third harmonic signal, incorporating the side on perspective and only showing one leg. [*Middle*] Synthetic time series consisting of a fundamental mode, a third harmonic and (coloured) noise. This synthetic signal also underwent the same bandpass filter as was used on the data. [*Bottom*] the correlation plot calculated from data. The existence of the node of the third harmonic is clearly seen.

contaminated by additional noise, from integrating through more of the loop. Despite the shortcomings when applied to real data, the fact that the harmonic node behaviour is seen in the bandpass filtered data provides evidence of the third harmonic.

2.2.4 Determining oscillation parameters

To further confirm the spectral components' veracity as kink oscillation harmonics $n = 1$ & $n = 3$ and to compare the two, we consider the behaviour of the oscillation's parameters along the loop. The displacement of the loop at each slit location is modelled as a damped sinuosidal function in the form

$$A \exp\left(-\frac{t^2}{2\tau^2}\right) \sin\left(\frac{2\pi}{P}t - \phi\right). \tag{2.4}$$

A time-dependent background trend is not included. Although the loop displacements have a slight change in equilibrium position between start and end, fitting this end necessarily changes the frequency spectrum of the resultant time series in a subjective way. For this data the trend is sufficiently close to a single mean value that useful results can be obtained without detrending, even at the level of the small amplitude third harmonic. The loop length does not visibly change within the time of interest. Therefore to keep the results reproducible and reduce the number of parameters to estimate, only a mean value is fitted to each slit. Two example slits are shown in Figure 2.9. Although the difference between the peaks of the calculated sinusoids and the peaks visible on the time distance maps do vary slightly with time, these differences are indeed minor. As we see no obvious period drift in the wavelet plots such as Figure 2.6, the period is not allowed to vary in time in the fitting, but is fitted independently for different slit positions.

We choose to allow the amplitude to only evolve in time through a gaussian decaying term, ignoring any switch time to exponential damping (see Subsec. 2.1). This was chosen because introducing further free parameters to the fitting – as would be required to include both modes of damping – detracts from the clarity of following a single parameter along the loop. A single damping parameter, though potentially underestimating the mode coupling rate, is enough to compare how the damping is different between harmonics and between different spatial locations along the loop. A gaussian decay term is chosen because the simultaneous excitation of multiple harmonics implies the exciter is not an exact kink eigenmode (which would decay exponentially), and supported by the results seen in Pascoe et al. (2016c, e.g. Fig. 2).

For this model, Bayesian inference and Markov chain Monte Carlo sampling is used (see App. C), and we consider the best fit to be that with the maximum a posteriori probability (MAP) estimate returned for the parameters amplitude A,

phase ϕ, period P and damping time τ. Uniformly distributed priors are used, with upper and lower limits covering the expected range of reasonable values (for example $n = 3$ period between two and four minutes). The MCMC sampling is independently applied at each slit location, building a picture of how the oscillation parameters vary along the loop. The credible intervals, seen in Figure 2.10 and Figure 2.11 as grey shaded regions, are estimated as the 95% confidence level of the marginalised posterior distribution for that particular parameter.

For the purposes of this thesis, the oscillation parameters for the two spectral components are fitted separately. In Pascoe et al. (2017a) for each oscillation, a single time series is tested against models comprised of a simultaneous fundamental mode, higher harmonics, a trend, and a decay-less component. The relationship between harmonics is fixed for each compared model. This approach is not appropriate here because we are interested in measuring each harmonic's oscillation parameters separately. To keep the interpretation of our results – how an individual parameter changes with spatial location – simple, we choose to keep the number of parameters as small as possible and use the Bayes factor to determine which set of parameters is most probable. Therefore we use the bandpass filter and fitting to a simple model to directly compare the harmonics, whilst employing other additional techniques to confirm the harmonics' existence.

To investigate the $n = 1$ component, the unfiltered (original) time series data is used, as opposed to shorter signal minus filtered data, because the amplitude of the longer period component is so dominant that it was judged the effects of filtering would have a more detrimental effect to the fitting than the superposition of the shorter period component. The resulting MAP parameters from the MCMC sampling for each slit are displayed in the left hand column of Figure 2.10.

The fitted amplitude is seen to grow steadily with slit index, that is to say approaching the apex, as expected. The amplitude of the fundamental mode is constant near the apex, as the dependence is sine-like. The fitted period is approximately the same for all slits at an average of 7.8 minutes, although at the very apex the fitted period drops to about 7.6 minutes. The damping time is approximately the same for all slits, averaging at 26 minutes. There are wide credible intervals for most slits on the damping time, particularly down the loop leg, due to the difficulty of its estimation on so few cycles and the ambiguity of the precise damping profile at work. In line with common sense, the credible intervals seen on the fitted amplitude, period and damping time all decrease with slit index. This results from the amplitude growing with height for the fundamental mode, hence increasing the oscillation signal-to-noise. This can be seen explicitly in Figure 2.9, where the amplitude of the blue curve for slit 26 is smaller than that for slit 59

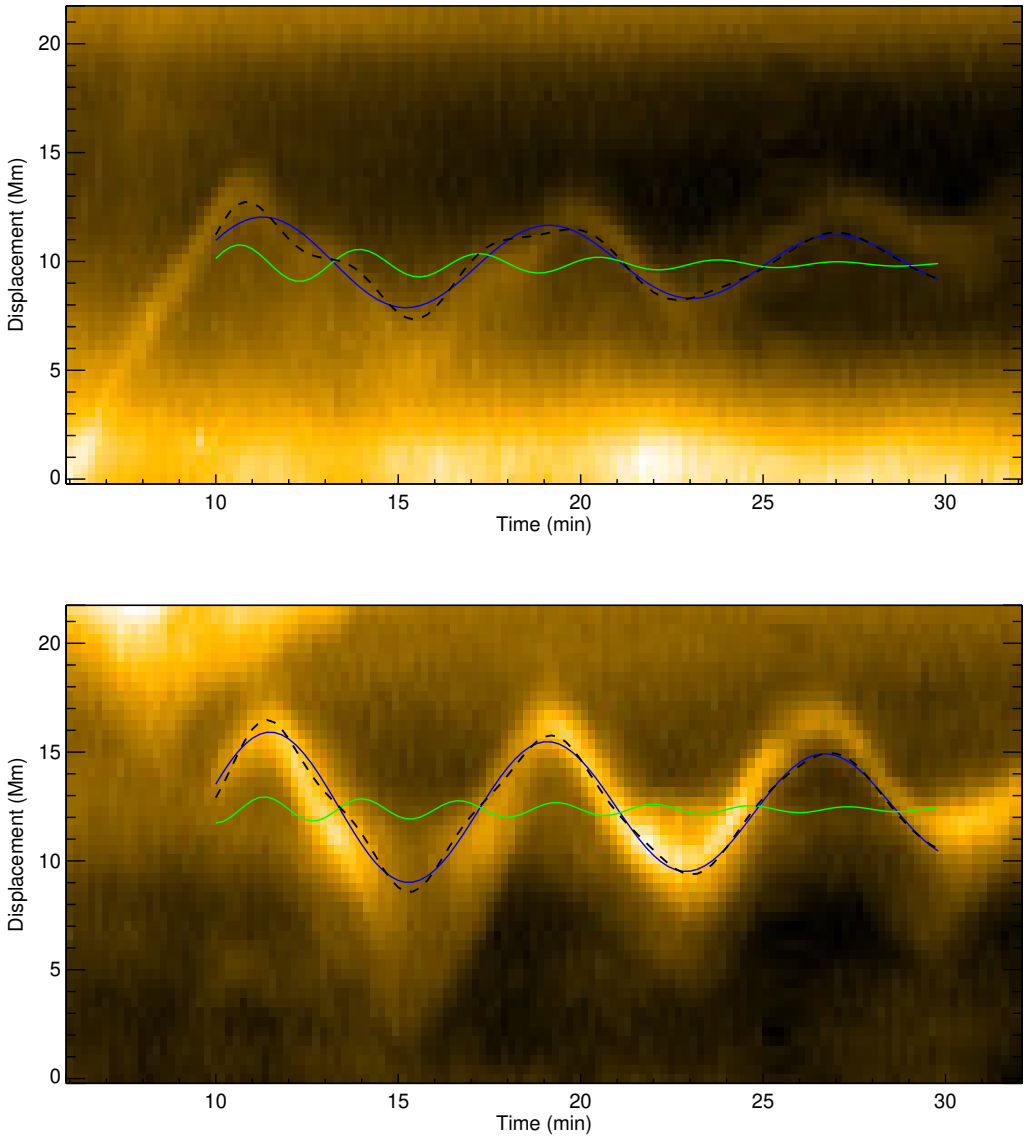

Figure 2.9: Time distance maps overlaid with sinusoids calculated using the MAP parameters output by the MCMC sampling for that respective slit. The sinusoid corresponding to $n = 1$ is in blue, the sinusoid corresponding to $n = 3$ is in green, and their sum is shown by the dashed black line. The average displacement of the loop for each slit has been added so the curves line up with time distance map behind it. [*Top*] Slit 26 as shown in Fig. 2.6. The summed curve clearly deviates from a pure sinusoid as per the time distance map behind it, as a result of the third harmonic. [*Bottom*] Slit 59 at the apex. Despite being an antinode for the third harmonic, the summed curve does not deviate far from a pure sinusoid due to the large amplitude of the $n = 1$ component.

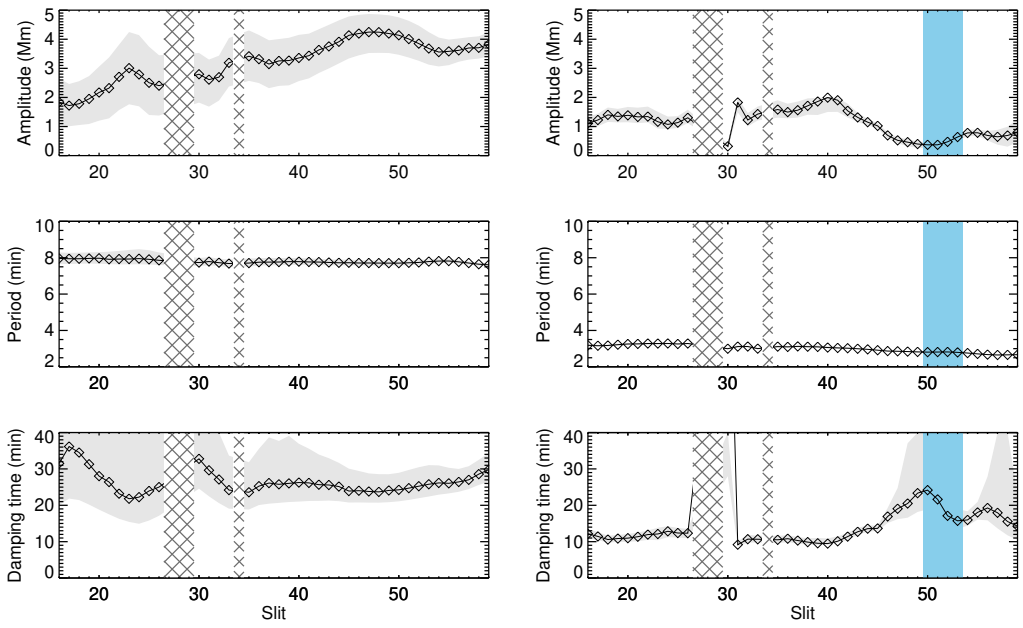

Figure 2.10: Resulting parameters from MCMC sampling to describe the unfiltered data (corresponding to the fundamental $n = 1$ mode) [*left column*], and to describe the filtered data (corresponding to the third harmonic $n = 3$) [*right column*]. The parameters are amplitude [*top*], period [*middle*], and damping time [*bottom*]. The black diamonds show the MAP parameter value from the MCMC sampling, and its credible interval is shaded light grey for each slit. The hashed regions correspond to slits where the data was not good enough to get reliable time series, predominantly caused by an overlapping loop. The blue region denotes the approximate node for the third harmonic, where amplitude is small and data is not to be trusted.

(apex), as expected.

To investigate the $n = 3$ harmonic, the bandpass filtered and truncated data are fitted in the same manner as before using Eq. 2.4, and displayed in the right hand column of Figure 2.10. This data is far noisier with a lower signal-to noise ratio, and so fitting with such functions everywhere is optimistic. Despite this, the amplitude MAP values follow the pattern expected: growing amplitude with height until about slit index 40, after which the amplitude drops to near zero at slit 51 (expected node), then beginning to grow again. The (initial) amplitudes are generally less than half that for the fundamental even without accounting for any phase shift, indicating the third harmonic has lower amplitude than the fundamental. The period MAP values output by the MCMC sampling have an average of 3.0 minutes, which agrees with the period seen with enhanced spectral amplitude in Figure 2.7.

Unexpectedly there appears a slight period difference between the apex and the loop leg for the third harmonic. For an oscillation satisfying a linear wave

equation with no steady flows in cylindrical coordinates, one expects the temporal behaviour to be the same everywhere spatially, or in other words we expect the period to be the same at the apex as down the legs. This holds even when the wave speed (C_{A}) is a function of space. We are motivated to assume the wave equation dictates the observed loop motion because of the great successes of coronal seismology, and because the loop does not exhibit other signatures of nonlinear behaviour. It is true that a steady flow would introduce another term in the wave equation that could introduce some variation in temporal behaviour, however in this observation no clear siphon flows were seen in this or neighbouring channels, and spectral observations of similar coronal loops imply the flows are of insufficient velocities to have a significant effect. Since we expect the period is constant, this period difference is attributed to spurious additional signal, be it from random noise, leakage from the filtered $n = 1$ signal, or some effect involving both loop legs along the line of sight. In any case the period difference should be disregarded. Looking at the bottom right plot of Figure 2.10, the $n = 3$ damping time MAP values are moderately constant, although two regions with large credible intervals stand out - one at the node (slit 51), and another nearest the apex. For the first, we expect the fitting on slits near the node to break down due to low amplitude and hence signal-to-noise, as indicated by the blue region. Regarding the second wide range of credible damping values, being near the apex implies something else could be contaminating the signal there. A similar increase in error is visible near the apex in the amplitude values, whilst the periods' credible intervals are so small they appear unaffected.

When MCMC sampling different realisations of the model specified in Equation 2.4, it is necessary to compute the phase ϕ. The values calculated for the filtered ($n = 3$) data broadly follow a similar shape to the correlations seen in the bottom panel of Figure 2.8, but are extremely noisy. There is leakage from the filtering, in which some signal attributed to the fundamental mode is redistributed into the filtered data. This leakage grows with height, since its origin has a greater amplitude near the apex. The sampling does a good job estimating the parameter values that best describe the amplitude, period, and damping time despite this additional noise, resulting in well confined histograms of the samples of these parameters' posterior probability density functions. However the phase parameter is especially sensitive to this noise, and reporting its MAP values would not do a good job of demonstrating this variability. The phase behaviour for the $n = 3$ data was discussed in Sec. 2.2.3, so in the interest of clarity the phase MAP values are not included.

2.3 Discussion and conclusions

The period measured from the maximum global wavelet amplitude summed over all loops was 7.9 minutes, which is consistent with the value of 7.7 minutes measured for the same oscillation in Pascoe et al. (2016c). We have shown here that the period is consistent throughout the observable length of the loop, rather than relying on fitting the oscillation profile at a single spatial location. Only by analysing multiple spatial positions such as in Pascoe et al. (2016a), and investigating the phase behaviours between them can claims of higher harmonics be convincingly made. Relying on the modelling a single time series leaves one susceptible to the choice of spatial location, particularly with respect to observing multiple harmonics. As an example, for this observation if one considered only slit 51 (the node for the third harmonic), one might incorrectly conclude the oscillation contains only one frequency. Similar circumstances would occur if only tracking a loop's apex, since a second harmonic would have its node there and thus presents little signal to be analysed. The technique outlined in this work, using information of phase and amplitude from across the whole loop, is less susceptible to spatially local biases. This technique would also be ideal for locating antinode positions, which has previously been used for seismology (Guo et al. 2015).

2.3.1 Comparison of harmonics

Motivated by the use of period ratio discussed in Subsection 2.1.2, let us consider the $P_1/3P_3$ ratio. A small departure from unity of the $P_1/3P_3$ ratio is seen in Figure 2.11, lying between 0.8 and 1.0 for all slits. The average value of $P_1/3P_3$ across all slits is 0.87. It should be noted that since a bandpass filter was applied to make visible the $n = 3$ signal, this would force the ratio to lie between 0.66 and 1.27 even for no signal. However because the ratio values calculated are far from these boundaries the filtering is not believed to limit the results. Separate calculations of this ratio for different spatial locations are used as separate measurements of the same quantity, and not to investigate how this quantity changes along the loop. Despite this ratio being closer to 1 for positions near the apex than for positions down the leg, we still interpret this oscillation as a collective standing mode of the entire loop. The variation in fact originates from the measure of $n = 3$ period described above and is disregarded.

This departure from unity may be attributed to the third harmonic experiencing a different (large-scale) spatial average of kink speed to that experienced by the fundamental (Jain and Hindman 2012). That the ratio is less than unity implies that the kink speed experienced by the third harmonic is on average lower than that

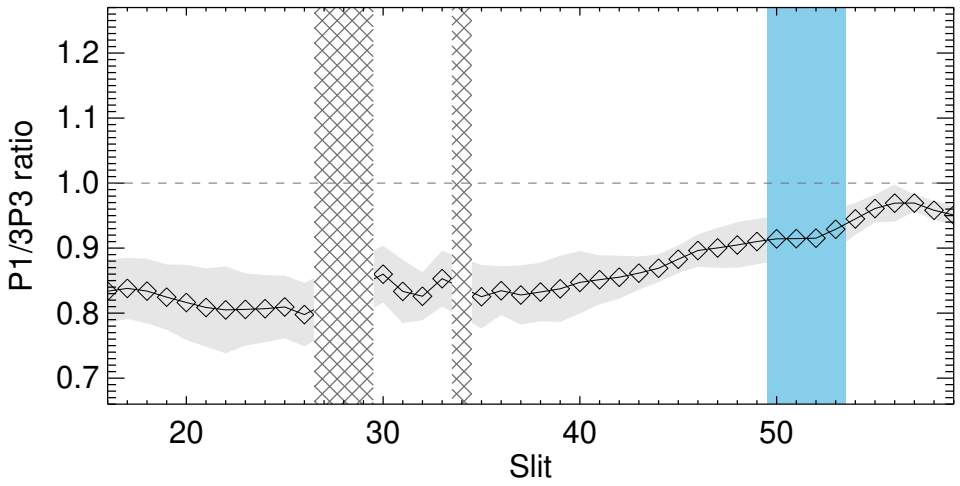

Figure 2.11: Ratio of fitted period of the fundamental to 3 times the fitted period for the third harmonic, for each slit. Unity is marked with a dashed grey line. The blue region denotes the approximate range in which the $n = 3$ node exists. The grey region shows an estimate of the credible intervals for this ratio. These are derived using the credible intervals on the periods measured separately for the two harmonics, and propagated through the formula $P_1/3P_3$ in the usual manner for errors.

for the fundamental.

One mechanism that could be responsible for changing kink speed along the loop, such that it is faster at the loop apex than further down the legs, is density stratification. The effects of density stratification upon the period ratio should be included when the scale height H is comparable with wavelength. The density scale height of the Sun is usually estimated to be around 50 Mm, assuming a hydrostatically stratified plasma with an (isothermal) temperature of 1 MK, corresponding to the observational bandpass 171 Å. Since this scale height is roughly the same as the vertical extent of the loop analysed here, this effect should be included.

Physically speaking, the effect of gravity will stratify the density along the loop such that the apex is less dense than at the footpoints – depending on the stratification inside and outside the loop, this will lead to a change in kink speed. However coronal loops are not always vertical to the solar surface, and the suppression of cross field thermal conduction in low-β plasma means that each loop may have a different scale height depending on the way they are heated and cool, so in reality each loop may have a longitudinal structuring. The effect of vertical density stratification $\rho(z) = \rho_0 \exp(-z/H)$ on the period ratio was studied analytically

in both Andries et al. (2005a) and McEwan et al. (2006): the former assuming a background vertical stratification projected onto a cylindrical loop, and the latter taking an exponential stratification within the loop itself. The influence of the density structure under the thin tube limit was considered in Dymova and Ruderman (2006a), and also in Safari et al. (2007). Analytical dispersion relations for multiple other specific density profiles, including those described above, were derived in Andries et al. (2005b); McEwan et al. (2008). The conclusion from these studies is that the observational determination of eigenfrequencies ($P_1/2P_2$) can yield information about the longitudinal structure, though the quantitative results are sensitive to the stratification law chosen. Nonetheless the stratification of the density inside coronal loops is predominantly taken to be exponential as an empirical fact.

Following from these works, if density stratification was the **only** structuring having an effect on the period ratio, we could estimate the density stratification height H for this loop from the measured departure from unity. To illustrate this, we use the functional form of the stratification considered by Andries et al. (2005a); Safari et al. (2007) to find

$$\begin{aligned} P_1 &= P_{\rm kink}\left(1+L/(3\pi^2 H)\right)^{-1}, \\ 3P_3 &= P_{\rm kink}\left(1+L/(35\pi^2 H)\right)^{-1}. \end{aligned} \tag{2.5}$$

Using the average value of the $P_1/3P_3$, measured to be 0.87, and the loop length of $L = 162 \pm 3$ Mm yields a value of $H = 32$ Mm. This value is very sensitive to small changes in period ratio however. To demonstrate, using the smallest measured period ratio of 0.80 coupled with $L = 159$ Mm yields a lower limit of H =18 Mm, whereas using the largest measured period ratio of 0.97 coupled with $L = 165$ Mm yields an upper limit of H =150 Mm.

The scale height H calculated here is in line with several other observational studies which have reported the ratio of harmonic periods, including Van Doorsselaere et al. (2007) who estimate a scale height of 109^{+22}_{-31} Mm for their own event, and 68^{+52}_{-21} Mm and 30^{+5}_{-4} Mm for the events recorded in Verwichte et al. (2004). Similar analysis was performed in Guo et al. (2015), who conclude the period ratio provided evidence of longitudinal density stratification ($P_1/2P_2 < 1$), though this was in conflict with their DEM results.

Probably, the assumption that the longitudinal variation in kink speed is caused solely by density structuring is flawed. Flux tube expansion may also be acting upon the period ratio, and if the usual case of weaker magnetic field at the loop apex is applicable to this loop, this effect would be counter to that from density stratification. This may be seen by taking the expression for mode frequency in

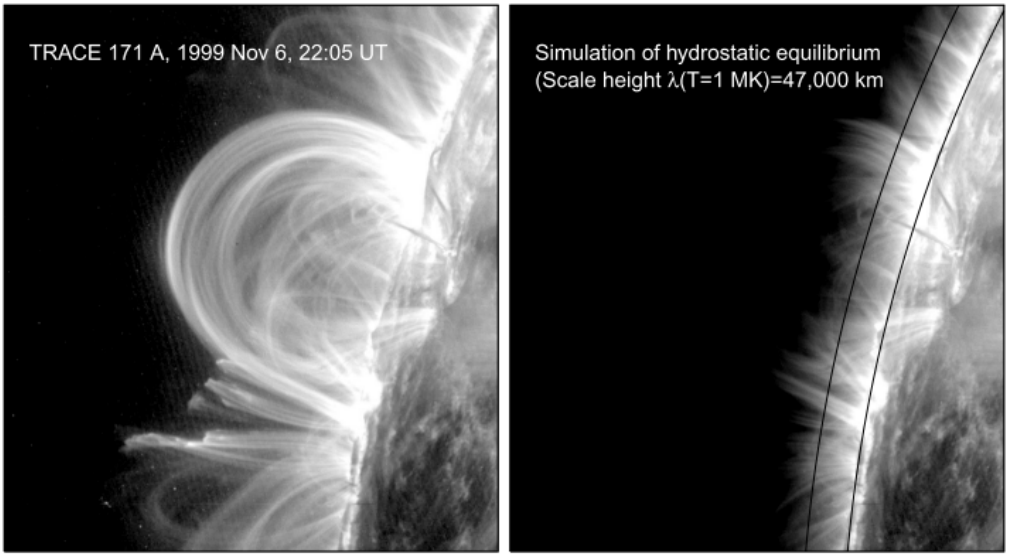

Figure 2.12: An illustration showing how the enforcement of a hydrostatic scale height upon coronal loops would drastically change the appearance of the corona in EUV. [*Left*] An observation of coronal loops, made with TRACE. [*Right*] The same observation, scaled to have a hydrostatic thermal scale height of $T = 1$ MK. This figure was taken from Aschwanden et al. (2001).

terms of expansion factor $\Gamma = a_{\rm apex}/a_{\rm foot}$ estimated in Verth and Erdélyi (Eq. 94, 2008a) as

$$\left(\frac{\omega_n}{C_{\rm K,f}}\right) \approx \frac{L}{\sqrt{\Gamma^2-1}}\left\{\left(\frac{n\pi}{2\arctan\sqrt{\Gamma^2-1}}\right)^2 - 1\right\},$$

where $C_{\rm K,f}$ is the kink speed for the parameters at the footpoint. From this it easily follows that (for a loop with constant density) the lowest order correction due to magnetic stratification is

$$\frac{P_1}{3P_3} \approx \left[1 + \frac{16(\Gamma^2-1)}{9\pi^2}\right]. \tag{2.6}$$

As an example if we were to take the extreme limits of a super-hydrostatic scale height of 150 Mm and the sub-hydrostatic case of 18 Mm from the observation, only a loop expansion factor of $\Gamma \approx 1.08$ or $\Gamma \approx 1.45$ is needed to bring the period ratio back to unity. These expansion factors are modest and easily in keeping with previous results. It is clear that neglecting loop expansion when attributing the departure from unity of the period ratio to density stratification causes the scale height to be overestimated; thus the estimates of H presented above are upper bounds (a similar conclusion is found in Andries et al. 2009).

Considering the inferred short density scale heights, there is a clear discrepancy between the seismological results for density scale height and the observations of coronal loops. The emission measure of coronal plasma is proportional to the square of the density (Eq. 1.1). Thus the emission measure scale height is equal to 1/2 of the density scale height, meaning that the intensity observed for these loops should fall by a factor of $1/e$ over some tens of megametres, demonstrated dramatically in Figure 2.12. This is clearly not the case, with many loops in the solar corona easily visible over their entire extent. The seismological results are consistent with previous findings with completely independent methods, such as the DEM described in Guo et al. (2015) and the comparison of coronal loop intensities with hydrostatic solutions in Aschwanden et al. (2001). This merely indicates further understanding of coronal loops is needed, in longitudinal density structuring and their thermal equilibria.

There are cases of kink oscillations in which the observed period ratio $P_1/2P_2$ is above unity, for example the spatially resolved harmonics in Pascoe et al. (2016a) had a $P_1/2P_2$ ratio of 1.15 ± 0.22, though this mean value does not reflect the fact that the spread of measured $P_1/2P_2$ values is around unity. Having a period ratio $P_1/2P_2$ of greater than unity implies either flux tube expansion dominates, or a negative density scale height. Such a density structuring might be appropriate for prominences, such as is suggested within Srivastava et al. (2013) – however note this observation is made in a cooler denser regime that the others, where intensity perturbations were attributed to the fast kink mode, applicable when the plasma-β is not necessarily small (for more information on the implications for prominence seismology, see Soler et al. 2015). For coronal loops a negative scale height seems unlikely, as the loop would be denser at the apex.

There are other effects that may explain the departure from unity of $P_1/3P_3$ apart from longitudinal density and magnetic structuring. Dymova and Ruderman (2006b) considered loops that were not exactly semi-circular and found the effect may be important; however in this study the effect of the curvature was inseparable from the effect of density structuring (note that all studies of magnetic field structuring along the flux tube are stymied by the condition $\nabla \cdot \vec{B} = 0$ disallowing a straight geometry, forcing all studies to mix in the effects of geometry such as field line curvature). Further investigation has come to the consensus the effect of dispersion from loop curvature (and ellipticity) may be safely neglected, at least for kink modes (e.g. Van Doorsselaere et al. 2004b, 2009). Siphon flows can cause a non-uniform kink speed along the loop, and numerical studies of steady field-aligned flows indicate this effect can reduce the period ratio moderately compared to the static case, acting in the same sense as density stratification (e.g. Yu et al. 2016). Note no evidence of siphon flows was seen in the observation presented here. Other more esoteric

cases such as temperature difference effects (Orza et al. 2012) could potentially play a significant role, though of course the role of coronal heating is still a very open question. To compare the relative likelihood of several different models explaining a non-uniform kink speed, one may use a Bayesian statistics methodology (for example see Arregui et al. 2013).

2.3.2 Measurement of quality factor

Figure 2.13 shows the first attempt to compare quality factors τ_i/P_i for different oscillation harmonics. The average quality factor of all slits from fitting of the original time series (taken to be the quality factor for the fundamental harmonic $n = 1$) was found to be $\tau_1/P_1 = 3.4$. The credible intervals found on the quality factors for the fundamental decrease with spatial index, as expected from higher amplitude signal nearer the loop apex having increased signal to noise ratio.

Quality factors for the third harmonic $n = 3$ are estimated from the fitting of the bandpass filtered time series with damped sinusoids. For slits 15 to 45 along the leg, sufficiently below the third harmonic node, the average quality factor is $\tau_3/P_3 = 3.6$. The average quality factor for all slits is 5.5, however this value is severely affected by uncertainty on the larger slit indices as can be seen on Figure 2.13. It is also clear that the uncertainty on the quality factors for the filtered data become substantially larger near slit 51. This also conforms to common sense, since this is the spatial location of the node of the third harmonic. The credible intervals reduce towards the apex, only to balloon at the very highest locations. The quality factor itself is larger at higher slit numbers, caused by the slight period difference making the denominator (period) smaller. As discussed above this effect is most likely not real. For all slits, the quality factor calculated for $n = 3$ agrees with the quality factor for $n = 1$ within the levels of uncertainty.

2.3.3 Conclusions

In this observation, it was shown that (within error) the quality factors for the third harmonic and the fundamental agree across the whole loop. This is as expected for a loop whose transverse density profile and density contrast does not vary longitudinally along the loop, in keeping with Equation 2.3. It is also expected that uniform density stratification would approximately preserve this relation between damping time and period (Dymova and Ruderman 2006a). However there is information about different density profiles at different heights embedded in the comparison of quality factors for different harmonics, because the damping rate is strongly dependent on transverse density profile (Pascoe et al. 2017a). If there was a longitudinal variation in the

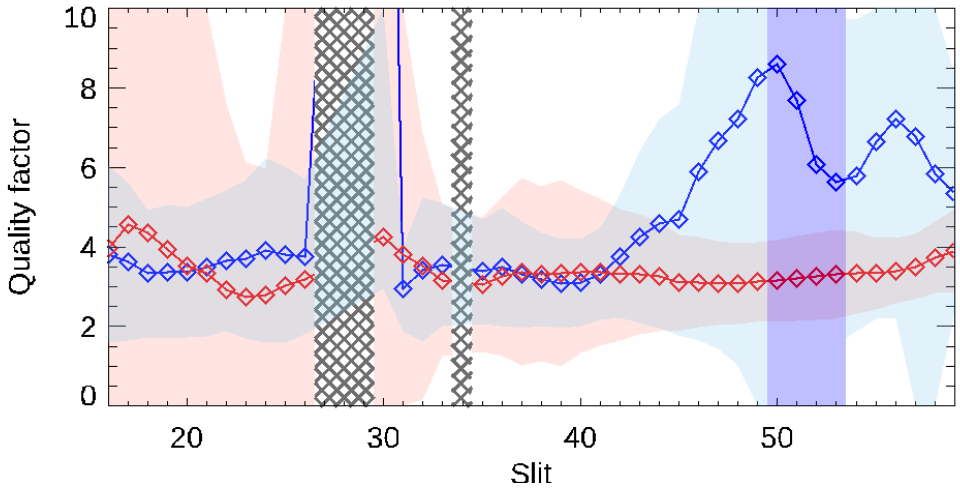

Figure 2.13: Signal quality factors calculated from fitting original ($n = 1$) data for each slit (red), and from fitting the bandpass filtered data in blue ($n = 3$). Diamonds show the quality factor value, and error estimates calculated using the credible intervals for τ_i and P_i propagated through standard error formula are shown in red for $n = 1$, and blue for $n = 3$. The purple region denotes the region in which the $n = 3$ node lies.

cross-field density profile (and/or the density contrast), different harmonics would experience different quality factors. Thus the constancy of quality factor along the loop for both harmonics (within our resolution), the fact that the loop cross section in AIA does not appear to vary between the apex and the loop leg, and the finding that $P_1/3P_3 < 1$, all imply that the inhomogeneous layer thickness ($l_{\rm inhomo}/a$) and density contrast did not vary significantly along the loop length.

To the best of our knowledge such an investigation of quality factor for multiple harmonics has not been done before. Thus the potential of such comparisons of quality factors is still largely unknown. It is imperative that more theoretical work is carried out to this end, particularly examination of the effect of spatially varying transverse density profile upon different harmonics' resonant absorption. For instance, the result presented here must be compared and harmonised with the suggestion in Goddard et al. (2018) that one signature of the Kelvin-Helmoltz instability may be the broadening of the transverse inhomogeneous layer in the cross-field density profile of loops, based on forward modelling oscillating loop simulations. This change in width of the inhomogeneous layer presumably impacts the resonant absorption rate (see Eq. 2.3). Moreover the effect is likely to be different for different harmonics, since there would be a variation in shear flow related to the varying number of nodes

and antinodes, though the details are unclear. Considering the large amplitude of the oscillation causes nonlinear effects such as the Kelvin-Helmoltz instability to grow more quickly (Magyar and Van Doorsselaere 2016a), this observation would appear to be an ideal candidate, having a presumably well-progressed instability. If such an effect is predicted to make a noticeable observational difference, the change with longitudinal profile for different positions along the loop could be probed using the comparison of periods and quality factors as outlined here, this would be an exciting tool for seismology to assist where limited spatial resolution and ambiguous DEM's are restricted.

It is interesting that the oscillation does not exhibit signatures of the second harmonic as strongly as for the third harmonic, which damps away faster. This absence of the second harmonic implies the perturbation was symmetric about the apex, as in the simulations in Pascoe and De Moortel (2014). This is in contrast to the observation in Pascoe et al. (2016a), where the second harmonic was excited by an eruption that clearly affected one leg more than the other and so was strongly asymmetric. We can be confident the third harmonic was not excited by some nonlinear cascade or evolution, because we would expect there to be some inertial period in which the nonlinearity grows, or in other words see the amplitude grow and then decrease. Yet it may be seen in Figure 2.10 that the third harmonic has its highest amplitude at the beginning of the oscillation, and both modes of oscillation appear to begin at the same time. Together these make the simultaneous excitation of the fundamental and third harmonic the simplest explanation for the observed behaviour. The fundamental mode being most strongly excited implies the spatial scale of the perturbation was comparable with the loop length, $k_{\mathrm{driver}} \geq k_1$. Because the driver does not coincide with the first harmonic we also get the third harmonic which is also symmetric about the apex. It is also possible that the temporal profile of the driver could influence the generation of higher harmonics, since an impulsive driver localised in space and time is broadband in $k - \omega$ space and allows a wide range of frequencies to be excited. This was recently demonstrated for the case of propagating sausage modes (Goddard et al. 2019). Either way we might expect the fifth harmonic to also be present with an amplitude about an order of magnitude weaker than the third harmonic, though that would be undetectable because of its very small period of oscillation, damping rate, and amplitude.

Since the exact structure of a coronal loop is still unknown, it is right to ask questions about the validity of applying linear MHD wave theory to observed oscillations. The assumption of magnetohydrostatic equilibrium may be broken if the density of the host loop changes, for example from mass accretion at the apex from the ponderomotive force (Terradas et al. 2008a), though there is no indication

this is happening here. It may be possible that radiative cooling can also change the loop density, on a timescale comparable to that of the wave period (Aschwanden and Terradas 2008). In some instances (not here), coronal loops fade over a few cycles implying that the plasma has cooled out of the passband of observation. However it is more common to find loops existing for tens of minutes before and after a kink oscillation has finished, and the radiative cooling time neglects the influence of coronal heating. The great successes of the application of coronal seismology are persuasive that the effects of density change in the loop are secondary effects for kink oscillations at best. The finding that 1d resonant absorption theory explains well the observation in Section 2.2 adds to these successes.

Chapter 3

Decay-less oscillations

In this chapter, the regime of small amplitude and persistent transverse oscillations known as decay-less oscillations, and their usefulness for coronal seismology, is reviewed. A review of decay-less oscillations to date is given in Section 3.1. The first detection of a higher harmonic of a decay-less kink oscillations is presented in Section 3.2. The implications of this observation and the outlook for using decay-less oscillations in routine seismology is presented in Section 3.4.

3.1 Introduction

The study of transverse oscillations of coronal loops has undoubtedly been greatly successful, demonstrating how observations, theory and simulations may combine to provide useful information through coronal seismology. However, a limitation of the high amplitude, rapidly decaying kink oscillations in terms of routine seismology is their irregular excitation: observers must wait for an explosive event or restructuring to occur before any probing of the coronal conditions may be done with this form of well-understood wave. The recent revelation of the existence of ubiquitous, low amplitude decay-less oscillations may open up the prospect of routine seismology, which would be valuable for space weather forecasting and modelling of the solar atmosphere. Yet, there are some serious gaps in our understanding of these decay-less transverse oscillations, most notably that their persistent nature is apparently at odds with 1d resonant absorption theory. Thus a robust investigation of decay-less oscillations through observations and simulations is of great importance for coronal seismology as a whole.

3.1.1 Decay-less oscillations as standing kink modes

The first report of a decay-less oscillation of a coronal loop was published by Wang et al. (2012) where long lasting kink oscillations in a coronal loop appeared to grow in amplitude over time. The oscillations were visible in several SDO/AIA warm passbands (1–2 MK) as seen in Figure 3.1, and at least a dozen full cycles may be seen, which is a stark contrast with the rapidly decaying transverse oscillations which had been observed up to that point. The nearby eruption of a CME at the same time, combined with the amplitude growth of the oscillations despite the damping it presumably experiences (like all kink modes), led the authors to speculate the oscillations were the result of forced driving with an energy input rate exceeding the rate of damping (discussed in Subsec. 3.2.4). Note that the analysis was confined to the loop apex, where the amplitude of the oscillation was greatest. This was not the case for the decay-less transverse oscillations studied in Anfinogentov et al. (2013), which were analysed at many positions along their respective loops and found to have the phase and amplitude behaviour of fundamental standing modes. Notably, these decay-less oscillations were not associated with any flaring activity or nearby eruptive events. The independence of decay-less oscillations from the usual, mechanical impulse-like driver was also found for the multi-thermal trans-equatorial loop studied in Nisticò et al. (2014).

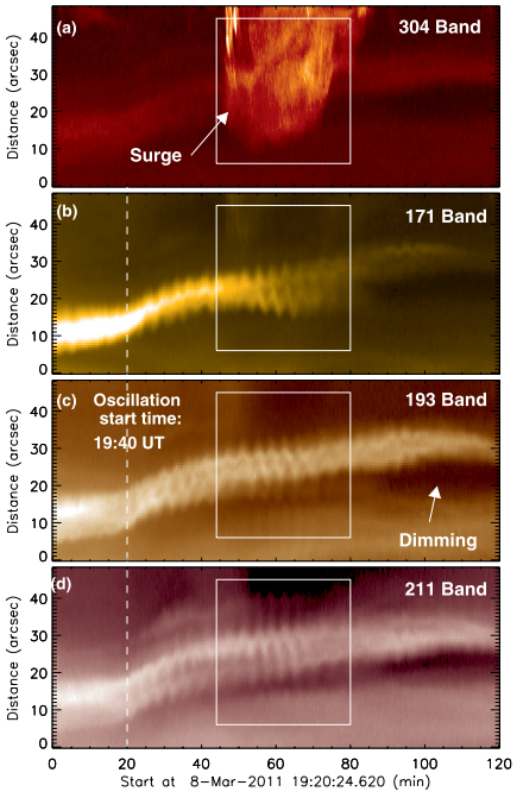

Figure 3.1: Time–distance maps at the apex of a coronal loop, showing the first reported detection of decay-less oscillations. Figure taken from Wang et al. (2012).

It was established in Nisticò et al. (2013) that **the decaying and decay-less regimes are able to coexist in the same loop**, with an eruption event triggering high-amplitude decaying oscillations whilst the decay-less oscillations were seen thirty minutes before and after the event – implying they have a distinct, continuous driver. These persistent decay-less oscillations had the same period as that for the decaying oscillations, with far smaller amplitude. One of the loops was found to expand to be

gradually expanding, and the period of decay-less oscillations appeared to gradually change with it. For another, steady loop with a slightly different length (inferred using stereoscopic measurements), the period was constant and slightly different to that detected in the expanding loop. Note this loop was re-examined in Pascoe et al. (2016c, 2017a, referred to as loop 3), and the decay-less component was measured to have an amplitude $\approx 7\%$ that of the fundamental mode amplitude. In this case, as with all the previous, the intensity of the loop as it undergoes transverse oscillation is steady. If the loop does fade away (moves out of the passband), such as the 171 Å channel in Figure 3.1, this does not seem to be related to the decay-less oscillation.

Recent results using motion magnification to make decay-less oscillations visible in the pre-flare phase for a small flare were presented in Li et al. (2020). The decay-less oscillations of a very faint, diffuse loop were seen for approximately three cycles, with no decay and a steady period of about 400 seconds. The light curve of the pre-flare phase, recorded in NoRH 17 GHz microwave emission and GOES soft X-ray, also showed a quasi-periodic pulsation (QPP) with growing period (300–500 seconds) which visually matched the phase of the motion magnified oscillation (one-to-one peaks). The diffuse loop seems to have been strongly affected by the small flare and disappeared from the 171 Å passband. It was concluded that the (probably thermal) QPP and observed decay-less loop oscillation were triggered by the same process.

Spectroscopic observations of a flaring loop with IRIS in the Fe XXI 1354.08 Å line also appear to show decay-less oscillations in the Doppler velocities (Li et al. 2018), however the questionable detrending applied, of subtracting a running 60 second average to arrive at dominant periodicities of roughly 60 and 120 seconds, throws doubt on the trustworthiness of these results. Nonetheless the commonality of QPPs in light curves of flares combined with these findings imply that decay-less oscillations, or their driver, may be present in flaring data in some cases.

When these observed properties of decay-less oscillations are combined – the different periods for different loops (of the order of several minutes), a loop experiencing a decay-less oscillation and a high amplitude oscillation of the same period, the consistent phase along the entire loop length, no clear thermal effects – the argument of their origin as standing kink modes is compelling. This was strengthened in a more statistically justified way in Anfinogentov et al. (2015), in which the period of decay-less oscillations measured from 72 coronal loops was seen to linearly scale with the length of the oscillating loop (as expected for $P_1 = 2L/C_K$) and having typical periods of 1.5 min to 10 min, as shown in Figure 3.2. Decay-less oscillations were found to typically have amplitude smaller than the minor radius of the loop at ~ 0.17 Mm, in contrast to the rapidly decaying kink modes of amplitude many times the minor radius at several Mm. This estimate forms an lower

limit to the amplitude of decay-less oscillations, because line of sight (LoS) effects mean that any transverse oscillation not in the plane of sky has a reduced apparent displacement. Moreover decay-less oscillations were observed in 19 of 21 active regions investigated, making them an omnipresent phenomenon in active region coronal loops.

This may corroborate the finding in Doschek et al. (2007), in which Hinode/EIS spectral observations detected non-thermal broadening at the edge of active region loops, slightly offset from intensity maxima. This is consistent with unresolved, persistent decay-less kink oscillations (as described in the forward modelling of kink oscillations in Yuan and Doorsselaere 2016). Futhermore, persistent oscillatory variations of the Doppler shift in EUV spectral observations of the tops and upper parts of coronal loops were also recognised in Tian et al. (2012, specifically the events referred to as "Type II"). These observations of undamped oscillations with periods around 4 minutes, symmetric line profiles (hence not flows) and amplitudes of some 1.6 km s^{-1} near the tops of loops (∼112 Mm) are completely consistent with low amplitude decay-less (kink) oscillations. Such small amplitudes would be incredibly tough to identify through its transverse displacement on images (motion magnification is unlikely to work well on disk centre), but is easily resolved with spectroscopic observations.

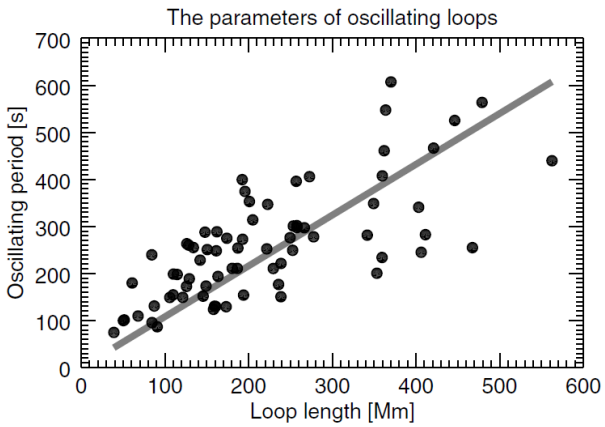

Figure 3.2: The scaling of decay-less oscillation period with loop length for 72 loops, with a Pearson correlation coefficient of $r = 0.72 \pm 0.12$ and a line of best fit $P = (1.08 \pm 0.04)L$. Figure taken from Anfinogentov et al. (2015).

3.1.2 Alternative explanations for decay-less oscillations

In Hindman and Jain (2014, 2018) an alternative explanation for decay-less oscillations is presented, as a series of interference patterns in a two-dimensional waveguide (arcade) formed by a multitude of MHD waves excited by a continuous, distributed and stochastic source. Note that in this model the rapid damping of large amplitude waves is attributed to interference effects without local dissipation. An attempt to probe an arcade of loops in search of decay-less oscillations using a novel autocorrelation approach was performed in Allian et al. (2019). The evidence for the existence

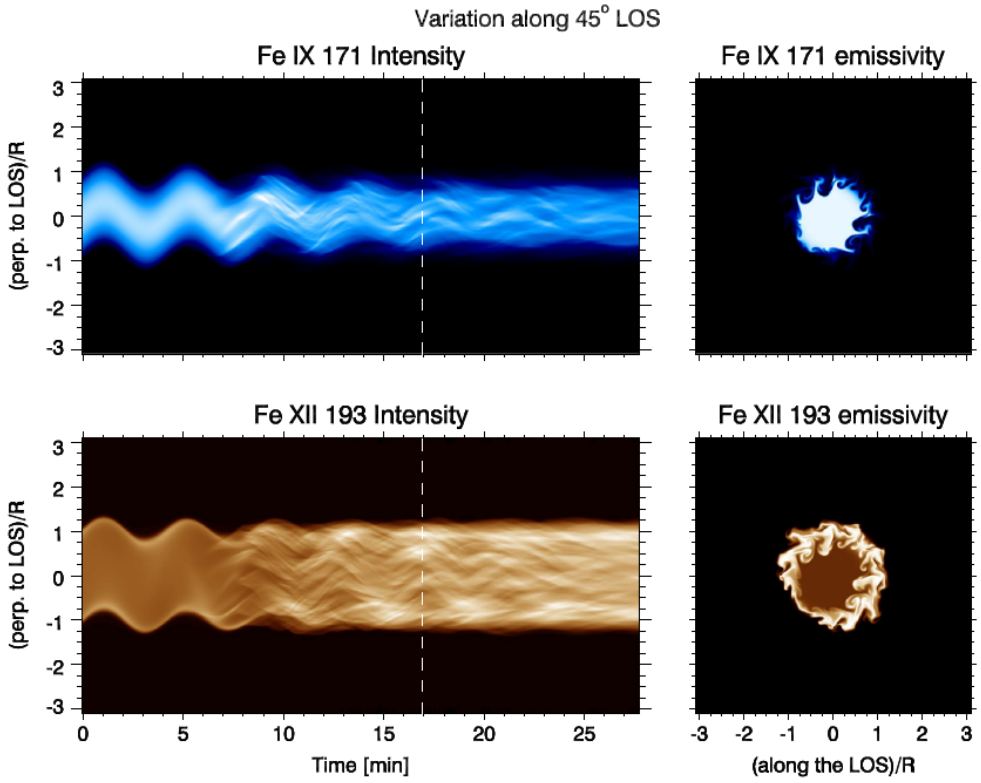

Figure 3.3: Forward modelled time-distance maps from a 3D MHD simulation of a loop perturbed by a fundamental standing kink mode. The development of small scales from KHi is clear in both 171 Å [*top row*] and 193 Å [*bottom row*], both from the time-distance maps at full numerical resolution [*left column*] and the loop cross sections [*right column*], taken at the time indicated by a white dashed line. Figure taken from Antolin et al. (2016).

of decay-less oscillations pre- and post-flare was strong, and the bundle of loops seemed to oscillate incoherently but with similar period – this would be as expected for a series of similar length but isolated flux tubes, but how this relates to an arcade model is not made clear. A prediction is made for the arcade model that a low frequency cut-off should exist for each mode order, corresponding to the frequency of modes propagating parallel to the magnetic field lines (so not moving any magnetic surface), and should be visible in heavily averaged Fourier (or wavelet) spectra of decay-less oscillations. A study answering this question should be undertaken, but until that point the interpretation of decay-less oscillations as the standing kink mode of a single flux tube seems more convincing.

A number of three-dimensional MHD numerical simulations have tried to address the nature of decay-less oscillations. In the beginning, the focus of attention was understanding the onset and evolution of the Kelvin-Helmholtz instability

(KHi). The shear flows induced by the transverse motions of a kink oscillation should be unstable to KHi, particularly at its antinodes according to theory, and the development of KHi in simulations is rife (for instance in Afanasyev et al. 2019; Antolin et al. 2017; Terradas et al. 2008a; Zaqarashvili et al. 2015). Yet there have been no direct observations of transverse wave induced instabilities. Kelvin-Helmholtz instabilities have been observed elsewhere in the solar corona but the detections so far pertain to large field-aligned plasma velocities (see discussion in Subsec. 1.2.4). As an example the reader is referred to Figure 2.5 in the previous chapter, and note that the beginning state and the end state of the loop appear the same despite the large amplitude kink oscillation, in contrast to simulations (although the effects of instrumental resolution should be taken into account, as in Antolin et al. 2017). It is unlikely that all simulations are in a different amplitude regime, particularly compared to the well studied high-amplitude regime of kink oscillations; moreover simulations show rampant KHi for even small amplitude cases and in the presence of enhanced dissipation (Antolin et al. 2014). Magnetic twist compatible with observations appears insufficient to suppress the onset of KHi (Howson et al. 2019). It may be that the distinctive vortices of KHi have not been resolved in coronal loops with current EUV instruments' resolution, and it is well known that the triggering Alfvén waves (shear flows) are themselves difficult to detect due to their weak compressibility.

In Antolin et al. (2016) it was suggested that the collective motion and periodic brightenings of these vortices following a kink-mode perturbation may appear as decay-less oscillations once LoS effects, spatial degradation and narrow bandpass filter of observations are taken into account. This collection of KHi vortices are often referred to as Transverse Wave Induced KHi (TWIKH) rolls, and one simulation exhibiting TWIKH rolls is shown in Figure 3.3. It is theorised the properties of the vortices would reflect the torsional Alfvén waves to which the kink mode resonantly couples, not the kink mode itself, except in terms of the synchronicity of the vortices along the loop. This model attributes the long-lived nature of decay-less oscillations to the relatively weak damping of azimuthal Alfvén modes (when compared to the damping of kink modes from resonant absorption). In the subsequent study of Antolin et al. (2017) it was found that such decay-less oscillations would not be observed for loops without a sufficient temperature contrast to the ambient surroundings, suggesting the "effect" is a consequence of mixing the different temperature plasmas together. Similar claims of TWIKH rolls appearing as decay-less oscillations were made in the recent work of Guo et al. (2019), however since the loop was continuously driven at the kink mode frequency the effect of the KHi would appear to be coincidental. This series of papers devote much attention to

the multi-thermal properties and spectral signatures which this model predicts would be observed, the onset of the KHi itself, and heating considerations for the corona (notably neglecting radiative losses and thermal conduction), which go beyond the discussion here.

In this thesis, TWIKH rolls are not believed to be the mechanism behind decay-less oscillations themselves. Some observations show steady decay-less oscillations before any large amplitude kink mode perturbation, and the TWIKH roll model requires at least an initial standing kink mode perturbation in order to synchronise the rolls, as shown by the lack of visible decay-less oscillations in the case driven purely by an Alfvén driver in Guo et al. ("A-model", Fig. 7 in 2019). Moreover the results of simulations involving KHi have an issue matching observations, particularly for the loop cross-section during and after a large kink oscillation (e.g. see the end states in Pagano and De Moortel 2019), which needs to be addressed. This is not to say that KHi does not affect loops in the way simulated at all – rather that the key question about decay-less oscillations is how they are supplied enough energy continuously to overcome the damping from resonant absorption.

3.2 Detection of second harmonic

In this section, the first detection of multiple harmonics of decay-less kink oscillations in a coronal loop is described. As explained before, due to the small amplitude of the decay-less oscillations, insufficient resolution of EUV imagers prevented their detection and measurement prior to 2012. Since then decay-less oscillations have been observed as fairly monochromatic displacements usually observed best at the loop apex , and best fitted to a sinuosoid of single frequency – in Anfinogentov et al. (2015) the time-distance map from the single "best" slit along the loop was selected, but again only a single frequency fitted. This means that only the fundamental harmonic of the standing kink mode may be seen, except perhaps for visual signs of anharmonicity in the oscillation profile. The fact that only fundamental modes have been detected is not unexpected, since resonant absorption theory implies that higher frequency oscillations will damp faster, making the job of detecting already difficult-to-see oscillations even harder. However it is important to search for the existence of higher harmonics, since this provides some constraints on the decay-less oscillations' origins and driver. This section follows very closely my publication Duckenfield et al. (2018).

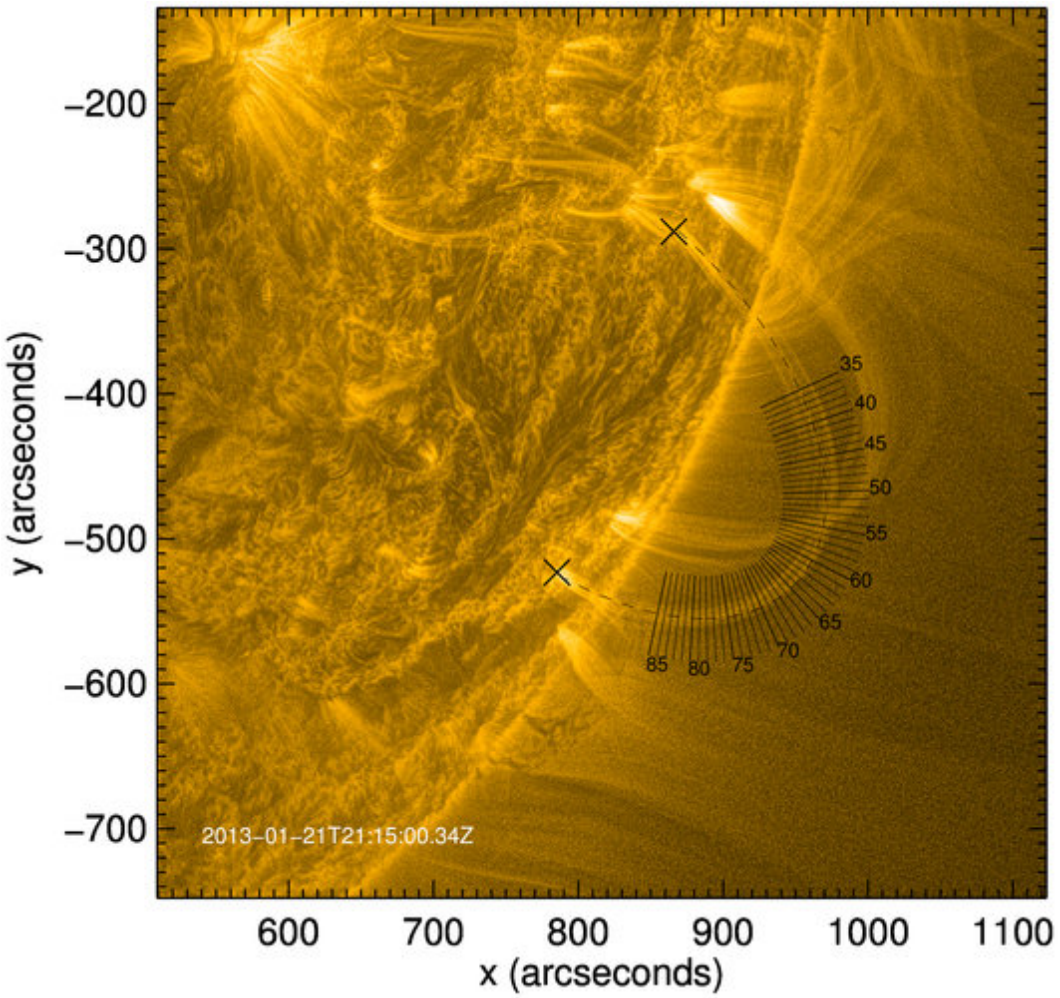

Figure 3.4: SDO/AIA 171 Å image of the loop at data start time 2013/01/21 12:15:00 UT. Note that this intensity image has been enhanced using the Multi–scale Gaussian Normalisation (Morgan and Druckmüller 2014). Slits that were used for the analysis are displayed, taken perpendicular to an elliptical fitting of the loop, whose footpoints are shown by the black crosses.

3.2.1 Observation

We choose to re-examine the decay-less oscillation identified in Nisticò et al. (2014), which is well contrasted and off-limb, simultaneous STEREO data available, and is isolated from other loops. The coronal loop of interest is not associated with any active region and appeared on the (south westerly) limb of the Sun on 21 January 2013, as seen in Figure 3.4. It remained visible in 171 Å for approximately ten hours. The loop is also visible in 193 Å and 211 Å channels. The three dimensional reconstruction of the loop from stereoscopic observations found the loop to be almost perpendicular to the solar surface, and well modelled by an ellipse with only a moderate ellipticity, having a major axis only 1.27 times the minor axis (Nisticò et al. 2014). Thus we can safely assume the loop to be approximately semi-circular, and using this approximation with footpoint locations selected as (866,-288) arcsec and (785,-523) arcsec (seen in Fig. 3.4) its length was estimated as $L \approx 292\,\mathrm{Mm}$. During the observation time, the length remains constant and no flares or eruptions were detected in EUV or appeared on the GOES flux. A subfield of 1024×1024 pixels was extracted for 30 minutes of data (150 frames) representing the region of interest, throughout which the loop extends beyond the limb allowing good contrast. Our loop is observed above the limb therefore derotation is not required.

One method to overcome the low amplitude nature of decay-less oscillations for further analysis was developed and presented in Anfinogentov and Nakariakov (2016), where a motion magnification routine uses both spatial and temporal information to reconstruct the image with magnified transverse oscillations *over an unchanged stable background*. The magnification is independent of oscillation period for a broad range of periods, and scales linearly with the displacement amplitude, and thus makes a suitable tool to help clearly determine the oscillation parameters. For further information on motion magnification and its implementation in this thesis, the reader is referred to Appendix B. In order to study the more rapidly damped higher harmonics, which usually are of lower amplitude than the fundamental for most kink oscillations, the need for motion magnification is apparent. Motion magnification was tested on this data for a range of magnification factors (x3, x6, x9) and smoothing widths (50, 80, 100, 120 frames). Comparisons were made to check the oscillation periods observed are independent of magnification and the time-distance maps could be more easily analysed (see Figs. B.3 and B.2 for examples). It was found that a magnification factor of $\times 6$ and a smoothing width of 50 frames was optimal.

The (projected) loop axis was fitted with a segment of an ellipse, and one hundred straight slits of length 100 pixels were created perpendicular to this axis at equal increments along the loop's axis as depicted in Figure 3.4. By analysing the oscillation signal in many locations, a good precision may be obtained in a similar

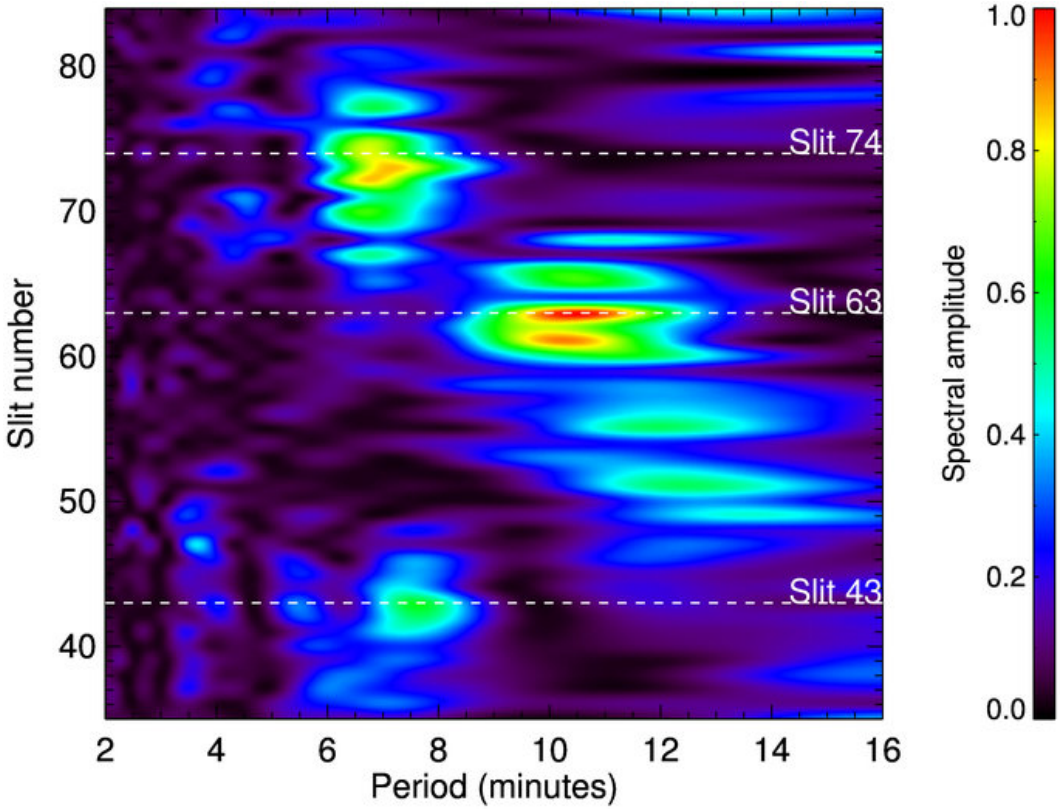

Figure 3.5: Two-dimensional distribution of (normalised) spectral amplitude calculated from a Lomb-Scargle periodogram per slit against period and slit number.

manner to Van Doorsselaere et al. (2007), and for this well-contrasted loop segment the spatial distribution of any harmonics is resolvable. Time-distance maps are made from these slits, and for each slit the intensity is averaged over a width of five pixels in order to improve the signal-to-noise ratio. Only in slits 35 to 85 was the loop contrasted well enough to be used reliably in further analysis, due to the presence of the limb and time-varying noise from the lower corona. The motion magnification also suffers distortion from motions in the background, making slits nearby unusable at the relatively active limb. The length of loop segment between consecutive slit index numbers varies slightly along the loop due to loop curvature and projection. However, this dependence is small since the loop plane is reasonably perpendicular to the observer, and the loop is approximately semi-circular. So, its curvature is approximately constant along the loop.

3.2.2 Results

Each of the fifty slit's time-distance maps underwent the intensity fitting procedure at each frame creating a time series that follows the highest intensity peak through

time which is assumed to be the position of the loop axis, in the manner described in Subsection C.1. No detrending was necessary, thanks to the stability of the loop equilibrium position. Lomb-Scargle periodogram analysis was performed to obtain the frequency spectrum of each time series. Figure 3.5 shows these spectra stacked to form a two-dimensional distribution of (normalised) spectral amplitude as a function of period and distance along the loop (the slit index). Three regions of significant spectral power are visible. The strongest signal is seen for slit numbers ~ 63, which is near the loop apex, with a period of $10.3^{+1.5}_{-1.7}$ minutes. This value was measured by summing the Lomb-Scargle periodograms for the slits with spectral amplitude above a threshold value (in this case slits 60 to 68), and extracting the period value corresponding to this sum's peak. The error is estimated as the full width at half maximum, for this slightly asymmetric peak. For slit numbers ~ 74, corresponding to the southern loop leg, there is significant spectral amplitude with a period of $7.1^{+0.8}_{-1.0}$ minutes. This period and full width at half maximum was measured through summing periodograms from slits 70–78. A similar region of significant amplitude is seen for slit numbers ~ 43 corresponding to the northern loop leg, with a period of $7.7^{+0.8}_{-0.9}$ minutes. This value was measured from the summation of periodograms from slits 40-48.

These results are interpreted as the fundamental and second harmonic of the standing kink mode for the following reasons. Firstly, there are two distinct periods, one being approximately half of the other. The longer period ~ 11 minutes lies within the range expected for the fundamental standing kink mode for a loop of this size, i.e. $C_{\mathrm{K}} \approx 0.9\,\mathrm{Mm/s}$. The shorter period component lies at slightly greater than half of this value at ~ 7.4 minutes, with both regions being measured as the same period within error. This period is consistent with a second harmonic modified by effects such as density stratification, or flux tube expansion as discussed in Subsection 2.1.2. The spatial distribution of the nodes and antinodes for the two periodicities (Fig. 3.5) is also consistent with the fundamental and second harmonic standing modes.

We note that the region of high spectral amplitude around slit 43 has an apparently slightly longer period than on its opposite leg, whereas for the second harmonic these periods should be identical assuming similar background plasma conditions. The amplitude around slit 43 appears as though the region has been split in two (in period). This could be caused by amplitude modulation of a single frequency component (not unexpected given the signal-to-noise ratio), which when transformed into Fourier space would split the power into two peaks.

To verify the detection of the second harmonic, we must confirm the correct phase behaviour in addition to the spatial distribution of nodes. Figure 3.6 compares

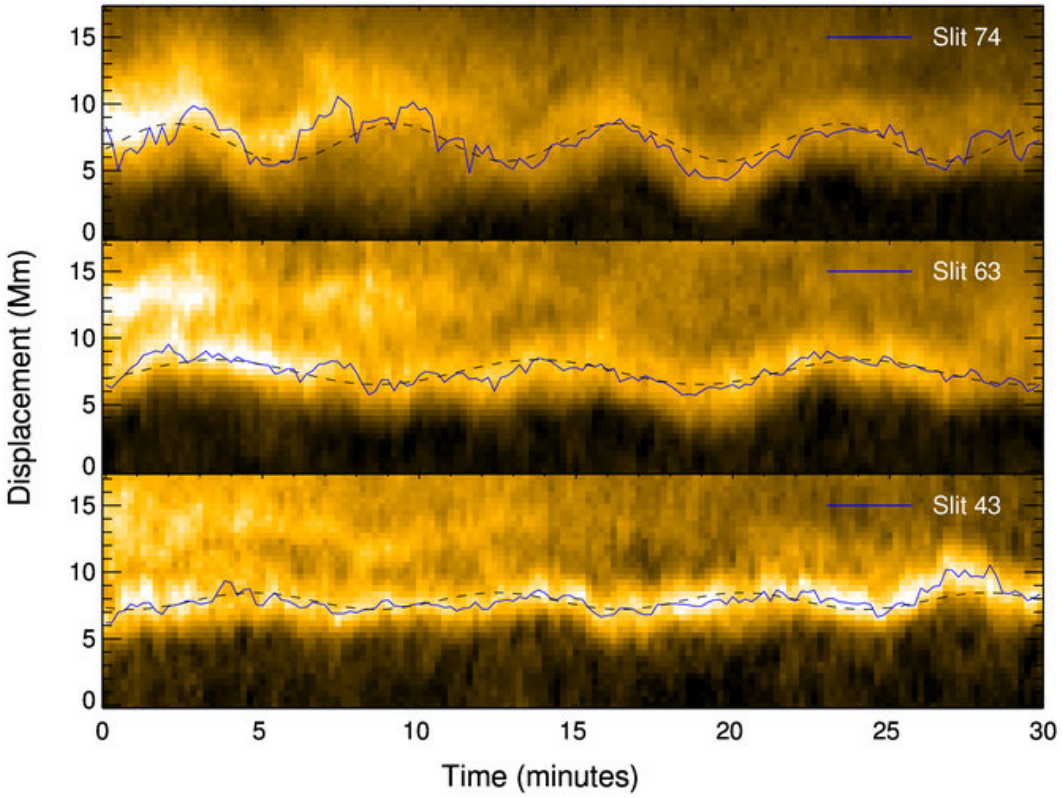

Figure 3.6: Time distance maps for slits 43 (top), 63 (middle), 74 (bottom). The solid blue line shows the time series output from the time-distance map intensity fitting. The dashed black line is the least squares fit of the time series to a single sinusoid. Thus for slit 43 (top) the dashed black line is a sinusoid of period 7.8 minutes, amplitude 0.62 Mm, phase 128 degrees. For slit 63 (middle), the dashed black line is a sinusoid of period 10.3 minutes, amplitude 0.93 Mm, and phase 33 degrees. For slit 74 (bottom), the dashed black line is thus a sinusoid with fitted period of oscillation of 7.0 minutes, amplitude 1.4 Mm, and phase of 20 degrees.

time distance maps from slits 43 (northern leg), 63 (near apex) and 74 (southern leg). Each map is over plotted with the fitted intensity time series in black, and a sinusoid that has been fitted to the time series in blue. By comparing the top and bottom plots, one can see that the periods of fitted sinusoids are similar (7.8 and 7.0 minutes, respectively) and the oscillations are approximately in anti-phase as expected for two antinodes of the second harmonic. The time-distance map for slit 63 exhibits a much longer period of 10.3 minutes. Comparing at the time of about 19 minutes, where the fundamental mode (on slit 63) reaches its minimum, a corresponding modification is seen on the other slits: this is consistent with the effect of the (in phase) fundamental mode superposing on to the more dominant second harmonic down the legs.

Further evidence that the higher frequency component is an even harmonic is

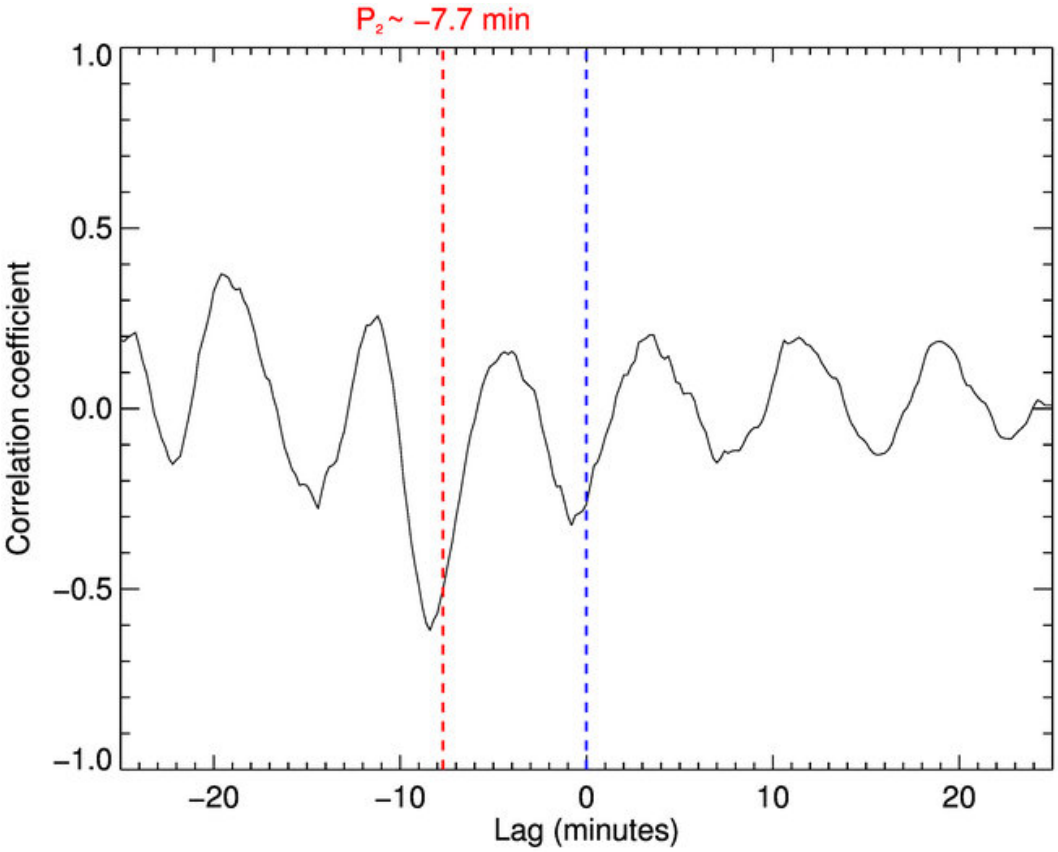

Figure 3.7: The cross correlation between slits 43 and 74 as a function of lag. The dotted blue line at lag 0 intersects the cross-correlation at the Pearson coefficient value. The dotted red line at lag -7.7 minutes is displayed to show the period of the higher frequency component P_2 calculated from the periodogram analysis (interval between the red and blue lines). The cross correlation is oscillatory with this period.

seen in Figure 3.7, which clearly shows the existence of the same frequency component in both slits 74 and 43, that is on both legs as expected. The value at lag zero (blue dashed line) is negative and has a local minimum, meaning the two legs are in anti-phase, as expected for an even harmonic. The oscillation is apparent for all lags without significant decay of amplitude, showing the oscillation is decay-less, especially considering that for greater lags there is less signal to contribute to the cross-correlation.

3.2.3 Application to seismology

Decay-less oscillations have several seismological applications. In addition to estimating the local Alfvén speed C_{A0} from the (fundamental) kink mode period (assuming a density contrast), if a higher order harmonic of the decay-less standing kink mode is also detected this allows for further seismology through the ratio of periods, as

described in Subsections 2.1.2 and 2.3.1.

In this case, we estimate the $P_1/2P_2$ ratio as $10.3/(7.1+7.7) \approx 0.69 \pm 0.16$, with the error calculated using the standard error propagation formula as $P_1/2P_2 * \sqrt{((1.7/10.3)^2 + (1.3/7.4)^2)}$. Clearly this value has a large departure from the expected value of unity, and since this is less than 1 this implies density stratification is the dominant cause of dispersion. Using the model considered by Andries et al. (2005a); Safari et al. (2007) for a density scale height H gives the following (in a similar way as Eq. 2.5):

$$\begin{aligned} P_1 &= P_{\rm kink}\left(1 + L/(3\pi^2 H)\right)^{-1}, \\ 2P_2 &= P_{\rm kink}\left(1 + L/(15\pi^2 H)\right)^{-1}. \end{aligned} \tag{3.1}$$

Assuming density stratification is the sole cause of dispersion (especially no flux tube expansion), and that Equation 3.1 is valid for this data, the period ratio can provide an estimate for the density scale height. For this loop of length of $L = 292$ Mm, then we find $P_1/2P_2 = 0.69 \pm 0.16 \implies H = 16^{+29}_{-9}$. This value of H is less than the expected hydrostatic value (usually estimated at 50 Mm), while it is consistent with the value of 30^{+5}_{-4} Mm reported in Van Doorsselaere et al. (2007), and the value of 18–42 Mm reported in Pascoe et al. (2017a).

A measurement of the spatial distribution of nodes and antinodes of the second harmonic may illuminate whether the eigenfunction of the loop oscillation has been affected by longitudinal structuring of the density or magnetic field (see Sec. 4 in Andries et al. 2009). In principle if the magnetic field becomes weaker towards the loop apex (from flux tube expansion for example), the antinode positions of the second harmonic will shift towards the loop apex, whilst density stratification will cause a shift toward the loop footpoints (see Figs. 6 & 7 in Andries et al. 2009). Using the methods outlined here to find the amplitude profile along the loop, any shifts of the antinodes may be combined with the period ratio and therefore assess the relative importance of loop expansion versus density stratification with more certainty.

As with the discussion of intensity scale height being half that of H (Subsec. 2.3.1), the scale height in the range 7–45 Mm inferred here is clearly not physical since this would imply an intensity scale height of under 25 Mm. The loop apex is just less than 100 Mm above the solar surface yet shows a similar intensity as near the footpoints (Fig. 3.4). We reiterate that the results of density scale height derived from this seismological approach are consistent with other techniques (e.g. see review in Schmelz and Winebarger 2015), and so the unrealistic stratification heights inferred indicate that current models of coronal loops and their equilibria

are missing something. We need to stress that other effects may be important such as cross-section (magnetic) variation (e.g. Pascoe and Nakariakov 2016; Verth and Erdélyi 2008a), temperature difference effects (e.g. Guo et al. 2015; Lopin and Nagorny 2017), siphon flows (e.g. Yu et al. 2016) and ellipticity of the loop (Dymova and Ruderman 2006b). For more information of these effects, the reader is referred to the review in Andries et al. (2009). Here the estimation is presented as an illustration of seismological application.

3.2.4 Implication upon proposed excitation mechanisms

The finding that there exist multiple, spatially resolved harmonics within the decay-less regime provides further evidence that these are the same kink mode standing waves as the large amplitude decaying regime. However, their excitation mechanism is unknown and they are presumably subject to the same damping mechanisms as the large amplitude, decaying regime attributed to resonant absorption. This begs the question: what is driving these decay-less oscillations, or else supplying the energy required to overcome the losses to resonant coupling with Alfvén modes?

Several excitation mechanisms for low amplitude kink oscillations have been proposed in the literature. It is natural to start by considering the one-dimensional differential equation of a damped oscillator (transverse oscillations of 1d string). Let $a(t)$ represent the displacement of the loop apex, δ be the damping coefficient (which may be found empirically), $f(t)$ represent the external driving force to compensate the losses to dissipation and/or mode conversion, and recall $P_{\rm K}$ is the natural period of the loop oscillation determined by the loop ($P_{\rm K} = 2L/C_{\rm K}$). Then we may contemplate the following equations:

$$\frac{d^2a(t)}{dt^2} + \delta\frac{da(t)}{dt} + \left(\frac{2\pi}{P_{\rm K}}\right)^2 a(t) = f(t), \tag{3.2}$$

$$\frac{d^2a(t)}{dt^2} + \left[\Delta - \alpha\left(\frac{da(t)}{dt}\right)^2\right]\frac{da(t)}{dt} + \left(\frac{2\pi}{P_{\rm K}}\right)^2 a(t) = f(t). \tag{3.3}$$

Equation 3.2 corresponds to the classic driven damped harmonic oscillator equation, whilst Equation 3.3 includes a nonlinear modification to arrive at a Van der Pol equation. Nisticò et al. (2013) considered a model equivalent to the former with $f(t) = \exp\left(-2\pi it/P_{\rm K}\right)$. A natural choice for a harmonic driver in the solar corona are sunspot oscillations with periodicity of 3 minutes, discussed in Subsection 1.1.6. The difficulty with a harmonic driver is the resonant behaviour: the amplitude of oscillation is proportional to the difference between the driving frequency and the natural frequency ($2\pi/P_{\rm K}$), and in the asymptotic state the

loop should oscillate with the driver frequency. We would expect to see a peak in amplitude when the driver frequency matches the natural frequency (period) of the loop, yet no such increase is seen in Figure 3.8. The fact that we see steady decay-less oscillations of different periods, and their presence in loops not rooted in a sunspot (such as the one in Sec. 3.2) suggests that the driver would have to vary spatially with period varying over an order of magnitude (see Fig. 3.2), but be very stable temporally to explain the constancy of amplitude over many cycles. Moreover the remarkable monochromaticity of decay-less oscillations conflicts with the finding in Ballai et al. (2008) that a harmonic driver typically excites a mixture of harmonics with properties of both the loop and the driver period, thus predominantly carrying information about the driver rather than the loop itself. This is inconsistent with the scaling of loop length with period seen in Anfinogentov et al. (2015). Also the observation presented in Section 3.2 shows the fundamental mode and second harmonic exist, simultaneously and enduringly, which are very likely associated with the loop – no mixture of another period was seen, again showing inconsistency with a harmonic driver.

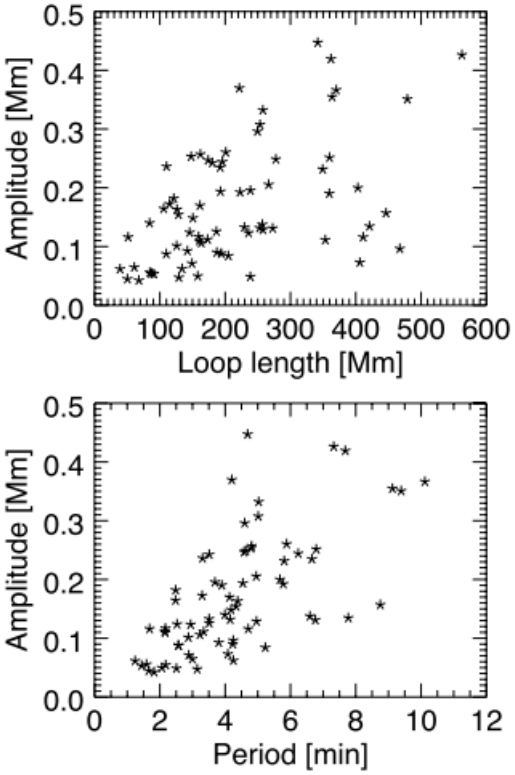

Figure 3.8: Scaling of displacement amplitude versus loop length [*top*] and period [*bottom*], for decay-less oscillations observed in 21 active regions. Figure adapted from Nakariakov et al. (2016a).

Recently, all of Guo et al. (2019), Afanasyev et al. (2019) and Karampelas et al. (2019) considered full 3d MHD simulations of a loop continuously (harmonically) driven with transverse oscillations. The focus of their studies was on the development of KHi and the energetics involved, and so the 'decay-less oscillations' in their studies were in fact driven oscillators. In Guo et al. (2019) the driver frequency was chosen to match the fundamental mode frequency, and so tells us little about the driver of decay-less oscillations. Similarly Karampelas et al. (2019) used a monoperiodic driver at the fundamental frequency, finding that once the TWIKH rolls had fully developed, the (driven) oscillations' amplitudes were only weakly correlated with the driver

strength – perhaps partially explaining why the amplitude of decay-less oscillations can appear so stable. However the normalisation of intensity used in order to display time-distance maps in this simulation belies the extreme changes in intensity that occurred when the strength of the driver changes (e.g. see their Fig. 2). Their loop was cool with respect to the background, so the mixing effect is strong; interestingly, their results somewhat match Wang et al. (2012). We repeat that their oscillations are driven unlike in observations, so these results do not match observations yet. The approach in Afanasyev et al. (2019) explored the range of driving frequencies near the fundamental: one can clearly see the resonant peak in their Figure 2, which is not seen in (this thesis') Figure 3.8 from observations. **Overall it is more likely that the driver $f(t)$ is not harmonic, and the periods of the decay-less oscillations are the natural responses of the loops themselves.**

Equation 3.3 corresponds to the model outlined in Nakariakov et al. (2016a) in which decay-less oscillations are the manifestation of a loop *self-oscillation*. The loop would be analogous to a violin string, with driving super-granulation flows near the loop footpoints acting as the bow. The coefficients Δ and α are a specific nonlinear form of the damping term δ. This necessarily dissipative model relies on this nonlinear term (in square brackets) to remove energy from large amplitude oscillations but also feed energy into small amplitude ones: the decay-less oscillations are thought of as the limit cycle. The period of the oscillation is thus determined by the loop parameters and not the driver, consistent with the observed scalings of amplitude and period with loop length. The independence of amplitude on period is also explained, since the specified periods for each loop will extract different amounts of energy from the steady flow, with the rate that balances the dissipative losses. However this model is seriously limited in its current form. The authors themselves state that its semi-empirical, low dimensional description can only be used as a conceptual model: it has not been linked with the MHD equations, and misses important effects central to the observation in Section 3.2, such as multiple harmonics and spatial non-uniformity. Until this model is developed further, for instance relating parameters Δ and α to observable quantities, its usefulness is slight.

Other mechanisms for exciting kink oscillations include coronal rain, that is condensations of plasma due to thermal instability, which forms at a loop apex and falls under gravity have the potential to excite kink modes (Kohutova and Verwichte 2017). However this struggles to explain the constancy of decay-less oscillations in amplitude and intensity within a passband, and the observations made here and in Nisticò et al. (2013). Nonlinear effects from flows such as the centrifugal force and colliding flows could be investigated as drivers of decay-less oscillations (e.g. Antolin et al. 2018), however their importance seem unlikely due to the small amplitudes

involved, their steadiness, and would require a whole new understanding of the generality of flows within loops (especially apparently stable loops).

Very recently, claims of the detection of decay-less *torsional* oscillations were made in Aschwanden and Wang (2020), using 3d measurements of the magnetic field using a nonlinear force-free model of their own design, fitted to decimated SDO/AIA observations of loops. By fitting a sinusoid to the "free energy" derived from their fitted magnetic field on datasets containing large flares, they concluded that there were torsional oscillations (measured as azimuthal magnetic field component). These "oscillations" were decay-less, occurred in all analysed flares, and have periods of 10–20 minutes, yielding a phase speed of 315 ± 120 km s^{-1} (assuming they are standing modes). If the interpretation of these results as torsional Alfvén waves is believed, then these modes would seem likely to couple with the fast-mode MHD wave. The link with observed decay-less kink oscillations is not yet clear, but worth consideration in future.

What is clear is that the driver $f(t)$ must supply energy to the kink mode quasi-continuously, to maintain oscillations with no visible damping. It has been suggested that the driver $f(t)$ must be driving at the footpoints, from photospheric motions/super-granulation flows which buffet the loops randomly but constantly. Such a model was considered in Anfinogentov et al. (2015) but dismissed due to an argument that both horizontal and vertical polarisations should be excited equally, whereas only horizontal polarisations were seen. This argument is important to address, it must be checked that a random driver does indeed drive both polarisations equally and matched with data. However it may not be a deal breaker – not least because current theories are generally based on low-dimensional models, and the observations so far are biased with a preference for loops off-limb. The appeal of this model is that multiple harmonics of the loop would naturally be excited due to the random frequencies of the (broadband) driver.

Recent simulations in Afanasyev et al. (2020) have demonstrated that **kink oscillations randomly driven at the loop footpoints, with a broadband driver whose power spectrum is of coloured noise, can exhibit multiple harmonics** of what appear as decay-less oscillations. Further, any non-uniformity in the kink speed along the loop would lead to a departure from unity of the ratio of harmonic periods P_1/nP_n as was observed in Section 3.2, even in this randomly excited case. Being a simple model there are inevitably shortcomings; the time evolution of the periods is not properly accounted for, since the damping mechanism of resonant absorption has not yet been fully included (a linear damping term is added to the wave equation instead). Since resonant absorption acts quicker for higher harmonics, this may be important. Nonetheless this result places random

footpoint driving as the current best candidate for decay-less oscillations.

3.3 Conclusions

Decay-less oscillations are prevalent throughout the corona, and the evidence suggests they are the small amplitude standing kink modes of coronal loops. In Section 3.2 we described the first detection of a simultaneous fundamental mode and second harmonic of decay-less oscillation of a loop, made possible through the use of motion magnification. Spectral analysis found two periods to be prominent: $10.3^{+1.5}_{-1.7}$ minutes and $7.4^{+1.1}_{-1.3}$ minutes. The spatial distribution of spectral amplitude revealed the shorter period component had an anti-node on each loop leg, and the longer component had an anti-node near the apex of the loop, confirming the harmonics' amplitude distribution through the loop. Direct comparison of the time-distance maps and the cross correlation analysis showed that the shorter period oscillations observed in different legs of the loop are in anti-phase, confirming the harmonics' phase distribution through the loop. This observation supports this interpretation of decay-less oscillations as the excited natural eigenfunctions and eigenfrequencies of the loop (not driven), and implies that the driver of decay-less oscillations must be capable of exciting multiple harmonics. This is in agreement with the recent numerical work using a random footpoint driver to excite multiple harmonics (Afanasyev et al. 2020). An important finding in the observation in Section 3.2 was the inferred non-uniform kink speed along the loop, implied by the measured period ratio $P_1/2P_2 = 0.69 \pm 0.16$. This suggests that the loop studied had some longitudinal structuring of density, and/or other dispersion mechanisms, although it would seem any flux tube expansion is weak due to the period ratio being less than unity, not more.

In general the ubiquity of decay-less oscillations (Anfinogentov et al. 2015) makes any seismological applications of decay-less oscillations particularly appealing, since the number of potential targets would hugely increase, particularly in quiet regions. This point is expanded upon in the recent paper of Anfinogentov and Nakariakov (2019), in which the same techniques used here (in addition to estimating the loop density contrast) are applied to many loops in the same active region and a picture of the variation of Alfvén speed is formed. The merits of further information from multiple harmonics (such as the $P_1/2P_2$ ratio) to better constrain the inversions is also clear, now it is confirmed higher harmonics of decay-less oscillations exist. Thus the potential of decay-less oscillations for routine seismology is extremely exciting, as these first steps show their capability for the widespread estimation Alfvén speed and, potentially, of the magnetic field and free magnetic energy available for the release in preflaring active regions.

Chapter 4

Slow magnetoacoustic waves and their use in coronal seismology

In this chapter, propagating slow modes above a sunspot fan are discussed. The underlying theory, particularly slow mode damping, is reviewed in Section 4.1. Observations of such modes above one sunspot are presented in Section 4.2, from which evidence supporting the multi-thermal structuring of coronal loops is found and outlined in Section 4.3.

4.1 Introduction

4.1.1 Slow modes in the solar atmosphere

One of the ubiquitous MHD modes observed in the solar corona is the (compressive) slow magnetoacoustic wave, often seen as intensity enhancements in extreme ultraviolet and soft X-ray observations. Slow modes are also often put forward as candidates for quasi-periodic pulsations (QPPs) seen in flare emission both on the Sun and in other stars (Sych et al. 2009). The first detections of periodic brightenings were made using the SOHO satellite in white light and EUV, in which coronal plumes high above the limb exhibited periodic, propagating intensity perturbations visible using time-distance plots, and later analysed using Fourier power spectra compared with numerical simulations (DeForest and Gurman 1998; Ofman et al. 1997, 1999). Transient brightenings in EUV were also seen in coronal loops around the same time using time-distance plots and wavelet analysis (Berghmans and Clette 1999; De Moortel et al. 2000). The typical periods and velocities of these upwardly propagating disturbances were in the range of 180–420 seconds and 70–165 km/s. Since then,

examples of both the standing mode and propagating mode oscillations have been routinely observed in the solar corona.

Parameter	Value	Unit
Temperature, T_0	0.5–20	MK
Number density, n_0	10^8–10^{11}	cm^{-3}
Slow wave time scale, τ	3–20	min
Plasma non-uniformity length, L	180	Mm
Spitzer conductivity, $\kappa_{\parallel}$	$10^{-11}T_0^{5/2}$	$\mathrm{W\,m^{-1}\,K^{-1}}$
Adiabatic index, γ	5/3	
Mean particle mass, m	$\sim (0.6) \times 1.67 \times 10^{-27}$	kg
Boltzmann constant, k_B	1.38×10^{-23}	$\mathrm{J\,K^{-1}}$
Specific heat capacity, C_V	$(\gamma - 1)^{-1} k_\mathrm{B}/m$	$\mathrm{J\,K^{-1}\,kg^{-1}}$

Table 4.1: Typical physical and thermodynamic parameters of the coronal plasma. The wave time scales τ correspond to the typical periods of propagating slow waves, for example observed in loops ($\tau \simeq 155 - 550$ seconds, De Moortel 2009) and plumes ($\tau \simeq 10 - 20\,\mathrm{min}$, Banerjee et al. 2011) and standing SUMER-type oscillations ($\tau \simeq 8 - 18\,\mathrm{min}$, Nakariakov et al. 2019; Wang 2011).

Standing modes are rarer to observe directly than propagating intensity disturbances, and there is some discrepancy between the periodicities seen with different instruments and temperatures. Doppler shift measurements of hot emission lines (typically > 6 MK) show periodic variations, detected by the spectrometer SOHO/SUMER – similar signals are also seen with BCS aboard Yohkoh. These oscillations are impulsively generated (by flares), have periods on the order of minutes to tens of minutes, and damp extremely quickly with a ratio of exponential damping time to period (quality factor) of around unity. The phase speeds of these waves are near the sound speeds estimated for their corresponding loops' temperatures. A quarter-period phase lag between the disturbance in velocity and intensity, as detected in some cases, provides convincing evidence that these observed oscillations are standing modes, probably of flare-induced slow magnetoacoustic modes (Wang et al. 2002, 2003). A review of these oscillations observed by SUMER may be found in Wang (2011). The local plasma-β and magnetic field have been estimated through performing seismology on these SUMER oscillations, though the range of uncertainty is large (Wang et al. 2007).

Other instruments have also been used in claims of detecting similar standing oscillations after flares, such as intensity perturbations seen by EIS onboard Hinode (for example Srivastava and Dwivedi 2010) and seen by SDO/AIA (Wang et al. 2015, 2018). Oscillations are also seen in the modulation of microwave emission of

a flare loop observed with NoRH (Kupriyanova et al. 2014). Despite the potential of such oscillations for seismology, applications are stymied by the uncertainty of the damping mechanism. For example, the analytical considerations in MacNamara and Roberts (2010) found that longitudinal structuring probably has a greater effect on the $P_1/2P_2$ ratio than it has an effect on the damping, but this (already weak) conclusion depends on whether compressive viscosity is a significant damping mechanism in its own right. Nonetheless in some cases observations have been used to investigate the damping mechanism itself (Wang and Ofman 2019).

Propagating intensity disturbances (slow modes) are commonplace in the corona, moving upwards and occurring in warm quiescent loops, both near sunspots and far from them (De Moortel et al. 2002a,b). Slow modes above sunspots are often studied, partly because of observational bias (sunspots are point of interest, often form stable loop systems etc) but also because the prevalent 3-minute sunspot oscillations detailed in Subsection 1.1.6 probably act as a driver for, or exciter of, the propagating slow modes. Such waves observed in EUV have been used to perform seismology in several ways, including searching for the wave damping mechanisms (De Moortel 2009), searching for the effective polytropic index (Prasad et al. 2018), and finding the sound speed and height difference between the transition region line 304 Å and the formation height of 1600 Å (Deres and Anfinogentov 2018). In principle the magnetic topology and longitudinal structuring of coronal loops could also be probed.

Slow modes are also seen on open field structures such as plumes in coronal holes (Banerjee et al. 2011). Propagating coronal disturbances are found to have little variation in amplitude compared to background noise floor which is also time-dependant, making the disturbances hard to detect and even more difficult to classify. Despite being best observed on the edge of active regions and above sunspots, these intensity variations are found to be typically under 5% of the underlying background and so ideally are observed during quiet (non-flaring) periods (De Moortel 2009). Although hot coronal loops are resolved in the X-ray band, in this temperature regime flaring plasma is dominant reaching temperatures of 100 MK (Reale 2014), thus propagating slow modes are usually imaged in EUV bands. Similar to the standing modes, these observed intensity perturbations appear to be subject to rapid damping as they propagate upwards (Abedini 2016).

Looking at NoRH data at 17 GHz above a sunspot, 3 minute oscillations have been observed to have amplitude modulation in the form of periodic wave trains (Reznikova et al. 2012; Sych et al. 2012). There may be additional support for the 3 minute oscillations seen in the corona being externally driven by photospheric p-mode via the observed amplitude modulation periods (Prasad et al. 2015). The

fact that amplitude modulation periods appear to coincide with those seen for the global p-mode spectrum for many spectral lines (and hence heights) may imply the waves' photospheric origin (Centeno et al. 2006; Chorley et al. 2010; Marsh et al. 2008). In addition, the 3 minute oscillations can be subject to frequency modulation or drift, the beginning and ends of which coincide with the amplitude modulation envelope's (Prasad et al. 2015). If not an instrumental or data processing artefact this is evidence of dispersion, possibly from change in host loop's curvature with height.

When considering the dispersion relation governing propagating modes, wave frequency ω is considered real and determined by the excitation, and one considers how the wavenumber $k(\omega)$ evolves. When a propagating mode is said to damp rapidly, this means that the *damping length* of the oscillation (also the e-folding length) is short compared to the wavelength. The damping length is found by solving dispersion relation $k(\omega) = 0$, and finding the imaginary component $\lambda_D = 1/Im(k)$ (from harmonic dependence $v \propto \exp ikz$). Example calculations of the damping length may be found in De Moortel and Hood (2003, 2004); Owen et al. (2009). There has been some discrepancy over the dependence of damping length upon frequency, described for different mechanisms Prasad et al. (table 1 in 2014) and discussed further in Mandal et al. (2016). There have been suggestions of a different scaling of damping time versus period for oscillations within hot loops (SUMER) compared to cool loops (TRACE, SDO/AIA), indicating several damping mechanisms may be acting. Yet, observational effects such as the unknown inclination of the magnetic field, or any change in density along the propagation path, make confident conclusions on dissipation mechanisms difficult (for example off-limb observations in a polar coronal hole Gupta 2014). For a well-renowned review article on the topic of propagating longitudinal oscillations, the reader is referred to De Moortel (2009). Slow magnetoacoustic modes have also been extensively modelled, usually in 1D, exploring the effects of compressive viscosity, gravitational stratification, radiative cooling, temperature inhomogeneity and further nonlinear effects (Bradshaw and Erdélyi 2008; De Moortel and Hood 2003, 2004; Mandal et al. 2016; Mendoza-Briceno et al. 2004; Ofman and Wang 2002; Owen et al. 2009; Selwa et al. 2005; Wang and Ofman 2019; Wang et al. 2018).

4.1.2 Damping mechanisms: compressive viscosity and thermal conduction

There are several mechanisms which may damp longitudinal oscillations: thermal conduction, compressive viscosity, resistivity, magnetic flux tube divergence, footpoint leakage and radiative cooling being mechanisms which at one time or another were

considered important for the corona. Each of these effects may be enhanced or inhibited by the local plasma conditions such as any gravitational stratification, nonlinear cascade to smaller length scales, non-equilibrium ionisation balance, to name a few.

Leakage of the wave's energy at the oscillating loop's footpoints was investigated as a mechanism for the rapid damping, but this mechanism is generally thought to be negligible due to the high reflectivity of the chromosphere (Nakariakov et al. 1999; Ofman 2002), at least for typical loops observed with TRACE. It should be noted that this mechanism has not been assessed for slow oscillations. Similarly, finite resistivity can become important when the wave contains magnetic field perturbations, yet the effects are thought to be unimportant for longitudinal waves in the corona since these modes perturb the magnetic field only weakly. Sometimes the effect of finite resistivity is incorporated with the general dissipation transport coefficient η, but this is rarely considered important compared with thermal conduction and viscous dissipation.

Viscosity is a natural choice to investigate for the damping of longitudinal waves. For field-aligned waves the classical value has compressive viscosity as

$$\mathcal{F}_{\text{vis}} = \frac{4}{3}\frac{\partial}{\partial z}\left(\eta_0 \frac{\partial}{\partial z} v_z\right) \tag{4.1}$$

where $\eta_0 \simeq 10^{-17} T^{5/2}$ kg m^{-1} s^{-1}, derived first in Braginskii (1965) and again in a more physically motivated way in Hollweg (1985). In general, viscous dissipation results in an increase of the wave period and damps the wave. However in many 1d simulations, the damping effect of compressive viscosity has been found to be insignificant for coronal conditions when compared to thermal conduction. Only when the compressive viscosity coefficient is enhanced by a factor of 10 was the effect noticeable in simulations conducted by De Moortel and Hood (2003). Similarly it was concluded that viscosity must be enhanced by an order of magnitude to dissipate slow waves on the observed timescale in SUMER oscillations (Ofman and Wang 2002). This conclusion has led to a tradition of assigning the rapid damping of slow magnetoacoustic modes to the effect of thermal conduction.

Yet several subsequent studies have found cases in which thermal conduction is insufficient to explain observations (Bahari and Shahhosaini 2018; Mariska et al. 2008; Marsh et al. 2011; Prasad et al. 2014, 2018; Sigalotti et al. 2007; Wang et al. 2015). In one example, stereoscopic measurements from Hinode/EIS and STEREO A and B of propagating intensity disturbances in a cool loop (< 1 MK) led to the conclusion that the damping by thermal conduction is insufficient to explain the rapid damping (Marsh et al. 2011), corroborating previous findings with Hinode/EIS

(Mariska et al. 2008). Through loop modelling it was found that a combination of thermal conduction and compressive viscosity is needed to arrive at SUMER observed damping times in Sigalotti et al. (2007). Similarly it was concluded that for hot loops compressive viscosity is as important as thermal conduction, in the study of longitudinal MHD oscillations in slowly cooling loops using the WKB method in Bahari and Shahhosaini (2018). This is further supported by simulations searching for the enhancement of the classical viscosity coefficient and thermal conduction coefficient that best fits data, finding that viscosity may indeed be enhanced and thermal conduction suppressed (Wang and Ofman 2019; Wang et al. 2015, 2018). Gravitational stratification may enhance the viscous dissipation rate, but only reducing the damping time by some 10% (Mendoza-Briceno et al. 2004; Sigalotti et al. 2007). Under stratification the wave also grows in amplitude as it propagates into less dense plasma – making nonlinear effects more important (De Moortel and Hood 2004). In conclusion, when considering the damping rates of slow mode oscillations in the solar atmosphere, one should consider compressive viscosity as at least one of the wave's damping mechanisms.

Linear studies of damping rates may underestimate the importance of compressive viscosity and other damping mechanisms, and SUMER oscillations especially may have large enough amplitude (velocities up to 70% Mach number) to necessitate nonlinear treatment. For example, shock formation in simulations has been shown to greatly enhance dissipation, increasing the damping rate up to 50% above that of thermal conduction alone (Nakariakov et al. 2000; Verwichte et al. 2008). Other nonlinear effects have been investigated, usually in the context of slow modes as a heating mechanism (see Subsec. 1.2.3), however in this thesis we restrict our attention to linear considerations. Accounting for obliquity, tube waves damp faster than the plane acoustic waves to which they are often approximated, although the difference is minimal for low-β plasmas (Afanasyev and Nakariakov 2015). The effect of radiative losses and some unspecified constant heating sustaining the local thermodynamical equilibrium are usually thought to be balanced over the time scales and length scales involved and therefore not contributing to the wave dispersion (for example see Provornikova et al. 2018, and references within). This assumption means many studies do not include radiative losses as a damping mechanism. However some studies suggest the effect can be important (e.g. Carbonell et al. 2006), and this effect is studied in detail in the next chapter, Chapter. 5. There can also be an effect on the damping timescale of a standing acoustic wave due to the radiative energy losses that arise from equilibrium and non-equilibrium ionisation balances (called the First Ionisation Potential Effect, see Laming 2012). By radiating more (from lower charge states), these effects may reduce the damping timescale by up to $\sim 10\%$

(Bradshaw and Erdélyi 2008). This last effect is probably inconsequential in the fully ionised corona, in which slow modes are still seen to be strongly damped.

As explained, the main damping mechanism of slow waves in the corona is still traditionally thought to be thermal conduction. Thermal conduction acts to smooth out any gradients in temperature, and in presence of strong magnetic field prefers to smooth along the field than across it. The strong damping of propagating slow waves in hot plasma by thermal conduction is evident in the 2.5D MHD simulations of Fang et al. (2015), which incorporated radiative losses and forward modelling. It is common to follow the seminal paper De Moortel and Hood (2003) for derivations and expressions regarding thermal conduction. The damping length of propagating slow modes from thermal conduction is usually found by calculating $\lambda_D = 1/Im(k)$ from numerically solving (this is the non-normalised form)

$$\omega^3 - i\omega^2\gamma d k^2 C_{\rm S}^2 - \omega k^2 C_{\rm S}^2 + i d k^4 C_{\rm S}^4 = 0, \tag{4.2}$$

where the "thermal conduction parameter" d is measured in seconds, and defined as

$$d = \frac{(\gamma - 1)\kappa_{\parallel} T_0}{\gamma C_{\rm S}^2 p_0}. \tag{4.3}$$

This parameter d in some way measures the effectiveness of the thermal conduction, when d is small the thermal conduction has little effect and vice versa. Thermal conduction is known to be different for different wavenumbers, damping shorter length scales faster, seen as $\lambda_D \propto 1/\omega^2$ for propagating modes, or equivalently $\tau_{\rm cond} \propto 1/k^2$ for standing modes. One common expression estimating the timescale $\tau_{\rm cond}$ which characterises the effect of thermal conductivity is

$$\tau_{\rm cond} = \rho_0 C_{\rm V} \lambda^2 / \kappa_{\parallel}, \tag{4.4}$$

where $\lambda = 2\pi/k$ is the wavelength. Generally the effect of thermal conduction on waves is taken to be a purely damping term – the effect on phase speed is negligible (see Prasad et al. 2014). This is justified through comparing the thermal conduction timescale $\gg$ oscillation period, and so $Re(\omega) \gg Im(\omega)$, which is to say the oscillatory component happens much more quickly than the variation on phase speed. However in the limit of extremely strong thermal conduction, acting so fast there are no thermodynamic perturbations – which is to say *isothermal* – the waves become undamped and travel at the slower isothermal speed $C_{\rm S}/\sqrt{\gamma}$. As mentioned in the introduction (Subsec. 1.2.3), there may exist different regimes of thermal conduction when effects such as turbulent scattering or ionisation effects may no longer be neglected. Also, interestingly the coupling between thermal conduction and

gravitational stratification leads to increased periods and decay times for stratified loops, compared to homogeneous loops (Sigalotti et al. 2007). However these effects will not be considered going forward.

The other major mechanism which can explain the damping of upwardly propagating slow modes is geometrical divergence, also known as flux tube expansion, area divergence etc. This effect occurs when the cross section of the flux tube, to which the slow mode oscillation is confined, changes in area. This is not a dissipation mechanism because energy is not dumped into the plasma. The divergence of the magnetic field lines merely causes the amplitude of the perturbations (along a given field line) to decrease (De Moortel and Hood 2004). This effect is independent of wavenumber k. The damping effect from geometric divergence will be present whenever there is some changing spatial structure of the plasma inhomogeneity. Since stratified loops are thought to be expanded at the apex compared to the footpoints, and the magnetic field forms wineglass-shaped funnels in the lower chromosphere, this effect is probably very common. The damping of a propagating slow mode was mostly attributed to this effect in the stereoscopic observations made in Marsh et al. (2011). We stress that geometric effects such as this could not explain the damping of standing modes.

4.2 Using slow modes to infer the thermal structure of coronal loops

In this section work on observations of propagating intensity disturbances measured in a fan of coronal loops anchored above a sunspot are presented and interpreted in terms of the thermal structure of loops along the line of sight. This is similar to previous studies using TRACE data (King et al. 2003), and in AIA data with different bandpasses (Prasad et al. 2017). The novel elements of this work are the first accurate comparison of the propagating disturbances' instantaneous velocity against instantaneous period, an unexpected difference in the velocities measured along the same line of sight (LoS) in two passbands, and the resolution of this velocity difference through the estimation of the distinct inclination angles between multiple strands of different temperatures along the LoS.

The disturbances are understood to be slow mode oscillations characterised by flows predominantly parallel to the magnetic field, $C_{\mathrm{T}} < v_{ph} < C_{\mathrm{S}}$, and are highly oblique waves (locally) because their longitudinal wavelength ($2\pi/k_z$) is much greater than the transverse spatial scale of the waveguide (the radius of the loop a). Accounting for this obliqueness causes the wave speed to depend on the absolute

value of the magnetic field, defined through the *tube speed*

$$C_{\rm T}^{-2} = C_{\rm A}^{-2} + C_{\rm S}^{-2} \qquad \Longrightarrow \qquad C_{\rm T} = \sqrt{\frac{C_{\rm S}^2 C_{\rm A}^2}{C_{\rm S}^2 + C_{\rm A}^2}}. \tag{1.25}$$

Clearly as the magnetic field strength grows infinitely strong ($\beta \to 0$) the tube speed degenerates to the sound speed. In low-β plasma these waves can be well approximated as plane acoustic modes (Afanasyev and Nakariakov 2015), such that the apparent phase speed is the local sound speed,

$$v_{ph} \approx C_{\rm S} = \sqrt{\frac{\gamma p_0}{\rho_0}} \approx 151\sqrt{T[\rm MK]} \quad [\rm km\ s^{-1}], \tag{4.5}$$

where it is assumed the adiabatic index γ and mean molecular weight are constant within a small observing area (see Table. 4.1). This is justified by evidence of a square root dependence of velocity against temperature seen for similar warm loop fans (Uritsky et al. 2013).

4.2.1 Observations of slow modes in a coronal fan

We analyse propagating coronal disturbances seen in a coronal loop fan surrounding active region AR12628 observed by SDO/AIA on 2017 January 24 between 21:19-23:29 UT (a 2 hour data set). No flares were registered by GOES during this time interval. This active region, shown in Figure 4.1, was observed as it passed the central meridian in order to minimise the extreme LoS effects that would occur should it have been observed off limb. To avoid artificial periodic jumps in data, caused by the active region traversing across to different pixels at the Carrington rotation rate of the Sun, the data was derotated with interpolation between frames. Located at approximately N12 W05 at the time the images were taken, this active region shows a comparatively symmetric fan-like structure.

Time-distance maps along the loops were made using the derotated data, for six slits at different angles about the same sunspot as shown in Figure 4.1. An example time-distance map may be seen in Figure 4.2. The data from this active region showed intensity perturbations with a periodicity of approximately three minutes. For this study, data from the 171 Å and the hotter 193 Å bandpasses were used. The oscillations are clear in both, and the short damping length of the intensity perturbations is also visible, having faded to a background level after an apparent propagation of roughly 10 Mm (roughly 25 pixels). This short damping length is consistent with previous observations (Abedini 2016; De Moortel 2009; Mandal et al. 2016; Marsh et al. 2011; Prasad et al. 2014).

Each slit was partitioned into four equal length, 30 minute segments from

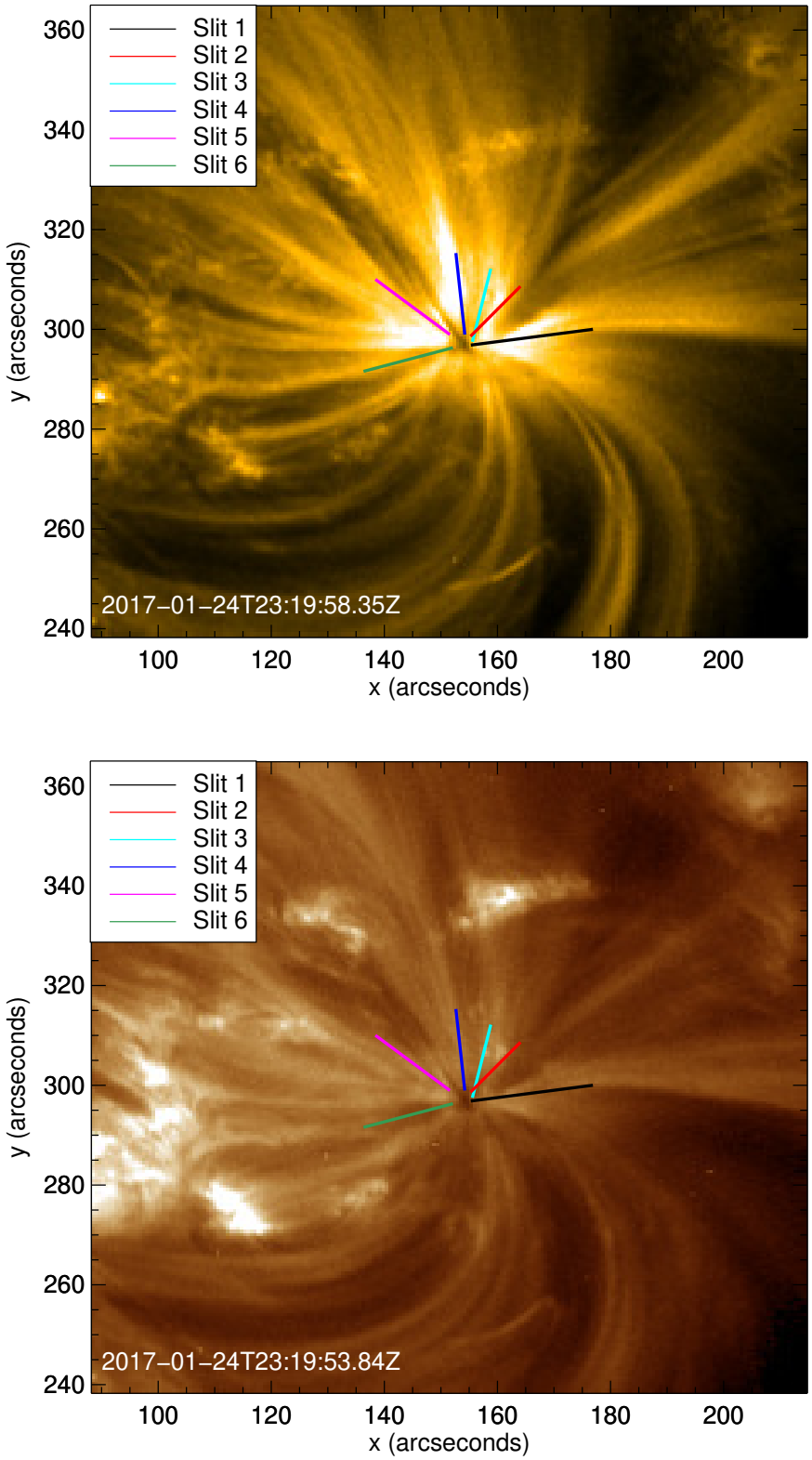

Figure 4.1: Image of the active region AR12628 in 171 Å [*top*] and 193 Å [*bottom*] from which the analysed slow propagating waves originate. The slits used for analysis (radiating outward) are marked in colour, consistent throughout this section.

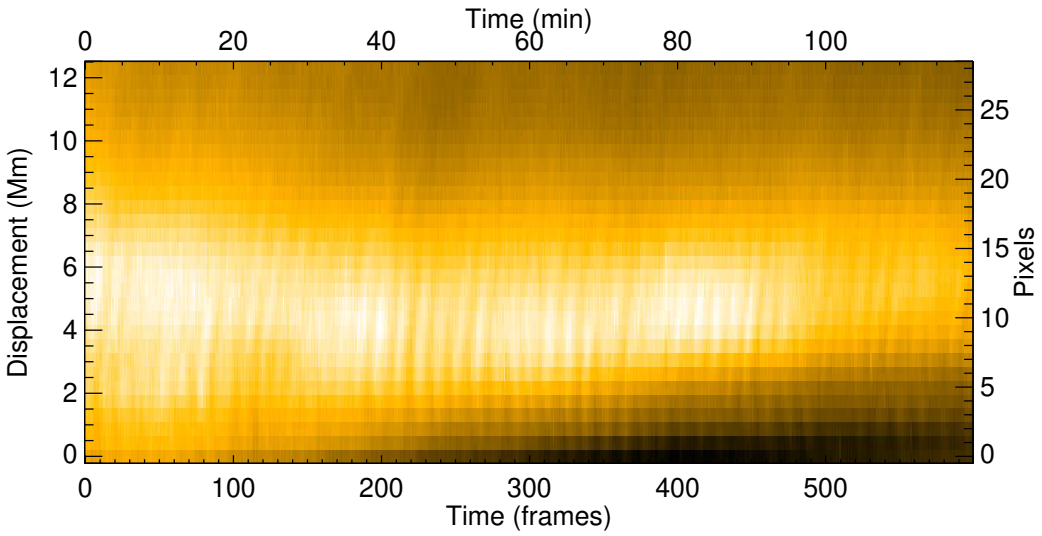

Figure 4.2: Time-distance plot of slit 1 shown in Fig. 4.1, with displacement starting from the point closest to the sunspot. Generated using the data in 171 Å. The periodic intensity perturbations are clear, as is their slant indicating upward propagation.

which an instantaneous period and velocity was measured. This allows any velocity/period changes in a single wave to be measured, hence permitting the observation of period drift and wave acceleration, as the intensity perturbation propagates along the fan loop, should they be present in the data. This also enables comparisons within the time scales of a single data set, as well as between different slits and bandpasses.

To accurately determine the instantaneous period, the intensity curves from each segment were formed using macro-pixels in order to suppress noise by averaging over neighbouring pixels. A small range of macro-pixel dimensions were tested, justified by taking estimates for the expected sound speed, period and known resolution. Very roughly, assuming the sound speed as being of the order 100 km s^{-1} and period of some 200 seconds gives an order of magnitude estimate for the wavelength as $\sim 20,000$ km. The pixel size of SDO/AIA (171 Å channel) can be approximated as 900 km, thus the wavelength is expected to cover 22 pixels. In order to remain well below this threshold and avoid averaging over a half wavelength – recall observations are of the maximum intensity amplitude – macro-pixels of 1×1, 3×3, 5×5 and 7×7 were tested. Resulting histograms of the instantaneous period calculated for each macro-pixel size were compared in order to find the macro-pixel dimension that minimised the standard deviation, thereby maximising precision. The results for one slit may be seen in Figure 4.3, and considering all slits it was concluded that a macro-pixel size of 3×3 pixels was optimal. An example intensity curve using a 3×3 macro-pixel may be seen in Figure 4.4.

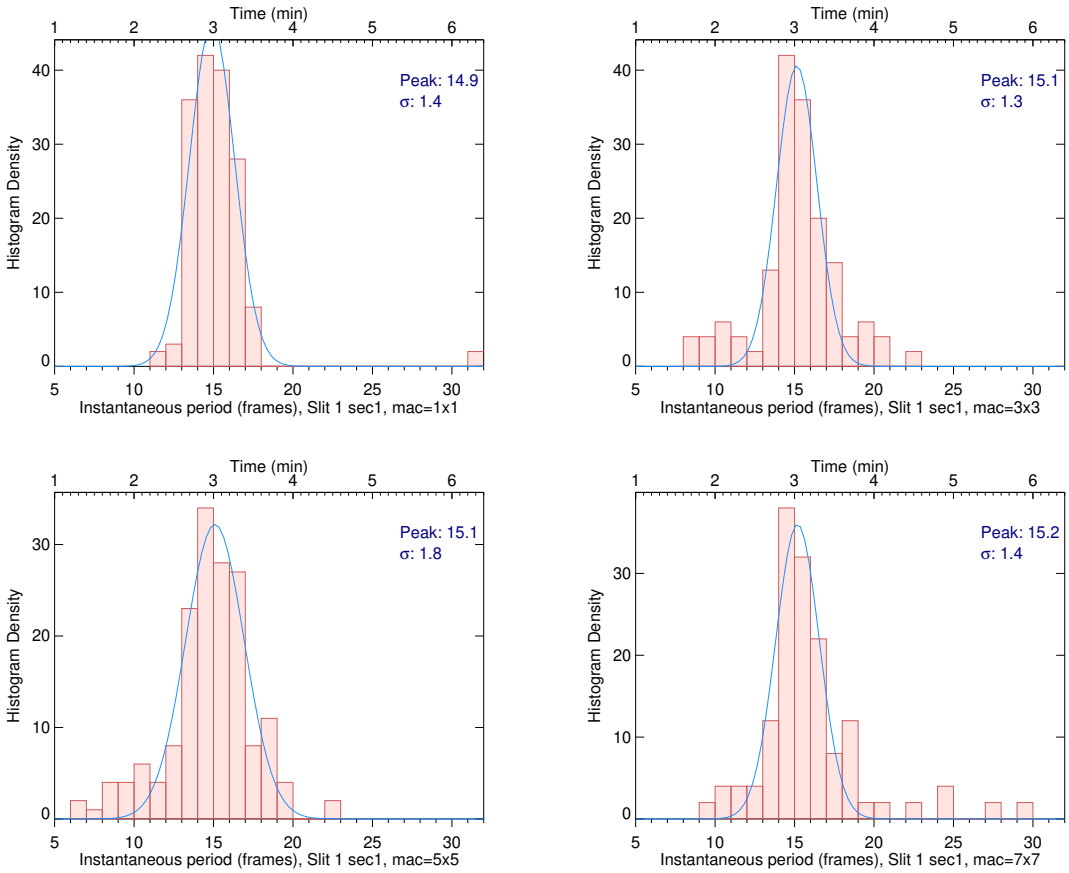

Figure 4.3: Histograms showing the period and standard deviation estimates for different cycles in the propagating 3-minute waves. This example corresponds to 193 Å data on Slit 4 segment 1, at a displacement of 5 Mm. All histograms are fitted with a Gaussian curve (blue) to measure the period and error by taking the standard deviation σ of the Gaussian. [Top left] Macro-pixel size 1×1 and resulting values of period = 14.91 frames, $\sigma = 1.41$ frames. [Top right] Macro-pixel size 3×3, period = 15.2 frames, $\sigma = 1.3$ frames. [Bottom left] Macro-pixel size 5×5, period = 15.0 frames, $\sigma = 1.9$ frames. [Bottom right] Macro-pixel size 7×7, period = 15.2 frames, $\sigma = 1.4$ frames.

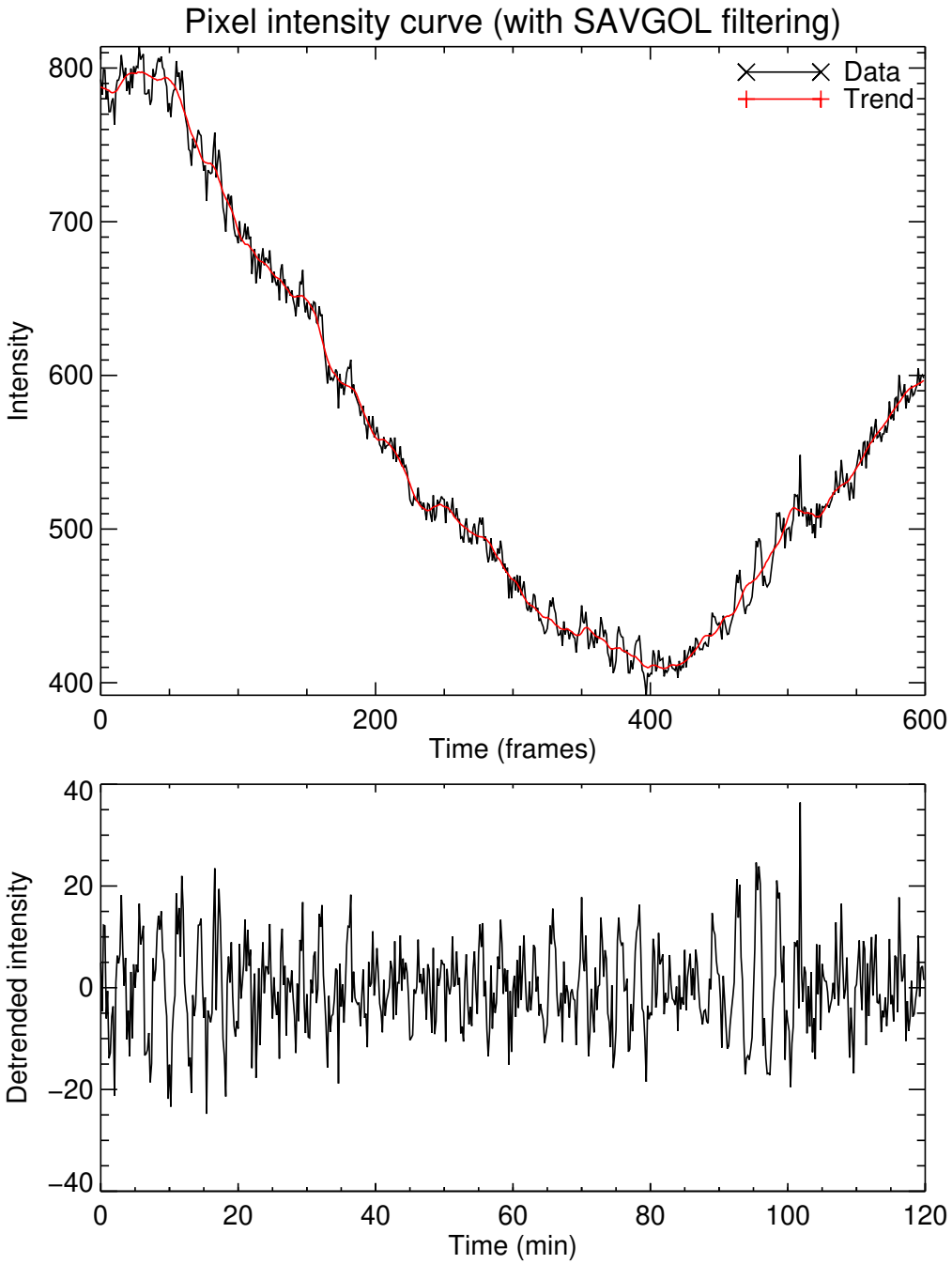

Figure 4.4: Intensity in the 171 Å channel showing clear three minute periodicities superimposed on a strong background trend. [*Top*] The trend calculated using a Savitzky-Golay filter of length 50 frames (red) shown on the intensity values (black). This signal comes from the first segment of slit 1 (closest to the sunspot, approximately pixel 5 in Fig. 4.2), averaged over 3×3 pixels. [*Bottom*] The detrended intensities clearly showing a three minute periodicity.

4.2.2 Measuring instantaneous period

In measuring the period of the observed waves, large background trends necessitate some detrending. The extent of the background trend compared to the amplitude perturbations from the slow modes can be seen in Figure 4.4. Detrending was achieved through convolution with a Savitzky-Golay filter of longer than 15 frames to avoid smoothing the periodic disturbances as much as possible (see Subsec. A.3 for further discussion). This background trend is found to be different for neighbouring pixels, as is usual for EUV images (Terzo and Reale 2010).

A widely used method to measure the period is to measure the position of the spectral peak obtained by Fourier or wavelet decomposition of a detrended variation of the intensity (or intensity difference) at a given pixel or macro-pixel. The wavelet decomposition of the detrended intensities was constructed for all segments, some example spectra for both bandpasses may be seen in Figure 4.5. In all slits and segments it was clear that the dominant periodicity lies around three minutes for both bandpasses, visible as regions of enhanced amplitude in the wavelet spectrum for the whole two hours, and also as a clear peak in the global wavelet spectra (GWS). In particular it is clear from the wavelet spectra that there was no discernible period drift over the two hours of observation, in any of the slits analysed. Nor is there any strong evidence of changing periodicity with distance along the slit in any of the slits. In terms of calculating periodicities, the GWS are sufficient to indicate any large changes, but their lack of precision – due to the tradeoff by all wavelet spectra in reducing spectral resolution to gain some temporal resolution – means that the instantaneous periods within this data may be measured more precisely with other methods.

Knowing there was no (strong) period drift, Fourier spectra were constructed for this data after detrending, one example being shown in Figure 4.6. In all slits and segments the dominant frequencies of the data were clearly around 3 minutes ($5.\dot{5}$ mHz) as expected. However as this example shows, the Fourier spectra typically show several peaks, and it was found that the precise frequency and magnitude of these peaks varies with even small changes in detrending width and data length. In particular using different trends led to unacceptably volatile values for the frequency of greatest peak (varying by up to 4 frames $\simeq$ 50 seconds).

There is clear evidence of amplitude modulation in all the periodic intensity perturbations. This is apparent in the intensities of the time-distance maps, shown in Figure 4.2 as the bulges of white lasting roughly 15-20 minutes, and also apparent in the wavelet plots such as Figure 4.5. Recall that amplitude modulation of a sinusoidal signal will result in a splitting of the spectral peak(s) in Fourier space into several peaks, perhaps explaining the twin peaks seen in Figure 4.6. This effect,

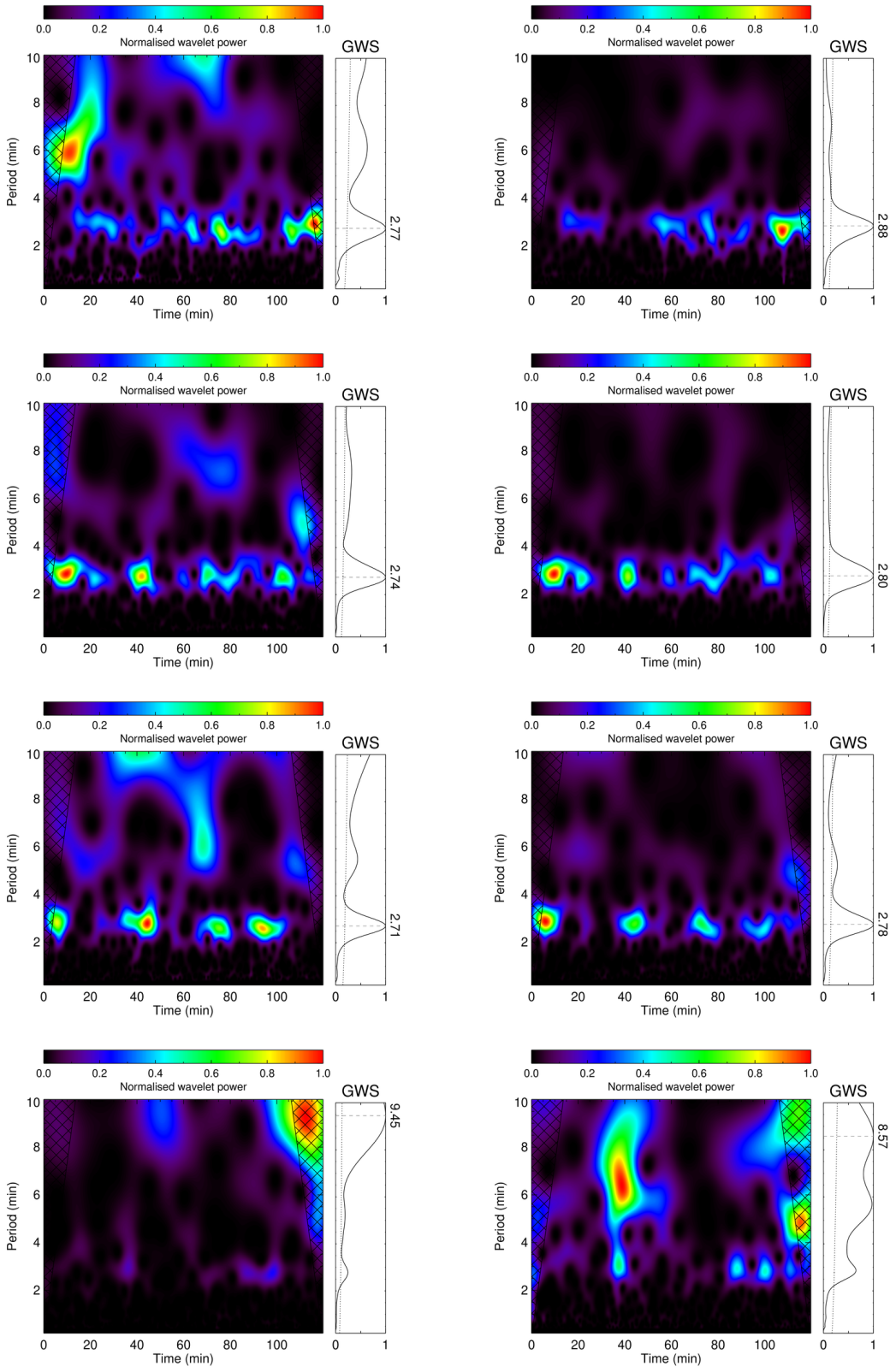

Figure 4.5: Wavelet plots of detrended light curves from Slit 4 at equidistant lengths along the slit (segments): 1 Mm [*Top row*], 6 Mm [*Second row*], 11 Mm [*Third row*], 16 Mm [*Bottom row*]. The left column comprises the 171 Å data, whilst the right column comprises 193 Å data in the same locations. The periods of the global wavelet spectrum's peaks are labelled.

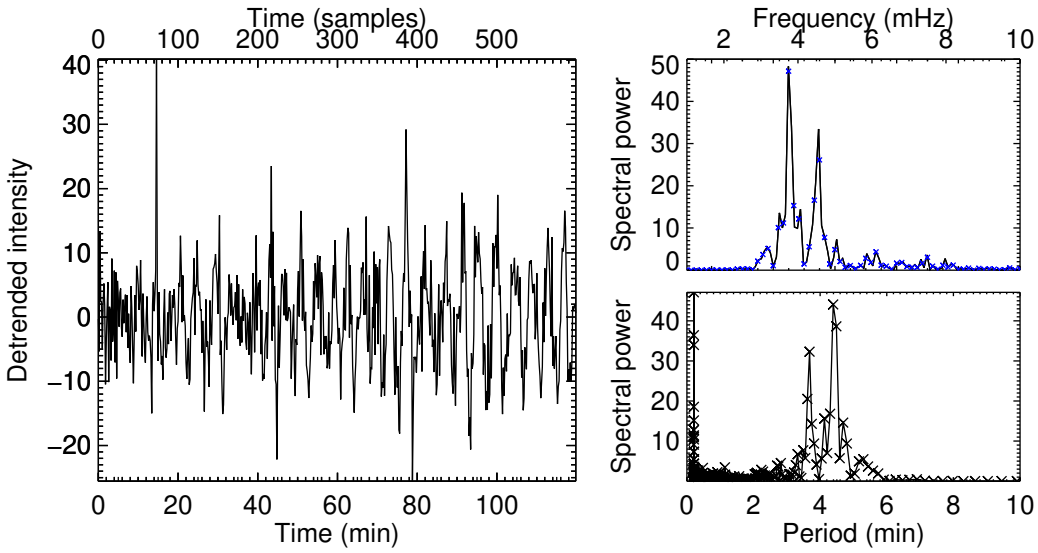

Figure 4.6: Spectral decomposition of a detrended intensity curve. [*Left*] The intensity curve after detrending for slit 4, section 3 in 193 Å. [*Right top*] Fourier power spectrum, showing several peaks principally at 3.7 mHz and 4.6 mHz. [*Right bottom*] Periodogram showing the same power spectrum.

combined with the subjective nature of the detrending (Auchère et al. 2016), makes the direct application of Fourier decomposition to find the periodicity in this data too variable to be used consistently.

An alternative way to measure the (instantaneous) period is to measure the distance between extrema in given oscillatory signals (for instance this was used in Nisticò et al. 2013). However measuring the extrema directly suffers from double peaks and sporadically low amplitudes, which are commonplace in real data (e.g. Fig. 4.4). Therefore in this work we devised a workflow which takes advantage of the large number of observation cycles detected in this event and the fact that they propagate, allowing the dependence on individual pixel trends to be minimised. For each slit segment, the one-dimensional signals at 1/4 and 3/4 along the segment length were auto-correlated and then cross-correlated to find the periodicity in common, which is the period of the propagating mode. An example of the resulting cross-correlation is seen in Figure 4.7; the resulting signal is far less noisy than individual detrended time series allowing a periodicity to be robustly measured. Histograms of the distance between extrema in the cross-correlation (positive lags only to avoid double counting) were calculated – taking advantage of the large number of intensity peaks within the two hour observing window whilst avoiding the difficulties introduced by the obvious amplitude modulation. This allows an average period to be estimated accurately with sub-frame resolution, which is useful for

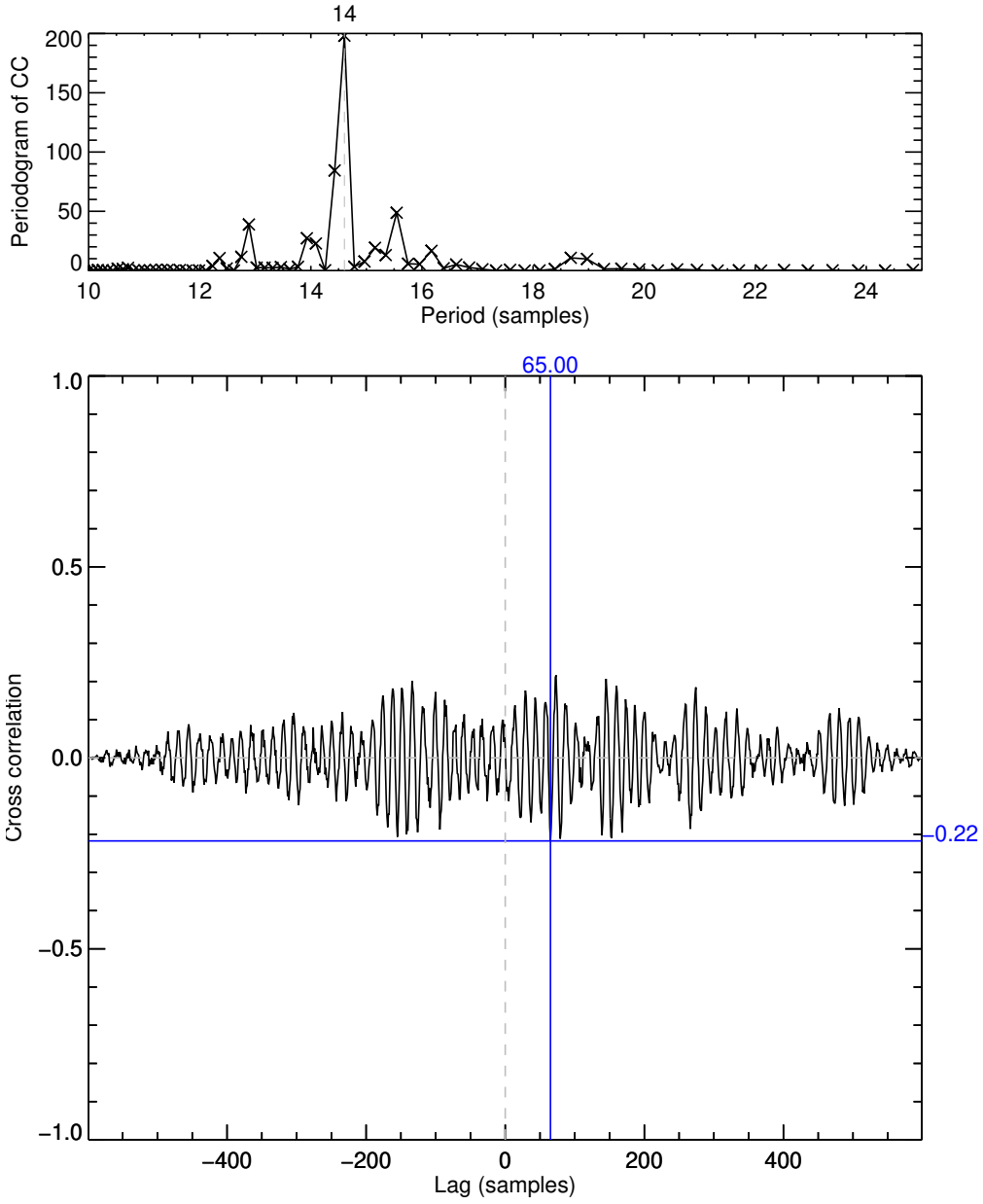

Figure 4.7: An example cross correlation, calculated between the intensity signals from two points along slit 1 some 15 pixels apart. [*Top*] The periodogram of the cross correlation showing a clear periodicity of around 3 minutes (lag of 15 samples). [*Bottom*] The cross correlation as a function of lag; the maximum (absolute) cross correlation value is found at a lag of 65 samples. There is significant amplitude modulation of the signal, and asymmetry about zero lag implies time evolution of the periodic disturbances.

resolving 3 minute oscillations with the 12 second cadence of AIA observations. This method relies on the period remaining stable between the two light curve positions, which was verified by the wavelet plots. This workflow is shown graphically in Figure 4.8. Overall this method for determining period was found to be more robust and reliable than the Fourier, wavelet or direct extrema methods.

4.2.3 Measuring instantaneous velocity

There have been many proposed techniques, direct and indirect, for measuring the phase speed from a propagating disturbance on EUV data. Several best-fitting to time-distance plot techniques have been proposed, generally relying on running difference images and detrending (Yuan and Nakariakov 2012). However in many cases the average from ten or so lines of best fit judged from a human observer is used, for example in De Moortel et al. (2002b); DeForest and Gurman (1998); Guo et al. (2015). The work-flow for determining the apparent phase speed of the wave used in this research is as follows: initially the user manually clicks along the line of maximum intensity for a single fringe. This is then fitted with a line of best fit and is repeated 5 times along a single fringe. The gradient of the averaged line is taken to be the apparent instantaneous velocity (phase speed) of the wave. This is compared to two automatically generated lines of best fit for quality control. An interval of 15 frames centred at the user line is taken for each spatial location, and within this interval the maximal pixel amplitude is located, and independently an estimate of the peak within the interval is made. This is repeated for each spatial location building up a series of points, whose lines of best fit are calculated and compared with the averaged line. These methods and their results can be visualised in Figure 4.9. The method using maxima is similar to that described in Abedini (2016), however using this method alone for this data was not robust enough to replace the user-picked lines. By quality checking the user picks, there is some mitigation of the subjectivity, although in future a method not relying on user clicks is preferred (testing underway). It should be noted that by fitting the fringe on a time-distance map to a straight line, an implicit assumption of constant apparent velocity is being made. At least one counter-example has been observed showing an accelerating apparent phase velocity (Prasad et al. 2017), although visual inspection of the data used here clearly shows that if there is any curvature to the ridges, the curvature must be minor. Nonetheless the velocity measurements will not account for possible curvature of the waveguide along the propagation path, and may explain at least some of the variation seen in the instantaneous velocity.

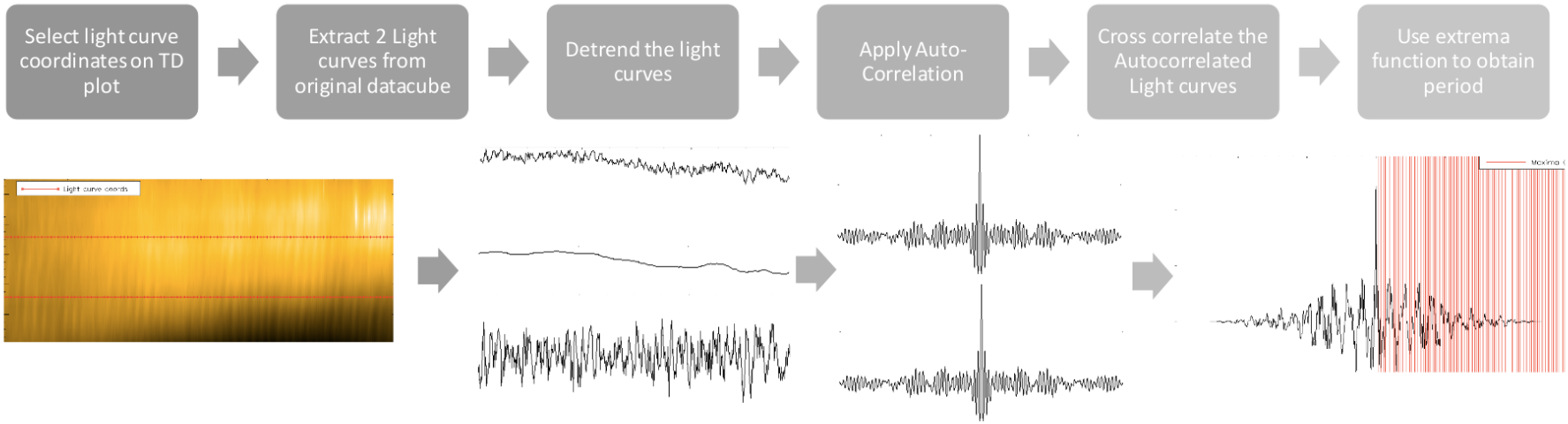

Figure 4.8: A description of the work-flow to obtain values for the period of the periodic intensity perturbations from time-distance data of a coronal fan.

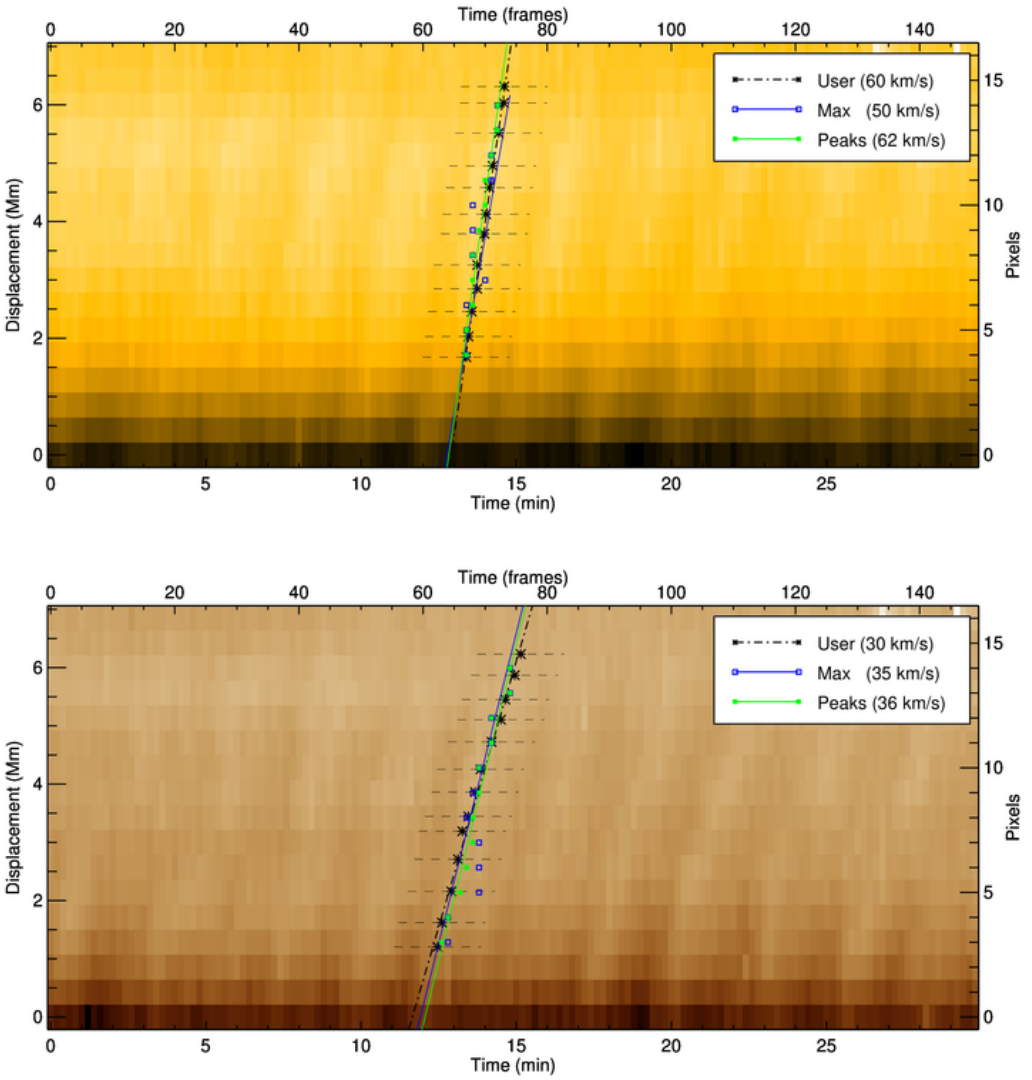

Figure 4.9: Instantaneous velocities calculated for slit 5 (zoomed). [Top] The estimated instantaneous velocities for a fringe in the 171 Å data. [Bottom] estimated instantaneous velocities for the same location seen in 193 Å . The manual clicks are seen in black, with the line of best fit by least squares overplotted with a dot-dashed black line. Blue squares show the maximum pixel value within the interval denoted by horizontal dashed line, and their line of best fit is overlaid in blue. Green dots show the estimated peak of the interval (for example peak of Gaussian) and their line of best fit is shown in green. This example shows clear evidence that the gradient is more steep in the 171 Å channel and hence results in a larger apparent velocity measurement.

4.2.4 Results

Figure 4.10 shows there is no clear variation between slits for either instantaneous period or instantaneous velocity, that is to say, there was no apparent dependence on the direction across the magnetic field, This result implies the driver and host plasma conditions for the oscillations are similar in all the coronal fan loops analysed in this study.

There is a relatively wide spread of instantaneous velocities measured, but all speeds are sub-Alfvénic and sub-sonic (expected sound speed ∼150 km/s) with ranges of 28–59 km/s and 21–42 km/s for 171 Å and 193 Å respectively. The error on instantaneous velocity can be large (up to 60%), and is likely to be affected by overlapping structures in the line of sight. The apparent phase speed will likely be much lower than the true phase speed because of an inclination angle $v_{obs} = v_{ph} \sin\theta$, where θ is the angle between the LoS and the local magnetic field (that is, the phase speed direction). For this data it is found there is no clear correlation between period and velocity, for data in either bandpass as shown in right column of Figure 4.10 as uncorrelated data clouds.

For both the data in 171 Å and 193 Å, the instantaneous period is stable along the propagation path and for the whole two hours, in line with other studies (De Moortel 2009; King et al. 2003). There is negligible difference in period measured between the two bandpasses, clearly shown in the top plot of Figure 4.11. Nor is there any consistent change in instantaneous velocity with height, indicating the inclination angle does not vary much and that the waves are not accelerating along the propagation path, in contrast to Prasad et al. (2017).

The amplitude of the intensity perturbation clearly reduces as the perturbation travels higher along the loop, until it has damped beyond detection, indicating at least one strong damping mechanism (e.g. thermal conduction) is acting upon the waves. This damping is clearly seen in Figure 4.2, and when scanning downwards in Figure 4.5, the short damping length is also apparent since after 16 Mm apparent distance the amplitude has decreased sufficiently that the three minute oscillation peak no longer dominates the global wavelet spectrum.

Clear amplitude modulation is seen in all signals, consistent with resonant filter theories which predict multiple closely space frequencies which subsequently beat (Prasad et al. 2015). Other examples of observed amplitude modulation in propagating slow modes include the Bayesian analysis conducted in Marsh et al. (2008), in which it was found that there is evidence to suggest the detection of the characteristic periods of the photospheric p-modes in oscillations observed in the solar transition region. Also amplitude modulation of three minute signals is seen in NoRH 17GHz data (Chorley et al. 2010; Reznikova et al. 2012; Sych et al. 2012).

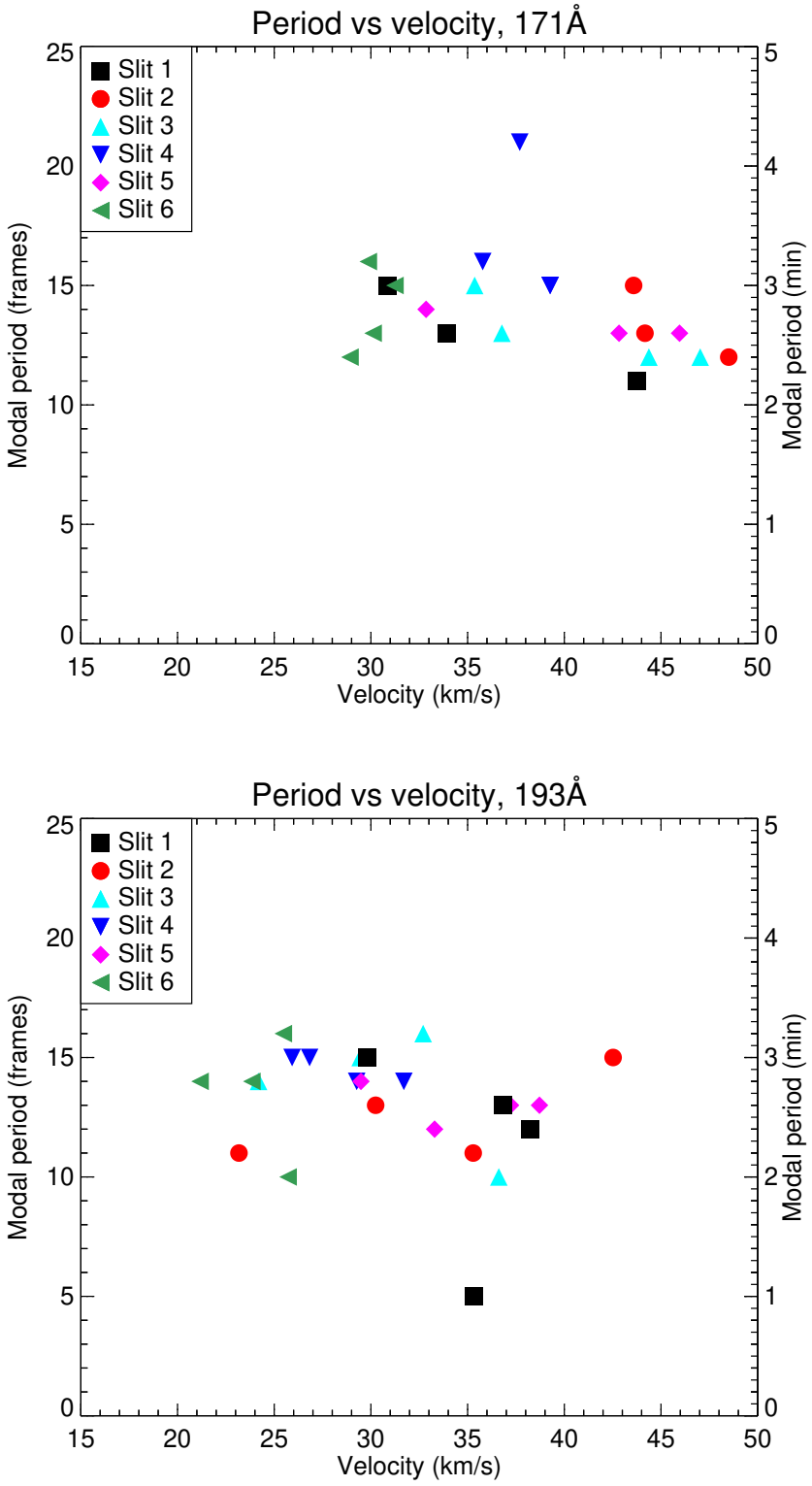

Figure 4.10: Instantaneous velocity against instantaneous period plotted for different slits in both 171 Å [*top*] and 193 Å data [*bottom*]. Each slit was partitioned into 4 equal segments, each of which had an instantaneous period and instantaneous velocity calculated. Thus there are four points for each slit – individual labels are not shown, since no trend in velocity or period against distance along slit was found.

Taking these conclusions altogether it is clear the propagating intensity perturbations are indeed propagating slow magnetoacoustic modes.

Curiously, a shift in the range of apparent velocity measurements is seen when comparing the simultaneous bandpasses of 171 Å and 193 Å, shown in Figure 4.10. The distribution of velocities observed in 171 Å are generally higher than the velocities measured in 193 Å. This is also apparent from the steepness of the ridges seen in the time-distance maps directly, for example in Figure 4.9.

4.2.5 Interpretation of results: inclination angle

In order to explain this discrepancy of velocity measured in 171 Å and 193 Å, consider that the sound speed varies with temperature. The sound speed may be estimated for each bandpass using Equation 4.5 by taking an approximation for the temperature as the peak in the AIA/SDO response function. For bandpasses 171 Å and 193 Å, the peak temperatures are 0.63 MK and 1.58 MK respectively (see Fig. 1.10 in Subsec. 4.2.1 for the AIA temperature response functions), from which the sound speeds may be estimated as 120 km/s and 190 km/s respectively. Taking the ratio of sound speeds obtained for each bandpass, assuming the waves are co-spatial then the angle between the line of sight and the wave ($\sin\theta$) can be effectively cancelled out.

$$\frac{C_{S[193]} = 151\sqrt{T_{193}}}{C_{S[171]} = 151\sqrt{T_{171}}} = \frac{190}{120} \approx 1.6. \tag{4.6}$$

This ratio of 1.6 represents an estimate for the expected increase in velocity of the waves seen in 193 Å over the velocity seen in 171 Å, along the same propagation path. This is making the assumption however that we observe a **single** temperature along the LoS for each bandpass range, which is known to not always to be the case (Lemen et al. 2012). Nonetheless it does indicate that one expects to see a faster instantaneous velocity in 193 Å than in 171 Å. Indeed the observations of a different set of propagating waves in Prasad et al. (2017, specifically Figs. 3 and 5) show that the estimated velocities seen in the 171 Å channel is $\sim 1.3\times$ faster than for those in the 131 Å channel. This is in accordance with the ratio expected from their peak bandpass temperatures, when taking the cooler (non-flaring) peak of the 131 Å at ≈ 0.5 MK.

In this study however, contrary to the expected, **the velocities observed in** 171 Å **are generally higher than the velocities measured in** 193 Å. Comparing the estimated peaks of the velocity distributions (40 ± 8 km/s for 171 Å, 31 ± 6 km/s for 193 Å) yields a measured ratio of approximately 0.78.

The discrepancy between the measured ratio and the expected value of 1.6 is most likely explained by a different inclination angle for the waves seen in the

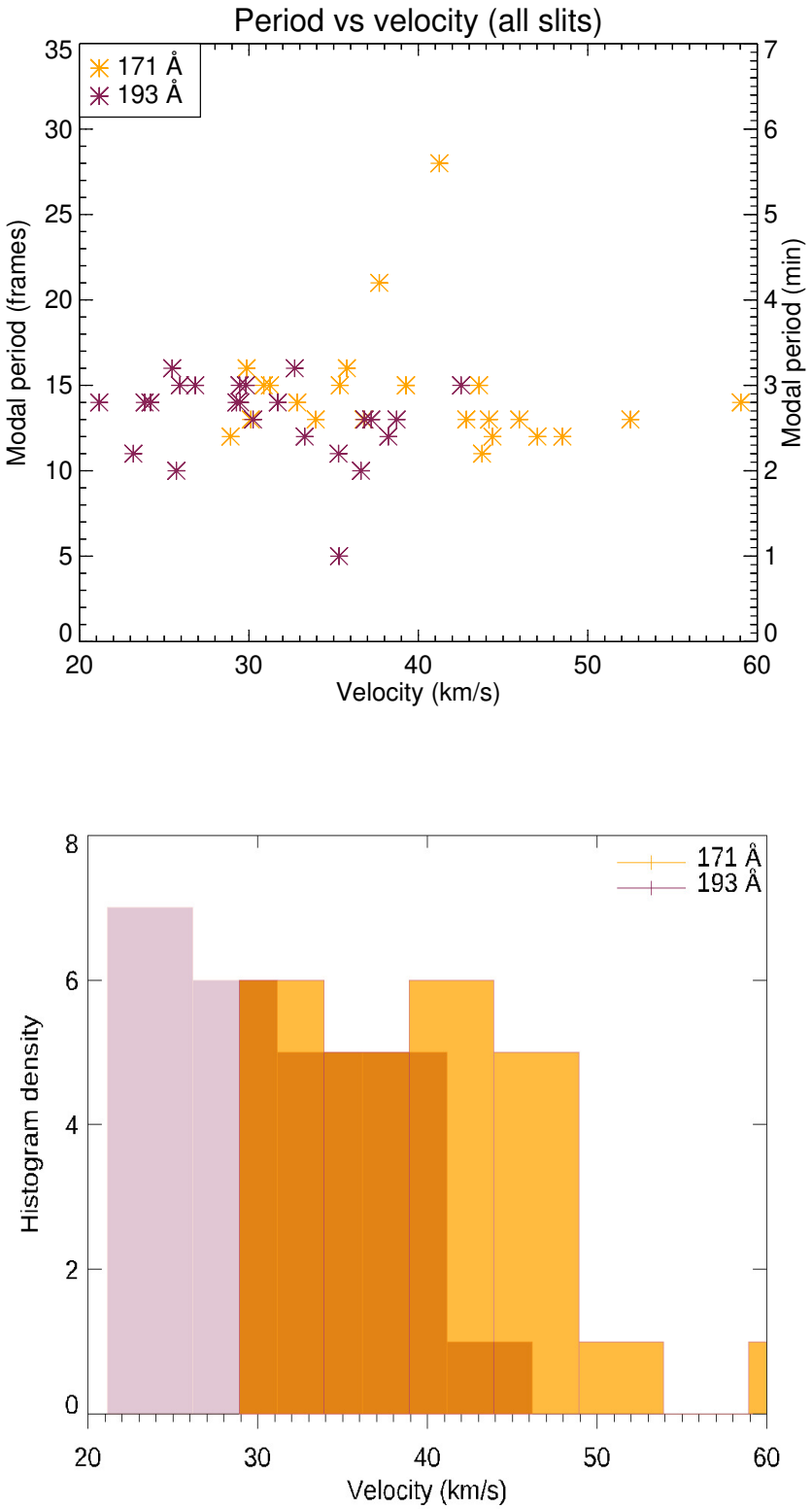

Figure 4.11: Comparison of the instantaneous velocities measured in 171 Å and 193 Å. [*Top*] A combined scatter plot of instantaneous period against instantaneous velocity for data from both bandpasses. [*Bottom*] The velocity data shown as histograms of modal period values from all six slit locations, in both 171 Å (orange) and 193 Å (pink). The darker orange corresponds to overlap.

two bandpasses, obscured by integration along the LoS. By taking the mean of the measured instantaneous velocity values in both bandpasses it is possible to obtain an average inclination angle to the LoS using the above estimates of C_S:

$$\begin{aligned} C_{S[171]} \approx \; & 120 \sin\theta_{171} \; \approx 40 \pm 8 \text{ km/s} \\ \implies & \theta_{171} \; \approx 19^\circ \pm 4^\circ, \end{aligned} \tag{4.7}$$

$$\begin{aligned} C_{S[193]} \approx \; & 190 \sin\theta_{193} \; \approx 31 \pm 6 \text{ km/s} \\ \implies & \theta_{193} \; \approx 9^\circ \pm 3^\circ. \end{aligned} \tag{4.8}$$

The difference in inclination angle required to explain the observed ratio of velocities between the 171 Å and 193 Å bandpasses is shown to be around 10°, with the waves seen propagating in 193 Å being 10° closer to the line of sight (approximately vertical to the sunspot). This geometry is depicted schematically in Figure 4.12. This difference in angle suggests that the observations of the slow waves may not be co-spatial and come from different locations along the LoS. This is taken to be evidence supporting the theory of loops being comprised of multiple strands with distinct temperatures.

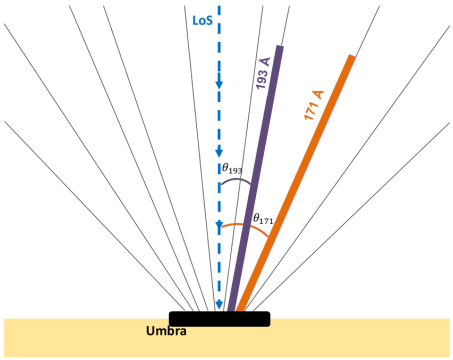

Figure 4.12: A schematic representing the interpretation of the difference in calculated angle between strand seen in bandpass 193 Å (pink) and 171 Å (orange). The LoS is represented by a blue dashed line. It is assumed that any curvature of the field lines may be ignored.

4.3 Conclusions

Almost monochromatic propagating intensity perturbations emanating from a sunspot into a symmetric coronal fan in active region AR12628 were analysed. Time-distance maps showed clear steady upwards slanting ridges with no obvious curvature, implying the perturbations had constant velocity and constant period over the two hours used in the analysis. Methods to robustly measure the instantaneous period and instantaneous velocity were developed, using detrending, auto-correlation, cross-correlation and large numbers of extrema to overcome the limitations imposed by large background trends. The instantaneous period and velocity were measured for six slits partitioned into four sections, and applied to data in both 171 Å and (co-spatially) in 193 Å. It was found that the period of the intensity perturbations

seen in both 171 Å and 193 Å was constant at 15 frames (to the nearest frame), which is exactly 3 minutes. This period did not drift over time or change over the propagation path. Amplitude modulation of the slow modes was observed, consistent with previous works and supporting the interpretation of the constructive interference between photospheric p-mode drivers (Centeno et al. 2006; Chorley et al. 2010; Marsh et al. 2008). No correlation was found between instantaneous period and instantaneous velocity. No consistent difference was found in either period or velocity between different slits, which were taken at different angles about the sunspot. The interpretation of the propagating intensity disturbances as propagating slow magnetacoustic modes was taken to be unambiguous.

The average apparent velocity ratio estimated at 193 Å to 171 Å is measured to be $\sim$0.78, which contradicts theoretical estimations of the velocity ratio being $\sim$1.6 if observations in both these bandpasses show a wave propagating along the same path. The theoretical ratio was calculated assuming the plasma radiating in the individual bandpasses has a temperature equal to the temperature of the peak of the bandpass response, and that the phase speed of the perturbations is the local sound speed. The first assumption is justified by the similar intensities seen for the two bandpasses, as would be expected for the plasma radiating at the temperature of peak response (see temperature response 'heights' in Fig. 1.10) – the (stable non-flaring) loop is unlikely to be so hot as to be radiating at the temperature of the secondary peak of the 193 Å channel at $\approx$ 10 MK. The second assumption of the waves being acoustic modes is made under the zero plasma-β approximation, which is reasonable for this part of the corona. It was concluded that the discrepancy in velocity ratio is most likely explained by a difference in the inclination angle along which the slow waves propagate in the different bandpasses. The difference in angle was estimated at 10°, neglecting any curvature of the propagation path, and neglecting any nonlinear effects which would affect the local phase speed. This provides evidence that the coronal fan loops are comprised of distinct multi-thermal strands below the resolution of AIA, probably with spatial scales of $\sim$500 km (see results by Williams et al. 2020). Our results are consistent with the conclusions presented in Prasad et al. (2017), in which similar analysis between 131 Å data and 171 Å data was conducted in conjunction with a nonlinear force-free magnetic field extrapolation to conclude the multithermal structuring of the target loop. The results presented here supporting multi-stranded, multi-thermal loops joins a growing body of evidence (Gupta et al. 2015; Mulu-Moore et al. 2011; Nisticò et al. 2014; Schmelz and Winebarger 2015; Williams et al. 2020).

Chapter 5

Dispersion of slow magnetoacoustic waves by thermal equilibrium misbalance

In this chapter the dispersion effects on slow magnetoacoustic waves by the (wave-induced) misbalance between plasma heating and cooling processes is discussed. The physical effects of this misbalance are extremely rich and varied, so in the interest of clarity this thesis will restrict attention to the linear regime. Therefore the results described here are widely applicable when a compressive plasma has its thermal equilibrium perturbed by a small amplitude perturbation. Its applicability may also extend to finite-amplitude, linearly or elliptically polarised Alfvén waves whose nonlinear self-interaction lead to a density perturbation via the ponderomotive force.

The motivation for this work, and an overview of the previous works on the effect of thermal misbalance is given in Section 5.1. Using the thin flux tube approximation, the dispersion relation in the presence of a finite plasma-β is derived, expressions for its characteristic timescales are found, and the dispersion relation in the limits of weak and strong non-adiabaticity are explored in Section 5.2. New results on how observations of slow modes may constrain on the coronal heating function using instability criteria are given in Section 5.3. Finally a summary and the outlook for the research of dispersion by thermal misbalance on slow modes is given in Section 5.4.

5.1 Introduction

5.1.1 Motivation

The question of how the solar corona retains kinetic temperatures over one million Kelvin despite continuous energy losses is one of the most important open problems in astrophysics (for a review see De Moortel and Browning 2015). The radiative loss rate for optically thin plasmas depends on temperature, ionisation fraction and elemental abundances, whilst the magnitude of the downward conductive flux depends upon the local temperature gradient in the transition region and the thermal conduction coefficient κ, of which none of these quantities is reliably known. Both the thermal conduction and radiative loss function also have a strong dependence on density. Therefore the combined effect of plasma heating and cooling will likely have a dependence on the equilibrium plasma parameters, making the continued existence of the corona in spite of continual perturbations to the thermal and mechanical equilibrium all-the-more remarkable. These perturbations come from many dynamic phenomena which vary in scale and frequency, including ubiquitous small-scale waves of various frequency, wavelength and orientation through to more infrequent but globally consequential explosive restructuring events, such as flares and coronal mass ejections. It must be concluded that the unknown coronal heating mechanism may depend on temperature, density and magnetic field, and the corona is a thermally active medium, which is to say there must be an additional natural mechanism for the exchange of energy between the plasma and its internal motions such as waves.

A compressive wave (especially the slow magnetoacoustic mode in low-β plasma) modifies the equilibrium quantities of density, temperature, and magnetic field in different ways, and since these are responsible for the internal energy losses and gains, this may cause a local thermal equilibrium misbalance. This leads to the transfer of energy between the wave and the plasma which we refer to as a *heating/cooling misbalance*. This misbalance, like any dissipative process, necessarily has some characteristic timescale(s) associated with it. Thus any imbalance between the heating and cooling rates will introduce a timescale into the system and hence dispersion to the slow magnetoacoustic wave. This dispersion is distinct from the effect from the finite radius of the waveguide (as described in Edwin and Roberts 1983). Due to the prevalence of slow waves in the solar atmosphere as previously described in Section. 4.1, it is important to understand this dispersion in order to perform seismology with them.

It has been shown in previous works that slow magnetoacoustic waves are sensitive to non-adiabatic effects, with particular focus given to the effect of thermal conduction, and compressive viscosity (see Section. 4.1 for references). Such studies

were conducted in light of observations of slow-mode waves damping exceptionally rapidly, as seen in hot coronal loops (Nakariakov et al. 2019; Ofman and Wang 2002; Wang 2011), warm loops (De Moortel 2009), open plasma structures in coronal holes (Banerjee and Krishna Prasad 2016), and also in prominences (Arregui et al. 2018).

Several observational studies have found that compressive viscosity and thermal conduction are insufficient to explain their results. For example observations of a flaring loop which led to a superposition of several longitudinal waves showed a minor phase shift ($\sim 12°$) between the density and temperature perturbations (Wang et al. 2015). This is in conflict with theoretically derived value of $\sim 35°$, predicted for when thermal conduction dominates in the energy equation (Owen et al. 2009). Serious discrepancies between the measured phase shifts and those predicted from theory were also found in the analysis of 20 additional examples studied in the same way by Prasad et al. (2018). Additionally, in all these cases, a growth in the effective polytropic index with temperature (measured following the method discussed in Van Doorsselaere et al. 2011) remains unexplained. The mystery deepens because of a follow up study, which reached the conclusion of no decrease in damping length with temperature, as would be expected by the stronger thermal conduction (Prasad et al. 2019). This is supported by previous results, in which a wide spread of different dependencies of the damping time upon wave period were observed between warm coronal loops and cooler plumes (figure 6 in Prasad et al. 2014), SUMER oscillations (figure 6 in Wang 2011), and between propagating waves observed at different heights in the corona (Gupta 2014). In the limit of weak thermal conduction ($d\omega << 1$, recall Eq. 4.3), the theory predicts a slope of 2 in the log–log plot of damping length versus the wave period, whilst in the strong limit the damping length from thermal conduction is independent of wave period (see section 4.1 and table 1 in Prasad et al. 2014). When plotting the full solution (numerically) to the linear dispersion relation with thermal conduction for a few periods between 3–13 minutes and typical coronal conditions (not adhering to either the weak nor the strong limit of thermal conduction), a positive slope of 1.2 was found (Mandal et al. 2016). It is possible that thermal conduction is acting with different strengths in all these observations, and of course thermal conduction is dependent on the spatial scales involved (wavelength-dependent), which may explain the spread of gradients from zero to two. However this would not explain the negative slopes of wave period against damping length seen in Prasad et al. (2014) for plumes, nor does it adequately explain the frequency dependence of waves at low heights (0–10 Mm above the limb) in Gupta (2014).

There is also evidence of suppressed thermal conduction in the solar flare loop analysed in Wang et al. (2015). **The wide spread of dependencies of wave**

period against damping length may be explained by the presence of other damping mechanisms. Some authors have attempted to attribute these effects to enhanced compressive viscosity (e.g. Wang and Ofman 2019; Wang et al. 2018), yet the physical understanding why this is the case is lacking. Gravitational stratification may enhance compressive viscosity, however simulations disagree on the importance of this effect and nonlinearity has to be included to agree with observations (Sigalotti et al. 2007). If the only damping mechanisms included in the simulation are thermal conduction and compressive viscosity, and the thermal conductivity is incompatible with some observations, it is unsurprising that the compressive viscosity becomes the supposed dominant damping factor. The real damping effect may be from physics not included in the simulation. Thus understanding of additional non-adiabatic effects, even in the linear case such as the effect of misbalance expounded here, is sorely needed by the community.

5.1.2 Review of the literature

It is well known that thermal equilibrium should be taken into account during the consideration of MHD wave dynamics together with the mechanical equilibrium, and thus the effect of imbalance between cooling and heating has been studied before. In a thermally active plasma there can be at least two types of thermal instability: one by the acoustic (or magneto-acoustic) mode and one by the entropy mode. Studies in the area of thermal imbalance have therefore encompass both investigations of the occurrence and growth rates of these thermal instabilities, as well as the effect of non-adiabaticity upon acoustic and magneto-acoustic waves. A detailed analysis of perturbations to an infinite homogeneous plasma was conducted in Field (1965), in which it was explained how a thermal instability can originate from exchange of energy with the medium via radiative cooling effects (denoted by the function $\mathcal{L}$) plus heating, and a fifth order dispersion relation is derived. The presence of non-adiabatic effects couples the Alfvén modes into the fast and slow solutions, and endows the thermal mode with a purely imaginary term. As explained back in Subsection 1.2.2, the remaining roots of this dispersion relation are two pairs of complex conjugate roots, corresponding to the forwards- and backwards- propagating fast and slow magnetoacoustic wave modes, all of them modified by non-adiabatic effects. Condensations of plasma from the thermal instability was also explored in Dahlburg and Mariska (1988), in which the effect under different coronal heating models proposed by Rosner et al. (1978) was considered. These heating models can be parameterised using power law indices as $\mathcal{H}(\rho, T) \propto \rho^a T^b$ – the reader is warned that different authors use different definitions for $\mathcal{H}$, for example as a heating rate per unit volume or per unit mass. Such a parameterisation might not capture potentially

important physical effects, for example it may be that the heating is a function of wavenumber $\mathcal{H} = \mathcal{H}(k)$, or the power indices vary such as $b = b(\rho)$. Yet it is agreed that because of the lack of knowledge about $\mathcal{H}$, a power law parameterisation is the logical place to start; the convention used in this thesis is that $\mathcal{H}(\rho, T) \propto \rho^a T^b B^c$, and the combined heating cooling function $Q = \mathcal{L} - \mathcal{H}$ has units of [W kg^{-1}].

Jumping ahead a few years, Porter et al. (1994) also derive a dispersion relation for a homogeneous plasma with viscous dissipation and thermal conduction. The authors concluded that for some slow mode periods there is sufficient dissipation to heat corona, and indeed it is speculated that the localised heating from slow mode dissipation at reconnection sites may be the origin of coronal loops. They find that damping of slow modes depends weakly, if at all, upon magnetic field strength, but strongly upon temperature; in their analytical work, the adiabatic assumption breaks down for sufficiently large wavenumber. Other authors disagree about the role of slow modes in heating (for example see De Moortel 2009; De Moortel and Browning 2015) and this remains an open question. Thus a robust understanding of the interaction between waves and the thermal equilibrium is important.

Around the same time, the explicit analytical conditions for slow wave dispersion from non-adiabatic effects (thermal conduction, heat/loss function) was considered in Ibanez S. and Escalona T. (1993). Five different heating scenarios were considered, again from Rosner et al. (1978), hinting at the potential of using slow mode observations for constraining the coronal heating model. The five heating models from Rosner et al. (1978) and Ibanez S. and Escalona T. (1993) are posited as: Ohmic heating ($a = 0$, $b = 1$), constant heating per unit volume ($a = -1$, $b = 0$) and mass ($a = 0$, $b = 0$), heating by Alfvén waves via mode conversion ($a = 1/6$, $b = 7/6$) and anomalous conduction damping ($a = -0.5$, $b = -0.5$). Note the difference in the units of the heating function chosen in this thesis [W kg^{-1}] from theirs [W m^{-3}], leading to a difference in the density index a by 1.

A similar study in the context of prominences found that the dispersive effects from heating and cooling misbalance can be as important as thermal conduction (Carbonell et al. 2006). The effect of dispersion from misbalance specifically is to either damp the wave in addition to the damping from thermal conduction (which always attenuates the wave), or else act to counteract this damping. The amplification effect from misbalance is able to become so great in some cases it overpowers the damping from thermal conduction and leads to so-called "over-stability". The weakly non-adiabatic effects on slow waves were discussed in Nakariakov et al. (2000), in joint consideration with weakly nonlinear effects and shock formation in particular. It was found shocks are more quickly formed in the linearly unstable case, as opposed to the adiabatic case. A focused numerical study of non-adiabatic effects to general

MHD perturbations in a solar prominence context was performed in Carbonell et al. (2006). By considering the five heating models already discussed, in conjunction with thermal conduction and radiative losses, it was concluded that the damping from thermal misbalance can indeed have a greater effect than thermal conduction for some situations, and that the relative importance of each mechanism varies with density, temperature, magnetic field and heating model. The work presented here follows the same idea, with the inclusion of finite-β effects and an attempt at decoding the governing equations and dependencies, without resorting to numerical solutions.

Note that in **several of the works above, the coronal heating function is considered to not be perturbed by the slow wave, whilst the cooling mechanism is – this thesis assumed both the heating and cooling are perturbed.** Another key result found in Carbonell et al. (2006) was that whilst the fast mode is affected by non-adiabatic effects in a similar way to the slow mode (at least in terms of damping), it is far less affected, by an order of magnitude if comparing damping lengths. This is corroborated by the similar, expanded study into instability growth rates in Claes and Keppens (2019).

Another important investigation of wave-induced thermal misbalance was conducted in Kumar et al. (2016), in which it was demonstrated that the behaviour of slow magnetoacoustic oscillations (in coronal loops) is very sensitive to the exact peculiarities of the combined cooling and heating function. Equivalently and as is shown below, it is the derivatives of the heating/cooling function which control the effects. This is important because several different versions of radiative loss function exist, such as those derived with the ATOMIC code (Colgan et al. 2008), and there is disagreement between different radiative loss models on the precise number and locations of local extrema – though they all follow the same general trends, their derivatives and second derivatives are varied. This may be clearly seen in Figure 5.1: at some temperatures (indicated by blue shading), the different calculated loss functions have different derivatives. Due to the complexities and ambiguities involved in calculating these loss functions, particularly the incomplete knowledge of the effects of the atomic physics associated with the presence of minor species there is not a preferred version of the function. Studies have also compared different radiative loss functions in the context of thermal instability, finding that the choice can significantly impact the threshold of stability (Soler et al. 2012). Note that in the examples in this work, the optically thin radiation function is synthesised from the CHIANTI atomic database v. 9.0.1 (Dere et al. 1997, 2019).

Some other honourable mentions of publications that the reader may be interested in consulting, but do not have direct bearing on this work, are Bahari and

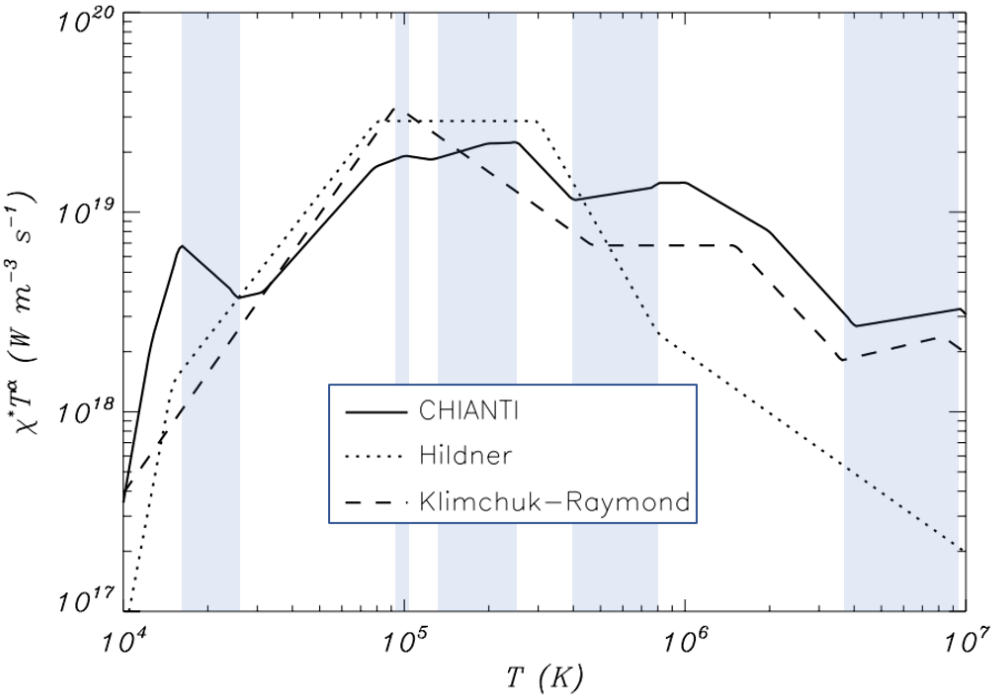

Figure 5.1: Three different radiative loss functions (loss rate per unit volume) as a function of temperature. The ranges of temperature for which at least one of the three radiative loss functions has the opposite gradient to another is shaded light blue. Adapted from Figure 1, Soler et al. (2012).

Shahhosaini (2018) who use a WKB method to consider non-adiabatic effects though within an approximation of only slow cooling, and Perelomova (2018) focusing on the mathematics of thermal misbalance and additional nonlinearity in a plasma. Also Sigalotti et al. (2007) (following from Mendoza-Briceño and Luna-Cardozo 2006) simulate gravitationally stratified hot loops to probe non-adiabatic effects, particularly compressive viscosity and thermal conduction.

The following papers are of particular pertinence to this work. Finite-β and weakly nonlinear effects on long-wavelength slow magnetoacoustic waves in the presence of local thermal equilibrium misbalance were investigated in Nakariakov et al. (2017), in which an evolutionary equation of the Burgers–Malthus type was derived. It was shown that the cooling/heating misbalance affects the wave rather strongly. Much of the same formalism in Nakariakov et al. (2017) is the same as is used for this thesis, however we also consider beyond the limit of weak non-adiabaticity. The question of thermal misbalance and its characteristic timescales was considered in Zavershinskii et al. (2019), examining for example the dispersal of a broadband pulse into a slow magnetoacoustic oscillatory wave train, with an imparted period. Since

thermal conduction only acts to damp, its dispersive effects cannot manifest over long time, potentially making the observations of slow wave trains a clearer route for seismology utilising the effect of imbalance between heating and cooling. In a similar quest for seismological application, Kolotkov et al. (2019) began to connect the observable damping periods of slow magnetoacoustic waves with constraints on the coronal heating function. In both of these papers, two characteristic timescales of the thermal imbalance are found; $\tau_1 = \gamma C_{\mathrm{V}} / \left[Q_T - (\rho_0/T_0)Q_\rho\right]$ and $\tau_2 = C_{\mathrm{V}}/Q_T$ with Q_T, Q_ρ denoting the partial derivatives of the combined heating cooling function, and C_V being the specific heat capacity at constant volume. This work loosely follows both of these publications, a key difference being that these papers use the assumption of plane acoustic waves and hence the effect of the magnetic field can not be ascertained. The effects of obliquity (thin flux tube), resistivity, conduction, and viscosity upon slow magnetoacoustic waves were discussed in Afanasyev and Nakariakov (2015), who concluded that tube waves are satisfactorily described as plane acoustic waves in low-β regime. However the effects of wave-induced thermal misbalance were not included.

This chapter aims to bring together the understanding that may be derived from the characteristic timescales of the thermal misbalance, accounting for perturbations to both the heating and cooling functions in a linear regime, whilst incorporating a finite plasma-β with an eye to the future application of seismology.

5.2 Dispersion by thermal misbalance in the presence of a magnetic field

5.2.1 Derivation of dispersion relation and characteristic timescales

In this work we use the first order thin flux tube approximation, which formally corresponds to the first order of the Taylor expansion of the MHD variables with respect to the radial coordinate, derived by Roberts and Webb (1978) and Zhugzhda (1996). The governing equations are the same as for Nakariakov et al. (2017), neglecting the viscous dissipation in the momentum equation (5.2) and slightly adjusting the definition of the thermal heating/cooling function Q to have the units

of W kg^{-1} (matching Field 1965):

$$\frac{dp}{dt} - \frac{\gamma p}{\rho}\frac{d\rho}{dt} = (\gamma - 1)\left(\kappa_{\parallel}\frac{\partial^2 T}{\partial z^2} - \rho Q(\rho, T, B)\right), \tag{5.1}$$

$$\rho\frac{du}{dt} + \frac{\partial p}{\partial z} = 0, \tag{5.2}$$

$$p + \frac{B^2}{8\pi} = p_{\text{total}}^{\text{ext}}, \tag{5.3}$$

$$\frac{\partial B}{\partial t} + u\frac{\partial B}{\partial z} + 2Bv_r = 0 \tag{5.4}$$

$$\frac{\partial \rho}{\partial t} + 2\rho v_r + \frac{\partial}{\partial z}(\rho u) = 0, \tag{5.5}$$

$$p = \frac{k_{\text{B}}}{m}\rho T \tag{5.6}$$

As usual, p is the plasma pressure, ρ is the plasma density, T is the temperature, k_{B} is the Boltzmann constant, m is the mean particle mass (see Table. 4.1), and γ is the adiabatic index. Also u is the flow speed along the tube (i.e. in z direction), B is the component of magnetic field strength along the tube, $p_{\text{total}}^{\text{ext}}$ is the total external pressure and v_r is the radial derivative of the radial component of plasma velocity. All of these quantities are measured at the axis of the (infinitesimally thin) flux tube. The right hand side of the energy equation (5.1) represent thermodynamic processes ongoing inside the plasma. The first term is the (field-aligned) thermal conduction, for which we use the standard estimation of coefficient $\kappa_{\parallel} \approx 10^{-11}T^{5/2}$ Wm^{-1}K^{-1}. The second term is the combination of some unspecified heating $\mathcal{H}(\rho, T, B)$ and optically thin radiative cooling $\mathcal{L}(\rho, T)$, combined in the net heat/loss function $Q(\rho, T, B) = \mathcal{L} - \mathcal{H}$. Thus, in addition to the perturbation of the mechanical equilibrium provided by the force balance, in this work we consider a wave-induced perturbation of the thermal equilibrium of the corona, i.e. allow both the heating and cooling processes to be perturbed by the wave.

Let us consider linear perturbations of a mechanical equilibrium, characterised by the constant quantities denoted p_0, ρ_0, B_0, T_0, and $p_{\text{total}}^{\text{ext}}$, and without steady flows. In addition we consider the isothermal equilibrium $Q_0 = 0$, motivated by the continued existence of the corona. The parallel thermal conduction does not contribute to this equilibrium because the plasma temperature is uniform. More general equilibria could be taken into account, for example including loop footpoints into a chromosphere. Let the perturbations of the equilibrium quantities be small,

$$p = p_0 + p_1,\ \rho = \rho_0 + \rho_1,\ T = T_0 + T_1,$$
$$B = B_0 + B_1,\ v_r = v_1,\ u = u_1,$$

where the subscript 1 denotes small but finite perturbations. In the following, exceptions are made for v_r, u since these are small quantities about zero anyway and so we leave their subscripts alone. We substitute these quantities into the Equations. (5.1) - (5.6) and keep only the linear terms of the small quantities to find:

$$\frac{\partial}{\partial t}p_1 - C_{\rm S}^2\frac{\partial}{\partial t}\rho_1 = (\gamma-1)\left(\kappa_{\parallel}\frac{\partial^2}{\partial z^2}T_1 - \rho_0\left[Q_\rho\rho_1 + Q_T T_1 + Q_B B_1\right]\right), \tag{5.7}$$

$$\rho_0\frac{\partial}{\partial t}u + \frac{\partial}{\partial z}p_1 = 0, \tag{5.8}$$

$$p_1 + \frac{B_0 B_1}{4\pi} = 0, \tag{5.9}$$

$$\frac{\partial}{\partial t}B_1 + 2B_0 v_r = 0, \tag{5.10}$$

$$\frac{\partial}{\partial t}\rho_1 + 2\rho_0 v_r + \rho_0\frac{\partial}{\partial z}u = 0, \tag{5.11}$$

$$p_1 - \frac{k_{\rm B}}{m}\left(\rho_0 T_1 + T_0\rho_1\right) = 0. \tag{5.12}$$

The parameter $C_{\rm S}^2 = \gamma p_0/\rho_0$ is the sound speed at equilibrium, and Q_T, Q_ρ, Q_B are the partial derivatives of the combined heating/cooling function Q ($Q_x = \partial Q/\partial x$), evaluated at the equilibrium. By using these equations, several assumptions have been made which are worth mentioning. Firstly, since any change in the pressure external to the flux tube is neglected, we concentrate on waves propagating inside the flux tube taking that the slow waves are always in the trapped regime. Secondly, the obliqueness of the wavefronts are accounted for through the taking into account of v_r – this is valid when if the wavelength of the perturbations (parallel to the field) is much longer than the transverse spatial scale, determined by the width of the waveguiding plasma non-uniformity. This is the applicability condition of the thin flux tube approximation, and is a key difference to the plane acoustic wave case used elsewhere. Finally it should be noted that, for all non-adiabatic processes (let us denote with i) in general the assumption $\gamma = C_P/C_V$ is only valid when $\omega \gg \tau_i$ i.e. when the wave is of sufficiently high frequency that it is practically adiabatic (for example see the discussion in Van Doorsselaere et al. 2011). In general non-adiabatic scenarios, the ratio of specific heats can vary in the presence of heating/cooling imbalance. However in the limit of weak non-adiabaticity – that is to say if the right hand side of the perturbed energy equation (5.7) is small – we do not include variations in γ, since they are a higher order effect.

Uniformity in the t direction (no flows) and uniformity in the z direction allow Fourier transforms to be taken, by making the ansatz of plane waves, that is to say we assume a harmonic dependence upon the time and spatial coordinates for all perturbed variables $\propto \exp\left(-i\omega t + ikz\right)$ where ω is the frequency and k is the

parallel wavenumber. Thus we may take $\frac{\partial}{\partial t} \to -i\omega$, and $\frac{\partial}{\partial z} \to ik$.

Letting $\vec{b} = [\rho_1, T_1, p_1, u, v_r, B_1]^{\mathrm{T}}$, we thus form the matrix equation $\mathrm{A}\vec{b} = \vec{0}$ and setting the determinant $||\mathrm{A}||$ to zero, we find

$$\begin{Vmatrix} iC_{\mathrm{S}}^2\omega + \rho_0(\gamma-1)Q_\rho & (\gamma-1)(\kappa_\parallel k^2 + \rho_0 Q_T) & -i\omega & 0 & 0 & \rho_0(\gamma-1)Q_B \\ 0 & 0 & k & -\rho_0\omega & 0 & 0 \\ 0 & 0 & 1 & 0 & 0 & B_0/(4\pi) \\ 0 & 0 & 0 & 0 & 2B_0 & -i\omega \\ -i\omega & 0 & 0 & i\rho_0 k & 2\rho_0 & 0 \\ -k_{\mathrm{B}}T_0/m & -k_{\mathrm{B}}\rho_0/m & 1 & 0 & 0 & 0 \end{Vmatrix} = 0. \tag{5.13}$$

This forms an equation that is cubic in ω yet quartic in k, that is to say asymmetric with respect to space and time. In order to simplify this form of the dispersion relation, we use the expressions for Alfvén speed C_{A}, specific heat C_V, the plasma-β and tube speed C_{T}:

$$C_{\mathrm{A}}^2 = \frac{B_0^2}{4\pi\rho_0}, \qquad (\gamma-1)\frac{m}{k_{\mathrm{B}}} = \frac{1}{C_V},$$
$$\beta = \frac{2}{\gamma}\frac{C_{\mathrm{S}}^2}{C_{\mathrm{A}}^2}, \qquad \frac{1}{\gamma}\frac{1}{C_V} = (\gamma-1)\frac{T_0}{C_{\mathrm{S}}^2} = \frac{1}{C_P},$$
$$C_{\mathrm{T}}^{-2} = C_{\mathrm{S}}^{-2} + C_{\mathrm{A}}^{-2} \quad \Longrightarrow \quad \frac{C_{\mathrm{T}}^2}{C_{\mathrm{S}}^2} = \frac{B_0^2}{4\pi\rho_0 C_{\mathrm{S}}^2 + B_0^2} = \left(1 + \gamma\frac{\beta}{2}\right)^{-1} = \frac{2}{2+\gamma\beta}$$

From using these the dispersion relation can succinctly be expressed as:

$$\omega^3 + i\frac{C_{\mathrm{T}}^2}{C_{\mathrm{S}}^2}\left\{\frac{Q_T}{C_V} + \frac{\kappa_\parallel}{\rho_0 C_V}k^2 + \frac{(\gamma-1)}{C_{\mathrm{A}}^2}\left[T_0 Q_T - B_0 Q_B - \rho_0 Q_\rho + \frac{T_0}{\rho_0}\kappa_\parallel k^2\right]\right\}\omega^2$$
$$- C_{\mathrm{T}}^2 k^2\omega - i(\gamma-1)\frac{C_{\mathrm{T}}^2}{C_{\mathrm{S}}^2}\left(T_0 Q_T - \rho_0 Q_\rho + \frac{T_0}{\rho_0}\kappa_\parallel k^2\right)k^2 = 0. \tag{5.14}$$

This equation describes slow waves and an entropy mode, made into a thermal mode by the non-adiabatic effects. The tube speed appears in the ω term of the dispersion, thus in the limit $Im(\omega) \to 0$ the equation reduces to the wave equation with C_{T}^2 as the speed as expected. This expression also agrees exactly with the infinite magnetic field case (Kolotkov et al. 2019, Eq. 7) in the limit $B \to \infty$. Regarding the thermal conduction terms, we see the first term with $\kappa_\parallel$ in the ω^2 coefficient is the same as Kolotkov et al. (2019), but modified by the ratio of tube to sound speed squared.

This implies there is a finite-β modification to the effect by thermal conduction on the waves, which is qualitatively consistent with the result in Afanasyev and Nakariakov (2015).

It is convenient to re-express the thermal misbalance terms using characteristic timescales, fully determined by the equilibrium parameters and partial derivatives Q_ρ, Q_B, Q_T. In this work we choose to express everything in terms of the variables ρ, T, B and not p, since these can be "directly" observed. In the case with infinite magnetic field, the characteristic timescales were written in terms of $Q_{T[p]}$ and $Q_{T[\rho]} = Q_T$, where $Q_{T[p]}$ means the partial derivative taken with respect to temperature assuming constant pressure (Zavershinskii et al. 2019). The introduction of a finite magnetic field means there is a separate magnetic pressure term $B^2/8\pi$, accounted for through the coupling via p of the radial pressure balance and the equation of state. Thus in this work we consider separately the derivative with respect to constant gas pressure $Q_{T[\text{gas } p]}$, and with respect to constant magnetic pressure $Q_{T[\text{mag } p]}$. To write the additional terms in the derivatives of Q by the magnetic field, the relevant equations are the ideal gas law (Eq. 5.12) and the radial pressure balance (Eq. 5.9). Using these we find:

$$\left.\begin{aligned} \frac{\partial \rho}{\partial T} &= -\frac{m}{k_\mathrm{B}}\frac{p_0}{T_0^2} = -\frac{\rho_0}{T_0}, \\ \frac{\partial p}{\partial T} &= \frac{k_\mathrm{B}}{m}\rho_0, \\ \frac{\partial B}{\partial T} &= -\frac{4\pi}{B_0}\frac{\partial p}{\partial T} = -\frac{\beta}{2}\frac{B_0}{T_0} \end{aligned}\right\} \Longrightarrow \begin{aligned} Q_{T[\text{gas } p]} &= Q_T - \frac{\rho_0}{T_0}Q_\rho \\ Q_{T[\text{mag } p]} &= Q_T - \frac{\beta}{2}\frac{B_0}{T_0}Q_B. \end{aligned}$$

Using these definitions and gathering terms in the dispersion relation we can define two characteristic timescales with units of seconds [s],

$$\tau_1 = \frac{C_P}{Q_{T[\text{gas } p]}} = \frac{\gamma C_V}{Q_{T[\text{gas } p]}}, \qquad \tau_2 = \frac{C_V}{Q_{T[\text{mag } p]}}. \tag{5.15}$$

Comparing these timescales with the two in Kolotkov et al. (2019); Zavershinskii et al. (2019) we see that τ_1 is identical, whilst τ_2 is different only by the magnetic term in $Q_{T[\text{mag } p]}$, which goes to Q_T as the plasma-β goes to zero. Thus the only difference between the characteristic times in Kolotkov et al. (2019); Zavershinskii et al. (2019) and the ones used in this thesis is the magnetic correction $Q_T \to Q_{T[\text{mag } p]}$ in τ_2. It is worth explicitly stating that the ratio of specific heats is defined in relation only to constant gas pressure, $\gamma = C_{P[\text{gas}]}/C_V$. Pulling these definitions together with the thermal conduction timescale $\tau_\text{cond}(k) \propto \rho_0 C_V/\kappa_\parallel k^2$ (Eq. 4.4) we can write the

dispersion relation as

$$\omega^3 + i\frac{2}{2+\gamma\beta}\left\{\frac{4\pi^2}{\tau_{\rm cond}(k)}\left(1+\frac{\beta}{2}\right)+\frac{1}{\tau_2}+\frac{\gamma\beta}{2}\frac{1}{\tau_1}\right\}\omega^2 \\ - C_{\rm T}^2 k^2\omega - iC_{\rm T}^2\left\{\frac{1}{\gamma}\frac{4\pi^2}{\tau_{\rm cond}(k)}+\frac{1}{\tau_1}\right\}k^2 = 0. \tag{5.16}$$

Note that many of the terms can be expressed in terms of the ratio of characteristic speeds, $C_{\rm T}^2/C_{\rm S}^2 = 2/(2+\gamma\beta)$ and $C_{\rm T}^2/C_{\rm A}^2 = \beta\gamma/(2+\gamma\beta)$. This prefactor shows analytically how the plasma-β modifies the slow mode propagation in the manner described as an "effective adiabatic index" in Equation 13 of Nisticò et al. (2017). It may be seen that Equation (5.16) is affected by the magnetic field in several ways: the phase speed $C_{\rm S} \to C_{\rm T}$, the terms with plasma-β, and also implicitly through the timescale τ_2. Only the last of these is affected by the dependence of Q upon magnetic field B. This means that even if the heating model is independent of magnetic field, the properties of the wave are affected by the magnetic field strength. These finite-β effects on the real part of ω are well known, and it has been demonstrated they may be important for slow waves in some wave guides such as hot flaring loops (Afanasyev and Nakariakov 2015), as well as the determination of cut-off frequency in the solar atmosphere. By accounting for the obliqueness of the waves, the wave speed is made to depend on the absolute value of the magnetic field via $C_{\rm T}$, which is always subsonic and sub-Alfvénic.

5.2.2 Limit of weak non-adiabaticity

Similar to the previous works on damping of magnetoacoustic waves by thermal conduction (e.g. Table 1 in Banerjee and Krishna Prasad 2016), the upper and lower limits of non-adiabaticity are now derived. Let us begin with the limit of weak non-adiabaticity, in which the wave is only mildly affected by transfer with the active medium. In this limit $\omega \gg 1/\tau_{1,2,\rm cond}$, thus we rearrange the dispersion relation (5.16) (assuming $\omega \neq 0$) into

$$\omega^2 = C_{\rm T}^2 k^2\left\{1 - i\left[\frac{1}{C_{\rm T}^2}\frac{\omega^2}{k^2}\left(\frac{1}{\omega\tau_2}+\frac{\gamma\beta}{2}\frac{1}{\omega\tau_1}\right)\frac{C_{\rm T}^2}{C_{\rm S}^2}-\frac{1}{\omega\tau_1} \right.\right. \\ \left.\left. + \frac{4\pi^2}{\omega\tau_{\rm cond}(k)}\left(\frac{1}{C_{\rm T}^2}\frac{\omega^2}{k^2}\left[1+\frac{\beta}{2}\right]\frac{C_{\rm T}^2}{C_{\rm S}^2}-\frac{1}{\gamma}\right)\right]\right\}$$

where the ratio $(C_{\rm T}/C_{\rm S})^2 = 2/(2+\gamma\beta)$, kept in this form here for easier comparison with Nakariakov et al. (Eq. 21, 2017), which deals with the same limiting case. Taking the limit of $1/\omega\tau_{\rm cond}$ and $1/\omega\tau_{1,2}$ as small parameters, the Taylor expansion

of the dispersion relation reduces to

$$\omega^2 \approx C_{\rm T}^2 k^2 \left\{ 1 - i\omega^{-1} \frac{2}{2+\gamma\beta} \left[\left(\frac{\gamma-1}{\gamma} \right) \frac{4\pi^2}{\tau_{\rm cond}} + \frac{1}{\tau_2} - \frac{1}{\tau_1} \right] \right\}. \tag{5.17}$$

To evaluate the ω^{-1} in the imaginary component of Equation (5.17), perturbation theory is used. In the zeroth order $\omega \approx C_{\rm T} k$, and using this yields the following solution to the weakly non-adiabatic dispersion relation:

$$\omega_{\rm R} \approx C_{\rm T} k, \tag{5.18}$$

$$\omega_{\rm I} \approx -\frac{1}{2} \left(\frac{2}{2+\beta\gamma} \right) \left[\frac{\gamma-1}{\gamma} \frac{4\pi^2}{\tau_{\rm cond}} + \frac{1}{\tau_2} - \frac{1}{\tau_1} \right]. \tag{5.19}$$

The phase speed of the weakly non-adiabatic wave is the tube speed $C_{\rm T}$ as expected, and in the limit of $\beta \to 0$ this equation coincides exactly with Kolotkov et al. (Eq. 9, 2019). From Equation 5.19 we are motivated to form the timescale $\tau_M(\tau_1, \tau_2)$ which appears in the weakly non-adiabatic expression, and can be referred to as a characteristic damping time of the heating/cooling misbalance:

$$\begin{aligned} \frac{1}{\tau_M} &= \frac{C_{\rm T}^2}{C_{\rm S}^2} \left(\frac{1}{\tau_2} - \frac{1}{\tau_1} \right), \\ &= \left(\frac{2}{2+\beta\gamma} \right) \left(\frac{1}{\tau_2} - \frac{1}{\tau_1} \right), \\ &= \frac{2}{2+\beta\gamma} \left\{ \frac{\gamma-1}{\gamma} \frac{Q_T}{C_V} + \frac{1}{\gamma} \frac{\rho_0}{T_0} \frac{Q_\rho}{C_V} - \frac{\beta}{2} \frac{B_0}{T_0} \frac{Q_B}{C_V} \right\}. \end{aligned} \tag{5.20}$$

$$\implies \omega_{\rm I} \approx -\frac{1}{2} \left(\frac{2}{2+\beta\gamma} \frac{\gamma-1}{\gamma} \frac{4\pi^2}{\tau_{\rm cond}} + \frac{1}{\tau_M} \right). \tag{5.21}$$

If the limit of weak non-adiabaticity applies, and $\tau_M > 0$, then we may interpret τ_M as the damping time over which the thermal misbalance is attenuating the slow wave. Similarly if the limit of weak non-adiabaticity applies and $\tau_M < 0$, energy is supplied from the medium into the wave, amplifying the slow wave over the characteristic timescale τ_M. In the weak non-adiabatic limit, the effect of damping from thermal conduction and the effect of damping from thermal misbalance are additive, shown in Equation (5.21). The damping due to thermal conduction is modified by a factor of $C_{\rm T}^2/C_{\rm S}^2 = (1+\gamma\beta/2)$, thus **in the limit of weak non-adiabaticity, the damping effect of thermal conduction is reduced as the plasma-β increases.**

5.2.3 Limit of strong non-adiabaticity

Now we turn our attention to the limit of strong non-adiabaticity, which describes slow magnetoacoustic waves for which $\omega \ll 1/\tau_{1,2,\mathrm{cond}}$, which is to say these waves are highly affected by the exchange of energy with the active medium. Such unexplained dissipative effects have been seen before in numerical simulations of flares (Selwa et al. 2005). We should keep in mind that by assuming the state equation is the ideal gas law (Eq. 5.6) and neglecting the non-adiabatic effects of γ, some of the results in this stronly non-adiabatic limit may not capture the full dynamics. Nonetheless we can rewrite the dispersion relation in the following way (where we have divided through by $\omega \neq 0$):

$$\omega^2 = C_{\mathrm{T}}^2 k^2 \frac{1 + i\left\{\dfrac{1}{\gamma}\dfrac{4\pi^2}{\omega\tau_{\mathrm{cond}}} + \dfrac{1}{\omega\tau_1}\right\}}{1 + i\left\{\dfrac{2}{2+\gamma\beta}\left(\dfrac{(1+\beta/2)4\pi^2}{\omega\tau_{\mathrm{cond}}} + \dfrac{1}{\omega\tau_2} + \dfrac{\beta\gamma}{2}\dfrac{1}{\omega\tau_1}\right)\right\}} \tag{5.22}$$

For the strong limit, $\omega\tau_{\mathrm{cond}}$ and $\omega\tau_{1,2}$ are taken to be small parameters. After Taylor expansion we find the strong limit to be

$$\omega^2 \approx C_{\mathrm{S}}^2 k^2 \left\{ \frac{\left(\dfrac{4\pi^2}{\gamma\tau_{\mathrm{cond}}} + \dfrac{1}{\tau_1}\right)}{\dfrac{4\pi^2}{\tau_{\mathrm{cond}}} + \dfrac{1}{\tau_2} + \dfrac{\gamma\beta}{2}\left(\dfrac{4\pi^2}{\gamma\tau_{\mathrm{cond}}} + \dfrac{1}{\tau_1}\right)} - i\omega \frac{\left(\dfrac{\gamma-1}{\gamma}\right)\dfrac{4\pi^2}{\tau_{\mathrm{cond}}} + \dfrac{1}{\tau_2} - \dfrac{1}{\tau_1}}{\left(\dfrac{4\pi^2}{\tau_{\mathrm{cond}}} + \dfrac{1}{\tau_2} + \dfrac{\gamma\beta}{2}\left(\dfrac{4\pi^2}{\gamma\tau_{\mathrm{cond}}} + \dfrac{1}{\tau_1}\right)\right)^2} \right\}. \tag{5.23}$$

The change from C_{T}^2 to C_{S}^2 is caused by pulling out a factor of $1 + \gamma\beta/2$. Equation (5.23) agrees with strong limit in the infinite field limit as $\beta \to 0$ as it should (Zavershinskii et al. 2019). In order to deal with the ω in the imaginary component, we again apply the perturbation approach. Thus ω is approximated in the zeroth order by ω_{R} as seen in Equation (5.23), yielding the following solution to the highly

non-adiabatic dispersion relation:

$$\omega_{\mathrm{R}} \approx \frac{1}{\sqrt{\gamma}} C_{\mathrm{S}} k \frac{\left(\dfrac{4\pi^2}{\tau_{\mathrm{cond}}} + \dfrac{\gamma}{\tau_1}\right)^{1/2}}{\left[\dfrac{4\pi^2}{\tau_{\mathrm{cond}}} + \dfrac{1}{\tau_2} + \dfrac{\beta}{2}\left(\dfrac{4\pi^2}{\tau_{\mathrm{cond}}} + \dfrac{\gamma}{\tau_1}\right)\right]^{1/2}} , \tag{5.24}$$

$$\omega_{\mathrm{I}} \approx -\frac{1}{2} C_{\mathrm{S}}^2 k^2 \left(1 + \frac{\gamma\beta}{2}\right) \frac{\left(\dfrac{\gamma - 1}{\gamma}\dfrac{4\pi^2}{\tau_{\mathrm{cond}}} + \dfrac{1}{\tau_2} - \dfrac{1}{\tau_1}\right)}{\left[\dfrac{4\pi^2}{\tau_{\mathrm{cond}}} + \dfrac{1}{\tau_2} + \dfrac{\beta}{2}\left(\dfrac{4\pi^2}{\tau_{\mathrm{cond}}} + \dfrac{\gamma}{\tau_1}\right)\right]^2} . \tag{5.25}$$

Note that in order to consider the propagating modes described in Chapter 4, one would solve Equation (5.23) for k, and find the damping length $\lambda_{\mathrm{damp}} \propto k_{\mathrm{I}}^{-1}$ is proportional to $1/\omega^2$. Equations (5.24)–(5.25) capture the behaviour of these highly non-adiabatic waves, but with so many variables it is difficult to understand what these mean. To aid understanding, we examine these equations in the limiting cases of dominating and negligible thermal conduction, noting that the limit of $\beta = 0$ applied straight to the above equations is exactly the "low frequency" regime in Zavershinskii et al. (2019). In the limit of negligible thermal conduction $\tau_{\mathrm{cond}} \gg \tau_{1,2}$, the above equations may be simplified to

$$\omega_{\mathrm{R}} \approx C_{\mathrm{S}} k \left(\frac{\tau_2}{\tau_1 + (\gamma\beta/2)\tau_2}\right)^{1/2} \qquad \text{(no thermal conduction)}, \tag{5.26}$$

$$\omega_{\mathrm{I}} \approx -\frac{1}{2} C_{\mathrm{S}}^2 k^2 \left(1 + \frac{\gamma\beta}{2}\right) \frac{\tau_1\tau_2(\tau_1 - \tau_2)}{(\tau_1 + (\gamma\beta/2)\tau_2)^2} \qquad \text{(no thermal conduction)}. \tag{5.27}$$

In the absence of thermal conduction the non-adiabatic wave propagates at the speed ω_{R}/k determined by Equation (5.26), which in the infinite field case is simply $C_{\mathrm{S}}\sqrt{\tau_2/\tau_1}$. In finite-$\beta$ plasma, the phase speed of the highly non-adiabatic wave is reduced compared to the infinite magnetic field case. The slow wave damping/amplification due purely to the wave-induced thermal misbalance is determined by Equation (5.27). The wave (in absence of thermal conduction) will damp if $\tau_1\tau_2(\tau_1 - \tau_2) > 0$, and will do so such that its damping time $\tau_{\mathrm{damp}} \propto \omega_{\mathrm{I}}^{-1}$ is proportional to k^{-2}. Notice that $\tau_1\tau_2(\tau_1 - \tau_2) > 0$ is exactly equivalent to $\tau_{\mathrm{M}} > 0$ from Equation 5.21.

Now we consider the effect of finite-β purely on the thermal conduction term. Under the assumption of negligible misbalance $\tau_{1,2} \gg \tau_{\mathrm{cond}}$ we find the limit of

strong non-adiabaticity to be:

$$\omega_{\rm R} \approx \frac{C_{\rm S}k}{\sqrt{\gamma}}\left(\frac{1}{\sqrt{1+\beta/2}}\right) \qquad \text{(no thermal misbalance)}, \tag{5.28}$$

$$\omega_{\rm I} \approx -\frac{1}{2}C_{\rm s}^2k^2\left(\frac{\gamma-1}{\gamma}\right)\frac{\tau_{\rm cond}}{4\pi^2}\frac{(1+\gamma\beta/2)}{(1+\beta/2)^2} \qquad \text{(no thermal misbalance)}. \tag{5.29}$$

A common sense check is that the isothermal speed in the absence of thermal misbalance tends to the isothermal sound speed $C_{\rm S}/\sqrt{\gamma}$ as $\beta \to 0$, which clearly Equation (5.28) satisfies (De Moortel and Hood 2003). As before, for finite-β this phase speed is even slower. The effect of thermal conduction on the wave increment is always a damping effect ($\omega_{\rm I} < 0$), and since $\tau_{\rm cond} \propto k^{-2}$ this cancels with the k^2 in $\omega_{\rm I}$ to make the conductive damping in this limit independent of k. The effect of increasing β is to reduce $\omega_{\rm I}$ and hence increase damping times (equivalent to lessening the rate of damping). Unlike the weak non-adiabaticity regime (5.18)–(5.19), the effects of the parallel thermal conduction and of the wave-caused heating/cooling misbalance on the slow wave dynamics are **not** additive in the strong limit (Eqs. 5.24–5.25).

5.3 Constraining the coronal heating function

What makes the potential of slow magnetoacoustic modes for seismology particularly exciting is that they probe the local thermodynamic state of the plasma, allowing observations to constrain the enigmatic heating processes in the plasma. Using the easily-observed slow modes as an alternative to collating coronal loop scaling laws or differential emission measures could lead to huge ramifications in terms of addressing the coronal heating problem (Sec. 1.2.5). In this section we consider two ways in which the non-adiabatic effects described above may be exploited for just this.

5.3.1 Instability criteria

In order for a slow magnetoacoustic mode to exist in the corona, the coronal plasma must exist in the first place, ergo be it must stable to thermal perturbations. To get a feel for the instabilities, first consider thermal stability in a homogeneous, uniform, static and infinite plasma (Field 1965). There are two instability criteria:

$$T_0(\gamma-1)Q_T + \rho_0 Q_\rho < 0 \qquad \text{(Isentropic instability)}, \tag{5.30}$$

$$T_0 Q_T - \rho_0 Q_\rho < 0 \qquad \text{(Isobaric instability)} \tag{5.31}$$

The isentropic instability criterion if satisfied corresponds to the amplitude growth of sound waves, where the active medium provides energy into the wave (over-stability). The isobaric instability criterion corresponds to the amplification of the thermal mode and hence formation of condensed regions under constant pressure conditions if satisfied. The isobaric instability is considered instead of the isochoric (constant volume) for the reason that in the case of an iochoric perturbation, the induced pressures necessarily drive motions which change the background density, which is inconsistent with the force equation (Field 1965).

We now consider the instability criteria for dispersion relation 5.16, in terms of the characteristic timescales derived above. By considering both Equation (5.19) and Equation (5.25) for the threshold of amplitude growth of the slow mode ($\omega_{\rm I} < 0$), we find:

$$\frac{1}{\tau_2} - \frac{1}{\tau_1} + \frac{\gamma - 1}{\gamma}\frac{4\pi^2}{\tau_{\rm cond}} < 0 \quad \text{(for slow mode instability)}. \tag{5.32}$$

In the absence of thermal conduction, the sign of $\tau_{\rm M}$ is the same condition as instability criterion (5.32). Note that there is an implicit magnetic dependence within Equation (5.32) through the term τ_2, despite some coefficients (which are always positive) having been factored out. In the limit of infinite magnetic field, this instability criterion agrees with that of the (isentropic) instability criterion in Field (Eq. 25 1965) as it should, the only change being $\tau_2 = C_V/Q_T$ not $C_V/Q_{T[\text{mag } p]}$.

It is clear the magnetic field could be important to (isobaric) thermal stability due to the addition of magnetic pressure (for example see Eq. 47 in Field 1965). The effect of magnetic field on the stability of coupled magnetic and thermal modes was studied in Ireland et al. (1995), in which it was found some situations may exist where an over-stable, coupled magnetothermal mode grows significantly in only a few periods. A first order expansion for low-β plasmas was also performed in Soler et al. (2012), in the context of prominence dynamics, though results were placed in the context of enhanced magnetic diffusion due to ion-neutral collisions. However whilst detailed analysis of the finite-β effect on the thermal mode instability with heating/cooling misbalance is worthwhile to pursue in future, especially in the context of constraining the coronal heating function through observations of coronal rain, it is beyond the scope of this work. We have not explicitly solved the dispersion relation (Eq. 5.16) for the thermal mode, so instead consider the infinite magnetic field limit, accounting for the thermal conduction (e.g. Eq. 25 in Field 1965). After some algebra and expressing in terms of the characteristic timescales derived above, one finds

$$\frac{\gamma}{\tau_1} + \frac{4\pi^2}{\tau_{\rm cond}} < 0 \quad \text{(for thermal mode)}. \tag{5.33}$$

Although we do not consider growth rates here, the growth rates of the slow and

thermal modes are known to be comparable in magnitude up to approximately one million Kelvin, the latter being a few times stronger, and beyond 1 MK the thermal growth rate dominates (Claes and Keppens 2019). The fast mode growth rate is always at least two to three orders of magnitude smaller than the thermal growth rate, and its analysis is completely analogous to that of the slow mode, so we do not consider any instabilities associated with the fast mode here.

The characteristic time of the thermal conduction $\tau_{\rm cond}$ is essentially positive and therefore it always contributes to the damping (stabilising) of both thermal and slow magnetoacoustic modes. In contrast, the heating/cooling misbalance times $\tau_{1,2}$ as well as their difference can be both positive and negative depending on the equilibrium parameters of the coronal plasma and properties of specific plasma heating and cooling functions. Table 5.1 summarises qualitative behaviours of the thermal and slow modes for all possible combinations of positive and negative $\tau_{1,2}$. Specific regimes of the slow magnetoacoustic and thermal modes in these cases are determined by Equations (5.32)–(5.33) evaluated for a certain combination of plasma parameters and fixed heating/cooling model.

τ_1	τ_2	Thermal mode	Slow mode
>0	>0	damps stronger	can damp stronger, weaker, or be over-stable
<0	<0	can damp weaker or be unstable	can damp stronger, weaker, or be over-stable
<0	>0	can damp weaker or be unstable	damp stronger
>0	<0	damp stronger	can damp weaker or be over-stable

Table 5.1: The effect of dispersion from the misbalance between coronal heating and cooling processes upon the amplitude of a slow (acoustic) mode, in addition to the damping caused by thermal conduction alone. The possible regimes of the thermal and the slow magnetoacoustic modes are listed, partitioned by the signs of the two characteristic timescales of the misbalance τ_1, τ_2. The effect is described by dispersion relation (5.16) and the specific behaviours are determined by Eqs. (5.32) - (5.33).

Up to this point, all our results have been expressed in terms of a generic heating/cooling function Q, whose derivatives with respect to thermal equilibrium are treated as free parameters, and applicable to any plasma conditions for which the governing equations may be satisfied. In order to fully explore our results in the coronal context however, we now pin down a functional form of Q and pick some plasma parameter ranges to evaluate. We evaluate conditions (5.32)–(5.33) for a range of reasonable coronal plasma densities and temperatures (see Table

4.1), corresponding to the physical conditions in such coronal structures as hot jets, plumes, and interplume regions in coronal holes (e.g. Wilhelm et al. 2011); warm quiescent coronal loops and hot and dense flaring loops (see e.g. Reale 2014).

Moreover, we parameterise the coronal heating function as

$$Q = \mathcal{L}(\rho, T) - \mathcal{H}(\rho, T, B) \Longleftarrow \begin{cases} \mathcal{L}(\rho, T) = \chi \rho T^{\alpha}, \\ \mathcal{H}(\rho, T, B) = h_0 \rho^a T^b B^c. \end{cases} \tag{5.34}$$

where the coefficient h_0 is determined from the initial thermal equilibrium condition, $Q_0 = 0, \implies h_0 = \mathcal{L}_0/\rho_0^a T_0^b B_0^c$, and the power indices a, b and c are treated as free parameters. We synthesise the coronal optically thin radiation function $\mathcal{L}(\rho, T)$ from CHIANTI atomic database v. 9.0.1 (Dere et al. 1997, 2019) for the relevant densities and temperatures (essentially fixing χ and α). This allows us to re-write conditions (5.32)–(5.33) in terms of the coronal heating power indices a, b and c as

$$\text{(for slow mode instability)}: \quad b > \frac{1}{\gamma - 1}\left\{1 + \left(\frac{\beta\gamma}{2}\right)c - a\right\} + \frac{T_0}{\mathcal{L}_0}\left(\frac{\partial \mathcal{L}}{\partial T}\right)_{T_0,\rho_0} + \frac{C_{\rm V}}{\tau_{\rm cond}}\frac{T_0}{\mathcal{L}_0}, \tag{5.35}$$

$$\text{(for thermal instability)}: \quad b > a + \frac{T_0}{\mathcal{L}_0}\left(\frac{\partial \mathcal{L}}{\partial T}\right)_{T_0,\rho_0} + \frac{C_{\rm V}}{\tau_{\rm cond}}\frac{T_0}{\mathcal{L}_0} - 1. \tag{5.36}$$

Note that it is assumed that the radiative loss function has no dependence on magnetic field, which may not be the case, yet no data for such a dependence is easily available. To make this inequality with three parameters easier to deal with, for the moment we disregard the effect of the magnetic field and any dependence the heating function may have on it.Therefore we set $\beta, c = 0$ and focus on the remaining function $\mathcal{H} \propto \rho^a T^b$ to find

$$\text{(for acoustic instability)}: \quad b > -\frac{a}{\gamma - 1} + \frac{T_0}{\mathcal{L}_0}\left(\frac{\partial \mathcal{L}}{\partial T}\right)_{T_0,\rho_0} + \frac{1}{\gamma - 1} + \frac{C_{\rm V}}{\tau_{\rm cond}}\frac{T_0}{\mathcal{L}_0}. \tag{5.37}$$

The thermal instability remains the same. These analytical conditions are exceptionally important as they allow us to delineate the coronal heating models, i.e. values of a and b, for which slow magnetoacoustic and thermal modes either damp or grow due to violation of the thermal equilibrium of the corona, that could be directly verified in observations.

We begin analysis of Equations (5.36)–(5.37) for the regime of a suppressed

thermal conductivity (see e.g. the series of works by Wang and Ofman 2019; Wang et al. 2015, 2018), providing $\tau_{\rm cond} \to \infty$. Using this, we obtain the instability thresholds for both the thermal and acoustic modes. The thresholds are manifested as two intersecting families of parallel straight lines with the slopes of $-(\gamma-1)^{-1}$ and 1 in the parametric plane (a, b). From both sets, we pick the outermost boundaries that allow us to identify intervals of a and b for which thermal and acoustic modes damp for all considered plasma densities and temperatures, can damp or grow depending on a certain combination of plasma density and temperature, and always grow. In this way, the heating models which make the plasma unstable to the wave-induced destabilisation of the thermal equilibrium can be estimated graphically, as is done in the top panel in Figure 5.2. Since the corona exists despite constant thermal perturbations, we may assume that the heating model is unlikely to be one that is always unstable or even sometimes to the thermal mode, for any reasonable density or temperature. The caveat to this statement is that the heating model must allow condensations of plasma to occur in some instances, since coronal rain exists, and in fact appears quite common after flares (Antolin 2020). Whether coronal rain is instigated by the thermal instability for certain combinations of temperature, density and magnetic field, or by a change in heating mechanism altogether is unclear. Nonetheless for the general quiet Sun case (in which coronal rain appears rarely), we may disregard any heating models lying in the region of gridded lines in Figure 5.2, and probably disregard any in the region of horizontal lines also. Further, since observations of slow magnetoacoustic modes have overwhelmingly showed enhanced damping and not growth, we can disregard heating models lying in the region of consistent acoustic over-stability (the yellow region).

In the case of a finite Spitzer thermal conductivity and taking the characteristic parallel size of the plasma non-uniformity, $L \simeq 180\,\mathrm{Mm}$ (Wang 2011), these critical intervals soften as shown in the bottom panel of Figure 5.2, where the regions of omnipresent thermal and acoustic instabilities disappear. **Thermal conductivity acts to stabilise the plasma to thermal instability.** The effect of thermal conductivity weakens for larger values of L (smaller k). However, for all plausible values of L extending up to 1000 Mm, no radical change to the behaviour of the acoustic and thermal modes shown in the bottom panel in Figure 5.2 was detected. Likewise, the effect of the thermal conductivity strengthens for shorter L (that is to say $1/\tau_{\rm cond}$ increases), pushing the regions of omnipresent instabilities further away from the considered intervals of a and b. Encouragingly, this fits with the observation that the shorter loops in cores of active regions appear not to show rain.

One of the immediate outcomes of the performed analysis is that both modes are found to damp throughout the whole considered intervals of plasma densities and

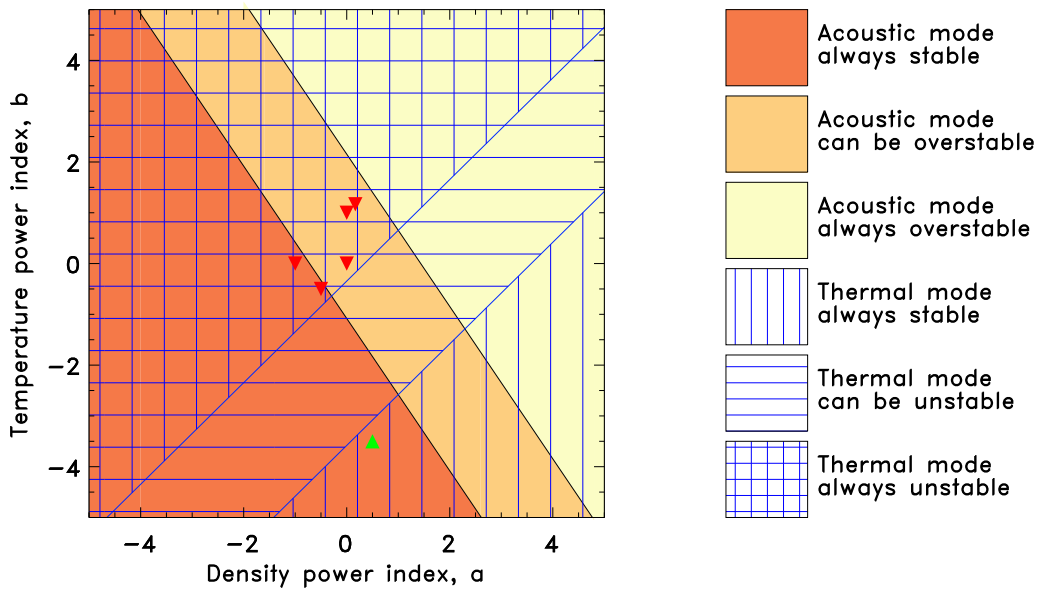

(a) Regions of instability without thermal conduction

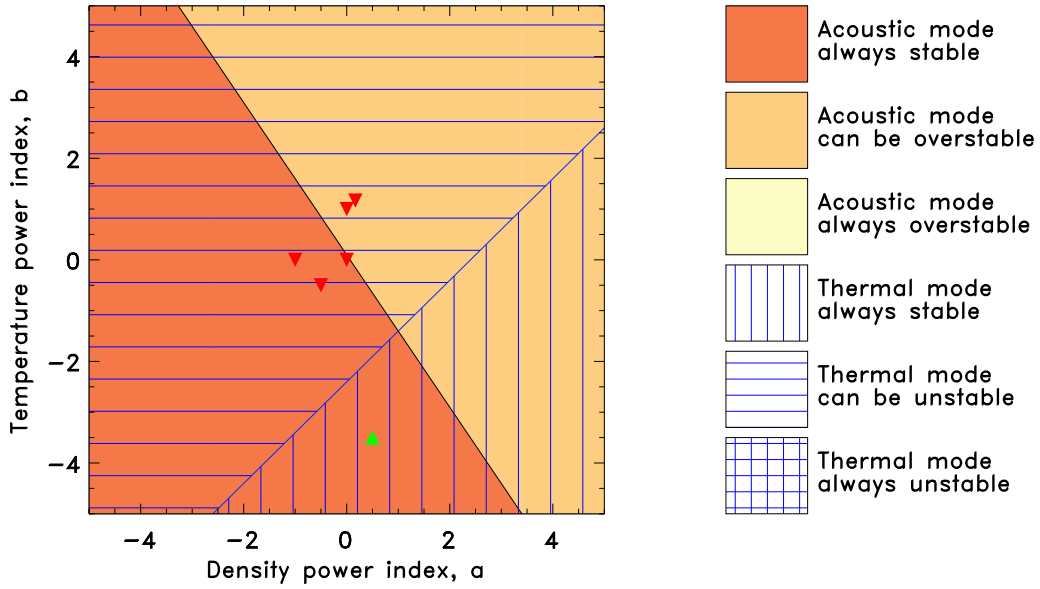

(b) Regions of instability including thermal conduction

Figure 5.2: Regions of the heating function power-law indices a and b determining stability of the acoustic and thermal wave modes, according to Equations (5.37)–(5.36) evaluated for typical densities and temperatures of the solar corona (Table 4.1) for characteristic length of 180 Mm. [*Top*] Instabilities considering wave-induced misbalance alone, [*Bottom*] Instabilities considering both wave-induced misbalance and thermal conduction. The red triangles show the values of a and b for the heating models from Ibanez S. and Escalona T. (1993). The green triangle shows the heating model used as an example in Sec. 5.3.2, $a = 0.5$ and $b = -3.5$.

temperatures for the values of a and b outlined by a triangle with approximate vertices $(-2.5, -5)$, $(1, -1.5)$, and $(3.5, -5)$. In other words, **for any heating model from this region the slow mode will be seen in observations as a damped wave in thermodynamically stable plasma.** This is in contrast to the five heating models proposed in Ibanez S. and Escalona T. (1993), which according to Figure 5.2 all lead to a thermal equilibrium that is unstable to the thermal mode in the case of suppressed conduction, and there are combinations of the coronal densities and temperatures for which the thermal mode can be either stable or unstable in the case of finite conduction. Likewise, two of these heating models ($a = 0$, $b = 1$ and $a = 1/6$, $b = 7/6$) lead to acoustic over-stability for certain densities and temperatures even with the additional suppression of finite conductivity. We propose that the unknown coronal heating model applicable to the quiet Sun should be constrained to one which, according to Equations (5.36)–(5.37), is always stable to both the thermal and acoustic mode. One example model would be $\mathcal{H} = \rho^{1/2}T^{-7/2}$. We repeat that this analysis is performed with the caveat that magnetic field effects, and any dependence of the coronal heating function upon magnetic field $\mathcal{H} \propto B^c$, can also affect the instability criteria, for example Equation (5.35). This would make the two dimensional plot in Figure 5.2 into a three dimensional parameter space, although the same logic for constraining the coronal heating may be applied.

5.3.2 Comparing characteristic timescales

In this section we provide estimates for the characteristic timescales of the thermal misbalance for varying temperature and density in the corona, since comparing the characteristic timescale of a process with the wave period indicates that processes' effectiveness. A process such as thermal conduction may be important for the wave's dynamics for some temperatures and/or densities, but the same process may be negligible or too fast-acting (isothermal) at a different temperature and/or density. This is demonstrated in Figure 5.3, depicting the timescales τ_1, τ_2 (in the infinite magnetic field limit) as a function of temperature – for their heating model, the effect of misbalance is important for slow

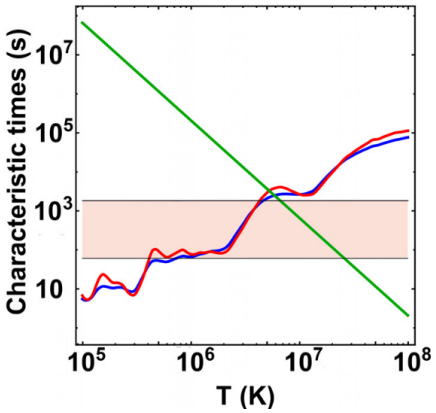

Figure 5.3: Plot showing how τ_1 (blue) and τ_2 (red) vary with temperature, assuming Ohmic heating ($a = 1, b = 0$) and radiative cooling, $n_0 = 10^{16}\ m^{-3}$ and infinite B. The pink shaded region corresponds to 1–30 minutes. The green line shows the characteristic timescale for thermal conduction, for a wavelength of $\lambda = 100$ Mm.

modes between 5×10^5 K and 5×10^6 K.

Thermal conduction is important for higher temperatures ($> 5 \times 10^6$), though this depends on wavenumber. Such variation in the importance of different terms can lead to confusing results, for example the change in the frequency-dependent damping observed as slow magnetoacoustic waves propagate outward through the corona (Prasad et al. 2014), and the enhanced damping seen in particularly hot loop despite suppressed thermal conduction (Wang et al. 2015).

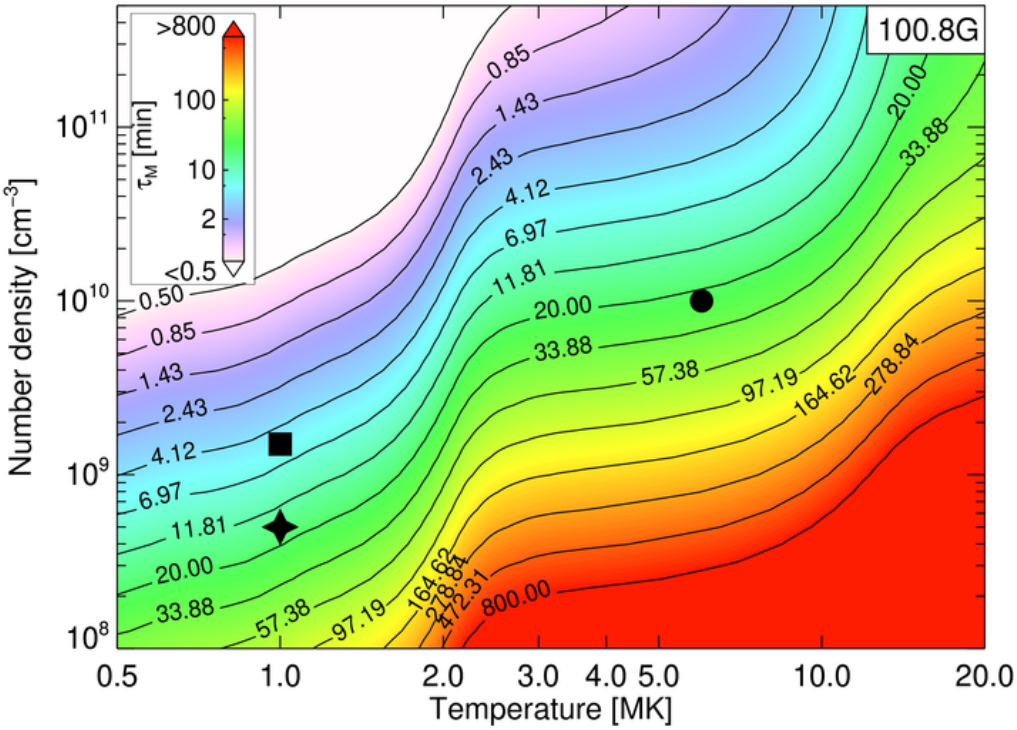

Figure 5.4: Variation of the characteristic thermal misbalance time τ_M (Eq. 5.20) for typical coronal densities and temperatures and a fixed heating model a=0.5, b=-3.5, c=0, for which both the slow and thermal wave modes described by Eq. (5.16) are found to be stable over the entire intervals of plasma densities and temperatures considered (see Fig. 5.2). This plot is calculated for magnetic field strength 100 G, which is practically unchanged from the infinite magnetic field case. For reference, the colour scheme is adjusted so that the values of τ_M from about 10 min to 100 min are shown in green. The black symbols illustrate typical combinations of coronal plasma density and temperature for such objects as hot and dense loops in active regions (circle), warm and less dense quiescent loops (square), and plumes in coronal holes (star), described in Table 5.2.

Figure 5.4 shows the variation of the misbalance time τ_M (Eq. 5.20) with plasma density and temperature for a fixed heating model, $a = 0.5$, $b = -3.5$, $c = 0$. This heating model is chosen as an illustrative example, for which both the

slow and thermal modes are found to be stable for all considered plasma densities and temperatures (see Subsection 5.3.1). As Figure 5.4 makes clear, the time τ_M varies from a few minutes to several tens of minutes for typical combinations of the plasma density and temperature. These values of $\tau_{\rm M}$ are similar to the slow wave periods detected in typical coronal plasma structures (for example see Table. 4.1). In particular, the value of $\tau_{\rm M}$ is similar – about several minutes – both in hot and dense plasmas, e.g. $T_0 \simeq 10\,{\rm MK}$ and $n_0 \simeq 10^{10}\,{\rm cm}^{-3}$ denoted by the circle, and in a cooler and less dense plasma, e.g. $T_0 \simeq 1\,{\rm MK}$ and $n_0 \simeq 10^{9}\,{\rm cm}^{-3}$ denoted by the square, and even the rarefied plasma of plumes in coronal holes, denoted by the star. **Because these characteristic timescales are comparable, the discussed effect of the heating/cooling misbalance is strong for these waves.** In contrast, in very dense and cool or very hot and rarefied plasmas, $\tau_{\rm M}$ is either very short (< 0.5 min) or long (> 800 min), meaning the effect of thermal misbalance is weak for slow waves in these plasmas. It should be noted that for flaring loops the limit of weak non-adiabaticity is not good, and the limit of strong non-adiabaticity is more appropriate: thus the separate comparison of τ_1, τ_2 with ω is advised over use of $\tau_{\rm M}$.

Table 5.2 compares $\tau_{\rm M}$ for a fixed heating model with several other characteristic timescales pertinent to the solar corona, making clear that there are many typical coronal situations in which the effect of misbalance between the heating and cooling process of the plasma, upon a slow magnetoacoustic wave, is important. Such a comparison is similar in spirit to Claes and Keppens (equations 30-31, 2019), and also Ireland et al. (Table 1, 1995).

Perhaps the most important effect to be included and contrasted against is the characteristic timescale for thermal conductivity, $\tau_{\rm cond}$. In the derivation above using the thin flux tube approximation, it was found that the effect of thermal conduction is modified compared to the zero-β limit. So for a finite-β plasma in the weakly non-adiabatic limit, the timescale transforms:

$$\tau_{\rm cond} = \rho_0 C_{\rm V} \lambda^2 / \kappa_{\parallel}, \quad [\text{seconds}], \tag{4.4}$$

$$\rightarrow \tau_{\rm cond} = \left(1 + \frac{\gamma\beta}{2}\right)\left(\frac{\gamma}{\gamma - 1}\right)\frac{\rho_0 C_{\rm V} \lambda^2}{\kappa_{\parallel}}. \tag{5.38}$$

where the wavelength λ may for example be related to the loop length $\lambda = 2L$ for a fundamental standing mode. As Table 5.2 makes clear, the variation of $\tau_{\rm cond}$ with both β and λ means that its relevance is extremely broad – only for long, dense loops in weak magnetic fields is its effect likely to be irrelevant. However in most cases the effect of thermal misbalance is at least as important, and does not change with wavenumber k meaning its effect is universal for different length structures.

Following from De Moortel and Hood (2004); Sigalotti et al. (2007), one can

associate a characteristic timescale to the viscous dissipation, acting on a length scale L:

$$\tau_{\rm visc} = \frac{3L^2\rho_0}{4\eta} \approx \frac{4}{3} \times 10^{17} L^2 \rho_0 T^{-5/2} \quad \text{[seconds]}. \tag{5.39}$$

The magnetic diffusivity η [m^2 s^{-1}] is taken to be constant. From this it is clear that compressive viscosity acts more quickly for hotter plasma, less dense plasma and for shorter length scales. In line with previous results, the timescale of compressive viscosity when evaluated for the typical coronal conditions is so long that its effect would need major enhancement to become pertinent. **We contest that the effect of thermal misbalance is a more natural way to explain anomalous damping, rather than enhancing dissipation, and should be accounted for before exotic or nonlinear effects are included.**

In the literature a characteristic timescale has often been assigned solely to the radiative cooling of the loop or structure. Following for example Aschwanden and Schrijver (2011); Aschwanden and Terradas (2008); De Moortel and Hood (2004); Provornikova et al. (2018) we can re-write the characteristic plasma temperature e-folding time due to the radiative cooling in the absence of any heating (see e.g. Eq. (6) in De Moortel and Hood 2004) in our terms as

$$\tau_{\rm rad} = \frac{\gamma C_{\rm V} T_0}{\mathcal{L}_0(\rho_0, T_0)}, \tag{5.40}$$

where $\mathcal{L}_0$ is the radiative loss function measured in W kg^{-1}. Clearly $\tau_{\rm rad}$ is determined purely by the magnitude of the radiative losses $\mathcal{L}_0$, simply put the more radiation the quicker the plasma cools down. Using the CHIANTI atomic database v. 9.0.1 the quantity $\mathcal{L}_0$ may be estimated in order to calculate $\tau_{\rm rad}$ (e.g. Table. 5.2). The magnitude of $\mathcal{L}_0$ for the corona is staggering, being of the order of 100 kW per gram (for typical coronal conditions $\sim$1.1 MK, density = 10^{10} cm^{-3}). Note there may be a discrepancy between the radiative timescales obtained here versus previous estimations due to the way the radiative loss function is calculated (for example Sigalotti et al. (2007) use 'Hildner's' estimate from 1974, visible in Figure 5.1) – we contest that the values calculated here using the modern CHIANTI database are more reliable.

There is an issue with the timescale $\tau_{\rm rad}$ – according to their values calculated for typical coronal conditions, radiative cooling would slash the temperature of coronal structures out of the EUV bands in tens of minutes, which is not (usually) observed, perhaps with the exception of so-called "catastrophic cooling" (Antolin 2020) – though we would attribute this to the (strongly related) thermal instability (Eq. 5.33). Yet many coronal structures persist and remain hot despite radiative

Typical value (Symbol on plots)	Hot loop (circle)	Warm loop (square)	Coronal hole plume (star)
Temperature, T_0	6 MK	1 MK	1 MK
Number density, n_0	1×10^{10} cm^{-3}	1.5×10^{9} cm^{-3}	0.5×10^{9} cm^{-3}
Period, P	$\approx 8 - 18$ min	$\approx 3 - 10$ min	$\approx 10 - 20$ min
$\tau_{\rm M}$, $B = \infty$	23 min	5 min	16 min
$\tau_{\rm M}$, $B = 34$ G	29 min (β=0.35)	5 min (β=0.01)	16 min (β=0.00)
$\tau_{\rm M}$, $B = 12$ G	76 min (β=2.9)	5 min (β=0.07)	16 min (β=0.02)
$\tau_{\rm M}$, $B = 4$ G	474 min $\simeq$ 8 hr (β=24.3)	8 min (β=0.64)	18 min (β=0.20)
$\tau_{\rm cond}$ ($\lambda = 100$ Mm), $B = \infty$	10 min	137 min	43 min
$\tau_{\rm cond}$ ($\lambda = 100$ Mm), $B = 34$ G	13 min (β=0.35)	138 min (β=0.01)	43 min (β=0.00)
$\tau_{\rm cond}$ ($\lambda = 100$ Mm), $B = 12$ G	33 min (β=2.9)	145 min (β=0.07)	44 min (β=0.02)
$\tau_{\rm cond}$ ($\lambda = 100$ Mm), $B = 4$ G	208 min (β=24.3)	210 min (β=0.64)	50 min (β=0.20)
$\tau_{\rm cond}$($\lambda = 10$ Mm), $B = \infty$	0.1 min	1.4 min	0.4 min
$\tau_{\rm cond}$ ($\lambda = 10$ Mm), $B = 34$ G	0.1 min (β=0.35)	1.4 min (β=0.01)	0.4 min (β=0.00)
$\tau_{\rm cond}$ ($\lambda = 10$ Mm), $B = 12$ G	0.3 min (β=2.9)	1.5 min (β=0.07)	0.4 min (β=0.02)
$\tau_{\rm cond}$ ($\lambda = 10$ Mm), $B = 4$ G	2.1 min (β=24.3)	2.1 min (β=0.64)	1.5 min (β=0.20)
$\tau_{\rm rad}$	68 min	14 min	43 min
$\tau_{\rm visc}$ ($L = 100$ Mm)	17.5 days	245 days	77.5 days
$\tau_{\rm visc}$ ($L = 10$ Mm)	4 hr	2.4 days	18 hr

Table 5.2: Table comparing the characteristic timescales calculated for the typical values of three coronal plasma non-uniformities in which rapidly decaying slow modes have been observed: hot dense loops (hosting SUMER-type oscillations) (Nakariakov et al. 2019; Wang 2011), warm quiescent loops (De Moortel 2009) and plumes in coronal holes (Banerjee and Krishna Prasad 2016). The three points (T, ρ) are marked on the plots in this chapter where relevant. The characteristic timescale τ_M was calculated using Eq. (5.20) for heating model $\mathcal{H} = \rho^{1/2}T^{-7/2}$, $\tau_{\rm cond}$ calculated from Eq. (5.38), $\tau_{\rm rad}$ from Eq. (5.40), and $\tau_{\rm visc}$ from Eq. (5.39). For the appropriate timescales a range of magnetic field strengths (and β) is indicated.

cooling. A more realistic view is a combination of cooling and heating that sustain the coronal temperature for sufficiently long time. Thus, $\tau_{\rm rad}$ and the characteristic timescales τ_1, τ_2 derived here describe fundamentally different physical processes. The former, determined by the magnitude of $\mathcal{L}$, shows how quickly the hot plasma cools down by radiation if for some reason the heating process switches off. An example of this may be the impulsive heating event from a flare, studied in Aschwanden and Schrijver (2011). In contrast, τ_M describes how quickly the plasma returns to the thermal equilibrium (or leaves it) being perturbed, and thus it is determined by the derivatives of the heat/loss function, and is essentially independent of the magnitudes of the heating and cooling processes. We note that the term thermal equilibrium in this sense means the background loop conditions do not vary much over the wave period ω, and that the loop itself may still be part of a limit cycle (Klimchuk 2019). The radiative timescale does not reflect if the effect of misbalance between heating and cooling is important for the slow magnetoacoustic wave, particularly if the magnetic field is not strong enough to be well approximated by the zero-β limit but in the zero-β case too. The error of dismissing the effects of heating and cooling upon a slow magnetoacoustic wave, because of estimates of the radiative cooling time $\tau_{\rm rad}$, has been made in previous works such as Sigalotti et al. (2007); Wang et al. (2015). This serves as a warning: **when dealing with non-adiabaticity, the heating/cooling imbalance may have a great effect on the slow wave even if $\tau_{\rm rad}$ is far from the wave period ω.** We propose the comparison of timescales τ_1, τ_2 and, if the wave is weakly non-adiabatic, $\tau_{\rm M}$ against the period (ω) is a better indicator of the relevance of thermal misbalance.

5.4 Conclusions

The widespread relevance of the heating/cooling misbalance has an important implication for the measurement of the effective polytropic (adiabatic) index in the solar corona, performed by Prasad et al. (2018, 2019); Van Doorsselaere et al. (2011) for sunspot coronal loop fans, and for the analysis of cool coronal rain in Vashalomidze et al. (2019). It was shown in Zavershinskii et al. (2019, e.g. see Fig. 2) that the wave-induced perturbation of the equilibrium manifests an effective adiabatic index, which is not accounted for in the observational studies. In the same way that thermal conduction introduces a phase shift between the density and temperature perturbations for slow waves (Owen et al. 2009), so the heating/cooling misbalance will also introduce a phase shift. Moreover these phase shifts are not mutually exclusive. This combination may explain why the polytropic indices determined from observations are so different to their corresponding theoretical values calculated from

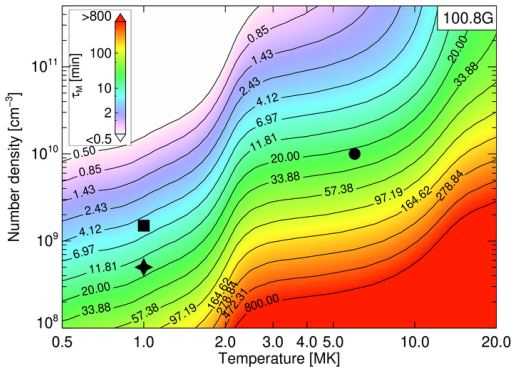

(a) Plot of τ_M with $c = 0$ at 100 G.

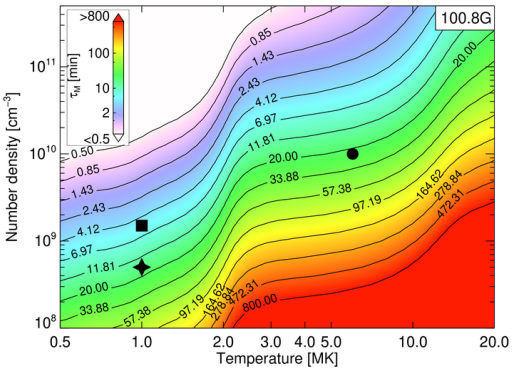

(b) Plot of τ_M with $c = 1$ at 100 G.

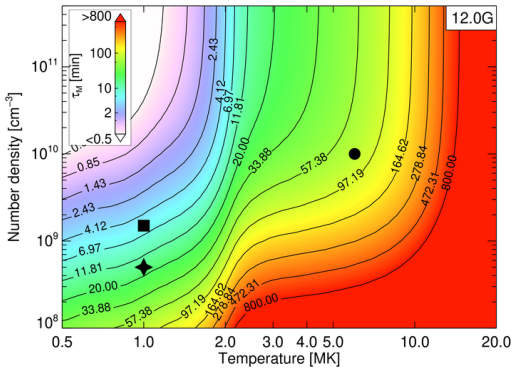

(c) Plot of τ_M with $c = 0$ at 12 G.

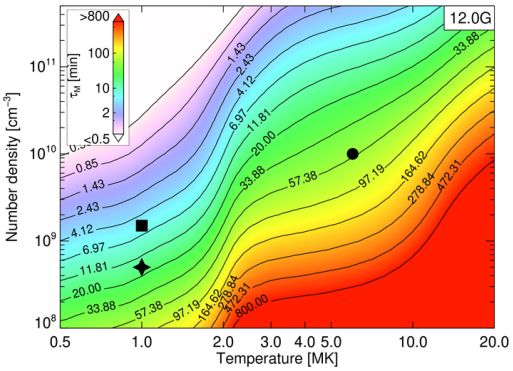

(d) Plot of τ_M with $c = 1$ at 12 G.

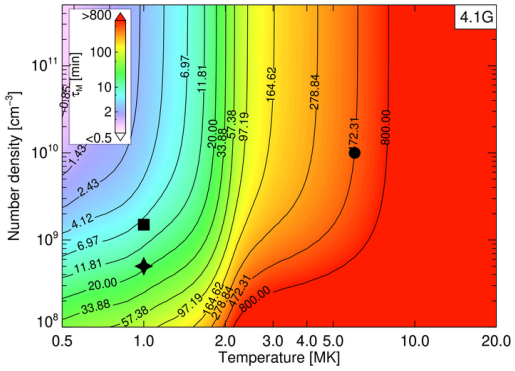

(e) Plot of τ_M with $c = 0$ at 4.1 G.

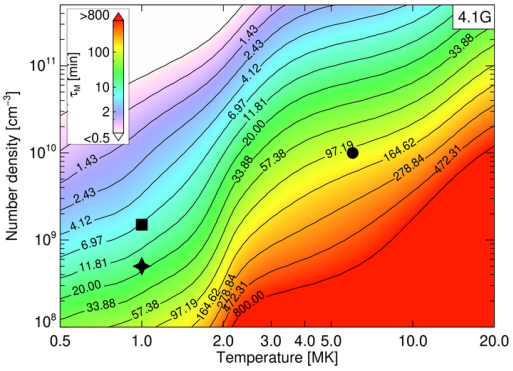

(f) Plot of τ_M with $c = 1$ at 4.1 G.

Figure 5.5: Variation of the characteristic damping timescale τ_M with magnetic field, and with different power law index c where $\mathcal{H} \propto \rho^{1/2} T^{-7/2} B^c$. Scanning down the column shows how the damping time changes as magnetic field B_0 decreases: $[a,b]$ at 100.8 G (practically infinite), $[c,d]$ at 12.0 G, $[e,f]$ at 4.1 G. Comparing left-to-right shows the effect of a different power law index c (left side $c = 0$, right side $c = 1$), whilst all other parameters are held the same. Symbols correspond to specific plasma conditions (see Table. 5.2).

the damping lengths assuming only Spitzer thermal conductivity, consistent with the discussion in Prasad et al. (2018, 2019). The strong damping from wave-induced thermal misbalance of the equilibrium, which we have shown will be different in plasma with different ρ_0, T_0 and B_0, may also explain why the measured damping lengths do not seem to change in line with the change in temperature as is expected Prasad et al. (2019); Wang (2011). In summary, the effect of wave-induced thermal misbalance is likely to be an important contributor to the effective adiabatic index in the solar corona, and should be explored in future studies.

The characteristic timescales of wave-induced thermal misbalance vary with T_0, ρ_0, B_0, as well as the free parameters dictating coronal heating a, b, c. Typical values of the magnetic field in coronal structures are difficult to observe directly, relying on seismology (see Chapter 2). However these are generally agreed to vary between around 1 G in coronal holes, up to several thousands of Gauss in exceptionally strong active regions (Anfinogentov et al. 2019). Thus an assumption of the limit of infinite magnetic field strength will break down in certain pertinent situations, particularly for hot dense loops. The effect upon the damping time $\tau_{\rm M}$ of a weaker magnetic field may be seen in Figure 5.5, for two different heating models. Looking purely at the effect of magnetic field (scanning downwards in Fig. 5.5) across the range of typical coronal magnetic field strengths, the damping time can vary due to finite-β effects, particularly over ~ 2 MK; the change in magnetic field strength has the most pronounced effect on hotter, denser plasma whereas the cooler loops and plumes remain largely unaffected. There is a difference introduced by the change in dependence of $\mathcal{H}$ upon B (scanning left to right in Fig. 5.5), but this is apparent only for lower magnetic field strengths; at infinite magnetic field, there is no difference between damping times for the two heating models. For this heating function the magnetic heating power law index dependence ($c = 0 \rightarrow c = 1$) has made the damping time vary *less* with magnetic field strength. We note also that in the instability criterion for slow magnetoacoustic waves (Eq. 5.32), the parameter c acts to stabilise the plasma when positive, and destabilise the plasma when negative. We stress that some finite-β effects are irrespective of the heating/cooling function, whilst further effects may occur if there is any dependence of Q upon of magnetic field. Moreover Q is a function of B only if the heating term $\mathcal{H}$ is a function of B, since the radiative losses $\mathcal{L}$ are known to be independent of B as the radio emission is a small fraction of the full flux. Understanding the finite-β effects upon the non-adiabatic damping and instabilities of slow magnetoacoustic waves is therefore important, as this may impact the observational constraints found upon the coronal heating function using the instability criteria (Eqs. 5.35–5.36).

The key results of this chapter may be summarised into the following:

1. The effect of wave-induced thermal misbalance upon slow magnetoacoustic waves is important for a wide range of coronal conditions (see Figure 5.4). This is backed up by the comparison in Table 5.2 between the characteristic timescales for damping by thermal misbalance τ_M, for damping by thermal conduction $\tau_{\rm cond}$ (Eq. 5.38), compressive viscosity $\tau_{\rm visc}$ (Eq. 5.39) and for the radiative cooling alone $\tau_{\rm rad}$ (Eq. 5.40) for three typical solar coronal environments: a hot dense loop, a warm loop, and a plume in a coronal hole.

2. The damping provided by wave-induced thermal misbalance may resolve some contradictions in observations of the damping of slow modes, since unexpected temperature dependencies and the inability of simulations to reproduce results without anomalous transport coefficients imply the presence of another damping mechanism in at least some cases (see Subsec. 5.1.1).

3. The dispersion relation governing slow magnetoacoustic waves along an infinitely thin cylinder with finite-β was derived (see Equations (5.14), (5.16)). Crucially, two timescales (τ_1 and τ_2) that characterise the effect of wave-induced thermal misbalance are generalised for the finite-β case (these timescales were found in the infinite magnetic field case in e.g. Kolotkov et al. 2019). These are inversely proportional to the combined heating/cooling functions' derivatives with respect to temperature at constant *gas* pressure, and with respect to temperature at constant *magnetic* pressure respectively (Eqs. 5.15). Additionally the effect of thermal conduction is included through its characteristic timescale $\tau_{\rm cond}$ (see Eq. 4.4, 5.38).

4. For the general situation, the derivative of the combined cooling and heating function with respect to constant gas pressure (τ_1^{-1}), and its derivative with respect to constant magnetic pressure (τ_2^{-1}), are a superior way to characterise the effect of thermal misbalance, instead of comparing Q_T, Q_ρ and Q_B separately.

5. The effect of heating/cooling misbalance in the limit of weak non-adiabaticity was found, applicable for waves in which the exchange of energy with the medium is only mild. Such waves propagate at the tube speed $C_{\rm T}$, and their amplitude damping or over-stability may be calculated through Equation (5.21). In this limit the two characteristic timescales for thermal misbalance may be combined into a single damping time τ_M, whose effect is additive to the damping effect from thermal conduction (Equations. (5.17)–(5.19)). Thermal conduction always acts to damp the wave, whilst the sign of τ_M may be positive (enhanced damping) or negative (reduced damping or over-stability). See Table. 5.1 for a

breakdown of these regimes partitioned by the signs of τ_1, τ_2.

6. The thermal misbalance in the limit of strong non-adiabaticity was found, applicable for waves in which the exchange of energy with their medium is extreme (Equations. (5.23)–(5.25)). In this limit, the effects of parallel thermal conduction and the thermal misbalance are not additive. The limit of negligible thermal conduction (Eqs. (5.26)–(5.26)), and the limit of negligible wave-induced thermal misbalance (Eqs. (5.28)–(5.29)) were also explored.

7. The isentropic (acoustic) and thermal instability criteria for these slow magnetoacoustic waves were expressed in terms of the characteristic timescales (Eqs. (5.32)–(5.33)). By assuming a power law dependence of the unknown coronal heating function $\mathcal{H} = T^a \rho^b B^c$, the instability criteria were rewritten as an inequality between a, b, c and the (modelled) radiative loss function. This is important because observations inform us that the corona is usually not unstable to these instabilities, and so we show a new way the unknown coronal heating function may be constrained. In a broad range of the coronal temperatures and densities, plausible heating models based on the stability of the acoustic and thermal modes are found in the infinite magnetic field limit (see Fig. 5.2). In particular, the widely used heating models from Ibanez S. and Escalona T. (1993) are all shown to be potentially unstable to the thermal mode in the regime of suppressed thermal conduction.

The seismological application of the theory developed here would be a great asset to the community. Not only could observations of instabilities (or lack thereof) constrain a, b, c in the manner described in Subsection 5.3.1, but if the heating function were modelled then observations of slow modes may be used to probe the magnetic field or thermal equilibrium in a similar way to Nisticò et al. (2017). Relating back to the multi-modal observations in Chapters 2–3, since any dispersive process can affect different longitudinal harmonics differently, any observations of propagating modes evolving into wavetrains or of standing modes with multiple harmonics may also yield information about the thermal equilibrium. There may be potential for repeating the work in Kumar and Kumar (2010) to find the effect on the $P_1/2P_2$ ratio, using the dispersion relation here – although on balance, because standing slow modes are rarely observed compared to the ubiquitous propagating slow modes, effort would be better spent applying the theory here to observations such as in Chapter 4. This is the target of future work. The reader will certainly agree that the physics of slow magnetoacoustic wave-induced thermal misbalance is an extremely rich area, with huge potential for constraining the unknown coronal heating model in particular.

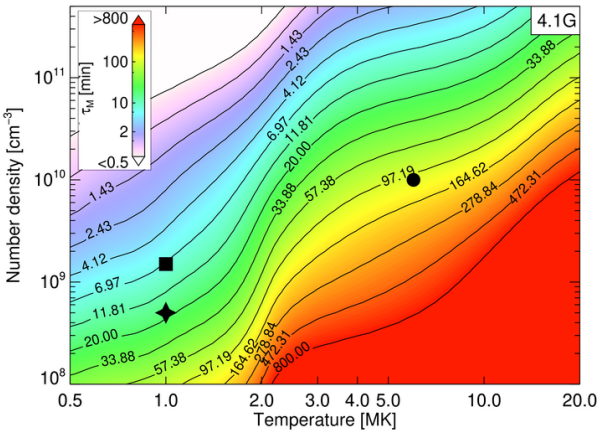

(a) Plot of τ_{M} with $\mathcal{L} \propto B^1$.

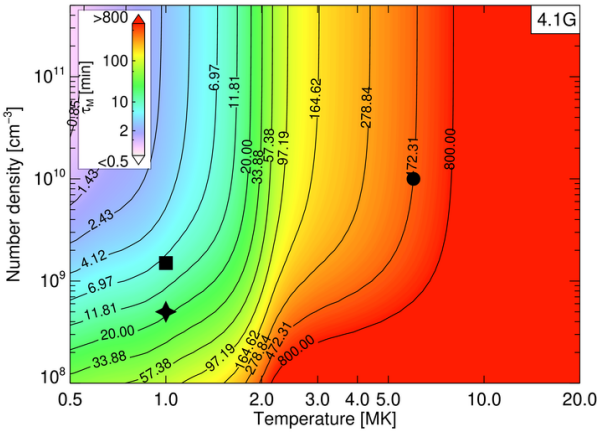

(b) Plot of τ_{M} with $\mathcal{L}$ having no dependence on B ($c = 0$).

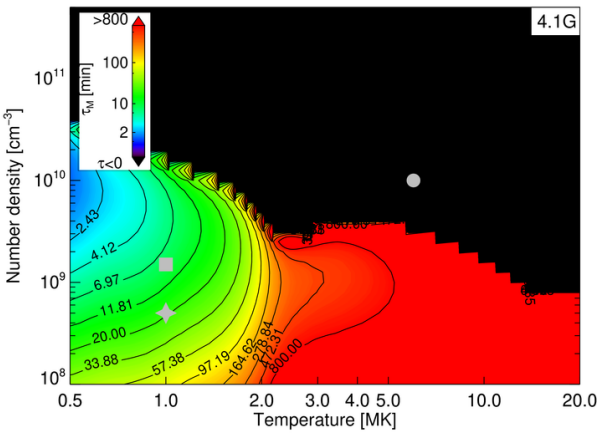

(c) Plot of τ_{M} with $\mathcal{L} \propto B^{-1}$

(d) INCLUDE? Variation of the characteristic damping timescale τ_{M} with different power law index c, where $\mathcal{L} \propto \rho^{1/2} T^{-7/2} B^c$, in the limit of weak non-adiabaticity (Eq. 5.20) and at a magnetic field strength of 4.1 G. Regions of black indicate the conditions for which the plasma is unstable to the slow-mode (the coarseness is from limited resolution of $\mathcal{L}$). The symbols refer to example values in Table. 5.2. In this case the destabilising effect from the $c = 1$ dependence has caused instability for hot dense plasma.

Chapter 6

Summary

The research presented in this thesis concerned the application of coronal seismology, that is relating the detection and analysis of oscillatory motions in the solar corona back to the local hosting plasma properties, through the theory of magnetoacoustic waves. In particular the role of dispersion on such magnetoacoustic modes, and how this may affect observations taken by SDO/AIA, is studied.

Chapter 1 introduces the composition of the Sun and describes the odyssey undertaken by energetic photons produced in the core, whose energy eventually makes its way out into the optically thin solar corona: the focus of attention in this thesis. The properties, morphology and observational implications of the solar atmospheric plasma is described in Section 1.1, and the mathematical framework of magnetohydrodynamics appropriate for magnetoacoustic waves in the context of the corona is outlined in Section 1.2.

In Chapter 2 the large amplitude, rapidly decaying transverse kink-mode oscillation is the focus. The theory behind these oscillations is described, including the successes of the theory of resonant absorption as a damping mechanism. The advantages of using multi-modal observations to extract information about the plasma inhomogeneity are explained. The first spatially resolved observation of a coronal loop oscillation comprising of the fundamental standing kink mode and its third harmonic is presented. The co-existence of the fundamental and third harmonic standing modes is verified by using their amplitude and phase distributions along the loop, and their periods are found to be 7.9 minutes for the fundamental mode and 3.0 minutes for the $n = 3$ harmonic. The period ratio of $P_1/3P_3$ is found to be 0.87, implying there is a non-uniform kink speed along the loop which may be caused by density stratification in particular. For the first time with spatially resolved data, the signal quality for a higher harmonic of a kink oscillation is reported, and compared with the signal quality of the fundamental mode. The measured signal qualities were ~ 3.4 for the fundamental mode, ~ 3.6 for the third harmonic, and crucially

these values agree everywhere along the loop within error. This further verifies one-dimensional resonant absorption theory. Further theoretical work examining the effect of a spatially varying transverse density profile upon different harmonics' resonant absorption is required, to unlock any further seismological potential of this approach.

In Chapter 3 the focus is on a different regime of transverse oscillation, in which the amplitudes are much smaller and there can be little or no damping – hence these are named decay-less kink oscillations. A detailed history of the observations and studies on decay-less oscillations is given, and their explanation as standing kink mode oscillations is asserted. The first detection of a higher harmonic of a decay-less kink oscillations is presented. This was achieved using motion magnification, and the two dominant periods of oscillation were found to be $10.3^{+1.5}_{-1.7}$ minutes and $7.4^{+1.1}_{-1.3}$ minutes. The spatial distribution of spectral power into nodes and anti-nodes throughout the loop, and anti-phase behaviour between the two legs was used to confirm the veracity of these oscillations as natural responses of the loop at the fundamental kink-mode frequency and its second harmonic. The potential for routine seismology using decay-less oscillations (which are extremely commonplace in the corona) is discussed, using as a demonstration the measured period ratio of $P_1/2P_2 \approx 0.69 \pm 0.16$ to arrive at a density stratification height of 7–45 Mm, assuming all dispersion in the loop is caused by longitudinal density structuring. The implications of the detection of higher harmonics of decay-less oscillations upon the unknown driver is deliberated.

Chapter 4 shifts from fast kink-mode oscillations to slow mode oscillations, which are commonplace in the lower corona. The theory behind slow mode oscillations is described, in particular their prevalence in the solar atmosphere above sunspots and how thermal conduction is thought to be the main damping mechanism in coronal conditions. Observations of propagating intensity disturbances in a coronal fan are presented, in bandpasses 171 Å and 193 Å. For the first time a measurement of instantaneous period against instantaneous velocity is presented, and no correlation is found. This relied on novel approaches to reliably measure periods of perturbations less than 5% above a strongly varying background, and to measure the slopes on time-distance maps. Justification of the interpretation of these continuous, propagating intensity perturbations as slow-modes is given through statistics of their periods, which remained remarkably stable over two hours of observation. Amplitude modulation of the intensities is seen, which may support the idea that these coronal slow modes are externally driven by photospheric p-modes. Interestingly it was seen that the velocities seen in 193 Å were on average *slower* than those seen in 171 Å. This is unexpected since we expect such slow waves to propagate at the local

sound speed, which for plasma seen in a hotter channel (such as 193 Å) should be faster than in a cooler channel. This discrepancy may be explained by a different propagation angle in the plane of sky between the waves seen in 171 Å and 193 Å, which we estimate is a difference of about 10° (with the latter being closer to the vertical). In particular this would appear to support the theory of coronal loops being composed of several distinct multi-thermal strands.

Chapter 5 is concerned with the theory describing the dispersion effects on slow magnetoacoustic waves by any (wave-induced) misbalance between plasma heating and cooling processes. The wave can experience a back-reaction, either losing or gaining energy from the plasma, meaning the solar corona acts as an active medium for slow magnetoacoustic waves. This is important because these slow magnetoacoustic modes may probe the poorly understood thermal equilibrium. Previous studies by a range of authors on incorporating the effect of thermal imbalance in the dispersion of slow modes are discussed. The dispersion relation describing slow magnetoacoustic modes guided by a thin flux tube, incorporating a wave-induced thermal misbalance term and thermal conduction, is derived. It is found that the characteristic timescales of the wave-induced heating/cooling misbalance may be expressed in terms of the partial derivatives of the combined heating/cooling function with respect to constant gas pressure and constant magnetic pressure. The slow wave's dispersion relation is examined in the limit of strong non-adiabaticity and in the limit of weak non-adiabaticity, fully incorporating the magnetic field. We demonstrate that in a broad range of coronal plasma densities and temperatures, the characteristic time scales coincide with the periods of slow magnetoacoustic waves observed in the corona, meaning the effect of heating/cooling misbalance upon these waves should not be neglected. Such effects may explain discrepancies of recent observations with theory assuming slow wave damping from thermal conduction and compressive viscosity alone.

We show how the stability of the slow magnetoacoustic mode and the thermal mode may be used to constrain the unknown coronal heating function in Section 5.3. The corona is observed to be stable to the thermal instability over a huge range of temperatures and densities (with the exception of coronal rain). Slow modes in the corona are only ever observed to damp and not be over-stable, thus the isentropic (slow mode) instability must be also suppressed. Using a parameterisation of the unknown coronal heating function $\mathcal{H} = \rho^a T^b B^c$, we express the thermal and isentropic instability criteria in terms of a, b, c, and hence provide constraints on the heating model $\mathcal{H}$. In particular, all five coronal heating models suggested in Ibanez S. and Escalona T. (1993) lead to a thermal equilibrium which is unstable to the thermal mode, which we would contest contradicts observations.

Appendix A

Time series analysis

Coronal seismology relies on extracting as much information as possible from observations of coronal oscillatory motions. The detection of waves can be difficult, having typical periods in the corona of several seconds to many minutes and spatial scales dependent on the plasma inhomogeneity. Thus the use of time series analysis to extract as much information is integral to the work in this thesis.

A.1 Discrete Fourier Transform and Periodograms

The most widely known technique for decomposing a time series into its constituent frequencies is the *Fourier transform*, which converts a signal from the time domain into the frequency domain in a reversible way. For solar data the signal is not continuous nor of infinite length, so the idealised Fourier transform is replaced by the *Discrete Fourier Transform* (DFT) which replaces the infinite integral with a finite sum:

$$\text{(Forward DFT)}: \quad X(\omega_k) = \sum_{k=0}^{N-1} x(t_n) \exp(-i\omega_k t_n), \qquad k = 0, 1, 2 \ldots, N-1 \tag{A.1}$$

$$\text{(Inverse DFT)}: \quad x(t_n) = \frac{1}{N} \sum_{n=0}^{N-1} X(\omega_k) \exp(i\omega_k t_n), \qquad n = 0, 1, 2 \ldots, N-1 \tag{A.2}$$

where $x(t_n)$ is the input signal amplitude at time t_n, t_n is the n^{th} sample out of the total of N samples, ω_k is the k^{th} frequency sample, and $X(\omega_k)$ is the spectrum of x at frequency ω_k. This transform assumes evenly spaced samples, say of sampling period ΔT so $t_n = n\Delta T$, and with no missing samples. When computing the DFT

or its inverse, virtually all computing programs utilise a universally known, efficient algorithm called the *Fast Fourier Transform*. It is important to note that while $N \in \mathbb{Z}$ and $\Delta T \in \mathbb{R}$, in general the time domain data and its spectrum may be complex ($t, \omega \in \mathbb{C}^N$). In the case that the input time series is real ($t_n \in \mathbb{R}$), its spectrum will be symmetric such that $X(\omega_k) = (X(\omega_{N-k}))^*$. To visualise the Fourier spectrum a choice must be made, since complex numbers are two dimensional: in this thesis was plotted the square of the magnitude $|X(\omega_k)|^2$ against frequency ω, called the *power spectrum*. Peaks in the power spectrum (*spectral peaks*) reveal periodicities within the time series data as well as the relative strengths of any periodic components, thus allowing seismology to begin. One could choose to show the phase spectrum of the frequencies, although for genuine data the phase spectrum is typically noisier and far more difficult to interpret than the amplitude (power) spectrum, and was not included in this thesis.

For a time limited dataset, there is a finite frequency resolution since the DFT is only defined for *natural frequencies* $\omega_k = 2\pi k(\Delta T)^{-1}/N$, which are spaced evenly apart by $\frac{1}{N\Delta T}$ (also called *bins*). The lowest resolvable frequency is $\frac{1}{N\Delta T}$, and the highest (the Nyquist frequency) is $\Delta T/2$. The only way to increase frequency resolution (the ability to resolve two peaks close in frequency) is to let the input data run for more time. Increasing the sample rate but keeping the total signal time constant increases the *bandwidth* (range of frequencies covered), by allowing higher frequency components to be resolved.

A finite time limit is equivalent to a rectangular window function, which becomes a sinc function in Fourier space: thus even data of a single frequency will be convolved with a sinc function and generate sidelobes which introduce unwanted *spectral leakage*, which is distributed to other frequency bins. This effect may be mitigated by convolving the time series with a window function of the same length, called *apodization*. By choosing a different apodization function (such as a Hanning function) which tapers towards the data boundaries, these sidelobes are reduced and less spectral energy is spread across other frequencies, at the expense of slightly widening the spectral peaks and losing some spectral resolution. For the coronal seismology in this thesis, using AIA data sampled at 12 seconds to measure periodicities of a few minutes, it is found that there was more need to suppress leakage in order to detect low amplitude periodicities, as opposed to resolve between two periodicities close in frequency, and hence a Hanning apodization filter was used. Zero-padding was applied for all plots of power spectra in this thesis, as well as subtraction of the mean prior to input into the FFT, in order to upsample the DFT from the natural frequencies for ease of interpretation – such considerations of zero-padding and choice of window filter apply to the bandpass filter as well.

In the case of uneven sampling or gaps in the data, which often occur for satellite observations, the DFT base functions are no longer orthogonal and hence may not be used to reconstruct the original signal. This may be remedied using interpolation, however this process may cause issues and the noise is no longer distributed in a statistically calculable way. Disregarding the phase spectrum one may instead calculate the *periodogram*, which estimates the spectral power at particular frequencies. In contrast with the DFT the user specifies the frequencies at which the periodogram is calculated, though confined by the same intrinsic limitations all time series face (e.g. Nyquist frequency, aliasing). When the time series is evenly sampled, its periodogram is equivalent to $\frac{1}{N}|DFT(\omega)|^2$. One efficient calculation of the periodogram is the Lomb-Scargle periodogram, proposed independently by Lomb (1976) and Scargle (1982), using a least-squares fitting to the data of sinusoids with differing frequencies and calculating the χ^2 goodness-of-fit statistic at each frequency. Another advantage of the Lomb-Scargle periodogram is the way in which white noise is statistically distributed and it is invariant to time translation. The implementation I_X used for this thesis, applied in situations where the FFT was inappropriate, was written based on the method described in Horne and Baliunas (1986):

$$I_X(\omega) = \frac{1}{2}\left\{ \frac{\left(\sum_n X_n \cos\left[\omega(t_n - \tau)\right]\right)^2}{\sum_n X_n \cos^2\left[\omega(t_n - \tau)\right]} + \frac{\left(\sum_n X_n \sin\left[\omega(t_n - \tau)\right]\right)^2}{\sum_n X_n \sin^2\left[\omega(t_n - \tau)\right]} \right\}, \tag{A.3}$$

where X_n is the signal at time t_n and τ is defined as

$$\tau = \frac{1}{2\omega} \arctan\left(\frac{\sum_n X_n \sin(2\omega t_n)}{\sum_n X_n \cos(2\omega t_n)} \right). \tag{A.4}$$

A.2 Wavelet analysis

One of the intrinsic properties of waves and oscillations in the solar corona is their transient nature, and the temporal modulation of the amplitude and period called *non-stationarity*. To extract temporal information from such a non-stationary signal the DFT is not suitable, and instead the popular *wavelet transform* may be more appropriate. Defined as the convolution of the time series with many scaled versions of a mother function, such as the Morlet function, the continuous wavelet spectrum yields information about the spatial, temporal and phase behaviour of the signal.

The *global wavelet spectrum* (GWS) may be found by averaging the wavelet spectrum in time, and provides a consistent estimation of the true power spectrum of a time series. In order to gain spatial information about the periodicities in the signal, a trade-off is made with spectral resolution versus the DFT, due to the width of the wavelet filter in Fourier space. The wavelet spectra calculated for this thesis were calculated with programs based on the popular software explained in Torrence and Compo (1998).

A.3 Detrending

One of the important issues in the data analysis of observations of coronal EUV observations is *detrending* of time series (for data such as that seen in Figure 4.4). The DFT of a signal which has a large amplitude, low frequency component compared to the frequencies of interest inevitably leads to a spectrum above which a higher frequency peak would struggle to be differentiated from noise. There are some statistically based techniques developed to account for a trend when evaluating the significance of a spectral peak. It is usual to consider the underlying power spectrum as manifested from *coloured noise*, such that the power spectral density of a "pure noise" time series is proportional to $|f|^{-\alpha_n}$, α_n being the "colour". White noise corresponds to $\alpha_n = 0$ such that the noise is evenly distributed with frequency. Modelling all noise in data as white noise is common due to statistical ease, since white noise follows a $\chi^2(2)$ distribution (because the real and imaginary parts are both drawn from a Gaussian distribution, Scargle 1982), but this is rarely justified for real data. Red noise corresponds to $\alpha_n = 2$, which is biased to lower frequencies and indicates there is some dependence between a data point and its previous – the system has a memory. Usually for on-disk solar data the power spectrum exhibits a power law somewhere between that red and white noise. The standard significance test for wavelet spectra, following Torrence and Compo (1998), essentially takes the background power law, assumes a $\chi^2(2)$ distribution, and plots the 95% confidence interval above the background as a threshold for significance. Caution must be used, as pointed out in Auchère et al. (2016). Pugh et al. (2017) devised a method to identify statistically significant periodic signals in time series studying flare data, which accounts for the underlying spectrum by fitting to a broken power law (white noise for high frequencies, red for low frequencies). Such techniques are appropriate for time series with many data points, but in this thesis this was not always possible, due to the limitations of EUV instruments, or the rapid damping of oscillations for example. Some detrending was required on occasion, the trend varying in x-t space (be comprised of a broad range of usually low frequencies). A major difficulty

of detrending lies in the user-dependence of the filter used: the choice of length for a running average (boxcar) combined with a choice of start and end time gives much leeway for user influence (for example false periodicities often appear after detrending the data used to study flares, yet detrending is necessary: see Dominique et al. 2018). Nonetheless the standard method to calculate the trend is to subtract a smoothed version of the time series convolved with a filter whose length far exceeds the periodicity of interest, from the original. Alternatively a low-order polynomial or spline is fitted to the data and then subtracted. In Pascoe et al. (2017a) it is noted that there is no theoretical justification for a polynomial trend nor its choice of order, so their trend was calculated by interpolating the points modelled to be the zeroes of the oscillation (plus a start and end) with a spline. Pixel intensity curves used in Chapter 4 were detrended using a Savitzky-Golay filter (sometimes also known as least squares smoothing) which is similar to a boxcar but vastly better at matching narrow peaks (Savitzky and Golay 1964). This uses a form of local polynomial regression to produce smoothed derivatives of the signal of the first order, second order... , for a user specified filter length and polynomial order. The Savitzky-Golay is widely used and is known in the solar community (e.g. used in Byrne et al. 2013). Since the periodicity of the signals analysed in Chapter 4 are well known (3 minutes) and measured independently, a Savitzky-Golay filter with a degree of four and filter length of 10 minutes was used to remove the background intensity variation.

An alternative to convolution with a pre-determined filter is the *auto-correlation*, where a signal is convolved with its own reversed conjugate $AC(\Delta t) = \int x(t)^* x(t + \Delta t)\ dt$. The auto-correlation is necessarily between 0 and 1, is uniquely determined (no user subjectivity) and is a function of lag Δt. Any persistent periodicities present in the time series will be present in the auto-correlation and amplified relative to the noise, making this a useful tool for searching for persistent periodicities (auto-correlations were used in this context in Kupriyanova et al. 2013). In this thesis auto-correlations were calculated via the Wiener–Khinchin theorem (that is, calculated using zero-padded Fourier transforms). The use of cross-correlations is also prevalent in the study of wave phenomena in the solar atmosphere, since the cross-correlation function between two locations will show a peak value at the lag that corresponds to the travel time of any periodic wave train that propagates between them (some examples being Reznikova et al. 2012; Zhao et al. 2016). The cross correlation may also be used to find the phase difference of the same oscillation at different locations or times (for instance confirming the phase behaviour of a fundamental standing mode in Anfinogentov et al. 2013). Other interesting phenomena may become apparent in the auto-correlation or cross-correlation function, such as amplitude modulation and time evolution.

Appendix B

Motion magnification

The advantages of improved spatial and temporal resolution of observations for the application of coronal seismology are clear, yet the time required to build new observational facilities producing data which improves upon current specifications can be many years, or be limited to only a short operational duration. Advanced data analysis techniques that maximise the seismological information mined from the available data are therefore intensively developed. *Motion magnification* is one such technique, in which an imaging sequence is processed such that small transverse motions in the plane of sky are magnified, thus acting like a microscope for videos. Motion magnification has only been applied to solar coronal data relatively recently, in order to address the large numbers of oscillatory phenomena which lie at the threshold of current observational capabilities.

An important example of coronal oscillations detected at the cusp of currently available spatial resolution is the regime of low-amplitude, long lived transverse oscillations of coronal loops known as *decay-less kink oscillations* (see Chapter 3). Decay-less oscillations are ubiquitous in the corona and their average amplitude has been measured at 0.17 Mm with a standard deviation of 0.1 Mm (Anfinogentov et al. 2015), thus these oscillations are of lower amplitude than a typical EUV imager's pixel size. For example AIA has a plate scaling of ~ 0.6 arcsec/pixel, and assuming the average distance of SDO from the Sun 1.49×10^{11} and $R_{\odot} = 636$ Mm (or use FITS keywords DSUN_OBS and RSUN_OBS) implies that a pixel corresponds to just over 0.42 Mm. Such small displacements of less than one pixel are only visible in conventional movies of SDO/AIA data because the changes in intensity are seen in several pixels across the loop, whose minor radius is typically blurred across a half dozen pixels (for a discussion on the spatial scales of loops seen with EUV imagers see Williams et al. 2020). The use of motion magnification can accentuate these displacements in a consistent way and thus allow their more complete analysis.

The motion magnification routine presented here has been applied to EUV

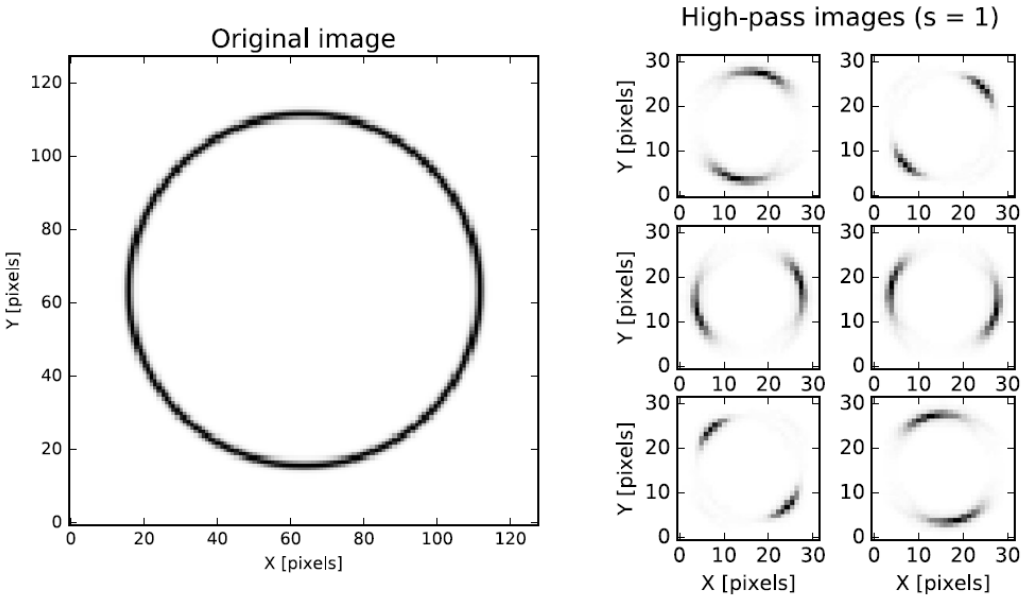

Figure B.1: Illustration of the high-pass components of the DT$\mathbb{C}$WT transform of an annulus [*left*]. [*Right*] The absolute values of the six high-pass images for a single spatial scale ($s = 1$), which clearly show the different orientations of the wavelets. This figure was taken from Anfinogentov and Nakariakov (2016).

observations of decay-less oscillations in Anfinogentov and Nakariakov (2019) and Li et al. (2020), in addition to the results presented in Section 3.2 corresponding to Duckenfield et al. (2018).

B.1 Dual-tree complex wavelet transform implementation

The motion magnification routine used in this thesis is discussed clearly in Anfinogentov and Nakariakov (2016). This implementation is based upon the 2d Dual Tree Complex Wavelet Transform (DT$\mathbb{C}$WT), whose features include perfect reconstruction of the data, near-perfect shift invariance, and computational efficiency (Selesnick et al. 2005). A key property of the DT$\mathbb{C}$WT for motion magnification is the fact that **the local displacement (motion) between two images can be estimated from the change of phase of the DT$\mathbb{C}$WT coefficients from one image to the next**. Thus by modifying the phases of the appropriate coefficients – which are separated by spatial scale and orientation – the selective enhancement (or subtraction) of motions may be performed. Naturally there are limitations: only small motions superposed on a steady background may be magnified, the maximum magnification factor is limited to about 10 for most data, and one must always be

careful to understand and test the effect of this processing. The steps involved in the motion magnification are outlined as follows.

1. Each image in the datacube (two spatial dimensions, one temporal) is decomposed into a set of complex-valued high-pass images, which are partitioned into six differently oriented (rotated) sub bands of different spatial scales s (using wavelets as described in Sec. A.2, but complex), plus a low pass residual image (the steady background). An example of the decomposition of an annulus is shown in Fig. B.1, for a single spatial scale.

2. The phases Φ_s of each pixel in the high-pass images are calculated, and a (phase) trend Φ_s^{trend} for this pixel calculated by smoothing in the time direction using a smoothing filter of length w (a flat-top filter is used in this implementation).

3. The high frequency deviations of the phase from the trend are calculated, since these linearly relate to the small amplitude motions we aim to amplify. The result is multiplied by a magnification factor k, which amplifies the motions with a frequency less than w,

$$\Phi_s^{\text{out}} = \Phi_s^{\text{trend}} + k\left(\Phi_s - \Phi_s^{\text{trend}}\right) \tag{B.1}$$

   for each frame. Note an additional two-frame smoothing is applied to Φ_s^{out} in the time direction, in order to minimise the effect of amplified high frequency noise which is incoherent across time.

4. The absolute values of the original high-pass images are combined with the new phases Φ_s^{out}, and finally the new high-pass images and the residual low-pass image are recombined and the inverse DT$\mathbb{C}$WT computed.

This implementation of motion magnification is designed to amplify rather broadband motions, allowing us to address multi-modal and non-stationary oscillations which are commonplace in coronal observations. The magnification is independent of oscillation period for a broad range of periods, and gives good results for both harmonic and quasi-harmonic non-stationary oscillations. The algorithm is freely available on Github courtesy of Dr. Sergey Anfinogentov, and is implemented in Python and in IDL using a wrapper function provided.

B.2 Application to SDO/AIA data

The motion magnification algorithm has two parameters: magnification coefficient k and smoothing width w. The effect of the magnification factor k is obvious yet

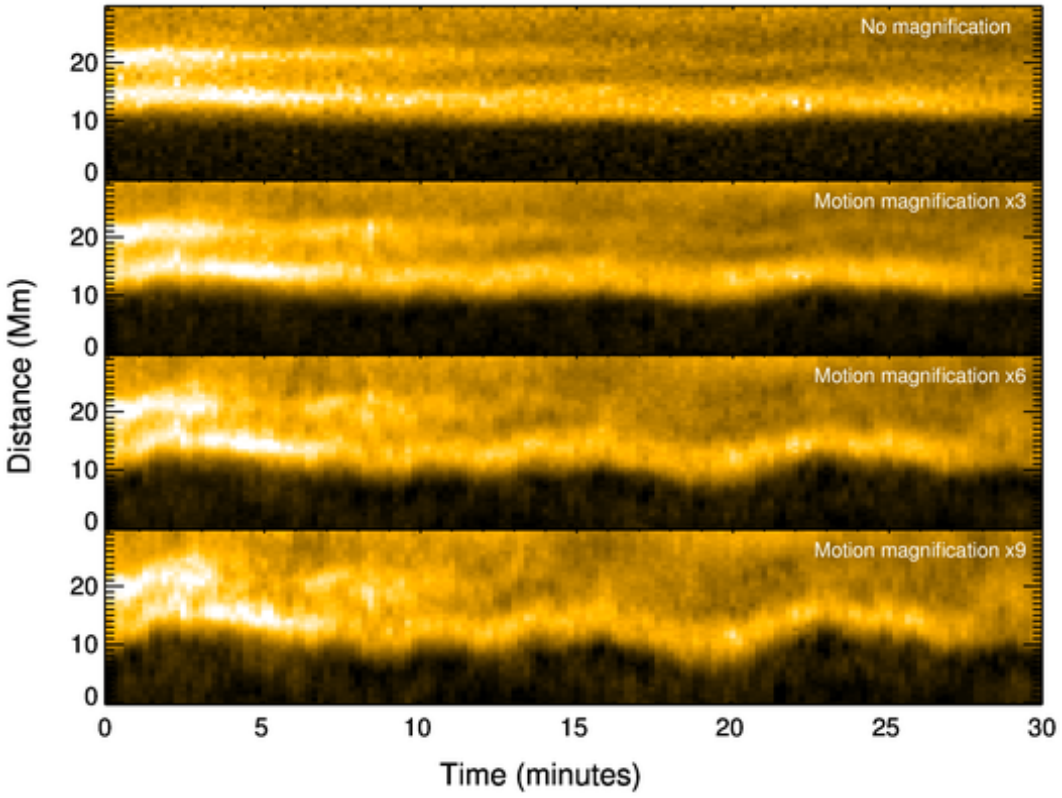

Figure B.2: Time distance maps for slit 63 near the apex, shown without magnification [*top*], and with successive images having applied motion magnification with smoothing width 50 and magnification factor $\times 3$, $\times 6$, and $\times 9$. This data corresponds to slit 63 in the analysis of decay-less oscillations in Sec. 3.2.

remarkable, as shown in Figure B.2. Previously imperceptible motions are made far more evident and the apparent amplitude increases with scaling factor, whereas the position of nodes and antinodes and hence period remains constant. It was found in Anfinogentov and Nakariakov (2016) that magnification factors up to 10 scale the test data with small amplitudes linearly, for a broad range of periods, whereas beyond magnifications of 10 the effect of noise becomes overwhelming. In Li et al. (2020) this linear scaling was used to infer the original oscillation amplitude from data which had been motion magnified by a factor of $\times 9$ (the smoothing width was not disclosed). The initial amplitudes must not be too great – however this is not a concern because amplitudes of a few pixels are easily seen on an unprocessed time-distance map. The transverse oscillations of interest in this thesis are standing kink mode oscillations with expected period of the order of $P \sim 5$ minutes $= 25$ frames, and so the smoothing widths must be chosen to be greater than this to ensure these frequencies are magnified sufficiently.

As can be seen from Figure B.3, the waveform visible after motion magnifica-

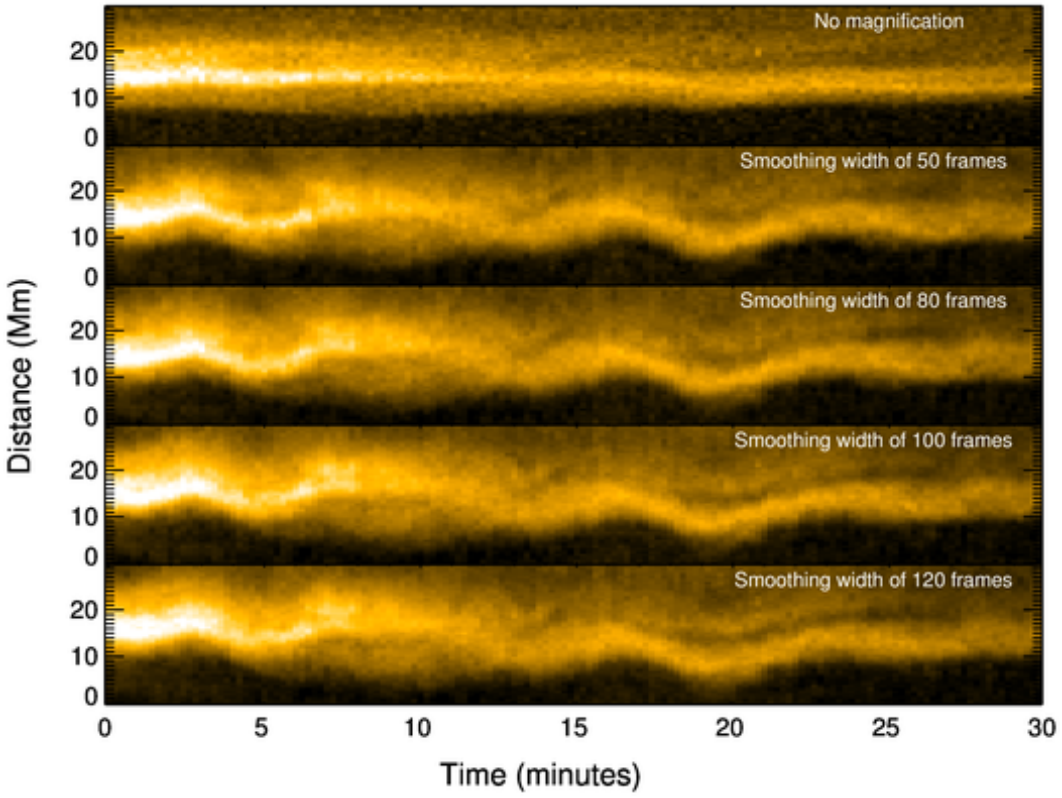

Figure B.3: Time distance maps showing tests of different smoothing widths, for a dataset with low-level transverse displacements of approximately 7 minute periodicity, with a constant magnification factor of $k = 6$. [*Top*] Time-distance map before motion magnification, and the subsequent time-distance maps utilised smoothing widths of 50 frames (10 min), 80 frames (16 min), 100 frames (20 min) and 120 frames (24 min). This data corresponds to slit 74 in the analysis of decay-less oscillations in Sec. 3.2.

tion is indeed independent of smoothing width if $w > P$. Note that *any* periodicities below w will be magnified honestly, therefore processing before magnification must be kept to a minimum. For instance the solar equator has an average rotation period of about twenty five days corresponding to a linear rotation speed of 2 km/s $\sim$ 17 pixels per hour for SDO/AIA data, depending on distance from disc centre, which introduces a periodic change to derotated data as the object jumps across pixels. In this thesis any interpolations used by standard derotation and object-tracking routines are avoided when using motion magnification to avoid magnifying artefacts.

In both Figure B.2 and Figure B.3 the original, very low amplitude oscillation can just be seen on the unprocessed data, giving confidence that the oscillations detected are not created in the motion magnification process. On the time-distance maps that have been magnified with different scaling factors, the intensities at the

point where there appears an adjacent thread or other structure appearing just above the main waveform (first five minutes) have been scaled slightly differently. The same effect is also just discernible on Figure B.3, but in the context of coronal seismology this difference is inconsequential. That there is an artefact appears from leakage where two oscillating structures are spatially close was to be expected, and as discussed in Anfinogentov and Nakariakov (2016) is mitigated by appropriate planning, and avoiding data with multiple structures along the LoS. The parameters of these oscillation profiles such as period or phase would be virtually impossible to extract with any certainty if motion magnification were not used, and a key result concerning the higher harmonics of decay-less oscillations is presented in Chapter 3 thanks to the robustness of this motion magnification technique.

Appendix C

Bayesian Inference

Bayesian statistics is a framework addressing the question of how to solve an inverse problem, and how confident one should be in the result given the collected data. The probability distributions derived from Bayesian statistics are identical to those derived from traditional (frequentist) statistics but offer a different perspective, in which probability is understood as the measure of belief in the parameter(s) of interest, and beliefs are revised in light of evidence. This is contrasted with the frequentist perspective, in which probability is considered as determining the distribution of results of many repeated measurements, assuming the "true" parameters are known. Bayesian statistics provides a robust way to infer information about the model parameters from data, a mechanism to update beliefs given new evidence, and allows a well defined quantitative comparison between the plausibility of different models.

The use of Bayesian inference in solar physics is well established, and coronal seismology in particular benefits from the principled and natural way of combining prior information, model predictions, and observations in order to provide inferences on ill-posed inversions (this point is expanded upon in Arregui and Goossens 2019). Applications include resolving multiple closely spaced periodicities in the slow magnetoacoustic waves emanating above sunspots (Marsh et al. 2008), the inference of density scale height, flux tube expansion and further parameters from observations of kink modes of coronal loops (Arregui et al. 2013, 2019; Pascoe et al. 2017a; Soler et al. 2014) and prominences (Arregui et al. 2018), and for inferring the quality factors of slow magnetoacoustic modes from many instruments (Nakariakov et al. 2019). A recent review on Bayesian coronal seismology may be found in Arregui (2018).

The aim is to obtain the set of parameters $\theta = [\theta_1, \theta_2 \ldots, \theta_N]$ corresponding to an assumed model (or models) M such that the model $M(\theta)$ best describes some observed data D. The calculation of a conditional probability uses Bayes' theorem,

which connects these in the following way (Bayes 1763; Laplace 1774):

$$P(\theta|D) = \frac{P(D|\theta)P(\theta)}{P(D)}. \tag{C.1}$$

Let us consider each term in turn.

1. The term $P(\theta|D)$ is known as the *posterior probability density function* (posterior PDF), which is the knowledge containing the information about what we think the best parameters θ are, updated by D. Computing this quantity is the main goal of Bayesian inference codes. It has as many dimensions as there are parameters in θ, and therefore has a global maximum for all parameters known as the *maximum aposteriori estimate* (MAP), which may be different to the set of most likely individual values for each parameter. To understand the most probable value of an individual parameter we must integrate over all the remaining parameters, resulting in a *marginal posterior* PDF. Taking the 5% and 95% percentiles gives an estimate of the *credible interval* for that parameter, and correspond to the confidence level of 90%.

2. The term $P(D|\theta)$ is the *likelihood function*, which describes how we expect data to be distributed for the given model $M(\theta)$, for example normally distributed with a mean θ_1.

3. The term $P(\theta)$ is called the *prior* PDF, and represents the (old) knowledge about model parameters θ before considering the new data D. For example a parameter may be known to be confined within a certain range, or the distributions inferred from previous measurements may be used. Often a uniform prior (equal probability of any parameter value) or a prior that gives equal probability in a logarithmic scale is used when no other constraints are known.

4. The term $P(D)$ is a normalisation constant called the *Bayesian evidence*, defined as the integral of $P(D) = \int P(D|\theta)P(\theta)d\theta$. This ensures the posterior PDF is between 0 and 1. Individually the Bayesian evidence has little meaning, however a comparison between the evidence of two competing models is possible using the Bayes factor $P(D|M_1)/P(D|M_2)$. The bigger the Bayes factor, the stronger the evidence favours M_1; traditionally twice the logarithm of the Bayes factor is considered strong evidence when it exceeds five, very strong when it exceeds ten. One must be careful to remember exactly what the evidence indicates – for which model is the result most consistent with the data. The Bayesian evidence is **not** saying how well the individual model fits the data.

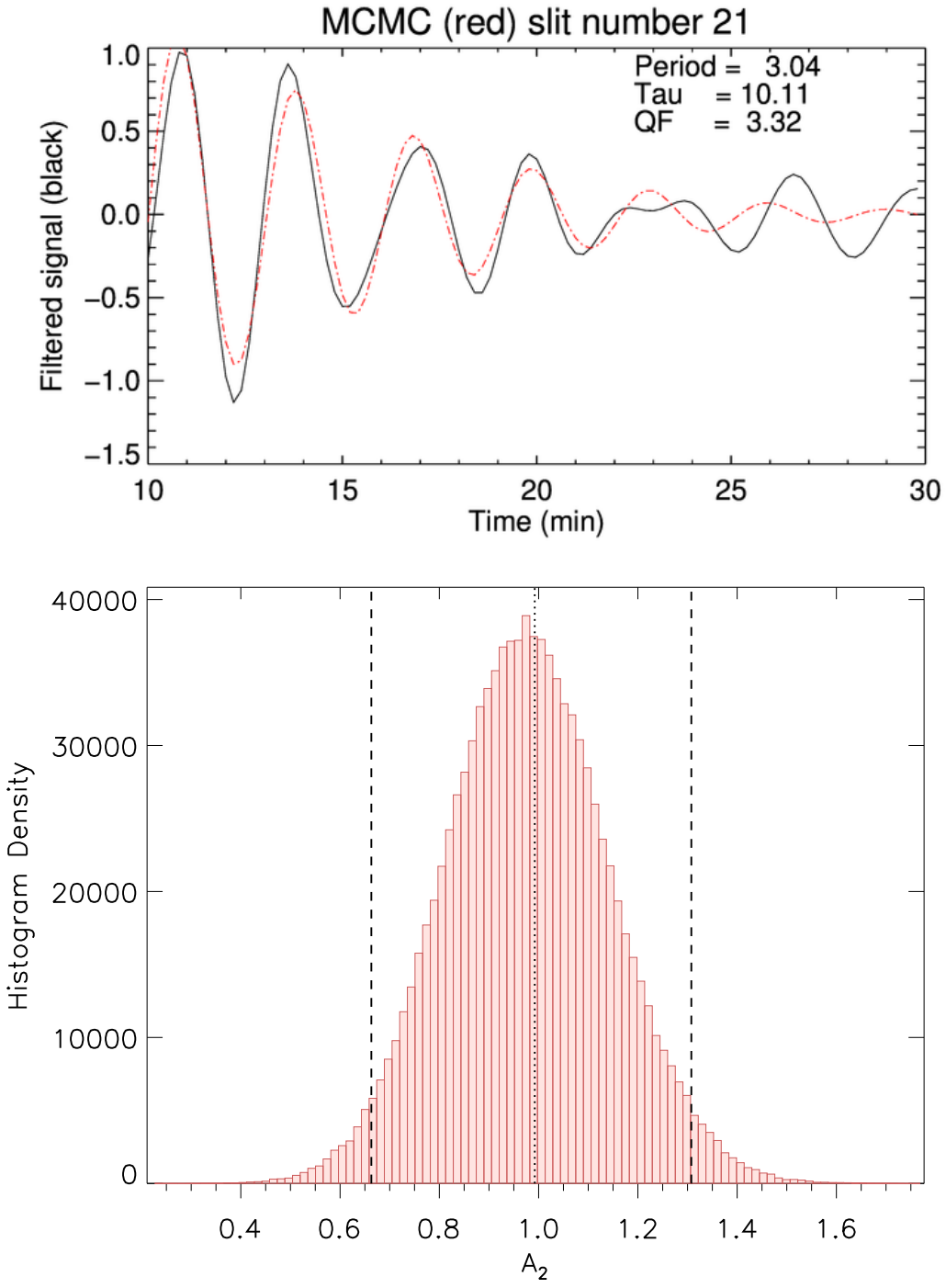

Figure C.1: An example of the application of Bayesian inference to data used in the thesis, specifically the best fitting of a (filtered) time series with a damped sinusoidal function (see Sec. 2.2, model M defined through Eq. 2.4). [*Top*] The data D used for in the Bayesian inference code is the time series in black, and the inferred model $M(\theta^{MAP}|D)$ calculated using the maximum a priori values θ^{MAP} is in dashed red. [*Bottom*] The histogram of MCMC samples for the (amplitude) parameter θ_2, which approximates the marginalised posterior PDF $P(\theta_2|D)$. The dotted line shows the value of θ_2^{MAP}, and the dashed lines correspond to the 5% and 95% percentiles.

C.1 Implementation with Monte-Carlo-Markov-Chain sampling

As explained above, Bayes' theorem allows the most probable value and corresponding uncertainties for a parameter θ_i to be calculated through a multi-dimensional integral, either to find the maximum a posteriori values $\theta = \theta_i^{MAP}$ which maximises $P(\theta|D)$ for the given model, or alternatively to find the full marginalised posterior

$$P(\theta_i|D) = \int P(\theta_1, \theta_2, \ldots, \theta_N|D) d\theta_{k\neq i}. \tag{C.2}$$

For low dimensional parameter spaces these integrals may be calculated directly, however in general a numerical approximation is more appropriate. The renowned Markov-Chain-Monte-Carlo (MCMC) algorithm allows for sampling from a probability distribution which, when constructed appropriately, yields a probability distribution (histogram) proportional to the true distribution being sampled, with more steps yielding more accuracy. In this way the posterior PDF may be estimated. An example of this is shown in Figure C.1, in which 1×10^6 samples have formed a histogram with a well defined shape, and it is clear the distribution is not undersampled. Both the MAP and the maximum of the marginalised posterior PDF agree, so we may conclude that the parameter value (amplitude) for which the model best fits the data is about 1, which looks reasonable when compared with the data. The implementation of MCMC sampling used for Bayesian inference in this thesis is the same IDL code discussed and applied in Pascoe et al. (2017a), which implements the standard Metropolis-Hastings MCMC sampler and has been made available on Github under the name of the Solar Bayesian Analysis Toolkit, courtesy of Dr. Sergey Anfinogentov.

One notable use of the Bayesian inference code throughout this thesis is the fitting of a time series to a time-distance map showing transverse displacements of a (bright) loop, which is used for subsequent analysis. At each instance of time the loop axis in the time-distance map is fitted by a forward modelled density structure (which leads to a Gaussian) plus a (spline-based) background trend. The trend is included only to improve the estimation of the peak intensity enhancements, since an asymmetric background would induce a shift in the fitted position. A demonstration of this application is shown in Figure C.2, for a moderately complicated time-distance map with several overlapping threads in the line of sight. This data comprises one of the time series used for analysis in Chapter 3 (there referred to as slit 43). In this fitting it was found that four density structures were needed in the model to keep the main "track" continuous. The density (emission) transverse profile of a coronal

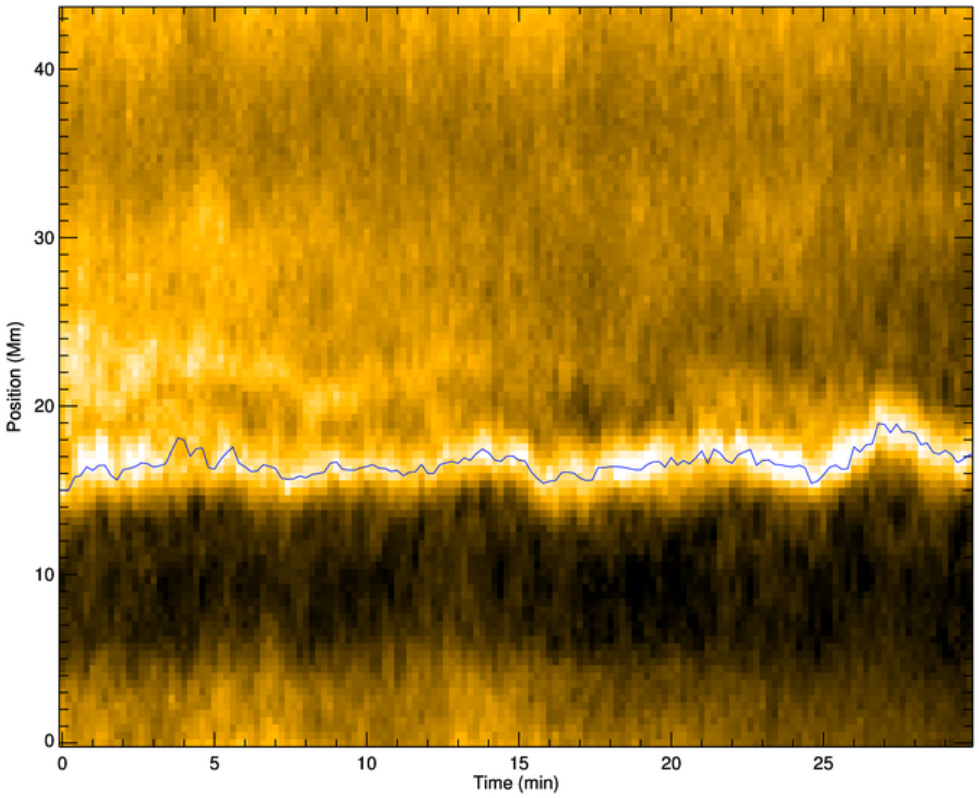

(a) Time distance map overlaid by resulting time series from the fitting procedure.

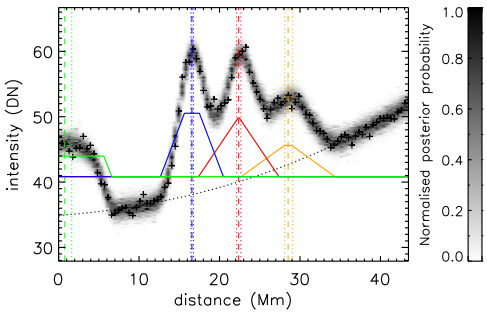

(b) Example fitting density structures to intensity profile.

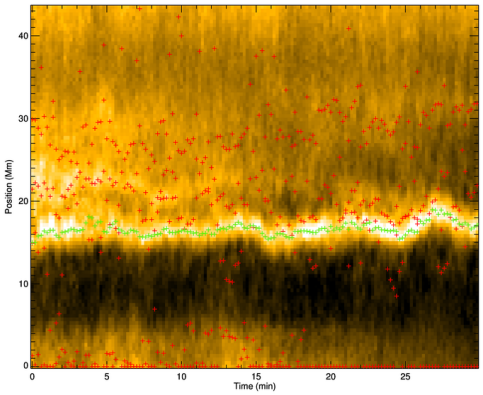

(c) Fitted density structures overlaid on time distance map.

Figure C.2: Figure demonstrating the fitting procedure on a time-distance map. [*Top*] Time-distance plot that was the input to the fitting procedure, overlaid with the resulting time series (blue) for the highest intensity structure. [*Bottom left*] Fitting of the intensity profile (black crosses) at time 3 minutes by four density structures (coloured trapezoids) and a background intensity trend. Ten thousand MCMC samples based on this four structure model are overplotted in greyscale. [*Bottom right*] All points output by the fitting procedure are shown overlaid with the main structure of interest calculated to contain the green points, whilst red points denote points with lower Bayes factors or belonging to other threads.

inhomogeneity is not necessarily a trapezoid (for a discussion see Goddard et al. 2017), but for our purposes this is sufficient to provide an estimate of the spatial position and width of the axis. Given that the transverse density profile is modelled (the blue trapezoid in Fig. C.2b), a study of the transverse density profile could be performed at this step providing more information for seismology (see Subsec. 2.1.1), however such a step is not included in this thesis. The process of inferring the loop axis position is repeated for each time instant, building up an estimate of the profile seen on the time-distance map as a time series, with the credible intervals forming an estimate of the uncertainty.

An important point is that this approach of finding the axis position at each instant of time does not assume any functional form of the loop displacement with time, and therefore any anharmonicity in the signal is preserved. Nor does this method rely on subjective "user-clicking" to acquire the time series (for example clicking was argued as the best available method in De Moortel and Brady 2007; Li et al. 2020; Verwichte et al. 2005).

Bibliography

A. Abedini. Phase speed and frequency-dependent damping of longitudinal intensity oscillations in coronal loop structures observed with AIA/SDO. *Astrophys. Space Sci.*, 361(4):133, mar 2016. ISSN 1572946X. doi: 10.1007/s10509-016-2717-0. URL http://arxiv.org/abs/1603.04207http://dx.doi.org/10.1007/s10509-016-2717-0.

A. N. Afanasyev and V. M. Nakariakov. Nonlinear slow magnetoacoustic waves in coronal plasma structures. *Astron. Astrophys.*, 573:A32, jan 2015. ISSN 14320746. doi: 10.1051/0004-6361/201424516. URL http://www.aanda.org/10.1051/0004-6361/201424516.

A. N. Afanasyev, K. Karampelas, and T. Van Doorsselaere. Coronal Loop Transverse Oscillations Excited by Different Driver Frequencies. *Astrophys. J.*, 876(2):100, may 2019. ISSN 1538-4357. doi: 10.3847/1538-4357/ab1848. URL https://iopscience.iop.org/article/10.3847/1538-4357/ab1848.

A. N. Afanasyev, T. Van Doorsselaere, and V. M. Nakariakov. Excitation of decay-less transverse oscillations of coronal loops by random motions. *Astron. Astrophys.*, 633:L8, dec 2020. ISSN 0004-6361. doi: 10.1051/0004-6361/201937187. URL https://doi.org/10.1051/0004-6361/201937187.

H. Alfvén. Existence of electromagnetic-hydrodynamic waves, oct 1942. ISSN 00280836.

F. Allian, R. Jain, and B. W. Hindman. A New Analysis Procedure for Detecting Periodicities within Complex Solar Coronal Arcades. *Astrophys. J.*, 880(1):3, jul 2019. ISSN 1538-4357. doi: 10.3847/1538-4357/ab264c. URL https://iopscience.iop.org/article/10.3847/1538-4357/ab264c.

J. Andries, I. Arregui, and M. Goossens. Determination of the Coronal Density Stratification from the Observation of Harmonic Coronal Loop Oscillations. *Astrophys. J.*, 624(1): L57–L60, may 2005a. ISSN 0004-637X. doi: 10.1086/430347.

J. Andries, M. Goossens, J. V. Hollweg, I. Arregui, and T. Van Doorsselaere. Coronal loop oscillations. Calculation of resonantly damped MHD quasi-mode kink oscillations of longitudinally stratified loops. *Astron. Astrophys.*, 430:1109–1118, feb 2005b. ISSN 0004-6361. doi: 10.1051/0004-6361:20041832. URL https://ui.adsabs.harvard.edu/abs/2005A{&}A...430.1109A.

J. Andries, T. Van Doorsselaere, B. Roberts, G. Verth, E. Verwichte, and R. Erdélyi. Coronal seismology by means of kink oscillation overtones. *Space Sci. Rev.*, 149(1-4):3–29, dec 2009. ISSN 00386308. doi: 10.1007/s11214-009-9561-2.

S. A. Anfinogentov and V. M. Nakariakov. Motion Magnification in Coronal Seismology. *Sol. Phys.*, 291(11):3251–3267, nov 2016. ISSN 1573093X. doi: 10.1007/s11207-016-1013-z.

S. A. Anfinogentov and V. M. Nakariakov. Magnetohydrodynamic Seismology of Quiet Solar Active Regions. *Astrophys. J.*, 884(2):L40, oct 2019. ISSN 2041-8213. doi: 10.3847/2041-8213/ab4792. URL http://arxiv.org/abs/1910.03809.

S. A. Anfinogentov, G. Nisticò, and V. M. Nakariakov. Decay-less kink oscillations in coronal loops*. *Astron. Astrophys.*, 560:A107, dec 2013. ISSN 00046361. doi: 10.1051/0004-6361/201322094.

S. A. Anfinogentov, V. M. Nakariakov, and G. Nisticò. Decayless low-amplitude kink oscillations: A common phenomenon in the solar corona? *Astron. Astrophys.*, 583:A136, nov 2015. ISSN 14320746. doi: 10.1051/0004-6361/201526195.

S. A. Anfinogentov, A. G. Stupishin, I. I. Mysh'yakov, and G. D. Fleishman. Record-breaking Coronal Magnetic Field in Solar Active Region 12673. *Astrophys. J.*, 880 (2):L29, aug 2019. ISSN 2041-8213. doi: 10.3847/2041-8213/ab3042. URL https://iopscience.iop.org/article/10.3847/2041-8213/ab3042.

P. Antolin. Thermal instability and non-equilibrium in solar coronal loops: From coronal rain to long-period intensity pulsations. *Plasma Phys. Control. Fusion*, 62(1):014016, nov 2020. ISSN 13616587. doi: 10.1088/1361-6587/ab5406.

P. Antolin, T. Yokoyama, and T. Van Doorsselaere. Fine strand-like structure in the solar corona from magnetohydrodynamic transverse oscillations. *Astrophys. J. Lett.*, 787 (2):L22, apr 2014. ISSN 20418213. doi: 10.1088/2041-8205/787/2/L22. URL http://dx.doi.org/10.1088/2041-8205/787/2/L22.

P. Antolin, I. De Moortel, T. Van Doorsselaere, and T. Yokoyama. Modeling Observed Decay-Less Oscillations As Resonantly Enhanced Kelvin–Helmholtz Vortices From Transverse Mhd Waves and Their Seismological Application. *Astrophys. J.*, 830(2):L22, oct 2016. ISSN 2041-8213. doi: 10.3847/2041-8205/830/2/l22.

P. Antolin, I. De Moortel, T. Van Doorsselaere, and T. Yokoyama. Observational Signatures of Transverse Magnetohydrodynamic Waves and Associated Dynamic Instabilities in Coronal Flux Tubes. *Astrophys. J.*, 836(2):219, feb 2017. ISSN 1538-4357. doi: 10.3847/1538-4357/aa5eb2.

Patrick Antolin and Tom Van Doorsselaere. Influence of resonant absorption on the generation of the Kelvin-Helmholtz instability, 2019. ISSN 2296424X. URL https://www.frontiersin.org/article/10.3389/fphy.2019.00085.

Patrick Antolin, Paolo Pagano, Ineke De Moortel, and Valery M. Nakariakov. In Situ Generation of Transverse Magnetohydrodynamic Waves from Colliding Flows in the Solar Corona. *Astrophys. J.*, 861(2):L15, 2018. ISSN 2041-8213. doi: 10.3847/2041-8213/aacf98. URL http://dx.doi.org/10.3847/2041-8213/aacf98.

T. D. Arber, A. W. Longbottom, C. L. Gerrard, and A. M. Milne. A Staggered Grid, Lagrangian-Eulerian Remap Code for 3-D MHD Simulations. *J. Comput. Phys.*, 171(1): 151–181, jul 2001. ISSN 00219991. doi: 10.1006/jcph.2001.6780.

I. Arregui. Wave heating of the solar atmosphere, may 2015. ISSN 1364503X.

I. Arregui. Bayesian coronal seismology. *Adv. Sp. Res.*, 61(2):655–672, jan 2018. ISSN 18791948. doi: 10.1016/j.asr.2017.09.031.

I. Arregui and M. Goossens. No unique solution to the seismological problem of standing kink magnetohydrodynamic waves. *Astron. Astrophys.*, 622:A44, feb 2019. ISSN 14320746. doi: 10.1051/0004-6361/201833813.

I. Arregui, A. Asensio Ramos, and A. J. Díaz. Bayesian analysis of multiple harmonic oscillations in the solar corona. *Astrophys. J. Lett.*, 765(1):L23, mar 2013. ISSN 20418205. doi: 10.1088/2041-8205/765/1/L23.

I. Arregui, R. Soler, and A. Asensio Ramos. Model comparison for the density structure across solar coronal waveguides. *Astrophys. J.*, 811(2):104, sep 2015. doi: 10.1088/0004-637X/811/2/104. URL http://dx.doi.org/10.1088/0004-637X/811/2/104.

I. Arregui, R. Oliver, and J. L. Ballester. Prominence oscillations. *Living Rev. Sol. Phys.*, 15 (1):2, apr 2018. ISSN 16144961. doi: 10.1007/s41116-018-0012-6.

I. Arregui, M. Montes-Solís, and A. Asensio Ramos. Inference of magnetic field strength and density from damped transverse coronal waves. *Astron. Astrophys.*, 625:A35, may 2019. ISSN 0004-6361. doi: 10.1051/0004-6361/201834324.

M. J. Aschwanden. MHD Oscillations. In *Phys. Sol. Corona*, pages 283–330. Springer Berlin Heidelberg, aug 2006. doi: 10.1007/3-540-30766-4˙7.

M. J. Aschwanden and R. W. Nightingale. Elementary Loop Structures in the Solar Corona Analyzed from TRACE Triple-Filter Images. *Astrophys. J.*, 633:499–517, nov 2005. ISSN 0004-637X. doi: 10.1086/452630. URL https://ui.adsabs.harvard.edu/abs/2005ApJ...633..499A.

M. J. Aschwanden and C. J. Schrijver. Coronal loop oscillations observed with atmospheric imaging assembly - Kink mode with cross-sectional and density oscillations. *Astrophys. J.*, 736(2):102, aug 2011. ISSN 15384357. doi: 10.1088/0004-637X/736/2/102.

M. J. Aschwanden and J. Terradas. The Effect of Radiative Cooling on Coronal Loop Oscillations. *Astrophys. J.*, 686(2):L127–L130, oct 2008. ISSN 0004-637X. doi: 10.1086/592963.

M. J. Aschwanden and T. J. Wang. Torsional Alfvénic Oscillations Discovered in the Magnetic Free Energy during Solar Flares. *Astrophys. J.*, 891(1):99, mar 2020. ISSN 0004-637X. doi: 10.3847/1538-4357/ab7120. URL https://ui.adsabs.harvard.edu/abs/2020ApJ...891...99A.

M. J. Aschwanden, L. Fletcher, C. J. Schrijver, and D. Alexander. Coronal Loop Oscillations Observed with the Transition Region and Coronal Explorer. *Astrophys. J.*, 520(2):880–894, aug 1999. ISSN 0004-637X. doi: 10.1086/307502.

M. J. Aschwanden, C. J. Schrijver, and D. Alexander. Modeling of Coronal EUV Loops Observed with TRACE . I. Hydrostatic Solutions with Nonuniform Heating. *Astrophys. J.*, 550(2):1036–1050, apr 2001. ISSN 0004-637X. doi: 10.1086/319796.

M. J. Aschwanden, R. W. Nightingale, J. Andries, M. Goossens, and T. Van Doorsselaere. Observational Tests of Damping by Resonant Absorption in Coronal Loop Oscillations. *Astrophys. J.*, 598(2):1375–1386, dec 2003. ISSN 0004-637X. doi: 10.1086/379104.

M. J. Aschwanden, P. F. Boerner, C. J. Schrijver, and A. Malanushenko. Automated Temperature and Emission Measure Analysis of Coronal Loops and Active Regions Observed with the Atmospheric Imaging Assembly on the Solar Dynamics Observatory (SDO/AIA). *Sol. Phys.*, 283(1):5–30, 2013. ISSN 00380938. doi: 10.1007/s11207-011-9876-5.

F. Auchère, C. Froment, K. Bocchialini, E. Buchlin, and J. Solomon. on the Fourier and Wavelet Analysis of Coronal Time Series. *Astrophys. J.*, 825(2):110, 2016. ISSN 1538-4357. doi: 10.3847/0004-637x/825/2/110. URL http://dx.doi.org/10.3847/0004-637X/825/2/110.

K. Bahari and N. Shahhosaini. The effect of compressive viscosity and thermal conduction on the longitudinal MHD waves. *Mon. Not. R. Astron. Soc.*, 478(1):342–350, jul 2018. ISSN 13652966. doi: 10.1093/mnras/sty1104. URL https://academic.oup.com/mnras/article/478/1/342/4990660.

I. Ballai, M. Douglas, and A. Marcu. Forced oscillations of coronal loops driven by EIT waves. *Astron. Astrophys.*, 488(3):1125–1132, 2008. ISSN 14320746. doi: 10.1051/0004-6361:200809833. URL https://doi.org/10.1051/0004-6361:200809833.

D. Banerjee and S. Krishna Prasad. MHD Waves in Coronal Holes. *Low-Frequency Waves Sp. Plasmas*, 216:419–430, feb 2016. doi: 10.1002/9781119055006.ch24.

D. Banerjee, G. R. Gupta, and L. Teriaca. Propagating MHD waves in coronal holes. *Space Sci. Rev.*, 158(2-4):267–288, jul 2011. ISSN 00386308. doi: 10.1007/s11214-010-9698-z.

Mihai Barbulescu, Michael S. Ruderman, Tom Van Doorsselaere, and Robert Erdélyi. An Analytical Model of the Kelvin–Helmholtz Instability of Transverse Coronal Loop Oscillations. *Astrophys. J.*, 870(2):108, 2019. ISSN 1538-4357. doi: 10.3847/1538-4357/aaf506. URL http://dx.doi.org/10.3847/1538-4357/aaf506.

T Bayes. An essay towards solving a problem in the doctrine of chances. 1763. *MD. Comput.*, 8(3):157–171, 1763. URL https://www.scopus.com/inward/record.uri?eid=2-s2.0-0026164330{&}partnerID=40{&}md5=0e67e808d62fd64805dad5af3ad2e6a7.

L. Bellot Rubio and D. Orozco Suárez. Quiet Sun magnetic fields: an observational view, dec 2019. ISSN 16144961.

D. Berghmans and F. Clette. Active region EUV transient brightenings: First Results by EIT of SOHO JOP 80. *Sol. Phys.*, 186(1-2):207–229, 1999. ISSN 00380938. doi: 10.1023/A:1005189508371.

T. J. Bogdan and P. G. Judge. Observational aspects of sunspot oscillations. *Philos. Trans. R. Soc. A Math. Phys. Eng. Sci.*, 364(1839):313–331, feb 2006. ISSN 1364503X. doi: 10.1098/rsta.2005.1701.

S. J. Bradshaw and R. Erdélyi. Radiative damping of standing acoustic waves in solar coronal loops. *Astron. Astrophys.*, 483(1):301–309, 2008. ISSN 00046361. doi: 10.1051/0004-6361:20079128.

S. J. Bradshaw, A. G. Emslie, N. H. Bian, and E.P. Kontar. Coronal Loop Scaling Laws for Various Forms of Parallel Heat Conduction. *Astrophys. J.*, 880(2):80, jul 2019. ISSN 1538-4357. doi: 10.3847/1538-4357/ab287f.

C. S. Brady and T. D. Arber. Damping of vertical coronal loop kink oscillations through wave tunneling. *Astron. Astrophys.*, 438(2):733–740, aug 2005. ISSN 00046361. doi: 10.1051/0004-6361:20042527.

C. S. Brady and T. D. Arber. Simulations of Alfvén and Kink Wave Driving of the Solar Chromosphere: Efficient Heating and Spicule Launching. *Astrophys. J.*, 829(2):80, oct 2016. ISSN 1538-4357. doi: 10.3847/0004-637x/829/2/80. URL https://ui.adsabs.harvard.edu/abs/2016ApJ...829...80B.

C. S. Brady, E. Verwichte, and T. D. Arber. Leakage of waves from coronal loops by wave tunneling. *Astron. Astrophys.*, 449(1):389–399, apr 2006. ISSN 00046361. doi: 10.1051/0004-6361:20054097.

S. I. Braginskii. Transport Processes in a Plasma. *Rev. Plasma Phys.*, 1:205, 1965.

A. M. Broomhall, P. Chatterjee, R. Howe, A. A. Norton, and M. J. Thompson. The Sun's Interior Structure and Dynamics, and the Solar Cycle, oct 2014. ISSN 15729672.

P. K. Browning and E. R. Priest. The structure of twisted magnetic flux tubes. *Astrophys. J.*, 266:848, mar 1983. ISSN 0004-637X. doi: 10.1086/160833.

J. P. Byrne, D. M. Long, P. T. Gallagher, D. S. Bloomfield, S. A. Maloney, R. T.J. McAteer, H. Morgan, and S. R. Habbal. Improved methods for determining the kinematics of coronal mass ejections and coronal waves. *Astron. Astrophys.*, 557:A96, sep 2013. ISSN 00046361. doi: 10.1051/0004-6361/201321223. URL https://ui.adsabs.harvard.edu/abs/2013A{&}A...557A..96B.

M. Carbonell, J. Terradas, R. Oliver, and J. L. Ballester. Spatial damping of linear non-adiabatic magnetoacoustic waves in a prominence medium. *Astron. Astrophys.*, 460(2): 573–581, dec 2006. ISSN 00046361. doi: 10.1051/0004-6361:20065528.

Mats Carlsson, Viggo H. Hansteen, Boris V. Gudiksen, Jorrit Leenaarts, and Bart De Pontieu. A publicly available simulation of an enhanced network region of the Sun. *Astron. Astrophys.*, 585:A4, jan 2016. ISSN 14320746. doi: 10.1051/0004-6361/201527226. URL https://ui.adsabs.harvard.edu/abs/2016A{&}A...585A...4C.

R. Centeno, M. Collados, and J. Trujillo Bueno. Spectropolarimetric Investigation of the Propagation of Magnetoacoustic Waves and Shock Formation in Sunspot Atmospheres. *Astrophys. J.*, 640(2):1153–1162, apr 2006. ISSN 0004-637X. doi: 10.1086/500185.

S. Chandrasekhar. Hydrodynamic and hydromagnetic stability. *Int. Ser. Monogr. Phys.*, 1961. URL https://ui.adsabs.harvard.edu/abs/1961hhs..book.....C.

F. Chen and H. Peter. Using coronal seismology to estimate the magnetic field strength in a realistic coronal model. *Astron. Astrophys.*, 581:A137, sep 2015. ISSN 14320746. doi: 10.1051/0004-6361/201526237.

N. Chorley, B. Hnat, V. M. Nakariakov, A. R. Inglis, and I. A. Bakunina. Long period oscillations in sunspots. *Astron. Astrophys.*, 513(4):1–7, 2010. ISSN 14320746. doi: 10.1051/0004-6361/200913683.

N. Claes and R. Keppens. Thermal stability of magnetohydrodynamic modes in homogeneous plasmas. *Astron. Astrophys.*, 624:1–14, 2019. ISSN 14320746. doi: 10.1051/0004-6361/201834699.

J. Colgan, J. Abdallah, Jr., M. E. Sherrill, M. Foster, C. J. Fontes, and U. Feldman. Radiative Losses of Solar Coronal Plasmas. *Astrophys. J.*, 689(1):585–592, dec 2008. ISSN 0004-637X. doi: 10.1086/592561.

S. R. Cranmer. Coronal Holes Imprint. *Living Rev. Sol. Phys.*, 6(1):3, sep 2009. ISSN 1614-4961. doi: 10.12942/lrsp-2009-3.

R. B. Dahlburg and J. T. Mariska. Influence of heating rate on the condensational instability. *Sol. Phys.*, 117(1):51–56, mar 1988. ISSN 00380938. doi: 10.1007/BF00148571.

I. De Moortel. Longitudinal waves in coronal loops. *Space Sci. Rev.*, 149(1-4):65–81, dec 2009. ISSN 00386308. doi: 10.1007/s11214-009-9526-5. URL http://link.springer.com/10.1007/s11214-009-9526-5.

I. De Moortel and C. S. Brady. Observation of Higher Harmonic Coronal Loop Oscillations. *Astrophys. J.*, 664(2):1210–1213, 2007. ISSN 0004-637X. doi: 10.1086/518830.

I. De Moortel and P. K. Browning. Recent advances in coronal heating. *Philos. Trans. R. Soc. A Math. Phys. Eng. Sci.*, 373(2042):20140269, may 2015. ISSN 1364503X. doi: 10.1098/rsta.2014.0269. URL https://royalsocietypublishing.org/doi/10.1098/rsta.2014.0269.

I. De Moortel and A. W. Hood. The damping of slow MHD waves in solar coronal magnetic fields. *Astron. Astrophys.*, 408(2):755–765, sep 2003. ISSN 00046361. doi: 10.1051/0004-6361:20030984. URL http://www.aanda.org/10.1051/0004-6361:20030984.

I. De Moortel and A. W. Hood. The damping of slow MHD waves in solar coronal magnetic fields. II. The effect of gravitational stratification and field line divergence. *Astron. Astrophys.*, 415(2):705–715, feb 2004. ISSN 00046361. doi: 10.1051/0004-6361:20034233. URL http://www.aanda.org/10.1051/0004-6361:20034233.

I. De Moortel and V. M. Nakariakov. Magnetohydrodynamic waves and coronal seismology: An overview of recent results. *Philos. Trans. R. Soc. A Math. Phys. Eng. Sci.*, 370 (1970):3193–3216, 2012. ISSN 1364503X. doi: 10.1098/rsta.2011.0640. URL http://rsta.royalsocietypublishing.org/content/370/1970/3193.

I. De Moortel and D. J. Pascoe. The effects of line-of-sight integration on multistrand coronal loop oscillations. *Astrophys. J.*, 746(1):31, feb 2012. ISSN 15384357. doi: 10.1088/0004-637X/746/1/31.

I. De Moortel, J. Ireland, and R. W. Walsh. Observation of oscillations in coronal loops. *Astron. Astrophys.*, 355(2):23–26, 2000. ISSN 00046361. doi: 10.1063/1.1324943.

I. De Moortel, J. Ireland, A. W. Hood, and R. W. Walsh. The detection of 3 & 5 min period oscillations in coronal loops. *Astron. Astrophys.*, 387(1):L13–L16, may 2002a. ISSN 00046361. doi: 10.1051/0004-6361:20020436. URL http://www.aanda.org/10.1051/0004-6361:20020436.

I. De Moortel, J. Ireland, R. W. Walsh, and A. W. Hood. Longitudinal intensity oscillations in coronal loops observed with trace: I. Overview of measured parameters, 2002b. ISSN 00380938.

C. E. DeForest and J. B. Gurman. Observation of Quasi-periodic Compressive Waves in Solar Polar Plumes. *Astrophys. J.*, 501(2):L217–L220, jul 1998. ISSN 0004637X. doi: 10.1086/311460.

K. P. Dere, E. Landi, H. E. Mason, B. C. Monsignori Fossi, and P. R. Young. CHIANTI - An atomic database for emission lines. I. Wavelengths greater than 50 Å. *Astron. Astrophys. Suppl. Ser.*, 125(1):149–173, oct 1997. ISSN 03650138. doi: 10.1051/aas:1997368.

K. P. Dere, G. Del Zanna, P. R. Young, E. Landi, and R. S. Sutherland. CHIANTI—An Atomic Database for Emission Lines. XV. Version 9, Improvements for the X-Ray Satellite Lines. *Astrophys. J. Suppl. Ser.*, 241(2):22, feb 2019. ISSN 0067-0049. doi: 10.3847/1538-4365/ab05cf. URL http://dx.doi.org/10.3847/1538-4365/ab05cf.

A. Deres and S. A. Anfinogentov. Probing the Sunspot Atmosphere with Three-Minute Oscillations. *Sol. Phys.*, 293(1):1–12, 2018. ISSN 1573093X. doi: 10.1007/s11207-017-1222-0. URL http://dx.doi.org/10.1007/s11207-017-1222-0.

M. Dikpati and P. A. Gilman. Global solar dynamo models: Simulations and predictions of cyclic photospheric fields and long-term non-reversing interior fields. *New J. Phys.*, 9:297, aug 2007. ISSN 13672630. doi: 10.1088/1367-2630/9/8/297. URL https://ui.adsabs.harvard.edu/abs/2007NJPh....9..297D.

M. Dominique, A. N. Zhukov, L. Dolla, A. Inglis, and G. Lapenta. Detection of Quasi-Periodic Pulsations in Solar EUV Time Series. *Sol. Phys.*, 293(4), 2018. ISSN 1573093X. doi: 10.1007/s11207-018-1281-x. URL http://dx.doi.org/10.1007/s11207-018-1281-x.

G. A. Doschek, J. T. Mariska, H. P. Warren, C. M. Brown, J. L. Culhane, H. Hara, T. Watanabe, P. R. Young, and H. E. Mason. Nonthermal Velocities in Solar Active Regions Observed with the Extreme-Ultraviolet Imaging Spectrometer on Hinode. *Astrophys. J.*, 667(1):L109–L112, sep 2007. ISSN 0004-637X. doi: 10.1086/522087.

M. Druckmuller. Phase correlation method for the alignment of total solar eclipse images. *Astrophys. J.*, 706(2):1605–1608, dec 2009. ISSN 15384357. doi: 10.1088/0004-637X/706/2/1605.

M. Druckmüller. A noise adaptive fuzzy equalization method for processing solar extreme ultraviolet images. *Astrophys. Journal, Suppl. Ser.*, 207(2):25, jul 2013. ISSN 00670049. doi: 10.1088/0067-0049/207/2/25. URL http://stacks.iop.org/0067-0049/207/i=2/a=25?key=crossref.7c1a4ee3e6e36dffddd5ce0b18daa7eb.

T. J. Duckenfield and A. M. Broomhall. Flares on the Sun and on other stars. *Astron. Geophys.*, 60(6):29–33, dec 2019. ISSN 14684004. doi: 10.1093/astrogeo/atz193.

T. J. Duckenfield, S. A. Anfinogentov, D. J. Pascoe, and V. M. Nakariakov. Detection of the Second Harmonic of Decay-less Kink Oscillations in the Solar Corona. *Astrophys. J.*, 854 (1):L5, feb 2018. ISSN 2041-8213. doi: 10.3847/2041-8213/aaaaeb.

T. J. Duckenfield, C. R. Goddard, D. J. Pascoe, and V. M. Nakariakov. Observational signatures of the third harmonic in a decaying kink oscillation of a coronal loop. *Astron. Astrophys.*, 632:A64, dec 2019. ISSN 14320746. doi: 10.1051/0004-6361/201936822. URL https://ui.adsabs.harvard.edu/abs/2019A{&}A...632A..64D.

G. Dumbadze, B. M. Shergelashvili, V. Kukhianidze, G. Ramishvili, T. V. Zaqarashvili, M. Khodachenko, E. Gurgenashvili, S. Poedts, and P. De Causmaecker. Long-period oscillations of active region patterns: Least-squares mapping on second-order curves. *Astron. Astrophys.*, 597(iii), 2017. ISSN 14320746. doi: 10.1051/0004-6361/201628213.

M. V. Dymova and M. S. Ruderman. Resonantly damped oscillations of longitudinally stratified coronal loops. *Astron. Astrophys.*, 457(3):1059–1070, oct 2006a. ISSN 14320746. doi: 10.1051/0004-6361:20065051.

M. V. Dymova and M. S. Ruderman. The geometry effect on transverse oscillations of coronal loops. *Astron. Astrophys.*, 459(1):241–244, nov 2006b. ISSN 00046361. doi: 10.1051/0004-6361:20065929.

P. M. Edwin and B. Roberts. Wave propagation in a magnetic cylinder. *Sol. Phys.*, 88(1-2): 179–191, oct 1983. ISSN 00380938. doi: 10.1007/BF00196186.

X. Fang, D. Yuan, T. Van Doorsselaere, R. Keppens, and C. Xia. MODELING of REFLECTIVE PROPAGATING SLOW-MODE WAVE in A FLARING LOOP. *Astrophys. J.*, 813(1):33, 2015. ISSN 15384357. doi: 10.1088/0004-637X/813/1/33. URL http://dx.doi.org/10.1088/0004-637X/813/1/33.

S. Feng, Z. Deng, D. Yuan, Z. Xu, and X. Yang. Propagating Slow Sausage Waves in a Sunspot Observed by the New Vacuum Solar Telescope. feb 2020. URL http://arxiv.org/abs/2002.03270.

G. B. Field. Thermal Instability. *Astrophys. J.*, 142:531, aug 1965. ISSN 0004-637X. doi: 10.1086/148317.

A. Fludra, C. Hornsey, and V. M. Nakariakov. Diagnostics of Coronal Heating in Active-Region Loops. *Astrophys. J.*, 834(2):100, jan 2017. ISSN 1538-4357. doi: 10.3847/1538-4357/834/2/100.

C. Foullon, E. Verwichte, V. M. Nakariakov, K. Nykyri, and C. J. Farrugia. Magnetic Kelvin-Helmholtz instability at the sun. *Astrophys. J. Lett.*, 729(1 PART II):L8, 2011. ISSN 20418213. doi: 10.1088/2041-8205/729/1/L8.

S L Freeland and B N Handy. Data Analysis with the SolarSoft System. *Sol. Phys.*, 182(2):497–500, 1998. ISSN 1573-093X. doi: 10.1023/A:1005038224881. URL https://doi.org/10.1023/A:1005038224881.

C. Froment, F. Auchère, Z. Mikić, G. Aulanier, K. Bocchialini, E. Buchlin, J. Solomon, and E. Soubrié. On the Occurrence of Thermal Nonequilibrium in Coronal Loops. *Astrophys. J.*, 855(1):52, feb 2018. ISSN 1538-4357. doi: 10.3847/1538-4357/aaaf1d. URL http://dx.doi.org/10.3847/1538-4357/aaaf1d.

C. R. Goddard, G. Nisticò, V. M. Nakariakov, and I. V. Zimovets. A statistical study of decaying kink oscillations detected using SDO/AIA. *Astron. Astrophys.*, 585:A137, jan 2016a. ISSN 14320746. doi: 10.1051/0004-6361/201527341.

C. R. Goddard, G. Nisticò, V. M. Nakariakov, I. V. Zimovets, and S. M. White. Observation of quasi-periodic solar radio bursts associated with propagating fast-mode waves. *Astron. Astrophys.*, 594:A96, oct 2016b. ISSN 14320746. doi: 10.1051/0004-6361/201628478.

C. R. Goddard, D. J. Pascoe, S. A. Anfinogentov, and V. M. Nakariakov. A statistical study of the inferred transverse density profile of coronal loop threads observed with SDO/AIA. *Astron. Astrophys.*, 605:A65, sep 2017. ISSN 14320746. doi: 10.1051/0004-6361/201731023.

C R Goddard, P Antolin, and D J Pascoe. Evolution of the Transverse Density Structure of Oscillating Coronal Loops Inferred by Forward Modeling of EUV Intensity. *Astrophys. J.*, 863(2):167, 2018. ISSN 1538-4357. doi: 10.3847/1538-4357/aad3cc. URL http://dx.doi.org/10.3847/1538-4357/aad3cc.

C. R. Goddard, V. M. Nakariakov, and D. J. Pascoe. Fast magnetoacoustic wave trains with time-dependent drivers. *Astron. Astrophys.*, 624:L4, apr 2019. ISSN 14320746. doi: 10.1051/0004-6361/201935401.

M. Goossens, J. Andries, and M. J. Aschwanden. Coronal loop oscillations. *Astron. Astrophys.*, 394(3):L39–L42, nov 2002. ISSN 0004-6361. doi: 10.1051/0004-6361:20021378. URL http://www.aanda.org/10.1051/0004-6361:20021378.

M. Guo, T. Van Doorsselaere, K. Karampelas, B. Li, P. Antolin, and I. De Moortel. Heating Effects from Driven Transverse and Alfvén Waves in Coronal Loops. *Astrophys. J.*, 870 (2):55, jan 2019. ISSN 1538-4357. doi: 10.3847/1538-4357/aaf1d0.

Y. Guo, R. Erdélyi, A. K. Srivastava, Q. Hao, X. Cheng, P. F. Chen, M. D. Ding, and B. N. Dwivedi. Magnetohydrodynamic seismology of a coronal loop system by the first two modes of standing kink waves. *Astrophys. J.*, 799(2):151, feb 2015. ISSN 15384357. doi: 10.1088/0004-637X/799/2/151. URL http://dx.doi.org/10.1088/0004-637X/799/2/151.

G. R. Gupta. Observations of dissipation of slow magneto-acoustic waves in a polar coronal hole. *Astron. Astrophys.*, 568:1–11, 2014. ISSN 14320746. doi: 10.1051/0004-6361/201323200.

G. R. Gupta, D. Tripathi, and H. E. Mason. Spectroscopic observations of a coronal loop: Basic physical plasma parameters along the full loop length. *Astrophys. J.*, 800(2):140, feb 2015. ISSN 15384357. doi: 10.1088/0004-637X/800/2/140.

B. N. Handy, L. W. Acton, C. C. Kankelborg, C. J. Wolfson, D. J. Akin, M. E. Bruner, R. Caravalho, R. C. Catura, R. Chevalier, D. W. Duncan, C. G. Edwards, C. N. Feinstein, S. L. Freeland, F. M. Friedlaender, C. H. Hoffmann, N. E. Hurlburt, B. K. Jurcevich, N. L. Katz, G. A. Kelly, J. R. Lemen, M. Levay, R. W. Lindgren, D. P. Mathur, S. B. Meyer, S. J. Morrison, M. D. Morrison, R. W. Nightingale, T. P. Pope, R. A. Rehse, C. J. Schrijver, R. A. Shine, L. Shing, K. T. Strong, T. D. Tarbell, A. M. Title, D. D. Torgerson, L. Golub, J. A. Bookbinder, D. Caldwell, P. N. Cheimets, W. N. Davis, E. E. Deluca, R. A. McMullen, H. P. Warren, D. Amato, R. Fisher, H. Maldonado, and C. Parkinson. The transition region and coronal explorer. *Sol. Phys.*, 187(2):229–260, jul 1999. ISSN 00380938. doi: 10.1023/A:1005166902804.

J. Heyvaerts and E. Priest. Coronal heating by phase-mixed shear Alfven waves. *Astron. Astrophys.*, 117:220–234, 1983. ISSN 0004-6361. URL https://ui.adsabs.harvard.edu/abs/1983A{%}26A...117..220H/abstract.

A. Hillier, A. Barker, I. Arregui, and H. Latter. On Kelvin-Helmholtz and parametric instabilities driven by coronal waves. *Mon. Not. R. Astron. Soc.*, 482(1):1143–1153, 2019. ISSN 13652966. doi: 10.1093/mnras/sty2742.

B. W. Hindman and R. Jain. An interpretation of flare-induced and decayless coronal-loop oscillations as interference patterns. *Astrophys. J.*, 784(2):103, 2014. ISSN 15384357. doi: 10.1088/0004-637X/784/2/103.

B. W. Hindman and R. Jain. A Novel Approach to Resonant Absorption of the Fast Magnetohydrodynamic Eigenmodes of a Coronal Arcade. *Astrophys. J.*, 858(1):6, apr 2018. ISSN 1538-4357. doi: 10.3847/1538-4357/aab9b1.

J. V. Hollweg. Viscosity in a magnetized plasma: Physical interpretation. *J. Geophys. Res. Sp. Phys.*, 90(A8):7620–7622, aug 1985. ISSN 0148-0227. doi: 10.1029/ja090ia08p07620.

J. V. Hollweg and G. Yang. Resonance absorption of compressible magnetohydrodynamic waves at thin "surfaces". *J. Geophys. Res.*, 93(A6):5423, jun 1988. ISSN 0148-0227. doi: 10.1029/ja093ia06p05423.

A. W. Hood, M. S. Ruderman, D. J. Pascoe, I. De Moortel, J. Terradas, and A. N. Wright. Damping of kink waves by mode coupling: I. Analytical treatment. *Astron. Astrophys.*, 551:A39, mar 2013. ISSN 00046361. doi: 10.1051/0004-6361/201220617.

J. H. Horne and S. L. Baliunas. A prescription for period analysis of unevenly sampled time series. *Astrophys. J.*, 302:757, mar 1986. ISSN 0004-637X. doi: 10.1086/164037.

T. A. Howson, I. De Moortel, and P. Antolin. Energetics of the Kelvin-Helmholtz instability induced by transverse waves in twisted coronal loops. *Astron. Astrophys.*, 607, aug 2017. ISSN 14320746. doi: 10.1051/0004-6361/201731178. URL http://arxiv.org/abs/1708.04124http://dx.doi.org/10.1051/0004-6361/201731178.

T. A. Howson, I. De Moortel, P. Antolin, T. Van Doorsselaere, and A. N. Wright. Resonant absorption in expanding coronal magnetic flux tubes with uniform density. *Astron. Astrophys.*, 631:A105, nov 2019. ISSN 0004-6361. doi: 10.1051/0004-6361/201936146.

M. H. Ibanez S. and O. B. Escalona T. Propagation of hydrodynamic waves in optically thin plasmas. *Astrophys. J.*, 415:335, sep 1993. ISSN 0004-637X. doi: 10.1086/173167. URL http://adsabs.harvard.edu/doi/10.1086/173167.

A. R. Inglis and V. M. Nakariakov. A multi-periodic oscillatory event in a solar flare. *Astron. Astrophys.*, 493(1):259–266, jan 2009. ISSN 00046361. doi: 10.1051/0004-6361:200810473.

R. C. Ireland, A. W. Hood, and R. A.M. Van Der Linden. Magnetothermal instabilities in coronal arcades. *Sol. Phys.*, 160(2):303–330, sep 1995. ISSN 00380938. doi: 10.1007/BF00732810.

R. Jain and B. W. Hindman. What can be learned from the seismology of a coronal loop using only a handful of frequencies? *Astron. Astrophys.*, 545:A138, sep 2012. ISSN 00046361. doi: 10.1051/0004-6361/201219930.

D. B. Jess, I. De Moortel, M. Mathioudakis, D. J. Christian, K. P. Reardon, P. H. Keys, and F. P. Keenan. The source of 3 minute magnetoacoustic oscillations in coronal fans. *Astrophys. J.*, 757(2), 2012. ISSN 15384357. doi: 10.1088/0004-637X/757/2/160.

D. B. Jess, T. Van Doorsselaere, G. Verth, V. Fedun, S. K. Prasad, R. Erdélyi, P. H. Keys, S. D. T. Grant, H. Uitenbroek, and D. J. Christian. An Inside Look at Sunspot Oscillations

with Higher Azimuthal Wavenumbers. *Astrophys. J.*, 842(1):59, 2017. ISSN 1538-4357. doi: 10.3847/1538-4357/aa73d6. URL http://dx.doi.org/10.3847/1538-4357/aa73d6.

J. Kang, J. Chae, V. M. Nakariakov, K. Cho, H. Kwak, and K. Lee. The Physical Nature of Spiral Wave Patterns in Sunspots. *Astrophys. J.*, 877(1):L9, 2019a. ISSN 2041-8213. doi: 10.3847/2041-8213/ab1f6c. URL http://dx.doi.org/10.3847/2041-8213/ab1f6c.

J. Kang, S. Inoue, K. Kusano, S.-H. Park, and Y.-J. Moon. Onset Mechanism of M6.5 Solar Flare Observed in Active Region 12371. *Astrophys. J.*, 887(2):263, dec 2019b. ISSN 1538-4357. doi: 10.3847/1538-4357/ab5582. URL http://arxiv.org/abs/1911.05337.

K. Karampelas, T. Van Doorsselaere, D. J. Pascoe, M. Guo, and P. Antolin. Amplitudes and Energy Fluxes of Simulated Decayless Kink Oscillations. *Front. Astron. Sp. Sci.*, 6, may 2019. ISSN 2296987X. doi: 10.3389/fspas.2019.00038.

A. Keiling, D. H. Lee, and V. M. Nakariakov. *Low-Frequency Waves in Space Plasmas*, volume 216. John Wiley & Sons, Inc, feb 2016. ISBN 9781119055006. doi: 10.1002/9781119055006.

L. Kepko, N. M. Viall, S. K. Antiochos, S. T. Lepri, J. C. Kasper, and M. Weberg. Implications of L1 observations for slow solar wind formation by solar reconnection. *Geophys. Res. Lett.*, 43(9):4089–4097, may 2016. ISSN 19448007. doi: 10.1002/2016GL068607. URL http://doi.wiley.com/10.1002/2016GL068607.

M. L. Khodachenko, H. O. Rucker, R. Oliver, T. D. Arber, and A. Hanslmeier. On the mechanisms of MHD wave damping in the partially ionized solar plasmas. *Adv. Sp. Res.*, 37(3):447–455, 2006. ISSN 02731177. doi: 10.1016/j.asr.2005.02.025.

E. Khomenko and M. Collados. Oscillations and waves in sunspots. *Living Rev. Sol. Phys.*, 12(1):6, 2015. ISSN 16144961. doi: 10.1007/lrsp-2015-6.

D. B. King, V. M. Nakariakov, E. E. Deluca, L. Golub, and K. G. McClements. Propagating EUV disturbances in the Solar corona: Two-wavelength observations. *Astron. Astrophys.*, 404(1):L1–L4, jun 2003. ISSN 0004-6361. doi: 10.1051/0004-6361:20030763. URL http://www.aanda.org/10.1051/0004-6361:20030763.

J. A. Klimchuk. The Distinction Between Thermal Nonequilibrium and Thermal Instability. *Sol. Phys.*, 294(12):173, nov 2019. ISSN 1573093X. doi: 10.1007/s11207-019-1562-z. URL http://link.springer.com/10.1007/s11207-019-1562-z.

P. Kohutova and E. Verwichte. Excitation of vertical coronal loop oscillations by plasma condensations. *Astron. Astrophys.*, 606:A120, oct 2017. ISSN 14320746. doi: 10.1051/0004-6361/201731417. URL https://ui.adsabs.harvard.edu/abs/2017A{&}A...606A.120K.

P. Kohutova, E. Verwichte, and C. Froment. First direct observation of a torsional Alfvén oscillation at coronal heights. *Astron. Astrophys.*, 633:L6, dec 2020. ISSN 0004-6361. doi: 10.1051/0004-6361/201937144. URL https://doi.org/10.1051/0004-6361/201937144.

D. Y. Kolotkov, V. M. Nakariakov, and D. I. Zavershinskii. Damping of slow magnetoacoustic oscillations by the misbalance between heating and cooling processes in the solar corona. *Astron. Astrophys.*, 628:A133, aug 2019. ISSN 0004-6361. doi: 10.1051/0004-6361/201936072. URL https://www.aanda.org/10.1051/0004-6361/201936072.

Takahiro Kudoh and Kazunari Shibata. Alfven Wave Model of Spicules and Coronal Heating. *Astrophys. J.*, 514(1):493–505, mar 1999. ISSN 0004-637X. doi: 10.1086/306930. URL https://ui.adsabs.harvard.edu/abs/1999ApJ...514..493K.

N. P. M. Kuin and P. C. H. Martens. On the thermal stability of hot coronal loops - The coupling between chromosphere and corona. *Astron. Astrophys.*, 108:L1–L4, apr 1982. ISSN 0004-6361. URL https://ui.adsabs.harvard.edu/abs/1982A{&}A...108L...1K.

N. Kumar and A. Kumar. Damping and the period ratio P1/2P2 of non-adiabatic slow mode. *Proc. Int. Astron. Union*, 6(S273):491–494, 2010. ISSN 17439213. doi: 10.1017/S1743921311015869.

S. Kumar, V. M. Nakariakov, and Y.-J. Moon. Effect of a Radiation Cooling and Heating Function on Standing Longitudinal Oscillations in Coronal Loops. *Astrophys. J.*, 824(1): 8, mar 2016. ISSN 1538-4357. doi: 10.3847/0004-637x/824/1/8. URL http://dx.doi.org/10.3847/0004-637X/824/1/8.

E. G. Kupriyanova, V. F. Melnikov, V. M. Puzynya, K. Shibasaki, and H. S. Ji. Long-period pulsations of the thermal microwave emission of the solar flare of June 2, 2007 from data with high spatial resolution. *Astron. Reports*, 58(8):573–577, oct 2014. ISSN 10637729. doi: 10.1134/S1063772914080022.

E. G. G. Kupriyanova, V. F. F. Melnikov, and K. Shibasaki. Spatially Resolved Microwave Observations of Multiple Periodicities in a Flaring Loop. *Sol. Phys.*, 284(2):559–578, jun 2013. ISSN 00380938. doi: 10.1007/s11207-012-0141-3. URL http://link.springer.com/10.1007/s11207-012-0141-3.

J. M. Laming. NON-WKB models of the first ionization potential effect: The role of slow mode waves. *Astrophys. J.*, 744(2):115, jan 2012. ISSN 15384357. doi: 10.1088/0004-637X/744/2/115.

P. Laplace. Memoire sur la probabilite des causes par les evenements. *L'Academie R. des Sci.*, (6):621–656, 1774.

J. R. Lemen, A. M. Title, D. J. Akin, P. F. Boerner, C. Chou, J. F. Drake, D. W. Duncan, C. G. Edwards, F. M. Friedlaender, G. F. Heyman, N. E. Hurlburt, N. L. Katz, G. D. Kushner, M. Levay, R. W. Lindgren, D. P. Mathur, E. L. McFeaters, S. Mitchell, R. A. Rehse, C. J. Schrijver, L. A. Springer, R. A. Stern, T. D. Tarbell, J. P. Wuelser, C. J. Wolfson, C. Yanari, J. A. Bookbinder, P. N. Cheimets, D. Caldwell, E. E. Deluca, R. Gates, L. Golub, S. Park, W. A. Podgorski, R. I. Bush, P. H. Scherrer, M. A. Gummin, P. Smith, G. Auker, P. Jerram, P. Pool, R. Soufli, D. L. Windt, S. Beardsley, M. Clapp, J. Lang, and N. Waltham. The Atmospheric Imaging Assembly (AIA) on the Solar

Dynamics Observatory (SDO). *Sol. Phys.*, 275(1-2):17–40, jan 2012. ISSN 00380938. doi: 10.1007/s11207-011-9776-8.

D. Li, D. Yuan, Y. N. Su, Q. M. Zhang, W. Su, and Z. J. Ning. Non-damping oscillations at flaring loops. *Astron. Astrophys.*, 617, sep 2018. ISSN 14320746. doi: 10.1051/0004-6361/201832991.

D. Li, Y. Li, L. Lu, Q. Zhang, Z. Ning, and S. A. Anfinogentov. Observations of a Quasi-periodic Pulsation in the Coronal Loop and Microwave Flux during a Solar Preflare Phase. *Astrophys. J.*, 893(1):L17, 2020. ISSN 2041-8213. doi: 10.3847/2041-8213/ab830c. URL http://dx.doi.org/10.3847/2041-8213/ab830c.

N. R. Lomb. Least-squares frequency analysis of unequally spaced data. *Astrophys. Space Sci.*, 39(2):447–462, feb 1976. ISSN 0004640X. doi: 10.1007/BF00648343. URL https://ui.adsabs.harvard.edu/abs/1976Ap{&}SS..39..447L.

D. M. Long, G. Valori, D. Pérez-Suárez, R. J. Morton, and A. M. Vásquez. Measuring the magnetic field of a trans-equatorial loop system using coronal seismology. *Astron. Astrophys.*, 603:A101, jul 2017a. ISSN 14320746. doi: 10.1051/0004-6361/201730413. URL https://ui.adsabs.harvard.edu/abs/2017A{&}A...603A.101L.

D. M. Long, G. Valori, D. Pérez-Suárez, R. J. Morton, and A. M. Vásquez. Measuring the magnetic field of a trans-equatorial loop system using coronal seismology (Corrigendum). *Astron. Astrophys.*, 607:C3, nov 2017b. ISSN 0004-6361. doi: 10.1051/0004-6361/201730413e. URL https://ui.adsabs.harvard.edu/abs/2017A{&}A...607C...3L.

I. Lopin and I. Nagorny. Kink Waves in Thin Stratified Magnetically Twisted Flux Tubes. *Astrophys. J.*, 840(1):26, 2017. ISSN 1538-4357. doi: 10.3847/1538-4357/aa6c5a. URL http://dx.doi.org/10.3847/1538-4357/aa6c5a.

C. K. MacNamara and B. Roberts. Effects of thermal conduction and compressive viscosity on the period ratio of the slow mode. *Astron. Astrophys.*, 515(6), 2010. ISSN 14320746. doi: 10.1051/0004-6361/200913510.

N. Magyar and T. Van Doorsselaere. Damping of nonlinear standing kink oscillations: A numerical study. *Astron. Astrophys.*, 595, 2016a. ISSN 14320746. doi: 10.1051/0004-6361/201629010. URL https://doi.org/10.1051/0004-6361/201629010.

N. Magyar and T. Van Doorsselaere. the Instability and Non-Existence of Multi-Stranded Loops When Driven By Transverse Waves. *Astrophys. J.*, 823(2):82, 2016b. ISSN 1538-4357. doi: 10.3847/0004-637x/823/2/82. URL http://dx.doi.org/10.3847/0004-637X/823/2/82.

N. Magyar, T. Van Doorsselaere, and M. Goossens. Understanding Uniturbulence: Self-cascade of MHD Waves in the Presence of Inhomogeneities. *Astrophys. J.*, 882(1):50, sep 2019. ISSN 1538-4357. doi: 10.3847/1538-4357/ab357c. URL https://ui.adsabs.harvard.edu/abs/2019ApJ...882...50M.

S. Mandal, N. Magyar, D. Yuan, T. Van Doorsselaere, and D. Banerjee. Forward Modeling of Propagating Slow Waves in Coronal Loops and Their Frequency-Dependent Damping. *Astrophys. J.*, 820(1):13, mar 2016. ISSN 1538-4357. doi: 10.3847/0004-637x/820/1/13.

C. H. Mandrini, P. Demoulin, and J. A. Klimchuk. Magnetic Field and Plasma Scaling Laws: Their Implications for Coronal Heating Models. *Astrophys. J.*, 530(2):999–1015, feb 2000. ISSN 0004-637X. doi: 10.1086/308398.

J. T. Mariska, H. P. Warren, D. R. Williams, and T. Watanabe. Observations of Doppler Shift Oscillations with the EUV Imaging Spectrometer on Hinode. *Astrophys. J.*, 681(1): L41–L44, jul 2008. ISSN 0004-637X. doi: 10.1086/590341. URL https://ui.adsabs.harvard.edu/abs/2008ApJ...681L..41M.

M. S. Marsh and R. W. Walsh. p -Mode Propagation through the Transition Region into the Solar Corona. I. Observations . *Astrophys. J.*, 643(1):540–548, may 2006. ISSN 0004-637X. doi: 10.1086/501450.

M. S. Marsh, J. Ireland, and T. Kucera. Bayesian Analysis of Solar Oscillations. *Astrophys. J.*, 681(1):672–679, apr 2008. doi: 10.1086/588751. URL http://dx.doi.org/10.1086/588751.

M. S. Marsh, I. De Moortel, and R. W. Walsh. Observed damping of the slow magnetoacoustic mode. *Astrophys. J.*, 734(2), jun 2011. ISSN 15384357. doi: 10.1088/0004-637X/734/2/81. URL http://dx.doi.org/10.1088/0004-637X/734/2/81.

M. P. McEwan, G. R. Donnelly, A. J. Díaz, and B. Roberts. On the period ratio P1/2P2 in the oscillations of coronal loops. *Astron. Astrophys.*, 460(3):893–899, dec 2006. ISSN 00046361. doi: 10.1051/0004-6361:20065313.

P. McEwan, J. Díaz, B. Roberts, M. P. McEwan, A. J. Díaz, and B. Roberts. Analytical determination of coronal parameters using the period ratio P1/2P2. *Astron. Astrophys.*, 481(3):819–825, apr 2008. ISSN 00046361. doi: 10.1051/0004-6361:20078016.

C. A. Mendoza-Briceño and M. Luna-Cardozo. Radiative cooling effects on oscillating loops. In *Proc. Int. Astron. Union*, volume 2, pages 179–180, mar 2006. doi: 10.1017/S1743921306001797.

C. A. Mendoza-Briceno, R. Erdelyi, and L. Di G. Sigalotti. The Effects of Stratification on Oscillating Coronal Loops. *Astrophys. J.*, 605(1):493–502, apr 2004. ISSN 0004-637X. doi: 10.1086/382182.

R. Mitalas and K. R. Sills. On the photon diffusion time scale for the sun. *Astrophys. J.*, 401:759, dec 1992. ISSN 0004-637X. doi: 10.1086/172103.

K. Mooroogen, R. J. Morton, and V. Henriques. Dynamics of internetwork chromospheric fibrils: Basic properties and MHD kink waves. *Astron. Astrophys.*, 607:A46, aug 2017. ISSN 0004-6361. doi: 10.1051/0004-6361/201730926. URL http://www.aanda.org/10.1051/0004-6361/201730926http://arxiv.org/abs/1708.03500http://dx.doi.org/10.1051/0004-6361/201730926.

M. G. Moreels, N. Freij, R. Erdélyi, T. Van Doorsselaere, and G. Verth. Observations and mode identification of sausage waves in a magnetic pore. *Astron. Astrophys.*, 579, jul 2015. ISSN 14320746. doi: 10.1051/0004-6361/201425096. URL https://doi.org/10.1051/0004-6361/201425096.

H. Morgan and M. Druckmüller. Multi-Scale Gaussian Normalization for Solar Image Processing. *Sol. Phys.*, 289(8):2945–2955, aug 2014. ISSN 1573093X. doi: 10.1007/s11207-014-0523-9.

R. J. Morton, S. Tomczyk, and R. F. Pinto. A GLOBAL VIEW OF VELOCITY FLUCTUATIONS IN THE CORONA BELOW 1.3 R WITH CoMP. *Astrophys. J.*, 828(2):89, 2016. ISSN 1538-4357. doi: 10.3847/0004-637x/828/2/89. URL http://dx.doi.org/10.3847/0004-637X/828/2/89.

D Müller, B Nicula, S Felix, F Verstringe, B Bourgoignie, A Csillaghy, D Berghmans, P Jiggens, J P García-Ortiz, J Ireland, S Zahniy, and B Fleck. JHelioviewer. Time-dependent 3D visualisation of solar and heliospheric data. *Astron. Astrophys.*, 606: A10, sep 2017. ISSN 0004-6361. doi: 10.1051/0004-6361/201730893. URL https://ui.adsabs.harvard.edu/abs/2017A{&}A...606A..10M.

F. M. Mulu-Moore, A. R. Winebarger, H. P. Warren, and M. J. Aschwanden. Determining the structure of solar coronal loops using their evolution. *Astrophys. J.*, 733(1):59, 2011. ISSN 15384357. doi: 10.1088/0004-637X/733/1/59.

V. M. Nakariakov and L. Ofman. Determination of the coronal magnetic field by coronal loop oscillations. *Astron. Astrophys.*, 372(3):L53–L56, jun 2001. ISSN 00046361. doi: 10.1051/0004-6361:20010607.

V. M. Nakariakov and E. Verwichte. Coronal waves and oscillations. *Living Rev. Sol. Phys.*, 2(1):3, dec 2005. ISSN 16144961. doi: 10.12942/lrsp-2005-3.

V. M. Nakariakov, L. Ofman, E. E. Deluca, B. Roberts, and J. M. Davila. Trace observation of damped coronal loop oscillations: Implications for coronal heating. *Science (80-.).*, 285(5429):862–864, aug 1999. ISSN 00368075. doi: 10.1126/science.285.5429.862.

V. M. Nakariakov, C. A. Mendoza-Briceno, and M. H. Ibanez S. Magnetoacoustic Waves of Small Amplitude in Optically Thin Quasi-isentropic Plasmas. *Astrophys. J.*, 528(2): 767–775, jan 2000. ISSN 0004-637X. doi: 10.1086/308195.

V. M. Nakariakov, S. A. Anfinogentov, G. Nisticò, and D. H. Lee. Undamped transverse oscillations of coronal loops as a self-oscillatory process. *Astron. Astrophys.*, 591:1–4, jun 2016a. ISSN 14320746. doi: 10.1051/0004-6361/201628850.

V. M. Nakariakov, V. Pilipenko, B. Heilig, P. Jelínek, M. Karlický, D. Y. Klimushkin, D. Y. Kolotkov, D. H. Lee, G. Nisticò, T. Van Doorsselaere, G. Verth, and I. V. Zimovets. Magnetohydrodynamic Oscillations in the Solar Corona and Earth's Magnetosphere: Towards Consolidated Understanding. *Space Sci. Rev.*, 200(1-4):75–203, apr 2016b. ISSN 15729672. doi: 10.1007/s11214-015-0233-0.

V. M. Nakariakov, A. N. Afanasyev, S. Kumar, and Y.-J. Moon. Effect of Local Thermal Equilibrium Misbalance on Long-wavelength Slow Magnetoacoustic Waves. *Astrophys. J.*, 849(1):62, oct 2017. ISSN 1538-4357. doi: 10.3847/1538-4357/aa8ea3. URL http://stacks.iop.org/0004-637X/849/i=1/a=62?key=crossref.6c3f9b376fac95bd6975a0e3eabb7968.

V. M. Nakariakov, M. K. Kosak, D. Y. Kolotkov, S. A. Anfinogentov, P. Kumar, and Y.-J. Moon. Properties of Slow Magnetoacoustic Oscillations of Solar Coronal Loops by Multi-instrumental Observations. *Astrophys. J.*, 874(1):L1, 2019. ISSN 2041-8213. doi: 10.3847/2041-8213/ab0c9f.

A. Nechaeva, I. V. Zimovets, V. M. Nakariakov, and C. R. Goddard. Catalog of Decaying Kink Oscillations of Coronal Loops in the 24th Solar Cycle. *Astrophys. J. Suppl. Ser.*, 241(2):31, apr 2019. ISSN 0067-0049. doi: 10.3847/1538-4365/ab0e86.

N. Nishizuka and H. Hara. Spectroscopic observations of continuous outflows and propagating waves from noaa 10942 with extreme ultraviolet imaging spectrometer/hinode. *Astrophys. J. Lett.*, 737(2):L43, aug 2011. ISSN 20418205. doi: 10.1088/2041-8205/737/2/L43.

G. Nisticò, V. M. Nakariakov, and E. Verwichte. Decaying and decayless transverse oscillations of a coronal loop. *Astron. Astrophys.*, 552:A57, apr 2013. ISSN 00046361. doi: 10.1051/0004-6361/201220676.

G. Nisticò, S. A. Anfinogentov, and V. M. Nakariakov. Dynamics of a multi-thermal loop in the solar corona. *Astron. Astrophys.*, 570:A84, oct 2014. ISSN 14320746. doi: 10.1051/0004-6361/201423970.

G. Nisticò, V. Polito, V. M. Nakariakov, and G. Del Zanna. Multi-instrument observations of a failed flare eruption associated with MHD waves in a loop bundle. *Astron. Astrophys.*, 600:1–13, 2017. ISSN 14320746. doi: 10.1051/0004-6361/201629324.

L. Ofman. Chromospheric Leakage of Alfvén Waves in Coronal Loops. *Astrophys. J.*, 568 (2):L135–L138, apr 2002. ISSN 0004637X. doi: 10.1086/340329.

L. Ofman and M. J. Aschwanden. Damping Time Scaling of Coronal Loop Oscillations Deduced from Transition Region and Coronal Explorer Observations. *Astrophys. J.*, 576 (2):L153–L156, sep 2002. ISSN 0004637X. doi: 10.1086/343886.

L. Ofman and T. Wang. Hot Coronal Loop Oscillations Observed by SUMER: Slow Magnetosonic Wave Damping by Thermal Conduction. *Astrophys. J.*, 580(1):L85–L88, nov 2002. ISSN 0004637X. doi: 10.1086/345548.

L. Ofman, M. Romoli, G. Poletto, G. Noci, and J. L. Kohl. Ultraviolet Coronagraph Spectrometer Observations of Density Fluctuations in the Solar Wind. *Astrophys. J.*, 491 (2):L111–L114, dec 1997. ISSN 0004637X. doi: 10.1086/311067.

L. Ofman, V. M. Nakariakov, and C. E. DeForest. Slow Magnetosonic Waves in Coronal Plumes. *Astrophys. J.*, 514(1):441–447, mar 1999. ISSN 0004-637X. doi: 10.1086/306944.

Takenori J. Okamoto, Patrick Antolin, Bart De Pontieu, Han Uitenbroek, Tom Van Doorsselaere, and Takaaki Yokoyama. Resonant Absorption of Transverse Oscillations and Associated Heating in a Solar Prominence. I. Observational Aspects. *Astrophys. J.*, 809(1):71, 2015. ISSN 15384357. doi: 10.1088/0004-637X/809/1/71. URL http://dx.doi.org/10.1088/0004-637X/809/1/71.

B. Orza, I. Ballai, R. Jain, and K. Murawski. The effect of the environment on the P1/P2 period ratio for kink oscillations of coronal loops. *Astron. Astrophys.*, 537:A41, jan 2012. ISSN 00046361. doi: 10.1051/0004-6361/201117957.

N. R. Owen, I. De Moortel, and A. W. Hood. Forward modelling to determine the observational signatures of propagating slow waves for TRACE, SoHO/CDS, and Hinode/EIS. *Astron. Astrophys.*, 494(1):339–353, jan 2009. ISSN 00046361. doi: 10.1051/0004-6361:200810828. URL http://www.aanda.org/10.1051/0004-6361:200810828.

P. Pagano and I. De Moortel. Contribution of observed multi frequency spectrum of Alfvén waves to coronal heating. *Astron. Astrophys.*, 623, 2019. ISSN 14320746. doi: 10.1051/0004-6361/201834158. URL https://doi.org/10.1051/0004-6361/201834158.

E. N. Parker. Dynamical theory of the solar wind. *Space Sci. Rev.*, 4(5-6):666–708, sep 1965. ISSN 00386308. doi: 10.1007/BF00216273.

D. J. Pascoe and I. De Moortel. Standing kink modes in three-dimensional coronal loops. *Astrophys. J.*, 784(2):101, apr 2014. ISSN 15384357. doi: 10.1088/0004-637X/784/2/101.

D. J. Pascoe and V. M. Nakariakov. Standing sausage modes in curved coronal slabs. *Astron. Astrophys.*, 593:A52, sep 2016. ISSN 14320746. doi: 10.1051/0004-6361/201526546. URL https://ui.adsabs.harvard.edu/abs/2016A{&}A...593A..52P.

D. J. Pascoe, I. De Moortel, and J. A. McLaughlin. Impulsively generated oscillations in a 3D coronal loop. *Astron. Astrophys.*, 505(1):319–327, oct 2009. ISSN 00046361. doi: 10.1051/0004-6361/200912270.

D. J. Pascoe, A. W. Hood, I. De Moortel, and A. N. Wright. Damping of kink waves by mode coupling: II. Parametric study and seismology. *Astron. Astrophys.*, 551:A40, mar 2013. ISSN 00046361. doi: 10.1051/0004-6361/201220620.

D. J. Pascoe, C. R. Goddard, and V. M. Nakariakov. Spatially resolved observation of the fundamental and second harmonic standing kink modes using SDO/AIA. *Astron. Astrophys.*, 593:A53, sep 2016a. ISSN 0004-6361. doi: 10.1051/0004-6361/201628784.

D. J. Pascoe, C. R. Goddard, G. Nisticò, S. A. Anfinogentov, and V. M. Nakariakov. Damping profile of standing kink oscillations observed by SDO/AIA. *Astron. Astrophys.*, 585:L6, jan 2016b. ISSN 14320746. doi: 10.1051/0004-6361/201527835.

D. J. Pascoe, C. R. Goddard, G. Nisticò, S. A. Anfinogentov, and V. M. Nakariakov. Coronal loop seismology using damping of standing kink oscillations by mode coupling. *Astron. Astrophys.*, 589:A136, may 2016c. ISSN 14320746. doi: 10.1051/0004-6361/201628255.

D. J. Pascoe, S. A. Anfinogentov, G. Nisticò, C. R. Goddard, and V. M. Nakariakov. Coronal loop seismology using damping of standing kink oscillations by mode coupling: II. additional physical effects and Bayesian analysis. *Astron. Astrophys.*, 600:A78, apr 2017a. ISSN 14320746. doi: 10.1051/0004-6361/201629702.

D. J. Pascoe, A. J.B. Russell, S. A. Anfinogentov, P. J.A. Simões, C. R. Goddard, V. M. Nakariakov, and L. Fletcher. Seismology of contracting and expanding coronal loops using damping of kink oscillations by mode coupling. *Astron. Astrophys.*, 607:A8, oct 2017b. ISSN 14320746. doi: 10.1051/0004-6361/201730915.

CH Payne. Stellar Atmospheres: Harvard College Observatory Monographs, No. 1. 1925.

A. Perelomova. Magnetoacoustic heating in nonisentropic plasma caused by different kinds of heating-cooling function. *Adv. Math. Phys.*, 2018, 2018. ISSN 16879139. doi: 10.1155/2018/8253210.

H. Peter and P. G. Judge. On the Doppler Shifts of Solar Ultraviolet Emission Lines. *Astrophys. J.*, 522(2):1148–1166, sep 1999. ISSN 0004-637X. doi: 10.1086/307672.

L. J. Porter. Scaling of heating rates in solar coronal loops. *Nature*, 377(6545):131–133, sep 1995. ISSN 00280836. doi: 10.1038/377131a0.

L. J. Porter, J. A. Klimchuk, and P. A. Sturrock. The possible role of MHD waves in heating the solar corona. *Astrophys. J.*, 435:482, nov 1994. ISSN 0004-637X. doi: 10.1086/174830.

S. K. Prasad, D. Banerjee, and T. Van Doorsselaere. Frequency-dependent damping in propagating slow magneto-acoustic waves. *Astrophys. J.*, 789(2), jul 2014. ISSN 15384357. doi: 10.1088/0004-637X/789/2/118.

S. K. Prasad, D. B. Jess, and E. Khomenko. On the source of propagating slow magnetoacoustic waves in sunspots. *Astrophys. J. Lett.*, 812(1):L15, 2015. ISSN 20418213. doi: 10.1088/2041-8205/812/1/L15. URL http://dx.doi.org/10.1088/2041-8205/812/1/L15.

S. K. Prasad, D. B. Jess, J. A. Klimchuk, and D. Banerjee. Unravelling the Components of a Multi-Thermal Coronal Loop Using Magnetohydrodynamic Seismology. *Astrophys. J.*, 834(2):103, 2017. ISSN 0004-637X. doi: 10.3847/1538-4357/834/2/103. URL http://dx.doi.org/10.3847/1538-4357/834/2/103.

S. K. Prasad, J. O. Raes, T. Van Doorsselaere, N. Magyar, and D. B. Jess. The Polytropic Index of Solar Coronal Plasma in Sunspot Fan Loops and Its Temperature Dependence. *Astrophys. J.*, 868(2):149, dec 2018. ISSN 1538-4357. doi: 10.3847/1538-4357/aae9f5. URL https://iopscience.iop.org/article/10.3847/1538-4357/aae9f5.

S. K. Prasad, D. B. Jess, and T. Van Doorsselaere. The Temperature-Dependent Damping of Propagating Slow Magnetoacoustic Waves. *Front. Astron. Sp. Sci.*, 6:57, aug 2019. ISSN 2296-987X. doi: 10.3389/fspas.2019.00057. URL https://www.frontiersin.org/article/10.3389/fspas.2019.00057/full.

Eric Priest. *Magnetohydrodynamics of the Sun*. Cambridge University Press, Cambridge, may 2014. ISBN 9781139020732. URL http://ebooks.cambridge.org/ref/id/CBO9781139020732.

E. Provornikova, L. Ofman, and T. Wang. Excitation of flare-induced waves in coronal loops and the effects of radiative cooling. *Adv. Sp. Res.*, 61(2):645–654, 2018. ISSN 18791948. doi: 10.1016/j.asr.2017.07.042.

C. E. Pugh, A. M. Broomhall, and V. M. Nakariakov. Significance testing for quasi-periodic pulsations in solar and stellar flares. *Astron. Astrophys.*, 602, 2017. ISSN 14320746. doi: 10.1051/0004-6361/201730595. URL https://doi.org/10.1051/0004-6361/201730595.

C. L. Raftery, D. S. Bloomfield, P. T. Gallagher, D. B. Seaton, D. Berghmans, and A. De Groof. Temperature Response of the 171 Å Passband of the SWAP Imager on PROBA2, with a Comparison to TRACE, SOHO, STEREO, and SDO. *Sol. Phys.*, 286:111–124, aug 2013. ISSN 0038-0938. doi: 10.1007/s11207-013-0266-z. URL https://ui.adsabs.harvard.edu/abs/2013SoPh..286..111R.

F. Reale. Coronal loops: Observations and modeling of confined plasma. *Living Rev. Sol. Phys.*, 11(1):1–94, jul 2014. ISSN 16144961. doi: 10.12942/lrsp-2014-4.

J. Reid, P. J. Cargill, A. W. Hood, C. E. Parnell, and T. D. Arber. Coronal energy release by MHD avalanches: Heating mechanisms. *Astron. Astrophys.*, 633:A158, 2020. ISSN 0004-6361. doi: 10.1051/0004-6361/201937051.

V. E. Reznikova, K. Shibasaki, R. A. Sych, and V. M. Nakariakov. Three-minute oscillations above sunspot umbra observed with the Solar Dynamics Observatory/Atmospheric Imaging Assembly and Nobeyama Radioheliograph. *Astrophys. J.*, 746(2):119, 2012. ISSN 15384357. doi: 10.1088/0004-637X/746/2/119.

J. M. Riedl, T. Van Doorsselaere, and I. C. Santamaria. Wave modes excited by photospheric p-modes and mode conversion in a multi-loop system. *Astron. Astrophys.*, 625:1–14, 2019. ISSN 14320746. doi: 10.1051/0004-6361/201935393.

B. Roberts and A. R. Webb. Vertical motions in an intense magnetic flux tube. *Sol. Phys.*, 56(1):5–35, jan 1978. ISSN 00380938. doi: 10.1007/BF00152630.

B. Roberts, P. M. Edwin, and A. O. Benz. On coronal oscillations. *Astrophys. J.*, 279:857, apr 1984. ISSN 0004-637X. doi: 10.1086/161956.

R. Rosner, W. H. Tucker, and G. S. Vaiana. Dynamics of the quiescent solar corona. *Astrophys. J.*, 220:643, mar 1978. ISSN 0004-637X. doi: 10.1086/155949.

M. S. Ruderman and B Roberts. The Damping of Coronal Loop Oscillations. *Astrophys. J.*, 577:475–486, sep 2002. doi: 10.1086/342130.

A. J.B. Russell, P. J.A. Simoes, and L. Fletcher. A unified view of coronal loop contraction and oscillation in flares. *Astron. Astrophys.*, 581:A8, sep 2015. ISSN 14320746. doi: 10.1051/0004-6361/201525746.

H. Safari, S. Nasiri, and Y. Sobouti. Fast kink modes of longitudinally stratified coronal loops. *Astron. Astrophys.*, 470(3):1111–1116, aug 2007. ISSN 00046361. doi: 10.1051/0004-6361:20065997.

A. Savitzky and M. J. E. Golay. Smoothing and Differentiation of Data by Simplified Least Squares Procedures. *Anal. Chem.*, 36(8):1627–1639, jul 1964. ISSN 15206882. doi: 10.1021/ac60214a047. URL https://doi.org/10.1021/ac60214a047.

J. D. Scargle. Studies in astronomical time series analysis. II - Statistical aspects of spectral analysis of unevenly spaced data. *Astrophys. J.*, 263:835, dec 1982. ISSN 0004-637X. doi: 10.1086/160554. URL http://adsabs.harvard.edu/doi/10.1086/160554.

J. T. Schmelz and A. R. Winebarger. What can observations tell us about coronal heating?, may 2015. ISSN 1364503X.

I W Selesnick, R G Baraniuk, and N C Kingsbury. The dual-tree complex wavelet transform. *IEEE Signal Process. Mag.*, 22:123–151, nov 2005. ISSN 1053-5888. doi: 10.1109/MSP.2005.1550194. URL https://ui.adsabs.harvard.edu/abs/2005ISPM...22..123S.

M. Selwa, K. Murawski, and S. K. Solanki. Excitation and damping of slow magnetosonic standing waves in a solar coronal loop. *Astron. Astrophys.*, 436(2):701–709, jun 2005. ISSN 00046361. doi: 10.1051/0004-6361:20042319.

G. Severino. *The Structure and Evolution of the Sun*. Undergraduate Lecture Notes in Physics. Springer International Publishing, Cham, 2017. ISBN 978-3-319-64961-0. doi: 10.1007/978-3-319-64961-0. URL https://doi.org/10.1007/978-3-319-64961-0.

J. Shetye, E. Verwichte, M. Stangalini, P. G. Judge, J. G. Doyle, T. D. Arber, E. M. Scullion, and S. Wedemeyer. Multiwavelength High-resolution Observations of Chromospheric Swirls in the Quiet Sun. *Astrophys. J.*, 881(1):83, 2019. ISSN 1538-4357. doi: 10.3847/1538-4357/ab2bf9. URL http://dx.doi.org/10.3847/1538-4357/ab2bf9.

L. Di G. Sigalotti, C. A. Mendoza-Briceño, and M. Luna-Cardozo. Dissipation of standing slow magnetoacoustic waves in hot coronal loops. *Sol. Phys.*, 246(1):187–212, nov 2007. ISSN 00380938. doi: 10.1007/s11207-007-9077-4.

R. Soler, J. L. Ballester, and S. Parenti. Stability of thermal modes in cool prominence plasmas. *Astron. Astrophys.*, 540:A7, apr 2012. ISSN 00046361. doi: 10.1051/0004-6361/201118492. URL http://www.aanda.org/10.1051/0004-6361/201118492.

R. Soler, M. Goossens, J. Terradas, and R. Oliver. The behavior of transverse waves in nonuniform solar flux tubes. I. Comparison of ideal and resistive results. *Astrophys. J.*, 777(2):158, oct 2013. ISSN 15384357. doi: 10.1088/0004-637X/777/2/158.

R. Soler, M. Goossens, J. Terradas, and R. Oliver. The behavior of transverse waves in nonuniform solar flux tubes. II. implications for coronal loop seismology. *Astrophys. J.*, 781(2):111, 2014. ISSN 15384357. doi: 10.1088/0004-637X/781/2/111.

R. Soler, M. Goossens, and J. L. Ballester. Prominence seismology using the period ratio of transverse thread oscillations. *Astron. Astrophys.*, 575:A123, mar 2015. ISSN 14320746. doi: 10.1051/0004-6361/201424205.

L. Spitzer. ON A POSSIBLE INTERSTELLAR GALACTIC CORONA* Lyman Spitzer, Jr. Princeton University Observatory Received March 24, 1956. *Astrophys. J.*, 34:20–34, jul 1956. ISSN 0004-637X. doi: 10.1086/146200.

L. Spitzer and R. J. Seeger. Physics of Fully Ionized Gases. *Am. J. Phys.*, 31(11):890–891, 1963. ISSN 0002-9505. doi: 10.1119/1.1969155.

H. C. Spruit. Propagation speeds and acoustic damping of waves in magnetic flux tubes. *Sol. Phys.*, 75(1-2):3–17, jan 1982. ISSN 00380938. doi: 10.1007/BF00153456.

A. K. Srivastava and B. N. Dwivedi. Signature of slow acoustic oscillations in a non-flaring loop observed by EIS/Hinode. *New Astron.*, 15(1):8–15, jan 2010. ISSN 13841076. doi: 10.1016/j.newast.2009.05.006.

A. K. Srivastava, B. N. Dwivedi, and M. Kumar. Observations of intensity oscillations in a prominence-like cool loop system as observed by SDO/AIA: Evidence of multiple harmonics of fast magnetoacoustic waves. *Astrophys. Space Sci.*, 345(1):25–32, may 2013. ISSN 0004640X. doi: 10.1007/s10509-013-1361-1.

J. T. Su, Y. Liu, S. Liu, Y. Z. Zhang, H. Zhao, H. Q. Xu, and W. B. Xie. Simultaneous observation of solar oscillations associated with coronal loops from the photosphere to the corona. *Astrophys. J.*, 762(1):42, dec 2013. ISSN 15384357. doi: 10.1088/0004-637X/762/1/42.

X. Sun, J. Todd H., Y. Liu, G. Aulanier, Y. Su, I. G. Hannah, and R. A. Hock. Hot spine loops and the nature of a late-phase solar flare. *Astrophys. J.*, 778(2):139, nov 2013. ISSN 15384357. doi: 10.1088/0004-637X/778/2/139. URL https://iopscience.iop.org/article/10.1088/0004-637X/778/2/139.

R. Sych. MHD Wave in Sunspots. In *Low-Frequency Waves Sp. Plasmas*, chapter 27, pages 467–487. Wiley Blackwell, feb 2016. doi: 10.1002/9781119055006.ch27. URL http://doi.wiley.com/10.1002/9781119055006.ch27.

R. Sych and V. M. Nakariakov. Wave dynamics in a sunspot umbra. *Astron. Astrophys.*, 569:1–8, 2014. ISSN 14320746. doi: 10.1051/0004-6361/201424049.

R. Sych, V. M. Nakariakov, M. Karlicky, and S. A. Anfinogentov. Relationship between wave processes in sunspots and quasi-periodic pulsations in active region flares. *Astron. Astrophys.*, 505(2):791–799, oct 2009. ISSN 00046361. doi: 10.1051/0004-6361/200912132.

R. Sych, T. V. Zaqarashvili, V. M. Nakariakov, S. A. Anfinogentov, K. Shibasaki, and Y. Yan. Frequency drifts of 3-min oscillations in microwave and EUV emission above sunspots. *Astron. Astrophys.*, 539:1–10, 2012. ISSN 00046361. doi: 10.1051/0004-6361/201118271.

J. Terradas, R. Oliver, and J. L. Ballester. Damping of Kink Oscillations in Curved Coronal Loops. *Astrophys. J.*, 650(1):L91–L94, oct 2006. ISSN 0004-637X. doi: 10.1086/508569.

J. Terradas, J. Andries, M. Goossens, I. Arregui, R. Oliver, and J. L. Ballester. Nonlinear Instability of kink oscillations due to shear motions. *Astrophys. J.*, 687(2):L115–L118, sep 2008a. doi: 10.1086/593203. URL http://arxiv.org/abs/0809.3664http://dx.doi.org/10.1086/593203.

J. Terradas, I. Arregui, R. Oliver, J. L. Ballester, J. Andries, and M. Goossens. Resonant Absorption in Complicated Plasma Configurations: Applications to Multistranded Coronal Loop Oscillations. *Astrophys. J.*, 679(2):1611–1620, jun 2008b. ISSN 0004-637X. doi: 10.1086/586733.

J Terradas, M Goossens, and G Verth. Selective spatial damping of propagating kink waves due to resonant absorption. *Astron. Astrophys.*, 524:A23, dec 2010. ISSN 0004-6361. doi: 10.1051/0004-6361/201014845. URL https://ui.adsabs.harvard.edu/abs/2010A{&}A...524A..23T.

S. Terzo and F. Reale. On the importance of background subtraction in the analysis of coronal loops observed with TRACE. *Astron. Astrophys.*, 515(1), feb 2010. ISSN 14320746. doi: 10.1051/0004-6361/200913469. URL http://dx.doi.org/10.1051/0004-6361/200913469.

H. Thackray and R. Jain. Fast magnetohydrodynamic waves in a solar coronal arcade. *Astron. Astrophys.*, 608:A108, dec 2017. ISSN 0004-6361. doi: 10.1051/0004-6361/201731193. URL http://www.aanda.org/10.1051/0004-6361/201731193.

J. O. Thurgood, R. J. Morton, and J. A. McLaughlin. First direct measurements of transverse waves in solar polar plumes using SDO/AIA. *Astrophys. J. Lett.*, 790(1):L2, jul 2014. ISSN 20418213. doi: 10.1088/2041-8205/790/1/L2.

H. Tian, S. W. McIntosh, T. Wang, L. Ofman, B. De Pontieu, D. E. Innes, and H. Peter. Persistent doppler shift oscillations observed with hinode/eis in the solar corona: Spectroscopic signatures of alfvénic waves and recurring upflows. *Astrophys. J.*, 759(2):144, nov 2012. ISSN 15384357. doi: 10.1088/0004-637X/759/2/144. URL https://ui.adsabs.harvard.edu/abs/2012ApJ...759..144T.

H. Tian, E. Deluca, K. K. Reeves, S. McKillop, B. De Pontieu, J. Martínez-Sykora, M. Carlsson, V. Hansteen, L. Kleint, M. Cheung, L. Golub, S. Saar, P. Testa, M. Weber, J. Lemen, A. Title, P. Boerner, N. Hurlburt, T. D. Tarbell, J. P. Wuelser, C. Kankelborg, S. Jaeggli, and S. W. McIntosh. High-resolution observations of the shock wave behavior for sunspot oscillations with the Interface Region Imaging Spectrograph. *Astrophys. J.*, 786(2):137, apr 2014a. ISSN 15384357. doi: 10.1088/0004-637X/786/2/137. URL http://dx.doi.org/10.1088/0004-637X/786/2/137.

H. Tian, L. Kleint, H. Peter, M. Weber, P. Testa, E. Deluca, L. Golub, and N. Schanche. Observations of subarcsecond bright dots in the transition region above sunspots with

the Interface Region Imaging Spectrograph. *Astrophys. J. Lett.*, 790(2), 2014b. ISSN 20418213. doi: 10.1088/2041-8205/790/2/L29.

S. Tomczyk, S. W. McIntosh, S. L. Keil, P. G. Judge, T. Schad, D. H. Seeley, and J. Edmondson. Alfvén waves in the solar corona. *Science (80-.).*, 317(5842):1192–1196, aug 2007. ISSN 00368075. doi: 10.1126/science.1143304.

T. Török and B. Kliem. Confined and Ejective Eruptions of Kink-unstable Flux Ropes. *Astrophys. J.*, 630(1):L97–L100, sep 2005. ISSN 0004-637X. doi: 10.1086/462412.

C. Torrence and G. P. Compo. A Practical Guide to Wavelet Analysis. *Bull. Am. Meteorol. Soc.*, 79(1):61–78, jan 1998. ISSN 00030007. doi: 10.1175/1520-0477(1998)079¡0061:APGTWA¿2.0.CO;2. URL http://journals.ametsoc.org/doi/abs/10.1175/1520-0477{%}281998{%}29079{%}3C0061{%}3AAPGTWA{%}3E2.0.CO{%}3B2.

I. Ugarte-Urra and H. P. Warren. Temporal variability of active region outflows. *Astrophys. J.*, 730(1):37, mar 2011. ISSN 15384357. doi: 10.1088/0004-637X/730/1/37.

V. M. Uritsky, J. M. Davila, N. M. Viall, and L. Ofman. Measuring temperature-dependent propagating disturbances in coronal fan loops using multiple SDO/AIA channels and the surfing transform technique. *Astrophys. J.*, 778(1):26, aug 2013. ISSN 15384357. doi: 10.1088/0004-637X/778/1/26. URL http://dx.doi.org/10.1088/0004-637X/778/1/26.

A. A. Van Ballegooijen, M. Asgari-Targhi, S. R. Cranmer, and E. E. Deluca. Heating of the solar chromosphere and corona by Alfvén wave turbulence. *Astrophys. J.*, 736(1):3, jul 2011. ISSN 15384357. doi: 10.1088/0004-637X/736/1/3.

T. Van Doorsselaere, J. Andries, S. Poedts, and M. Goossens. Damping of Coronal Loop Oscillations: Calculation of Resonantly Damped Kink Oscillations of One-dimensional Nonuniform Loops. *Astrophys. J.*, 606(2):1223–1232, may 2004a. ISSN 0004-637X. doi: 10.1086/383191.

T. Van Doorsselaere, A. Debosscher, J. Andries, and S. Poedts. The effect of curvature on quasi-modes in coronal loops. *Astron. Astrophys.*, 424(3):1065–1074, sep 2004b. ISSN 00046361. doi: 10.1051/0004-6361:20041239.

T. Van Doorsselaere, V. M. Nakariakov, and E. Verwichte. Coronal loop seismology using multiple transverse loop oscillation harmonics. *Proc. Int. Astron. Union*, 3(S247):140–146, oct 2007. ISSN 17439221. doi: 10.1017/S1743921308014798.

T. Van Doorsselaere, V. M. Nakariakov, P. R. Young, and E. Verwichte. Coronal magnetic field measurement using loop oscillations observed by Hinode/EIS. *Astron. Astrophys.*, 487(2):L17–L20, aug 2008. ISSN 00046361. doi: 10.1051/0004-6361:200810186.

T. Van Doorsselaere, E. Verwichte, and J. Terradas. The effect of loop curvature on coronal loop kink oscillations. *Space Sci. Rev.*, 149(1-4):299–324, dec 2009. ISSN 15729672. doi: 10.1007/s11214-009-9530-9.

T. Van Doorsselaere, N. Wardle, G. Del Zanna, K. Jansari, E. Verwichte, and V. M. Nakariakov. The first measurement of the adiabatic index in the solar corona using time-dependent spectroscopy of hinode/EIS observations. *Astrophys. J. Lett.*, 727(2 PART II):L32, feb 2011. ISSN 20418213. doi: 10.1088/2041-8205/727/2/L32. URL http://stacks.iop.org/2041-8205/727/i=2/a=L32?key=crossref.508dcbd9c59ef0cc338dc84212638e68.

T. Van Doorsselaere, P. Antolin, and K. Karampelas. Broadening of the differential emission measure by multi-shelled and turbulent loops. *Astron. Astrophys.*, 620:A65, nov 2018. ISSN 0004-6361. doi: 10.1051/0004-6361/201834086. URL https://ui.adsabs.harvard.edu/abs/2018A{&}A...620A..65V.

Z. M. Vashalomidze, T. V. Zaqarashvili, and V. D. Kukhianidze. Measurement of the Polytropic Index During Solar Coronal Rain Using a Diagram of the Electron Density Distribution as a Function of Electron Temperature. *Astrophysics*, 62(1):69–78, mar 2019. ISSN 05717256. doi: 10.1007/s10511-019-09565-8. URL https://doi.org/10.1007/s10511-019-09565-8.

G. Verth and R. Erdélyi. Effect of longitudinal magnetic and density inhomogeneity on transversal coronal loop oscillations. *Astron. Astrophys.*, 486(3):1015–1022, aug 2008a. ISSN 00046361. doi: 10.1051/0004-6361:200809626.

G. Verth and R. Erdélyi. Effect of longitudinal magnetic and density inhomogeneity on transversal coronal loop oscillations. *Astron. Astrophys.*, 486(3):1015–1022, 2008b. ISSN 00046361. doi: 10.1051/0004-6361:200809626.

G. Verth, R. Erdélyi, and D. B. Jess. Refined Magnetoseismological Technique for the Solar Corona. *Astrophys. J.*, 687(1):L45–L48, nov 2008. ISSN 0004-637X. doi: 10.1086/593184.

G. Verth, M. Goossens, and J. S. He. Magnetoseismological determination of magnetic field and plasma density height variation in a solar spicule. *Astrophys. J. Lett.*, 733(1 PART 2):L15, 2011. ISSN 20418205. doi: 10.1088/2041-8205/733/1/L15.

E. Verwichte, V. M. Nakariakov, L. Ofman, and E. E. Deluca. Characteristics of transverse oscillations in a coronal loop arcade. *Sol. Phys.*, 223(1-2):77–94, 2004. ISSN 00380938. doi: 10.1007/s11207-004-0807-6.

E. Verwichte, V. M. Nakariakov, and F. C. Cooper. Transverse waves in a post-flare supra-arcade. *Astron. Astrophys.*, 430(3):L65–L68, jan 2005. ISSN 00046361. doi: 10.1051/0004-6361:200400133.

E. Verwichte, C. Foullon, and V. M. Nakariakov. Seismology of curved coronal loops with vertically polarised transverse oscillations. *Astron. Astrophys.*, 452(2):615–622, jun 2006. ISSN 00046361. doi: 10.1051/0004-6361:20054437.

E. Verwichte, M. Haynes, T. D. Arber, and C. S. Brady. Damping of Slow MHD Coronal Loop Oscillations by Shocks. *Astrophys. J.*, 685(2):1286–1290, oct 2008. ISSN 0004-637X. doi: 10.1086/591077.

E. Verwichte, T. Van Doorsselaere, C. Foullon, and R. S. White. Coronal Alfvén speed determination: Consistency between seismology using AIA/SDO transverse loop oscillations and magnetic extrapolation. *Astrophys. J.*, 767(1):16, apr 2013a. ISSN 15384357. doi: 10.1088/0004-637X/767/1/16.

E. Verwichte, T. Van Doorsselaere, R. S. White, and P. Antolin. Statistical seismology of transverse waves in the solar corona. *Astron. Astrophys.*, 552:1–9, 2013b. ISSN 00046361. doi: 10.1051/0004-6361/201220456.

J. F. Vesecky, S. K. Antiochos, and J. H. Underwood. Numerical modeling of quasi-static coronal loops. I - Uniform energy input. *Astrophys. J.*, 233(3):987, nov 1979. ISSN 0004-637X. doi: 10.1086/157462.

T. Wang. Standing slow-mode waves in hot coronal loops: Observations, modeling, and coronal seismology. *Space Sci. Rev.*, 158(2-4):397–419, jul 2011. ISSN 00386308. doi: 10.1007/s11214-010-9716-1.

T. Wang and L. Ofman. Determination of Transport Coefficients by Coronal Seismology of Flare-induced Slow-mode Waves: Numerical Parametric Study of a 1D Loop Model. *Astrophys. J.*, 886(1):2, 2019. ISSN 1538-4357. doi: 10.3847/1538-4357/ab478f. URL http://dx.doi.org/10.3847/1538-4357/ab478f.

T. Wang, S. K. Solanki, W. Curdt, D. E. Innes, and I. E. Dammasch. Doppler Shift Oscillations of Hot Solar Coronal Plasma Seen by SUMER: A Signature of Loop Oscillations? *Astrophys. J.*, 574(1):L101–L104, jul 2002. ISSN 0004637X. doi: 10.1086/342189.

T. Wang, D. E. Innes, and J. Qiu. Determination of the Coronal Magnetic Field from Hot-Loop Oscillations Observed by SUMER and SXT. *Astrophys. J.*, 656(1):598–609, 2007. ISSN 0004-637X. doi: 10.1086/510424.

T. Wang, L. Ofman, J. M. Davila, and Y. N. Su. Growing transverse oscillations of a multistranded loop observed by SDO/AIA. *Astrophys. J. Lett.*, 751(2):L27, jun 2012. ISSN 20418205. doi: 10.1088/2041-8205/751/2/L27. URL https://ui.adsabs.harvard.edu/abs/2012ApJ...751L..27W.

T. Wang, L. Ofman, X. Sun, E. Provornikova, and J. M. Davila. Evidence of Thermal Conduction Suppression in a Solar Flaring Loop by Coronal Seismology of Slow-mode Waves. *Astrophys. J. Lett.*, 811(1), sep 2015. ISSN 20418213. doi: 10.1088/2041-8205/811/1/L13.

T. Wang, L. Ofman, X. Sun, S. K. Solanki, and J. M. Davila. Effect of Transport Coefficients on Excitation of Flare-induced Standing Slow-mode Waves in Coronal Loops. *Astrophys. J.*, 860(2):107, jun 2018. ISSN 1538-4357. doi: 10.3847/1538-4357/aac38a.

T. J. Wang, S. K. Solanki, W. Curdt, D. E. Innes, I. E. Dammasch, and B. Kliem. Hot coronal loop oscillations observed with SUMER: Examples and statistics. *Astron. Astrophys.*, 406 (3):1105–1121, aug 2003. ISSN 00046361. doi: 10.1051/0004-6361:20030858.

Micah J Weberg, Richard J Morton, and James A McLaughlin. Using Transverse Waves to Probe the Plasma Conditions at the Base of the Solar Wind. *Astrophys. J.*, 894(1):79, 2020. ISSN 1538-4357. doi: 10.3847/1538-4357/ab7c59. URL http://dx.doi.org/10.3847/1538-4357/ab7c59.

R. Wildt. Negative Ions of Hydrogen and the Opacity of Stellar Atmospheres. *Astrophys. J.*, 90:611, nov 1939. ISSN 0004-637X. doi: 10.1086/144125.

K. Wilhelm, L. Abbo, F. Auchère, N. Barbey, L. Feng, A. H. Gabriel, S. Giordano, S. Imada, A. Llebaria, W. H. Matthaeus, G. Poletto, N. E. Raouafi, S. T. Suess, L. Teriaca, and Y. M. Wang. Morphology, dynamics and plasma parameters of plumes and inter-plume regions in solar coronal holes, dec 2011. ISSN 09354956.

T. Williams, R. W. Walsh, A. R. Winebarger, D. H. Brooks, J. W. Cirtain, B. De Pontieu, L. Golub, K. Kobayashi, D. E. Mckenzie, R. J. Morton, H. Peter, L. A. Rachmeler, S. L. Savage, P. Testa, S. K. Tiwari, H. P. Warren, and B. J. Watkinson. Is the High-Resolution Coronal Imager Resolving Coronal Strands? Results from AR 12712. *Astrophys. J.*, 892(2):134, 2020. ISSN 1538-4357. doi: 10.3847/1538-4357/ab6dcf. URL http://dx.doi.org/10.3847/1538-4357/ab6dcf.

A. R. Winebarger, H. P. Warren, and J. T. Mariska. Transition Region and Coronal Explorer and Soft X-Ray Telescope Active Region Loop Observations: Comparisons with Static Solutions of the Hydrodynamic Equations. *Astrophys. J.*, 587(1):439–449, apr 2003. ISSN 0004-637X. doi: 10.1086/368017.

A. R. Yeates, T. Amari, I. Contopoulos, X. Feng, D. H. Mackay, Z. Mikić, T. Wiegelmann, J. Hutton, C. A. Lowder, H. Morgan, G. Petrie, L. A. Rachmeler, L. A. Upton, A. Canou, P. Chopin, C. Downs, M. Druckmüller, J. A. Linker, D. B. Seaton, and T. Török. Global Non-Potential Magnetic Models of the Solar Corona During the March 2015 Eclipse, aug 2018. ISSN 15729672.

H. Yu, S. X. Chen, B. Li, and L. D. Xia. Period ratios for standing kink and sausage modes in magnetized structures with siphon flow on the Sun. *Res. Astron. Astrophys.*, 16(6):92, jun 2016. ISSN 16744527. doi: 10.1088/1674-4527/16/6/092.

D. Yuan and T. Van Doorsselaere. Forward Modeling of Standing Kink Modes in Coronal Loops. I. Synthetic Views. *Astrophys. J. Suppl. Ser.*, 223(2):23, apr 2016. ISSN 0067-0049. doi: 10.3847/0067-0049/223/2/23. URL https://iopscience.iop.org/article/10.3847/0067-0049/223/2/23.

D. Yuan and V. M. Nakariakov. Measuring the apparent phase speed of propagating EUV disturbances. *Astron. Astrophys.*, 543:1–10, 2012. ISSN 00046361. doi: 10.1051/0004-6361/201218848.

D. Yuan, R. Sych, V. E. Reznikova, and V. M. Nakariakov. Multi-height observations of magnetoacoustic cut-off frequency in a sunspot atmosphere. *Astron. Astrophys.*, 561 (1977):1–6, 2014. ISSN 00046361. doi: 10.1051/0004-6361/201220208.